Workshop on New Views of the Moon II:

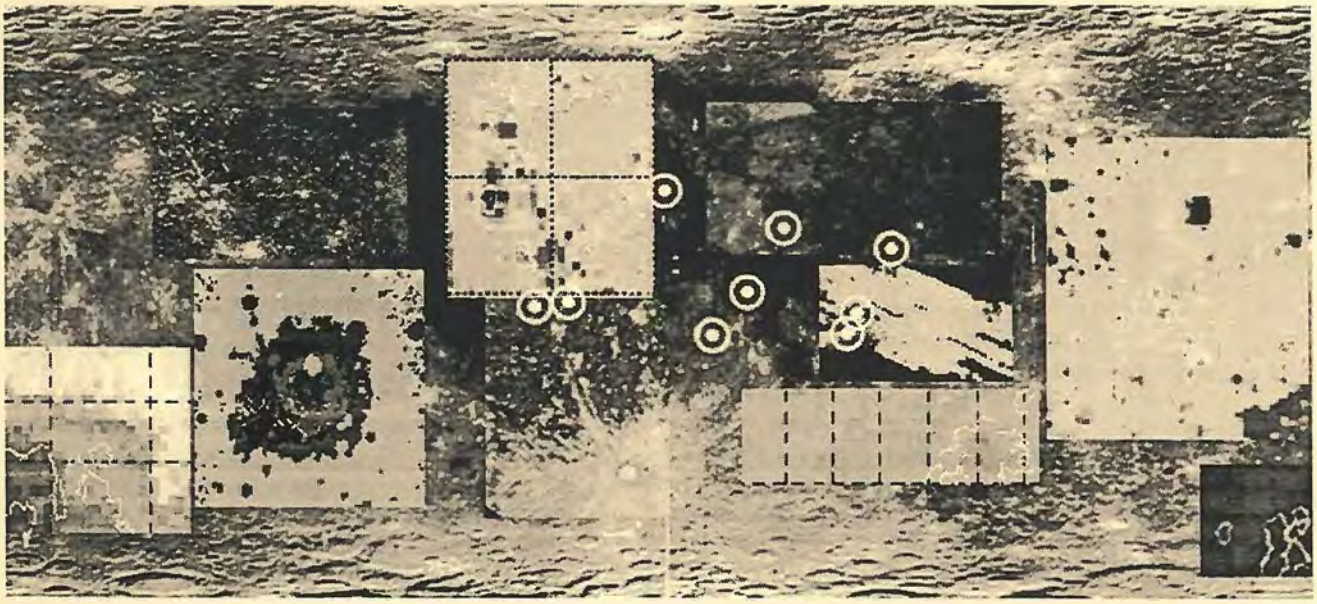

Understanding the Moon Through the Integration of Diverse Datasets

September 22–24, 1999

Flagstaff, Arizona

WORKSHOP ON
NEW VIEWS OF THE MOON II:
UNDERSTANDING THE MOON THROUGH THE INTEGRATION OF DIVERSE DATASETS

Flagstaff, Arizona
September 22–24, 1999

Conveners
Lisa Gaddis and Charles K. Shearer

Sponsored by
Lunar and Planetary Institute
Museum of Northern Arizona
National Aeronautics and Space Administration
U.S. Geological Survey, Flagstaff

Lunar and Planetary Institute 3600 Bay Area Boulevard Houston TX 77058-1113

LPI Contribution No. 980

Compiled in 1999 by
LUNAR AND PLANETARY INSTITUTE

The Institute is operated by the Universities Space Research Association under Contract No. NASW-4574 with the National Aeronautics and Space Administration.

Abstracts in this volume may be cited as

Author A. B. and Author C. D. (1999) Title of Abstract. In *Workshop on New Views of the Moon II: Understanding the Moon Throughout the Integration of Diverse Datasets.* LPI Contribution No. 980, Lunar and Planetary Institute, Houston.

This volume is distributed by

ORDER DEPARTMENT
Lunar and Planetary Institute
3600 Bay Area Boulevard
Houston TX 77058-1113, USA
Phone: 281-486-2172
Fax: 281-486-2186
E-mail: order@lpi.jsc.nasa.gov

Mail order requestors will be invoiced for the cost of shipping and handling.

Preface

This volume contains abstracts that have been accepted for presentation at the Workshop on New Views of the Moon II: Understanding the Moon Through the Integration of Diverse Datasets, September 22–24, 1999, in Flagstaff, Arizona. The workshop conveners are Lisa Gaddis (*U.S. Geological Survey, Flagstaff*) and Charles K. Shearer (*University of New Mexico*). Color versions of some of the images contained in this volume are available on the meeting Web site (http://cass.jsc.nasa.gov/meetings/moon99/pdf/program.pdf).

Logistics, administration, and publications support for this meeting were provided by the staff of the Publications and Program Services Department at the Lunar and Planetary Institute.

Contents

Abstracts

PROSPECTING FOR LUNAR RESOURCES WITH GLOBAL GEOCHEMICAL AND MULTISPECTRAL DATA. C. C. Allen, Lockheed Martin Space Operations Corporation, 2400 NASA Road 1, Houston TX 77058, USA (carlton.c.allenl@jsc.nasa.gov).

Introduction: Laboratory experiments have demonstrated correlations between the abundances of some lunar resources and specific chemical and mineralogical parameters of surface materials. Global remote sensing from the Apollo, Galileo, Clementine, and Lunar Prospector missions, combined with Earth-based observations, has now quantified these parameters. Combining experiments and remote sensing allows the first prospecting for resources across the entire lunar surface.

The Moon's rocks and soil contain resources that could be used to support a future lunar base for research or for launching expeditions into deep space. Lunar O is the resource most likely to be exploited first, for both propulsion and life support [1]. The efficiency of O extraction from lunar materials has been shown to depend strongly on the material's chemical and mineralogical composition.

Some lunar materials may be rare and vital enough on Earth to justify the cost of their return. The rare isotope ^{3}He, which can be used in an efficient and low-polluting fusion power reaction, has been cited as one such resource [2]. Solar-wind helium, including ^{3}He, is implanted in lunar regolith grains and can be released by heating. Helium concentration has been shown to correlate with soil composition.

O_2 — Correlated with Iron in Lunar Soil: *Experiments.* Over 20 different processes have been proposed for O production on the Moon [3]. Among the simplest and best studied of these processes is the reduction of oxides in lunar minerals and glass using H gas. Allen et al. [4] reported the results of O extraction experiments on 16 lunar soils. Each sample was reacted in flowing H for 3 h at 1050°C. Total O yield correlated strongly to each sample's initial Fe^{2+} abundance. A linear least-squares fit of O yield vs. Fe^{2+} for 16 lunar soils yielded a regression line with a slope of 0.19, an intercept of 0.55 wt% O and an r^2 value of 0.87. Oxygen yield did not significantly correlate with the abundance of any element except Fe. Thus, O yield from lunar soils can be predicted with nearly 90% confidence based solely on their iron abundances. The potential for O production at any location on the Moon can be predicted if the soil's Fe concentration is known.

Global Remote Sensing. On a global scale, Fe concentration in the near surface has been estimated from data returned by a variety of spacecraft. Iron was one of several elements measured from near-equatorial orbits during the Apollo 15 and 16 missions, using γ-ray spectrometry [5]. These data covered approximately 20% of the lunar surface, with spatial resolutions of ~100 km. An improved γ-ray spectrometer and a neutron spectrometer, flown on the Lunar Prospector spacecraft in a polar orbit, provided Fe abundance data for the entire lunar surface, again at a spatial resolution of ~100 km [6].

A technique for iron assessment based on orbital multispectral imaging has been developed by Lucey et al. [7]. This method correlates Fe abundance to a parameter derived from reflectance values at 750 and 900 nm. The authors use data from the Clementine spacecraft to map Fe abundances across nearly the entire lunar surface. These data can support identification of Fe-rich regions as small as a few hundred meters across. Clark and McFadden [8] and Elphic et al. [9] find good agreement between γ-ray/neutron and multispectral Fe determinations for most areas on the Moon.

O_2 — Correlated with Volcanic Glass Beads: *Experiments.* The H-reduction experiments cited above [2] also showed submillimeter volcanic glass beads could be highly desirable feedstocks for lunar O production. Iron-rich species, represented by glassy (orange) and crystalline (black) beads, promise particularly high O yields. Apollo 17 volcanic glass sample 74220, composed predominantly of orange glass beads with an average diameter of 40 mm, contains 17.8 wt% Fe^{2+}. Reduction of this sample yielded 4.3 wt% O, well above the regression line defined by the experiments on 16 lunar soils. Sample 74001 is dominated by black crystalline beads, the isochemical equivalent of orange glasses. Reduction of 74001 yielded 4.7 wt% O, the highest value for any lunar sample.

Global Remote Sensing. Extensive areas of the lunar surface covered by volcanic glass beads have been delineated using Earth-based data and spacecraft orbital photography [10]. Chemical compositions of the deposits have been estimated and mixing ratios of glassy and crystalline glass beads have been determined [11]. Clementine multispectral imagery has been employed to determine the precise extent and estimate the thickness of one widespread deposit, that of the Aristarchus Plateau [12].

Ice — Correlated with Hydrogen in Polar Cold Traps: *Theory.* Lunar ice could prove to be a highly advantageous O source, compared to O derived from soil reduction, in terms of process complexity and power requirements. Thus, a deposit of ice on the Moon is a potentially important resource.

Permanently shadowed polar craters have been modeled as possible cold traps for water ice, derived either from indigenous sources or from comets [13]. Any lunar ice deposits must occur in extremely restricted areas near the poles. Only crater interiors that are permanently shadowed from sunlight are cold enough to have retained volatiles for a significant part of the Moon's history.

Global Remote Sensing. Clementine images and Earth-based radar have demonstrated that craters whose interiors are never exposed to sunlight do exist near the lunar poles [14,15]. Water ice has been tentatively identified in some of these craters using Clementine bi-static radar data [14].

Lunar Prospector mapped the epithermal and fast-neutron fluxes across the entire Moon [16]. Low epithermal fluxes are correlated with concentrations of H, and by extension ice, in the near-surface. Such signatures were observed near permanently-shadowed craters at both lunar poles. Calculation of the actual amount of water ice in these cold traps is strongly model-dependent but each polar region could contain as much as 3×10^9 t of water ice.

^{3}He — Correlated with Titanium in Lunar Soil: *Experiments.* The concentration of solar wind-implanted He in mare regolith increases with the soil's Ti content [17]. This correlation is apparently due to preferential adsorption of He by ilmenite grains. Experiments simulating interaction of the solar wind with terrestrial ilmenite resulted in a release curve very similar to the release curve from the Apollo 11 regolith samples [18]. Thus, Ti in mare soils is a predictor of the ^{3}He resource [19].

Global Remote Sensing. Data from the Lunar Prospector γ-ray and neutron spectrometers have been used to determine regolith Ti abundances across the entire Moon at a spatial resolution of ~100 km [6]. Clementine multispectral data have also been employed to quantify Ti at a resolution of a few hundred meters [7]. Good correlation has been determined between Ti abundances determined by the two methods [9].

Challenges Remaining: The full integration of laboratory experiments has not been completed, and challenges remain for lunar resource prospecting, including: (1) integrating the higher precision of γ-ray chemical analysis with the higher spatial resolution of multispectral chemical analysis; (2) combining chemical and spectral datasets to locate additional deposits volcanic glass beads, corresponding to the full range of compositions found in lunar soils; (3) demonstrating the relationship of enhanced H concentrations to ice concentrations in permanently shadowed craters; and (4) refining the correlation of solar wind gas concentrations to soil chemistry and mineralogy.

References: [1] Joosten B. K. and Guerra L. A. (1993) *AIAA Space Prog. Tech. Conf. Paper 93-4784,* Am. Inst. Aeronautics Astronautics. [2] Wittenberg L. J. et al. (1986) *Fusion Tech., 10,* 167–178. [3] Taylor L. A. and Carrier W. D. III (1992) in *Engineering, Construction, and Operations in Space III,* pp. 752–762, Am. Soc. Civ. Eng. [4] Allen C. C. et al. (1996) *JGR, 101,* 26085–26095. [5] Davis P. A. Jr. (1980) *JGR, 85,* 3209–3224. [6] Feldman W. C. et al. (1996) *LPS XXVII,* 355–356. [7] Lucey P. G. et al. (1995) *Science, 268,* 1150–1153. [8] Clark P. E. and McFadden L. A. (1996) *LPS XXVII,* 227–228. [9] Elphic R. C. et al. (1996) *Science, 281,* 1493–1496. [10] Gaddis L. R. et al. (1985) *Icarus, 61,* 461–489. [11] Weitz C. M. et al. (1998) *JGR, 103,* 22725–22759. [12] McEwen A. S. et al. (1994) *Science, 266,* 1959–1962. [13] Arnold J. (1979) *JGR, 84,* 5659–5668. [14] Nozette S. et al. (1996) *Science, 274,* 1495–1498. [15] Margot J. L. et al. (1999) *Science, 284,* 1658–1660. [16] Feldman W. C. et al. (1998) *Science, 281,* 1489–1493. [17] Cameron E. N. (1988) in *The Second Conference on Lunar Bases and Space Activities of the 21st Century,* pp. 89–97, LPI. [18] Harris-Kuhlman K. R. and Kulcinski G. L. (1998) in *Engineering, Construction, and Operations in Space VI,* pp. 533–540, Am. Soc. Civ. Eng. [19] Taylor L. A. (1990) in *Engineering, Construction, and Operations in Space II,* pp. 68–77, Am. Soc. Civ. Eng.

PHOTOMETRIC IMAGING OF THE MOON FROM THE ROBOTIC LUNAR OBSERVATORY.

J. M. Anderson and H. H. Kieffer, U.S. Geological Survey, Flagstaff AZ 86001, USA.

Introduction: As part of the calibration program for the NASA Earth Observing System (part of NASA's Earth Science Enterprise) [1], the U.S. Geological Survey operates the Robotic Lunar Observatory (ROLO). The ROLO project is designed to produce a photometric model of the nearside lunar surface for all phase and libration angles visible from Flagstaff [2]. Goals for this photometric model are 2.5% absolute and 1.0% relative uncertainty. Although the model is principally intended to produce radiance images of the Moon for use in calibration of Earth-orbiting spacecraft, the ROLO data and model will also provide important information for studies of the lunar soil.

Instrumentation: An astronomical observatory dedicated to the radiometry of the Moon has been constructed on the campus of the U.S. Geological Survey Flagstaff Field Station in Arizona. Two separate camera systems are attached to a single telescope mount and boresighted to the same pointing direction. The visible/near infrared (VNIR) camera uses a 512 × 512 pixel CCD and 23 intermediate-width interference filters for wavelength selection. The shortwave infrared (SWIR) camera uses a 256 × 256 pixel cooled-HgCdTe infrared array and nine intermediate-width interference filters. Table 1 and Fig. 1 provide information on the instrumental passbands. Separate 20-cm-diameter Ritchey-Cretien telescopes are provided for the two cameras. The optics are designed to image the entire Moon within each camera's field of view, resulting in instrument pixel scales of 4 and 8 arcsec pixel^{-1} (~7.4 and 15 km pixel^{-1} for the sub-Earth point on the Moon) for VNIR and SWIR respectively. Detailed information on the instrumentation can be found in Anderson et al. [3].

TABLE 1. ROLO filter bandpasses.

λ_c (nm)	$\Delta\lambda$ (nm)	T (%)	QE (%)	Band
		VNIR		
347.3	32.5	62	15	*u*
352.5	31.6	52	15	*u*
405.0	16.2	54	15	*v*
412.7	12.5	52	15	*c*
415.1	17.8	56	15	*v*
441.8	9.6	61	15	*c*
466.5	20.0	86	16	*b*
475.7	18.4	85	16	*b*
488.1	7.9	81	17	*c*
545.0	18.8	91	25	*y,V*
550.3	8.7	72	25	*c*
554.9	18.1	92	25	*y,V*
666.7	8.3	87	35	*c*
694.8	16.8	84	36	*R*
705.5	16.7	87	36	*R*
747.1	8.7	72	32	*c*
765.6	16.8	95	28	
776.5	16.9	98	28	
867.7	13.9	78	16	*c*
875.3	18.4	92	15	*I*
885.2	16.0	94	15	*I*
934.6	17.6	94	7	
944.7	18.8	94	6	
		SWIR		
944.3	21.5	65	67	
1062.2	27.1	52	66	*J*
1246.5	23.3	62	66	*J*
1542.7	48.6	56	67	*H*
1637.8	23.4	66	67	*H*
1984.8	38.5	54	70	
2131.8	54.7	64	65	*K*
2256.3	48.2	54	63	*K*
2390.3	58.2	48	60	*K*

λ-effective wavelength for flat spectrum; Δl-half-power bandwidth; *T*-filter transmission for equivalent rectangular bandpass; *QE*-detector quantum efficiency; Band–corresponding standard magnitude band, if applicable, "*c*" indicates cross-calibration radiometer band.

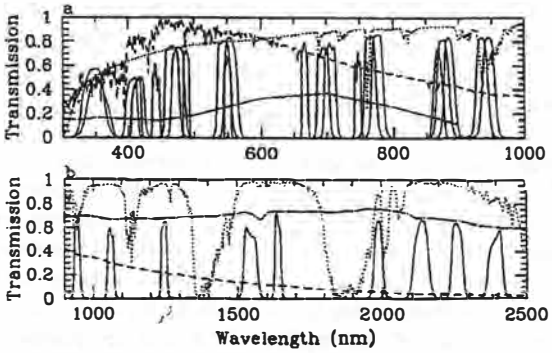

Fig. 1. Robotic Lunar Observatory Filter Response. The transmission curves for VNIR (a) and SWIR (b) filters (solid lines) are plotted as a function of wavelength. Also shown are a normalized solar spectrum (dashed), nominal atmospheric transmission (dotted), and the quantum efficiency of the ROLO detectors (dot-dash). (This plot is similar to Fig. 4 in Kieffer and Anderson [5].)

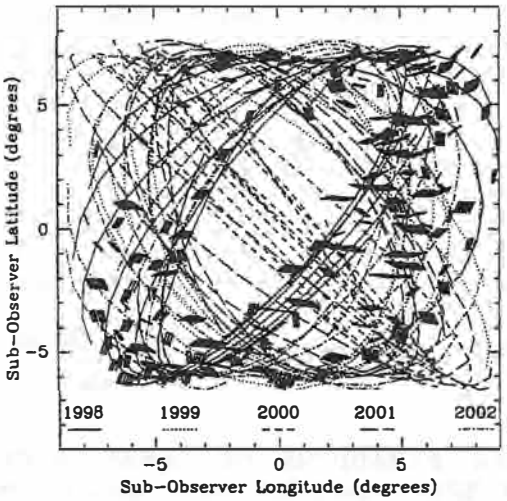

Fig. 2. Robotic Lunar Observatory Lunar Observations. Observations of the Moon made with the SWIR camera through 1999 June are shown as thick bars in the phase/libration space available to ROLO. Phase angle is indicated by the slopes of the bars — horizontal bars indicate 0° phase and vertical bars indicate 90° phase. Positive slopes correspond to observations after Full Moon. The thin lines connect topocentric libration angles for Flagstaff at midnight for consecutive nights between First and Last Quarter Moons from 1998 through 2002. Several years of continued observations are necessary to fill in the empty regions of the phase/libration space.

Observations: Routine imaging has been in progress since late 1995 for VNIR and late 1997 for SWIR, and is expected to continue through at least 2002. ROLO observes the Moon every clear night between the first and last quarter phases of the moon. On such nights, the Moon is imaged through all 32 filters at half-hour intervals during the time that the Moon is above the 60° zenith angle. Observations of standard stars to measure atmospheric extinction and detector responsivity drifts occupy the remainder of the nighttime. Measurements of the dark current and detector bias levels are made during the dusk and dawn periods for VNIR and throughout the night for SWIR. Flat field corrections and absolute radiance calibrations are provided through observations of a Spectralon plate illuminated by a NIST-traceable 1000 W FEL lamp. Raw data are converted to ISIS [4] cubes and stored on CD-ROM. Detailed information on the observing procedure is also found in Anderson et al. [3].

Data: As the development of data-reduction software for the ROLO project progresses and additional data are accumulated, the raw data are repeatedly processed into a calibrated form. Corrections for instrument response characteristics, photon scattering processes, and atmospheric extinction are applied to the raw lunar images to produce exoatmospheric radiance images of the Moon. These images are then transformed to a fixed selenographic-grid projection designed to accommodate all of the possible viewing geometries of the ROLO telescope [2]. A preliminary discussion of results for the total irradiance of the Moon derived from ROLO VNIR images acquired through April 1998 was published by Kieffer and Anderson [5]. At that time, difficulties in adequately determining the atmospheric extinction limited the accuracy of the derived lunar irradiance values. Significant improvements in the reduction software have been developed since that time and measurement scatter is expected to be reduced to ≤2% for the data-processing run planned for the summer of 1999.

As of June 1999 , ROLO has acquired over 2200 cubes of raw Moon images with VNIR and over 1200 cubes with SWIR. Figure 2 shows the phase/libration coverage for VNIR and SWIR together through June 1999. By 2002, ROLO expects to have acquired roughly 3500 images of the Moon through each VNIR filter and nearly 3000 images through each SWIR filter, or more than 100,000 absolutely calibrated images of the Moon. These data are used to create photometric models of the lunar surface that are position, phase, and wavelength dependent. Kieffer and Anderson [5] and Grant et al. [6] provide examples of calibrating spacecraft instruments with existing ROLO data. The dataset will also provide a wealth of information about the geological properties of the lunar surface. The photometric function of many thousands of points on the Moon will be measured for phase angles between 2° and 90° for wavelengths within 0.35–2.4 μm. Absolute and normalized color ratios and their phase-angle dependence will enable detailed studies of the mineral abundances of the Lunar soil. Information on the photometric function dependence on phase and wavelength will aid investigations of the surface particulate structure of the soil.

References: [1] Butler J. J. and Johnson B. C. (1996) *The Earth Observer, 8 (1).* [2] Kieffer H. H. and Wildey R. L. (1996) *J. Atmos. Ocean. Technol., 13,* 360. [3] Anderson J. M. et al. (1999) *Pub. Ast. Soc. Pacific, 111,* 737. [4] Gaddis L. et al. (1997) *LPS XXVIII,* 387. [5] Kieffer H. H. and Anderson J. M. (1998) *Proc. SPIE, 3498,* 325. [6] Grant I. F. et al. (1998) *Proc. SPIE, 3498,* 337.

THE LUNAR CRUSTAL THICKNESS FROM ANALYSIS OF THE LUNAR PROSPECTOR GRAVITY AND CLEMENTINE TOPOGRAPHY DATASETS.

S. Asmar[1], G. Schubert[1], A. Konopliv[2], and W. Moore[1], [1]Department of Earth and Space Sciences, Univeristy of California, Los Angeles, Los Angeles CA 70095, USA, [2]Jet Propulsion Laboratory, California Institute of Technology, USA.

The Lunar Prospector spacecraft has mapped the gravity field of the Moon to a level of resolution never achieved before, and a spherical harmonic representation to degree and order 100 is avail-

able. When combined with the topography dataset produced by the Clementine mission, the resulting Bouguer anomaly map is interpreted to model the thickness of the lunar crust. Such models are crucial to understanding the lunar thermal history and the formation of geological features such as mascon basins, several more of which have been newly discovered from this dataset. A two-layer planetary model was used to compute the variations of the depth to the lunar Moho. The thickness values ranged from near 0 to 120 km. There is significant agreement with previous work using the Clementine gravitational field data [1] with differences in specific locations such as South Pole-Aitken Basin, for example.

References: [1] Neumann G. A. etal. (1996) *JGR, 101,* 16841–16843.

THREE PARADIGMS OF LUNAR REGOLITH EVOLUTION. A. Basu[1], D. S. McKay[2], and S. J. Wentworth[3], [1]Department of Geological Sciences, Indiana University, Bloomington IN 47405, USA (basu@indiana.edu), [2]Mail Code SN2, NASA Johnson Space Center, Houston TX 77058, USA, [3]Mail Code C23, Lockheed Martin, 2400 NASA Road 1, Houston TX 77058, USA.

Introduction: Integration of diverse datasets on the Moon may render some paradigms of lunar science either better-defended or vulnerable. We will consider three paradigms commonly used for understanding the processes of lunar regolith evolution in light of new and accumulated data. Our premise is that all data-sets should converge to a single interpretation if a concept or model is to be accepted as a paradigm. If a convergence is lacking, the paradigm needs fresh scrutiny.

Steady State: Lunar regolith evolution is currently understood in terms of comminution, agglutination, and replenishment as described by McKay and coworkers [1–4]. Briefly, the model envisages continued micrometeoritic bombardment to comminute exposed soil particles to finer sizes while continued agglutination consumes finer sizes to produce larger constructional particles. Eventually, a balance between these two opposing processes achieves a steady state; soils at steady state maintain their mean grain size (M_Z). Episodic higher-energy impacts excavate fresh coarse material from below the soil cover, disturb the steady state, and restart the process to achieve a new steady state. It follows that the thickness of the regolith at any site would control the frequency of replenishment; indeed, the thickness of the regolith at Apollo landing sites was predicted by McKay et al. [1] from the average M_Z of local soils.

However, replenishment may come also from disintegrating boulders and cobbles at the lunar surface, and rates of comminution and agglutination may depend on the properties of target material. Regression between M_Z and I_S/FeO (a measure of maturity or total surface exposure) of Apollo soils at different sites shows the following relations and estimated M_Z at a high maturity of I_S/FeO=100:

Site	Regression	M_Z at y=100	
			øμ
A12	y = 0.016x + 3.29	4.89	34
A14	y = 0.030x + 1.55	4.55	43
A15	y = 0.023x + 2.72	5.02	31
A16	y = 0.013x + 2.30	3.6	82
A17	y = 0.015x + 2.91	4.41	47

($y = I_S$/FeO; $x = M_Z$ ø)

It is possible that Apollo 12 and 15 sites have the thickest regolith and the Apollo 16 site has the thinnest. It is also possible that Apollo 12 and 15 basalts are comminuted faster than Apollo 16 highland rocks and Apollo 14 and 17 soils are products of mixed parentage.

If a soil becomes continually finer as it matures until agglutination catches up, and if comminution is differential-dependent on the physical properties of the constituents, then the composition of the bulk soil has to match the composition of some "fulcrum" grain size fraction, say X. Grain size fractions >X and <X will complement each other; their mass balance is the bulk soil. It appears that the 10–20-μm size fraction may be the fulcrum. In general, trace-element chemistry (data of Laul in [5]) and IR reflectance spectra [6] of this size fraction are closest to that of the bulk soil, regardless of maturity that is surprising. Disaggregated products of regolith breccias may also show similar relationships [e.g., 7]. If the 10–20 μm is the fulcrum (i.e., X as above) for many soil properties (e.g., major-element composition, FMR, solar-wind-implanted elements), then this may be the ultimate mean grain size of lunar soils at steady state.

However, different properties of soils may find steady states at different grain size fractions. The steady state of solar-wind-implanted elements, on the other hand, will climb up the grain-size scale as agglutinates transfer surface-correlated components into volume-correlated components until a saturation level is reached or the rates of replenishment and implantation become equal. The same will be the case with vapor-deposited reduced metals as they too are incorporated inside constructional particles. Properties that are directly affected by soil-maturation processes will thus have different pathways of achieving steady states.

Ferromagnetic Resonance: Maturity, i.e., cumulative surface exposure, of lunar soils is best quantified by the amount of nanophase superparamagnetic Fe^0 (np-Fe^0) normalized to Fe content (=I_S/FeO). The majority consensus (paradigm?) for the production of np-Fe^0 is associated with the production of agglutinates. Because large doses of solar-wind H are implanted in all lunar soils upon exposure, any melting (e.g., during agglutinate production) triggers a chemical reduction of Fe-bearing minerals resulting in np-Fe^0 production [8–10]. The quantity of np-Fe^0 is thus dependent on melting events, (i.e., exposure), and limited by the Fe content of the soil. All freshly produced np-Fe^0 resides in agglutinitic glass, as new TEM images show [11]. Apparently, the correction procedure developed by Lucey et al. [12] to estimate the Fe content of the lunar surface from IR-reflectance spectra depends on accepting the above.

However, the process of producing np-Fe^0 may be physical rather than chemical. All np-Fe^0 could be deposits from a vapor produced by micrometeoritic impact on lunar soils [e.g., 13]. If metal-O bonds in target phases are broken, O being "most volatile" will escape leaving an O-deficient vapor to facilitate the production of np-Fe^0 [13]. If so, the quantity of np-Fe^0 is dependent on the vaporizing events, (i.e., exposure), and limited by the efficiency of breaking metal-O bonds and the escape of O. To the extent that strengths of metal-O bonds are dependent on the local crystal field, production of np-Fe^0 may be limited by the mineral composition of target soils and not by their total Fe content. According to this model, vapor-deposited np-Fe^0 should be found at any retentive sites on lunar soil grains. Indeed, TEM images show np-Fe^0 on plagioclase and ilmenite [11,14]. Incorporation of such pre-irradiated np-Fe^0-bearing grains into agglutinates may account for eventual increased emplacement of np-Fe^0 in agglutinates.

Such a paradigm shift in understanding the origin of np-Fe^0 will

raise questions ranging from the unquestionable use of I_s/FeO as the universal maturity parameter of lunar soils to global elemental maps of the Moon from remote-sensing data [e.g., 12,15].

Regolith Differentiation: Global distribution of rock types and global compositional variations on the Moon are interpreted from remotely sensed signals (UV-VIS-IR; γ-ray; secondary XRF). These signals integrate different depths of the regolith. Hence, convergence of raw data and first-order interpretation cannot be expected without calibration with actual samples. The very surface of the Moon is covered with very fine dust [16] that contributes significantly to all remote-sensing signals. Size fractions of the lunar regolith differ in chemical and mineralogic compositions. Many processes contribute to regolith differentiation including the loss of volatile elements such as Si [17]. In addition, the distribution of np-Fe^0 and larger grains of Fe^0 affects IR spectra [18]. It appears that the credibility of global maps from recent remote-sensing data (paradigm?) will increase if calibrations are carried out on different grain size fractions of the lunar regolith [e.g., 19].

Conclusion: Much of the global understanding of the Moon comes from remotely sensed and sample analyses of the regolith. Recent data, from TEM's nanometer-scale to kilometer-scale footprints of orbital and Earth-based observation, call for a review of paradigms in lunar regolith science.

Acknowledgments: This research was supported by NASA Grant NAG5-4018.

References: [1] McKay D.S. et al. (1974) *Proc. LSC5th,* 887–906. [2] Mendell W. W. and McKay D. S. (1975) *The Moon, 13,* 285–292. [3] Basu A. (1977) *Proc. LSC 8th,* 3617–3632. [4] McKay D. S. and Basu A. (1983) *Proc. LPSC 14th,* B193–B199. [5] Heiken G. et al., eds. (1991) *Lunar Sourcebook,* 736 pp. [6] Pieters C. M. et al. (1993) *JGR, 98,* 20817–20824. [7] Lindstrom D. J. (1999) *LPS XXX,* Abstract #2014. [8] Housley R. M. et al. (1973) *Proc. LSC 4th,* 2737–2769. [9] Taylor L. A. and Cirlin E-H. (1985) in *ESR Dating and Dosimetry,* pp. 19–29, Ionics. [10] Morris R. V. (1980) *Proc. LPSC 11th,* 1697–1712. [11] Keller L. P. and McKay D. S. (1997) *GCA, 61,* 1–11. [12] Lucey P. G. et al. (1995) *Science, 268,* 1150–1153. [13] Hapke B. (1998) *Workshop on the New Views on the Moon,* 34–35, LPI, Houston. [14] Christofferson R. et al. (1996) *MAPS, 31,* 835–848. [15] Blewett D. T. et al. (1997) *JGR, 102,* 16319–16325. [16] Hörz F. et al. (1972) *Apollo 16 Prelim. Sci. Rpt.,* pp. 7-24–7-54. NASA, Washington, DC. [17] Naney M. T. et al. (1976) *Proc. LSC 7th,* 155–184. [18] Keller L. P. et al. (1998) *Workshop on the New Views on the Moon, 44–45,* LPI, Houston. [19] Taylor L. A. et al. (1999) *LPS XXX,* Abstract #1885.

LUNAR GLOBAL PETROLOGIC VARIATIONS.

D. B. J. Bussey[1], P. D. Spudis[2], and J. J. Gillis[3], [1]Code SCI-SO, European Sapce Agency, European Space Research and Technology Centre, 2200 AG Noordwijk, The Netherlands, (bbussey@estec.esa.nl), [2]Lunar and Planetary Institute, Houston TX 77058, USA, [3]Department of Earth and Planetary Sciences, Washington University, St. Louis MO 63130, USA.

Introduction: An initial attempt at producing petrologic province maps of the lunar highlands combined orbital and sample geochemical data in variation diagrams [1]. Three different variation diagrams were produced: Mg* (= 100 Mg/Mg+Fe) vs. $[(Th/Ti)_c$, Al vs. Mg*/$(Th/Ti)_c$, and Fe vs. $(Th/Ti)_c$. ($[Th/Ti]_c$ is the ratio of Th to Ti, normalized to the chrondritic ratio for these elements.] Later work [2] applied a ternary diagram approach to look at global lunar petrologic variations. This work used the Fe-$(Th/Ti)_c$ technique as this had the most spatial coverage with the available data and also appeared to be adequate at distinguishing between different rock types. In the ternary diagram, the apexes were assigned the average Fe and $(Th/Ti)_c$ values of ferroan anorthosite, mare basalt, and KREEP rocks. Each apex was assigned a primary color while the center of the triangle was represented by gray. Each point on the lunar surface, covered by the Apollo geochemical instruments, was then assigned a color depending on where in the ternary their composition placed them. The resultant petrologic classification map shows how the petrologic units vary spatially. The main results from this work were as follows: (1) The highlands contain large areas of relatively pure ferroan anorthosite; (2) KREEP/Mg suite rocks represent a small percentage of the upper lunar crust; (3) farside outcrops of KREEP/Mg suite rocks are associated with areas of crustal thinning, particularly on the floor of South Pole Aitken Basin; (4) the average composition of the highlands is richer in Fe than ferroan anorthosite, which supports the magma ocean hypothesis of crystal formation; and (5) regions of the eastern limb and farside highlands are relatively more mafic than average highlands. These areas have a high density of dark halo craters, supporting the idea that mare volcanism occurred in this region before the end of the heavy bombardment.

Global Coverage: This earlier work utilized the Apollo gamma and X-ray orbital datasets. These data provided limited coverage of the lunar surface (mostly confined to the equatorial latitudes). The γ-ray instrument covered approximately 19% of the lunar surface while the X-ray only covered 9%. With the Clementine and Lunar Prospector datasets, we now have global maps of Fe, Ti, and Th [3–6]. Apart from global coverage, another important advantage of the new datasets is higher spatial resolution. The resolution of the Apollo instruments was 15 km for the X-ray and 100 km for the γ-ray [1]. The Fe and Ti maps are derived from the full-resolution Clementine UV-VIS data, i.e., ~250 m/pixel. The resolution of the Th data, obtained by Lunar Prospector's neutron spectrometer, is currently ~150 km [5], but will be available in the future with a spatial resolution of 60 km [7]. The other improvement provided by the recent lunar missions is the error associated with the data. The errors associated with the Fe, Ti, and Th values obtained by Apollo were 10–25 wt%. The error of the Clementine-derived Fe and Ti values is ~1%, while the Th data have an error of ~1 ppm.

We intend to investigate the petrologic variations on the Moon at a global scale using the new Clementine and Lunar Prospector elemental maps for Fe, Ti, and Th. We shall use the technique described in Davis and Spudis [2]. An initial study has been undertaken that looks at some regions that were covered by the Apollo geochemistry data. Two mare regions, one in Imbrium and the other in Procellarum, match well with the results using the Apollo data. The highland terrain appears problematic. The calibration of the Th data [6] is based on the assumption of a constant background. This is a valid assumption where Th counts are well above background limits, but as count rates decrease variations in Th concentration are more sensitive to background fluctuations. Eventually we will circumvent this problem by using the lower-altitude (i.e., higher resolution) Prospector data and a calibration derived from deconvolution of the γ-ray spectra with proper attention to background variations.

The Th/Ti vs. Fe technique provides more geologic information than can be extracted from solely using the elemental data because it

quantitatively determines each pixel's composition in terms of the end-member compositions: ferroan anorthosite, mare basalt, and KREEP rocks. Moreover, the digital map illustrates the extent and lateral transition of one rock-type to another, thus allowing the sample data to be placed in a regional and global context.

Initial examination confirms earlier conclusions [2] that the Mg suite is not a major contributor to at least the upper lunar crust. We summarize elsewhere in this volume evidence that Mg-suite rocks may be a significant contributor to the composition of the lower crust [8]. Work continues on the problem of the crustal fraction of the Mg suite, needed to determine the Mg# of the bulk crust, an important constraint on lunar origin [9].

References: [1] Davis P. A. and Spudis P. D. (1985) *LPS XXVI.* [2] Davis P. A. and Spudis P. D. (1987) *LPS XXVII.* [3] Lucey P. G. et al. (1998) *JGR, 103,* 3679. [4] Blewett D. T. et al. (1997) *JGR, 102,* 16319. [5] Lawrence D. J. et al. (1998) *Science, 281,* 1405–1560. [6] Gillis et al. (1999) *LPS XXX,* Abstract #1699. [7] Lawrence et al. (1999) *LPS XXX,* Abstract #2024. [8] Spudis P. D. et al., this volume. [9] Drake M. J. (1986) *Origin of the Moon,* LPI, 105 pp.

INTEGRATION OF THE ULTRAVIOLET-VISIBLE SPECTRAL CLEMENTINE DATA AND THE GAMMA-RAY LUNAR PROSPECTOR DATA: PRELIMINARY RESULTS CONCERNING FeO, TiO_2, AND Th ABUNDANCES OF THE LUNAR SURFACE AT GLOBAL SCALE.

S. D. Chevrel[1], P. C. Pinet[1], G. Barreau[1], Y. Daydou[1], G. Richard[1], S. Maurice[1], and W. C. Feldman[2], [1]Unité Mixte de Recherche 5562, Group for Space Research and Geodesy, Observatoire Midi-Pyrénées, Toulouse, France (Serge.Chevrel@cnes.fr), [2]Mail Stop D-466, Los Alamos National Laboratory, Los Alamos NM 87545, USA.

The Clementine mission (CLM) produced global multispectral data that resulted in a map of FeO and TiO_2 concentrations of the lunar surface [1,2]. The recent Lunar Prospector (LP) mission returned the first global data for the distribution of surface abundances of key elements in lunar rocks, using a γ-ray spectrometer (GRS) and neutron spectrometer (NS) [3,4]. Integrating CLM mineralogical spectral reflectance and LP chemical data is important to enhance our view of lunar crust origin and evolution, lunar volcanism, and surface processes.

Data Reduction (LP): Iron, Ti, and Th having relatively large compositional variation over the lunar surface, as well as strong isolated peaks in the GRS spectra, information concerning the distribution and concentration of these elements has been derived from maps of corrected (cosmic ray, nonsymmetric response of the instrument) counting rates only, without converting them into absolute abundances [3]. Maps produced contain count rates in equal-area projection averaged into 5 × 5° latitude/longitude bins, from –90° to +90° latitude and –180° to +180° longitude.

In this work, we have used the CLM global FeO and TiO_2 abundances (wt%) maps [2] converted at the LP spatial resolution (~150 km/pixel) to produce FeO and TiO_2 GRS abundance maps, through a linear regression based on the analysis of the scatter distribution of both datasets. The regression coefficients have been determined from the data taken between –60° and +60° latitude to avoid uncertainties in the CLM spectral data due to nonnominal conditions of observation at high latitudes. After a critical assessment of the validity of these coefficients for every class of absolute abundance, the LP data have been transformed into absolute abundances for the whole Moon.

The Th LP data have been converted into abundances (ppm) using Th concentrations in average soils from the Apollo and Luna sites given in [5]. Values of Th abundances for these samples range between 0.5 and 13 ppm [3,5]. A nonlinear regression has been applied to the LP data, except for low count rate values (corresponding to Th abundances below 1.27 ppm) for which a first-order linear regression has been applied.

Statistical tests demonstrate that the Lunar Prospector FeO, TiO_2, and Th abundances estimates we have produced through the regressions are reliable. For the LP maps, the uncertainty of absolute FeO and TiO_2 estimates is on the same order as that for CLM, i.e., 2 and 1.5 wt% respectively. For the Th, abundance estimates, the uncertainty is ~1–2 ppm.

Results: At first order, our global FeO and TiO_2 abundances maps from LP are in very good agreement with those obtained from CLM [2]. The Th abundance map is also in good agreement with a recent global Th abundance map by [6], although concentrations have a higher range (0–20 ppm) in our case, and may be slightly overestimated.

However, a more detailed comparison between CLM and LP abundance maps of FeO and TiO_2 reveals regional differences. Differences between the two datasets are expected because of instrumental and observational causes (spatial resolution, depth of observation), but also because they are sensitive to different types of information (mineralogy vs. chemistry). Maps of differences in abundances between LP and CLM data have been produced for both FeO and TiO_2. In relation to the precision of the LP and CLM data, we consider that differences between the two datasets exceeding 2 wt% are significant.

Concerning FeO contents, differences up to 4–5 wt% are observed in the South Pole Aitken Basin, and generally at high latitude (up to 70°) in the southern hemisphere, as well as in the northern border (Iridum-Gruithuisen domes region) and the southern border (Sinus Aestum) of the Imbrium Basin. Most important differences, up to 6–7 wt%, are found in Mare Serenitatis, Crisium, and Fecunditatis.

Concerning TiO_2, most important differences (4–5 wt%) between LP and CLM abundances are located within Mare Tranquillitatis. Differences (about 2–3 wt%) also occur in the northern border of the Imbrium Basin (Ir-Gruithuisen domes region) and in the western part of Oceanus Procellarum (from southwest of Kepler, up to the Aristarchus Plateau).

Regions for which differences in FeO and/or TiO_2 content may arise from the presence of heterogeneous terrains due to geological transitions at the scale of observation of LP have been identified on the basis of the spatially degraded FeO and TiO_2 CLM maps. These regions correspond to Mare Crisium, the western part of Procellarum, and Mare Humorum.

The surface heterogeneity effect cannot be invoked in the case of the South Pole Aitken (SPA) Basin interior and its immediate vicinity. However, LP indicates a lower content in FeO than CLM (8–11 wt% vs. 11–13 wt% respectively). This observation suggests that the SPA materials may contain a lower proportion of Fe than was previously thought. This may imply a smaller proportion of mantle materials excavated during the impact event than predicted in [7] and give some constraints to the models of large basin formation, [e.g., 7–9].

Some regions such as Mare Serenitatis, Tranquillitatis, Fecunditatis, and Crisium do present significant differences in FeO and TiO_2 abundances, the LP estimates being lower than the CLM ones. This might be ascribed to a different perception of the influence of the mare regolith reworking by the LP geochemichal observation, sensitive to the subsurface regolith, and the CLM reflectance spectroscopy observation, sensitive to the surface mineralogy.

In the case of the Gruithuisen domes/Iridum region, LP maps show FeO and TiO_2 with higher abundances (by ~30%) than CLM. They also display high concentrations of Th (4–6 ppm). In that particular case, the nonagreement between LP and CLM abundances could be linked to particular types of materials. More precisely, it may indicate that Fe and Ti are not present in the major mineral phase only, i.e., silicates and oxides respectively (oberved by CLM), but are also present in other minerals and/or amorphous phases . The Gruithuisen/ Iridium region corresponds to Imbrium ejecta materials mapped as Fra Mauro deposits [10]. Samples returned from the Fra Mauro formation (Apollo 14) are impact melts that have undergone multiple episodes of brecciation. They display a bulk composition of KREEP basalts and clasts of brecciated feldspathic rocks [10]. KREEP basalts have Th concentrations ranging between 3 and 10 ppm [5] which is in good agreement with the LP observation. The Gruithuisen region also corresponds to possible extended nonmare volcanism units having spectral characteristics close to those of Red Spots units (i.e., a strong absorption in the UV domain) associated with volcanic domes [11]. At the present time, the true nature of the Gruithuisen dome materials is still unknown. From morphologic evidence, these materials may result from silicic or felspathic-rich KREEP basalts [12]. The diffuse presence of such a material in the region may therefore also contribute to the high concentration of Th observed by LP. Higher concentrations of Fe and Ti observed by LP may result from their presence in the highly brecciated melt materials and in the nonmare volcanic materials (probably in an amorphous phase).

References: [1] Malaret E. and P. G. Lucey (1996) *LPS XXVII,* 797–798. [2] Lucey P. G. et al. (1998) *JGR, 103,* 3679–3699. [3] Lawrence D. J. et al. (1998) *Science, 281,* 1484–1489. [4] Feldman W. C. et al. (1998) *Science, 281,* 1489–1493. [5] Korotev R. L. (1998), *JGR, 103,* 1691–1701. [6] Gillis J. J. et al. (1999) *LPS XXX.* [7] Lucey P. G. et al. (1998) *JGR, 103,* 3701–3708. [8] Pieters et al. (1997) *GRL, 24,* 1903–1906. [9] Schultz P. H. (1997) *LPS XXVIII,* 1259–1260. [10] Spudis et al. (1988) *LPS XVIII,* 155–168. [11] Chevrel et al. (1999) *JGR,* in press. [12] Head H. W. et al. (1978) *LPS IX,* 488–489.

THE DISTRIBUTION OF TITANIUM IN LUNAR SOILS ON THE BASIS OF SENSOR AND *IN SITU* DATA FUSION.

P. E. Clark[1,2] and L. Evans[2,3], [1]Catholic University of America, [2]Mail Code 691, NASA Goddard Space Flight Center, Greenbelt MD 20771, USA (pamela.clark@gsfc.nasa.gov), [3]Computer Science Corporation, 645 Hembree Parkway, Suite A, Atlanta GA 30076, USA.

A variety of remote-sensing measurements have been used to map the distribution of elements on the Moon as a means of providing constraints on the processes from which its crust and major terranes originated [1,2]. Discussed here is Ti, which is incorporated into refractory minerals such as ilmenite during the latter stages of differentiation, and is thus a most useful element for understanding mare basalt petrogenesis. One of the earliest Ti maps [3] showed Ti variations in nearside maria on the basis of groundbased spectral reflectance measurements. A map of Ti derived from γ-ray measurements on Apollo 15 and 16 was produced at about the same time [4], and was improved upon considerably by Davis and coworkers [5], who effectively removed sources of spurious variation from Fe and Al or REE (e.g., Th) interference, and calibrated Ti on the bases of landing-site soil averages. In recent years, spectral reflectance measurements from Clementine have been used by Lucey and coworkers [6] to produce global Ti distribution maps as well. As we indicated previously, the Lucey and Davis maps agree to first order. Meanwhile, we are using the concept of sensor data fusion to combine measurements from the AGR (Apollo γ-ray) and CSR (Clementine Spectral Reflectance) techniques with ground truth from lunar soils to utilize the differences between the two maps to understand the distribution of Ti within lunar soil components, as we have done with Fe [7]. This technique should be verified and applied on Lunar Prospector γ-ray measurements of Ti [8], as the calibrated data become available within the next couple of years.

Lunar Ti is found principally in the mineral ilmenite, and is associated with certain components of lunar soil [9]: crystalline ilmenite mineral fragments and high Ti-bearing glass. All data indicate that Ti is associated with maria and mafic minerals. In AGR and CSR datasets, Ti is highest on the nearside and in the maria, particularly in southern Serenitatis/northern Tranquillitatis and northwestern Procellarum. Unlike CSR-derived values, AGR Ti values show modest increase (up to 0.7%) on the northern farside. Table 1 shows the relationship between average Ti values for typical regions [10]. Both techniques show a primarily unimodal distribution with a shoulder in the high Ti direction and a primary mode at approximately 0.2% (0.15% for CSR and 0.25% for AGR data), but the AGR Ti data have more structure in the shoulder, including an apparent minor mode at 1.2% Ti, representing nonhighland areas. Recalibrating the two datasets on the basis of matching the peaks and range on the histograms would not account for this additional structure in the AGR data. Low Ti areas, which occur predominantly on the farside, are not represented well in the lunar sample collection, although several meteorites thought to be of lunar highland origin show Ti abundances averaging ~0.2% [11]. (Errorbars on AGR Ti values are ~0.5%.)

Gamma-ray measurements reflect intrinsic Ti surface composition, regardless of the physical or chemical state of Ti [1]. Lucey and coworkers [6] have attempted to produce an equivalent bulk Ti map

TABLE 1. Regional AGR and CSR Ti abundances.

Region	AGR	CSR
Procellarum North	2.9	3.0
Procellarum South	2.4	2.5
Mare Imbrium East	1.3	1.8
Mare Imbrium West	2.4	2.6
Mare Tranquillitatis	3.0	3.5
Mare Serenitatis	2.5	3.0
Mare Crisium	1.3	2.4
Mare Smythii	2.6	1.5
Farside Northeast	0.9	0.5
Farside Northwest	1.3	0.4
Farside Southwest	0.7	0.6
Farside Southeast	0.5	0.6

by normalizing the spectral feature at 415 nm to remove the effects of physical variations from soil to soil. The normalization is based on laboratory measurements of available samples, primarily nearside maria, and is undoubtedly optimized for the proportions in which Ti-bearing components are found in these soils. In Table 2, AGR and CSR Ti abundances (with CSR filtered to match resolution and field of view of AGR data) for landing sites are compared to abundances of soil components in which Ti would principally be found: crystalline ilmenite fragments and Ti-bearing glass. In particular, mare soils tend to have a much higher proportion of opaque mineral grains [12], which appears to be well correlated with Ti abundance, as shown in Table 2. The relationship between Ti abundance and proportion of Ti-bearing glass ([12], weighted for Ti abundance according to [9]) is not as direct. Table 2 also shows the relationship between landing site soil average, AGR, and CSR Ti abundances (with CSR filtered to match resolution and field of view of AGR data) . AGR Ti values show the best agreement with Ti soil averages, CSR Ti values being somewhat higher in high-Ti soils, and lower in low-Ti soils. These results would tend to support the argument that the technique for deriving Ti from the CSR measurements is optimized for one of the primary Ti-bearing components, most likely opaque mineral grains, and is thus overcompensating and reporting higher Ti values in mare areas, and underreporting Ti in highland areas with much lower proportions of opaque mineral grains.

References: [1] Adler I. and Trombka J. (1970) *Geochemical Exploration of the Moon and Planets.* [2] Taylor S. R. (1986) *Origin of the Moon* (W. K. Hartmann et al., eds.), pp. 125–144, LPI, Houston. [3] Johnson T. et al. (1977) *Proc. LSC 8th,* 1029–1036. [4] Arnold J. et al. (1978) *LPS IX,* 25–26. [5] Davis P. (1980) *JGR, 85,* 3209–3224. [6] Lucey P. et al. (1998) *JGR, 102,* 3769–3699. [7] Clark P. and McFadden L. (1999) *JGR,* in press. [8] Feldman W. C. et al. (1998) *Science,* 1497–1500. [9] Heiken G. et al. (1991) *Lunar Sourcebook* (G. H. Heiken et al., eds.), Chapters 2 and 5, Cambridge Univ., New York. [10] Clark P. and Evans L. (1999) *LPS XXX.* [11] Lindstrom M. et al. (1991) *GCA, 55,* 2999–3007. [12] Papike J. et al. (1998) *Planetary Materials,* Chapter 5.

TABLE 2a. Landing site Ti abundances.

Site	%Ti SoilAv	%Ti AGR	%Ti CSR	%Ti AGR – CSR
Ap 12	1.8	1.6	2.4	+0.8
Ap 14	1.0	0.8	0.6	-0.2
Ap 15	0.95	1.0	0.6	-0.4
Ap 16	0.3	0.35	0.25	-0.2
Ap 17	2.5	3.6	4.2	+0.6

TABLE 2b. Landing site Ti-bearing components.

Site	Vol%OP Opaque Minerals	%TiG Ti-bearing Glass	OP/TiG
Ap 12	0.75	1.6	0.47
Ap 14	<.1	0.4	<.2
Ap 15	0.2	1.8	0.11
Ap 16	0.1	0.7	0.14
Ap 17	1.1	1.7	0.65

DIGITAL ELEVATION MODELS OF THE LUNAR SURFACE.

A. C. Cook[1] and M. S. Robinson[2], [1]Center for Earth and Planetary Studies, National Air and Space Museum, Washington DC 20560-0315, USA (tcook@ceps.nasm.edu), [2]Department of Geological Sciences, Northwestern University, Evanston IL 60208-2150, USA (robinson@eros.earth.nwu.edu).

Introduction: Several digital elevation models (DEMs) have been produced at a scale of 1km/pixel and covering approximately one-fifth of the lunar surface. These were produced mostly by semi-automatically matching the stereo available between Clementine UV-VIS images, although some localized DEMs have been produced by applying this technique to Apollo Metric stereo pairs, or by digitizing an existing Apollo Metric contour map. The DEMS that result from Clementine UV-VIS images, although of poorer height accuracy (±300–600 m for a single matched point) [1] than the Clementine laser altimeter point measurements (<±100 m) [2], do provide considerably higher spatial resolution (e.g., every kilometer vs. every tens of kilometers) and allow topography in the polar regions to be determined.

Method: Nadir-pointing Clementine UV-VIS stereo pairs are automatically stereo matched using a patch-based matcher [3] and fed through a stereo intersection camera model to yield a digital terrain model (DTM) of longitude, latitude, and height points. The DTM for each stereo pair is then replotted and interpolated to form map-projected DEM tiles. The DEM tiles can then be fitted to absolute height laser altimeter points, or iteratively to each other, to form a DEM mosaic. Uncertainties in UV-VIS camera pointing and the need to accumulate a sufficiently good topographic S/N ratio necessitates the use of 1 km pixels for the UV-VIS derived DEMs. For Apollo Metric stereo, an internal camera geometry correction and a full photogrammetric block adjustment must be performed using ground- control points to derive a DEM. The image scale of Apollo Metric, as well as the stereo angle, allow for a DEM with 100 m pixels and a height accuracy of ±25 m. Apollo Metric imagery had previously been used to derive contour maps for much of the lunar equatorial regions; however, to recover this information in digital form these maps must be digitized.

Regions Covered: Most of the mare areas mapped contain noticeable topographic noise (see Fig. 1). This results from the stereo matcher failing in regions of low texture and contrast. Below is a summary of the regions for which DEMs have been generated, and some of the features visible in each (heights are referenced to a 1738-km radius sphere):

Apollo 15 landing site (1°E–7°E, 20°N–30°N). Features include Hadley Rille (just visible) and several mountains [4].

Apollo 17 landing site (30.0°E–31.5°E,19.5°N–21.0°N). This DEM was derived by digitizing contours from a map [5].

Alpine Valley (2°W–8°E, 47°N–51°N). The valley and Trouvelot crater are visible [6]. Topography ranges from +1 km to –4 km. The valley walls are <1 km high.

Aristarchus (60°W–40°W, 20°N–30°N). Features visible include Aristarchus craters, Vallis Schröteri, and the craters Herodotus, Schiaparelli, and Prinz.

Copernicus Crater (30°W°–10°W, 0°N–20°N). Features visible include Montes Carpatus and the craters Copernicus, Eratosthenes, Reinhold, and Tobias Mayer.

Giordano Bruno Crater (101°E–106°E, 33°N–38°N). This DEM [7] reveals ~60% of the crater interior.

Kepler Crater (38°W, 8°N). Using this DEM [7] a perspective view of this crater has been produced with a USGS color-ratio map overlaid.

Korolev Basin (175°W–160°W, 10°S–20°N). Seventy-five percent of the Korolev basin is present in this DEM together with a pre-Nectarian basin the size of Korololev just to the north [8]. The topography in this DEM ranges from 0 km to 9.6 km. Named craters visible include Mach, McMath, Icarus, and Tsander.

Luna 9/13 landing site (70°W–60°W, 0°N–30°N). The topographic range is from ~0 km to –4.5 km, the latter being on the floor of Hevelius A crater.

Mare Crisium (50°E–70°E, 0°N–20°N). This DEM [4] covers the lower half of the basin and surrounding highlands. The topographic range is from +3 km to –5 km. Several protruding floor crater rims are visible on the basin floor (e.g., Picard, Yerkes, and Lick).

Mare Orientale (120°W–75°W, 40°S–0°N). This area was covered well in stereo, and a regional north-south slope is detectable across the basin [9]. The topography varies from +6 km on the western rim to –5 km on the bottom of Maunder crater. Three rings of the basin are clearly visible in the topography.

Mare Serenitatis (10°E–40°E, 10°N–40°N). Highland areas are well depicted in the DEM, as are craters Bessel, Dawes, Le Monier, Menelaus, Plinius, Posidonius, and Ross.

North polar region (60°–90°). An analysis of this DEM [10,11] revealed the newly discovered Sylvester-Nansen pre-Nectarian impact basin (300–400 km diameter, centered on 45°E, 83°N). The Schwarzchild and Be'lkovich basins are clearly visible, as is the northern extent of the Imbrium basin. Several secondary ejecta scour marks are present in the topography and spread out radially from Mare Imbrium. The crater Hayn contains a north-south running graben which bisects its central peaks.

Saha crater area (90°E–105°E, 5°S–5°N). Stereo imagery is missing in the center of this region [7].

Schickard (60°W–50°W, 50°S–40°S). The floor interior craterlets and surrounding highlands are clearly visible [7].

Sinus Iridum (40°W–30°W, 30°N–50°N). See Fig. 1 [4].

South polar region (90°S–60°S). An anaylsis of this DEM [4,7,10–15] has revealed two newly discovered pre-Nectarian impact basins (Schrodinger-Zeeman, 250 km in diameter, centered on 165°W, 81°S, and 330 km diameter Bailly-Newton, centered on 57°W, 73°S). Several other prominent basins are visible, including the southern half of the South Pole Aitken (SPA) Basin, Bailly, Schrodinger, part of Clavius, and the Amundsen-Ganswindt Basin. The topographic range in this DEM is considerably greater than the north polar DEM due to the presence of the SPA topgraphy.

Tsiolkovsky (124°E, 19°S). In this DEM [16] the western flanks of Tsiolkovsky are shown in great detail.

Tycho (20°W–0°W, 50°S–40°S). This DEM shows Tycho crater and its surroundings as well as the northern interior of Maginus Crater.

Discussion: The best results obtained from stereo matching lie over highland regions, where there exists much surface texture for the stereo matcher to lock onto. Mare regions are darker and relatively featureless and hence result in noisy DEMs, which largely preclude the detection of wrinkle ridges. Nevertheless, craters and peaks within mare areas can be resolved and profiles extracted from these features. One of the drawbacks of the Clementine-derived DEMs is that the stereo coverage at latitudes below ±60° in latitude contain many gaps. However, when compared to an interpolated Clementine laser altimeter DEM [2], the stereo-derived DEM contains considerably more spatial detail. The DEMs produced from Clementine stereo are also complementary to Clementine laser altimeter measurements, because the latter perform better over flat mare areas, but less well in highland regions. Some of these DEMs are available on the Internet at http://www.nasm.edu/ceps/research/cook/topo.html.

Fig. 1. Digital elevation models of Sinus Iridum. Black = low (or no data) and white = high.

Acknowledgments: We would like to thank DLR Berlin for the computing time for some of the earlier DEMs and University College London/Laser-Scan for the Gotcha stereo-matching software, originally written by T. Day.

References: [1] Cook A. C. et al (1997) *Planet. Space. Sci., 44,* 1135–1148. [2] Smith D. E. et al (1997) *JGR, 102,* 1591–1611. [3] Day T. et al (1992) *Int. Archv. Photgrm. Remot. Sens., 29-B4,* 801–808. [4] Cook. A. C. et al (1996) *Proc. 24th Vernadsky-Brown Micro.,* Moscow. [5] Robinson et al. (1999) *LPS XXX,* Abstract #1931. [6] Cook A. C. and Hiesinger H. (1996) *LPS XXVII,* 249–250. [7] Cook A. C. et al. (1996) *Annu. Geophys., 14(III),* C803. [8] Konopliv A. (1999) personal communication. [9] Cook A. C. et al. (1997) *Annu. Geophys., 15(III).* [10] Cook A. C. et al. (1999) *LPS XXX,* Abstract #1154. [11] Cook A. C. et al. (1999) *JGR,* submitted. [12] Hoffmann H. et al. (1996) *Annu. Geophys. 14(III).* [13] Cook A. C. and Robinson M. S. (1998) *3rd Intl. Conf. Expl. and Utiliz. of the Moon,* Moscow, 21. [14] Spudis P. D. et al. (1998) *Proc. of New Views of the Moon I.* [15] Cook A. C. and Robinson M. S. (1998) *3rd Intl. Conf. Expl. and Utiliz. of the Moon,* Moscow, 21. [16] Cook A. C. et al. (1994) *BAAS, 26,* 1097.

SIMULATING THE FORMATION OF LUNAR FLOOR-FRACTURE CRATERS USING ELASTOVISCOPLASTIC RELAXATION.

A. J. Dombard and J. J. Gillis, Department of Earth and Planetary Sciences and McDonnell Center for Space Sciences, Washington University, One Brookings Drive, St. Louis MO 63130, USA (rew@wurtzite.wustl.edu; gillis@levee.wustl.edu.)

Introduction: Lunar floor-fracture craters formed during the height of mare basalt emplacement. Due to a general temporal and spatial relation with the maria, these craters, numbering some 200, may be diagnostic of the thermal structure of the crust during this time [1]. As the name suggests, these craters exhibit brittle failure, generally limited to the central floor region. That, and a shallower depth than fresh lunar craters [1], has led to two main theories as to their formation: laccolith emplacement under the crater [1–3] and viscous relaxation [2,4]. The implications of each model for the state of the Moon's crust during this time are quite different [2], so the viability of each model must be checked. Laccolith emplacement has been treated elsewhere [1–3]. However, previous attempts to study the relaxation of the craters have assumed only a uniform, Newtonian viscous response of the near surface to the topographic driving forces, and simply postulated that the fractures resulted from tensile stresses associated with floor uplift [2,4]. Here, we use a more sophisticated rheological model [5] that includes not only non-Newtonian viscous behavior (i.e., the viscosity is stress-dependent), but also incorporates elastic behavior and a plastic component to the rheology to directly simulate the formation of the floor fractures. The results of our simulations show that while elastoviscoplastic relaxation is potentially viable for larger floor-fracture craters, it is not viable for craters with diameters ≤60 km, the size of the majority of floor-fracture craters [1].

The Model: We employ the finite element method, a numerical technique well suited for boundary-value problems, via the commercially available MARC software package. To test the viability of topographic relaxation, our goal is to prepare the simulations as to maximize the amount of relaxation.

We take advantage of the natural axisymmetry of craters, simulating one radial plane. Initial shapes are based on data for fresh craters from Pike [6]. To simplify implementation, a fourth order polynomial is used for the basin, while a third order inverse function is used for the rim. This form closely approximates the long-wavelength behavior of complex craters, while ignoring higher-frequency topography, save the rim. This approximation is appropriate because crater relaxation is strongly controlled by long-wavelength topography.

Loading is accomplished assuming a uniform gravity field (1.62 m s^{-2}) and a uniform density of 2900 kg m^{-3}. The initial stress state is set to be hydrostatic, with an additional pressure term to account for any overlying topography. This additional pressure term is tapered exponentially with depth [e.g., 7]. While the simulations quickly settle on a preferred stress state, and while the final solution is fairly insensitive to the choice of the *e*-folding depth of the taper, selecting an *e*-folding depth close to the diameter of the crater sets the initial stress state near the preferred state.

We assume a diurnally averaged surface temperature of –20 °C, and allow temperature to increase with depth at a rate of 50 K/km^{-1}. Assuming a thermal conductivity of 2 W m^{-1} K^{-1} [8], this gradient translates to a heat flow of 100 mW m^{-2}, an extremely high value for the Moon. Temperature, of course, will not increase without bound. To maximize relaxation, we allow our temperature profile to increase linearly until it reaches the solidus (assumed to be 1200 °C) at a depth of 24.4 km, at which point it is kept constant. The presence of melt will drop the bulk viscosity; however, we have no rheological control for partial melts. Therefore, we make no attempt to simulate this situation.

Elastoviscoplastic rheological model. In general, geologic materials can behave in three main ways: elastically, viscously (via solid-state creep), and brittly (plasticity is a continuum approach to simulate this phenomenon). We combine these three deformation mechanisms in an extended Maxwell solid, where the total strain can be broken down into a simple summation of the elastic, creep, and plastic strains.

In relaxation phenomena in general, the system takes advantage of any means possible to eliminate deviatoric stresses by relaxing away the topography. Previous analyses have only modeled the viscous response. Comparatively, the elastic response in our model can augment the relaxation, to a point. This effect decreases as the elastic response becomes stiffer; indeed, in the limit of infinite elastic Young's modulus (and with no plasticity), the solution converges on the purely viscous solution [5]. Igneous rocks common to the lunar near-surface have Young's modulii in the range of 10–100 GPa [8]. To maximize relaxation, we use a Young's modulus of 10 GPa. (There is negligible sensitivity to the other elastic modulus, the Poisson's ratio; we use 0.25.)

For the viscous response, we use a flow law for steady-state creep in thoroughly dried Columbia diabase [9], because the high plagioclase (~70 vol%) and orthopyroxene (~17 vol%) content is similar to the composition of the lunar highland crust as described by remote sensing [10] and sample studies [11]: noritic anorthosite. This flow law is highly non-Newtonian, i.e., the viscosity is highly stress dependent. That, and the variability with temperature, stands in strong contrast to previous examinations of lunar floor-fracture crater relaxation [2,4].

To model discrete, brittle faulting, we assume "Byerlee's rule," a standard geodynamical technique [e.g., 7]. We implement this "rule" with an angle of internal friction of ~40°, and a higher-than-normal cohesion of ~3.2 MPa (to approximate the breaking of unfractured rock). The actual behavior of geologic materials is more complex than in our rheological model, so the uncertainties in the plasticity do not represent the state-of-the-art error.

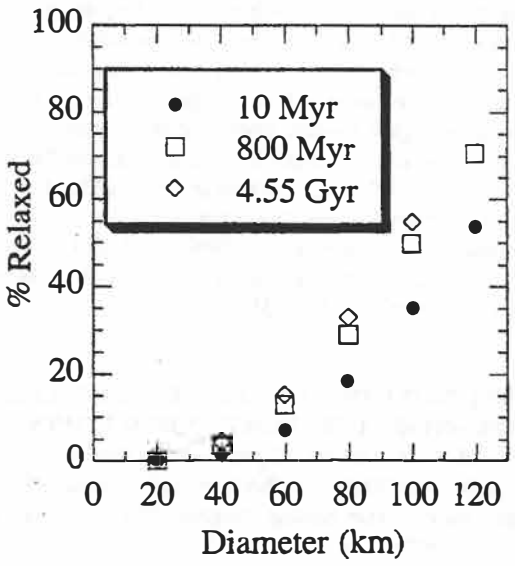

Fig. 1. State of relaxation for lunar craters of various sizes, based on apparent depth under our model assumptions. Craters <60 km see only minor relaxation.

Results: Figure 1 shows the relaxation state of lunar craters of various diameters, under our model assumptions. The relaxation state is based on comparing the current apparent depth with the initial apparent depth of the crater. (Apparent crater depth is the depth of the central point of the crater referenced to some outside, background elevation.) Figure 1 is plotted at 3 different times: 10 Ma (a time which both Hall et al. [4] and Wichman and Schultz [3] consider a reasonable length of time for relaxation), 800 Ma (an upper limit, based on the association of floor-fracture craters with maria emplacement [3]), and 4.55 Ga (an absolute upper limit for most geodynamic processes in this solar system). The simulation of a 120-km diameter crater terminated after ~3.5 Ga at ~75% relaxation because of a numerical instability; however, scaling from Fig. 1 indicates a final relaxation state of 80–85%.

As expected, larger craters relax more rapidly than smaller craters. Moreover, most relaxation occurs early on, particularly for larger craters, an effect that attests to the highly nonlinear rheology. While larger craters can experience substantial relaxation, the degree of relaxation of smaller craters can be quite small. Craters of 40 km diameter or less see relaxation of <5% after 4.55 Ga. For comparison, all of the craters examined by Hall et al. [4] were 40 km in diameter or less and saw relaxation of ~70%.

The inclusion of plasticity does speed up the relaxation process. For example, an 80-km crater relaxes to ~26% at 4.55 Ga without plasticity, compared to ~33% with plasticity (see Fig. 1). The resulting plastic strains, also as expected, are concentrated within the central floor region, with plasticity penetrating most deeply for larger craters. This plastic zone is, however, shallow (~8 km), and the magnitude of the strains is somewhat small (~3%). Indeed, a 20-km crater does not experience any brittle failure on its floor, nor is its relaxation sped up by the inclusion of plasticity.

Discussion: If it is assumed that one process was responsible for the formation of all floor-fracture craters, then this relaxation model clearly fails. However, the moderate degree of relaxation of larger craters, even within only 10 Ma, suggests that relaxation may have been at least partly responsible for the formation of larger floor-fracture craters. However, parameters in our simulations were selected to maximize the amount of relaxation. Using more plausible choices (e.g., lower heat flows) will result in less relaxation, potentially much less. Consequently, we conclude that topographic relaxation was not responsible for the formation of lunar floor-fracture craters.

Acknowledgments: This research is supported by a NASA GSRP Fellowship (AJD).

References: [1] Schultz P. H. (1976) *Moon, 15,* 241–273. [2] Wichman R. W. and Schultz P. H. (1995) *JGR, 100,* 21201–21218. [3] Wichman R. W. and Schultz P. H. (1995) *Icarus, 122,* 193–199. [4] Hall J. L. et al. (1981) *JGR, 86,* 9537–9552. [5] Dombard A. J. and McKinnon W. B. (1999) *LPSC XXX, Abstract* #2006. [6] Pike R. J. (1977) *In Impact and Explosion Cratering* (Roddy et al., eds.), Pergamon, 489–509. [7] Jaeger J. C. and Cook N. G. W. (1979) *Fundamentals of Rock Mechanics,* Chapman and Hall. [8] Turcotte D. L. and Schubert G. (1982) *Geodynamics,* Wiley. [9] Mackwell S. J. et al. (1998) *JGR, 103,* 975–984. [10] Pieters C. M. (1986) *Rev. of Geophys., 24,* 557–578. [11] Taylor S. R. (1975) *Lunar Science: A Post-Apollo View,* Pergamon.

SAMPLE RETURN MISSION TO THE SOUTH POLE AITKEN BASIN.

M. B. Duke[1], B. C. Clark[2], T. Gamber[2], P. G. Lucey[3], G. Ryder[1], and G. J. Taylor[3], [1]Lunar and Planetary Institute, 3600 Bay Area Boulevard, Houston TX 77058, USA (duke@lpi.jsc.nasa.gov; zryder@lpi.jsc.nasa.gov), [2]Lockheed Martin Astronautics, Denver CO 80201, USA (benton.c.clark@lmco.com), [3]University of Hawai'i at Manoa, Honolulu HI 96822, USA (lucey@pgd.hawaii.edu; gjtaylor@pgd.hawaii.edu).

The South Pole Aitken Basin (SPA) is the largest and oldest observed feature on the Moon. Compositional and topographic data from Galileo, Clementine, and Lunar Prospector have demonstrated that SPA represents a distinctive major lunar terrane, which has not been sampled either by sample return missions (Apollo, Luna) or by lunar meteorites. The floor of SPA is characterized by mafic compositions enriched in Fe, Ti, and Th in comparison to its surroundings [1,2]. This composition may represent melt rocks from the SPA event, which would be mixtures of the preexisting crust and mantle rocks. However, the Fe content is higher than expected, and the large Apollo basin, within SPA, exposes deeper material with lower iron content. Some of the Fe enrichment may represent mare and cryptomare deposits. No model adequately accounts for all of the characteristics of the SPA and disagreements are fundamental. Is mantle material exposed or contained as fragments in melt rock and breccias? If impact melt is present, did the vast sheet differentiate? Was the initial mantle and crust compositionally different from other regions of the Moon? Was the impact event somehow peculiar, (e.g., a low-velocity impact)? The precise time of formation of the SPA is unknown, being limited only by the initial differentiation of the Moon and the age of the Imbrium event, believed to be 3.9 b.y.

The questions raised by the SPA can be addressed only with detailed sample analysis. Analysis of the melt rocks, fragments in breccias, and basalts of SPA can address several highly significant problems for the Moon and the history of the solar system. The time of formation of SPA, based on analysis of melt rocks formed in the

event, would put limits on the period of intense bombardment of the Moon, which has been inferred by some to include a "terminal cataclysm." If close to 3.9 Ga, the presumed age of the Imbrium Basin, the SPA date would confirm the lunar cataclysm. This episode, if it occurred, would have affected all of the planets of the inner solar system, and in particular, could have been critical to the history of life on Earth. If the SPA is significantly older, a more orderly cratering history may be inferred. Secondly, melt-rock compositions and clasts in melt rocks or breccias may yield evidence of the composition of the lunar mantle, which could have been penetrated by the impact or exposed by the rebound process that occurred after the impact. Thirdly, study of mare and cryptomare basalts could yield further constraints on the age of SPA and the thermal history of the crust and mantle in that region. The integration of these data may allow inferences to be made on the nature of the impacting body.

Secondary science objectives in samples from the SPA could include analysis of the regolith for the latitudinal effects of solar-wind irradiation, which should be reduced from its equatorial values; possible remnant magnetization of very old basalts; and evidence for Imbrium Basin ejecta and KREEP materials. If a sampling site is chosen close enough to the poles, it is possible that indirect evidence of polar-ice deposits may be found in the form of oxidized or hydrated regolith constituents.

A sample return mission to the Moon may be possible within the constraints of NASA's Discovery Program. Recent progress in the development of sample return canisters for Genesis, Stardust, and Mars Sample Return missions suggests that a small capsule can be returned directly to the ground without a parachute, thus reducing its mass and complexity. Return of a 1-kg sample from the lunar surface would appear to be compatible with a Delta II class launch from Earth, or possibly with a piggyback opportunity on a commercial launch to GEO. A total mission price tag on the order of $100 million would be a goal. Target date would be late 2002. Samples would be returned to the curatorial facility at the Johnson Space Center for description and allocation for investigations.

Concentration of milligram-to gram-sized rocklets is a very effective strategy for sample studies of the lunar regolith. A rake accomplished this type of sampling in the Apollo missions. For the SPA sample return mission, either a small rover or an arm on a lander would deliver regolith to a sieving mechanism that retains fragments in the 1–10 mm size range. Approximately 10% of the mass of Apollo 16 regolith samples, which were from possibly similar highland terrain, consisted of fragments in the size range. To return 1 kg of rock fragments, approximately 5×10^3 cm^3 of regolith would have to be sampled. Warren et al. [3] suggested 7–10 mm as the optimum size for individual samples, which would require more regolith to be sieved.

This mission would represent the first lander mission to the lunar farside and, as such, would require that a communication link be established with the Earth. A growing number of assets at the Sun-Earth L-1 libration point may provide access to a viable communication link, avoiding the need for a communications orbiter. The mission need only be designed to last through a single lunar day, which could make it relatively straightforward; if a rover is chosen as the implementation for sampling, it may be possible to keep the rover alive for longer. This would be a cost/benefit tradeoff to be determined as part of the mission analysis.

Issues on which the lunar sample community should make input include: identification of additional scientific problems that can be addressed by samples from SPA; choice of landing site to maximize the probability of addressing the first-order problems; sample size and the distribution between regolith and rocklet samples; details of sample collection (range from lander, depth, avoidance of contamination from lander); and environmental control constraints on samples (maximum temperatures, acceptable leak rates on Earth). The premise is that this mission will have to be kept as simple and as low-cost as possible to be selected by the Discovery program.

References: [1] Lucey et al. (1998) *JGR, 103,* 3701–3708. [2] Lawrence et al. (1998) *Science, 281,* 1484–1489. [3] Warren et al. (1995) *Eos Trans. AGU, 77,* 33.

SUBPIXEL DETECTION OF PYROCLASTIC MATERIALS IN CLEMENTINE ULTRAVIOLET-VISIBLE DATA.

W. H. Farrand[1] and L. R. Gaddis[2], [1]Space Science Institute, 1540 30th Street #23, Boulder CO 80303, USA (farrand@colorado.edu), [2]U.S. Geological Survey, Astrogeology Program, 2255 N. Gemini Drive, Flagstaff AZ 86001, USA.

Introduction: Lunar pyroclastic deposits represent a style of volcanism different from that responsible for the flood basalts that fill the mare basins. As volatile-coated, primitive materials originating deep (~400 km) within the Moon, these products of explosive volcanic eruptions are also important as probes of mantle composition [1] and as a potential resource [2] for future settlers. While many of the lunar pyroclastic deposits are spatially restricted and relatively small in size, they are easily resolvable at the spatial scale (~100 m/pixel) of the Clementine UV-VIS camera. Recent studies confirm previous results indicating that these deposits are not compositionally uniform [3–4], and suggest that further analyses can help to identify possible genetic relationships among lunar pyroclastic deposits, characterize their juvenile components, and clarify their relationships to nearby maria.

Among the juvenile materials from sampled lunar pyroclastic deposits are the orange glass and devitrified black beads found in the Taurus-Littrow Valley [5–6] and the green glass found by Apollo 15 [1]. Recent studies [3–4] suggest that deposits dominated by materials such as these may represent end members in the observed compositional variations among the lunar pyroclastic deposits. Here we present preliminary results of analyses focused on the use of the Clementine UV-VIS data for characterizing the composition and distribution of juvenile pyroclastic materials. Our test case for detailed mapping of a lunar pyroclastic deposit is that of the Apollo 17 landing site in the Taurus-Littrow (TL) Valley (Fig. 1a, b). Although black beads dominate the observed spectral reflectance at this site [5–6], sample data show that the pyroclastic eruption changed character, producing first orange glass and then black beads [3]. To assess the compositional variability of this deposit, especially our ability to distinguish the orange glasses, we apply techniques based on spectral mixture analysis [7] to detect materials at subpixel scales. The low albedo and subdued absorption features of the Taurus-Littrow deposit make this a challenging task.

Detectability Analyses: In recent years, several subpixel detection techniques have been developed for use with terrestrial airborne imaging spectrometer data [e.g., 8–10]. A technique that is functionally equivalent to spectral mixture analysis, the orthogonal subspace projection (OSP) technique [11] is used for the simulations presented here. In OSP, a target spectrum is projected onto a sub-

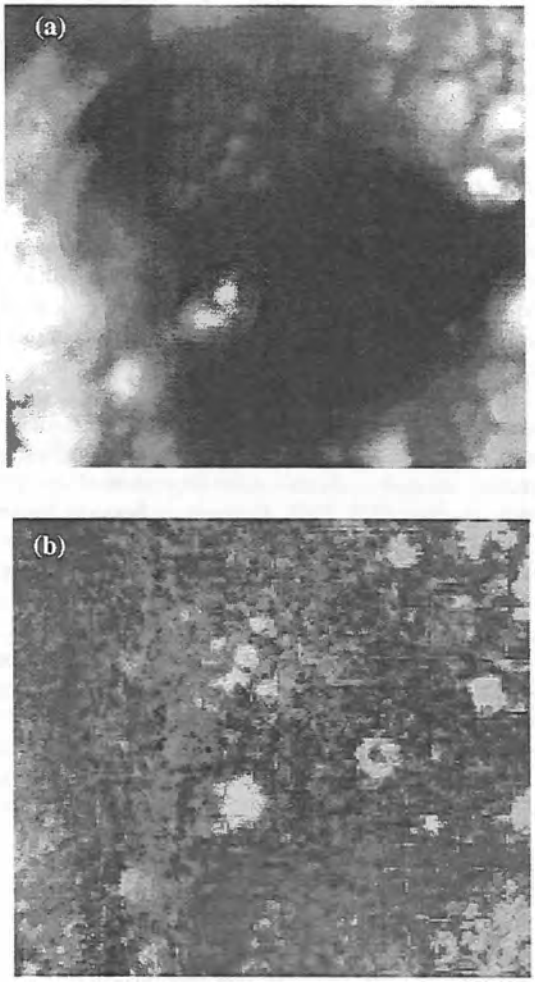

Fig. 1. **(a)** 750-nm band for Taurus-Littrow Valley. The Sculptured Hills are in the upper right and South Massif is in the lower left. North is toward the top. **(b)** Albedo-normalized [14] composite of 950-, 750-, and 415-nm bands. Colors are due to both compositional and maturity differences. Bright blue units such as those in the crater cluster (upper middle) expose fresh regolith of highland composition. Other green and blue-green features mark the locations of highland massifs and fresh craters. Soils with substantial pyroclastic components, primarily black beads, are shown in bright red with yellow overtones. (To view this figure in color, go to http://cass.jsc.nasa.gov/meetings/moon99/pdf/8053.pdf.)

space that is orthogonal to a set of background spectra. In this process, the response from the background spectra are nulled and that of the target is maximized. For the TL site, the spectra used for the simulation (Fig. 2) included three laboratory-measured sample spectra [12] convolved to the five UV-VIS bandpasses, and two spectra extracted from UV-VIS data over the TL Valley. The target spectrum was the orange soil sample 74220 from the Shorty Crater rim. "Background" spectra were from samples 74221 (a gray soil found near the orange soil) and 75111 (a dark mare soil). From the UV-VIS data, additional background spectra were obtained at the mare/highland interface and from the "crater cluster" area in the TL Valley. In the simulation, the background spectra were randomly mixed in each of 100 samples with 0.1% Gaussian noise added. For samples 20, 40, 60, and 80, the orange soil target was added in abundances of 90, 80, 60, and 40%. The 100-sample set was then reduced via OSP (Fig. 3). For this example, the orange soil was detectable only at the 90 and 80% abundance levels. It was found that the addition of higher noise levels (~1%), made the orange glass undetectable even at the 90% level. However, using background materials more representative of the highlands made the orange soil detectable at lower abundances.

Future Work: These results suggest that we should be able to map the distribution of juvenile pyroclastic materials, such as the orange glasses, using the Clementine UV-VIS data and subpixel analysis techniques such as spectral mixture analysis [7] and foreground background analysis [10]. Given the low albedo of these materials, a high fill factor will be required on a per pixel basis in order to achieve that mapping; however, observations made by

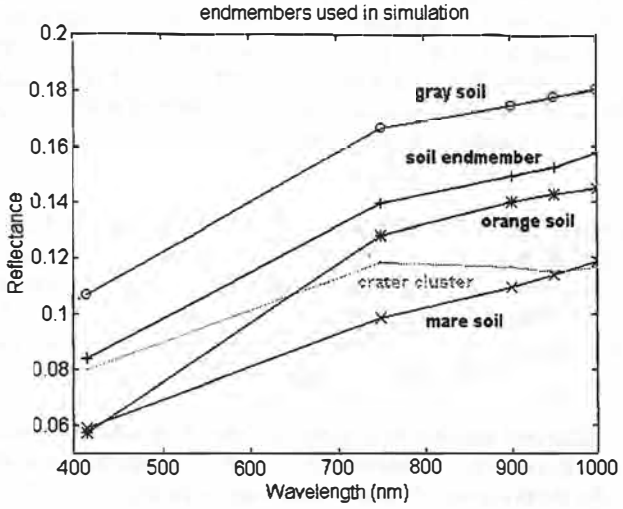

Fig. 2. End members used in detectability simulation.

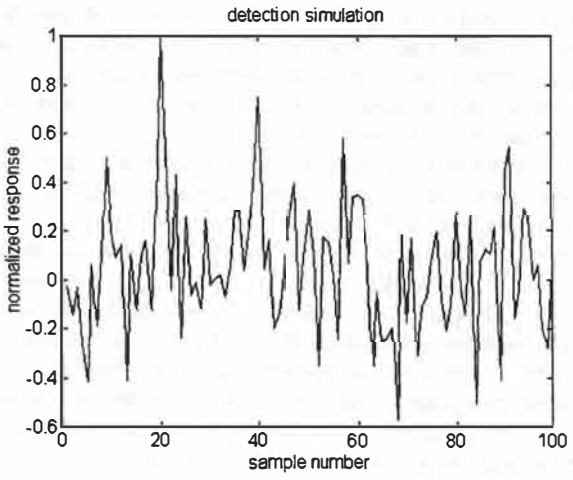

Fig. 3. Normalized response from detection simulation. Sample 20 contained 90% of the orange soil target, sample 40 contained 80%, sample 60 contained 60%, and sample 80 contained 20%. The higher response in samples 20 and 40 indicate detection of the target.

others, including orbital observations by the Apollo 17 astronauts [14], have indicated that these abundances are met for several pyroclastic deposits. The production of such maps will help to constrain the dynamics of pyroclastic eruptions on the Moon by providing information on the type, relative quantity, and distribution of juvenile volcanic materials [15].

References: [1] Delano J. W. (1986) *Proc. LPSC 16th*, in *JGR, 91*, D201–D213. [2] Hawke B. R. et al. (1990) *Proc. LPSC 20th*, 249–258. [3] Weitz C. A. et al. (1998) *JGR, 103*, 22725–22759. [4] Gaddis L. R. et al. (1999) *JGR*, in press. [5] Adams J. B. et al. (1974) *Proc. LSC 5th*, 171–186. [6] Pieters C. M. et al. (1974) *Science, 183*, 1191–1194. [7] Adams J. B. et al. (1993) in *Remote Geochemical Analysis* (C. Pieters and P. Englert, eds.), pp. 145–166. [8] Farrand W. H. and Harsanyi J. C. (1995) *JGR, 100*, 1565–1578. [9] Farrand W. H. and Harsanyi J. C. (1997) *Rem. Sens. Environ., 59*, 64–76. [10] Smith M. O. et al. (1994) *IGARSS '94*, 2372. [11] Harsanyi J. C. and Chang C-I. (1994) *TGARS, 32*. [12] Adams J. B. and McCord T. B. (1971) *Proc. LSC 2nd*, 2183–2195. [13] Lucchitta B. K. and Schmitt H. H. (1974) *Proc. LSC 5th*, 223–234. [14] Pouch G. W. and Campagna D. J. (1990) *PE & RS, 56*, 475–479. [15] Gaddis L. R., this volume.

ENHANCED HYDROGEN ABUNDANCES NEAR BOTH LUNAR POLES.

W. C. Feldman[1], S. Maurice[2], D. J. Lawrence[1], I. Getenay[2], R. C. Elphic[1], B. L. Barraclough[1], and A. B. Binder[3], Los Alamos National Laboratory, Los Alamos NM 87545, USA (wfeldman@lanl.gov), [2]Observatoire Midi-Pyrènèes, Toulouse, France, [3]Lunar Research Institute, Gilroy CA 95020, USA.

Chemical analyses of all samples of the Moon returned to Earth show that the lunar surface is highly depleted in volatiles [1]. Specifically, the H content of lunar soils averages only 50 ppm, which can be explained in terms of surface implantation of solar-wind H. We note that all returned samples come from near-equatorial latitudes where daytime temperatures are sufficiently high that water is not stable to evaporation, photo dissociation, ionization, and eventual loss to space through pickup by the solar wind. However, it has long been postulated that a significant fraction of water delivered to the Moon by comets, meteoroids, and interplanetary dust can be stably trapped within the permanently shaded floors of polar craters where temperatures are sufficiently low so that sublimation times can be longer than several billion years [2–3].

Recent results from analysis of the high-altitude (100 ± 20 km) portion of the Lunar Prospector Neutron Spectrometer (LPNS) dataset [4] have revealed that H abundances near both lunar poles are enhanced relative to that which exist at equatorial latitudes. Because this average enhancement is not much larger than the near-equatorial average of 50 ppm, it is reasonable to ask how much of the polar-H enhancement comes from the solar wind and how much comes from lunar impacts by solid interplanetary materials. Perhaps the low temperatures at polar latitudes could reduce loss rates of solar-wind-implanted H sufficiently to account for the inferred difference between average polar and equatorial H abundances.

Although the foregoing suggestion is plausible, neither laboratory simulations on returned soil samples nor numerical simulations of H loss rates from the radiation-damaged surfaces of soil grains have been performed to prove its feasibility. We try to address this question by analyzing the low-altitude (30 ± 15 km) portion of LPNS data to search for relatively small spatial-scale enhancements in H abundances at both lunar poles. Maps were constructed of epithermal-neutrons corrected for elemental abundance variations by subtracting 7% of measured thermal-neutron counting rates. Although the spatial resolution of the LPNS at 30-km altitude is ~55 km FWHM, we binned all the data in 0.5° × 0.5° spatial pixels and then applied a 30-km FWHM Gaussian smoothing algorithm. Resultant polar maps of corrected epithermal counting rates are shown in Fig. 1. Inspection reveals discrete depressions in counting rates that are superimposed on more generally distributed depressions that surround both poles. Comparison with the radar-measured polar topography shows that the areas of most depressed epithermal counts rates in the south overlie craters that have floors in permanent shade. Furthermore, these depressions are neither cylindrically symmetric about either pole nor do they minimize at the poles. Similar maps of fast neutrons (not shown here) reveal a single, statistically significant depression centered on the maximum depression of the epithermal neutrons at about 88°S, 20°E. Comparison between high-altitude and low-altitude epithermal maps reveals a larger depression at low altitudes in the south but the same magnitude of depression in the north. Hydrogen enhancements in the south must therefore have spatial scales comparable to the spatial resolution of LPNS, 55-km FWHM, yet consist of smaller clumps more uniformly distributed over the LPNS field of view in the north. A quantitative comparison between measured epithermal counting rates and numerical simulations using the measured polar topography [5] yields the following: (1) H abundances within the permanently shaded craters near the south pole are equivalent to a water-ice mass fraction of 1.5± 0.8%,

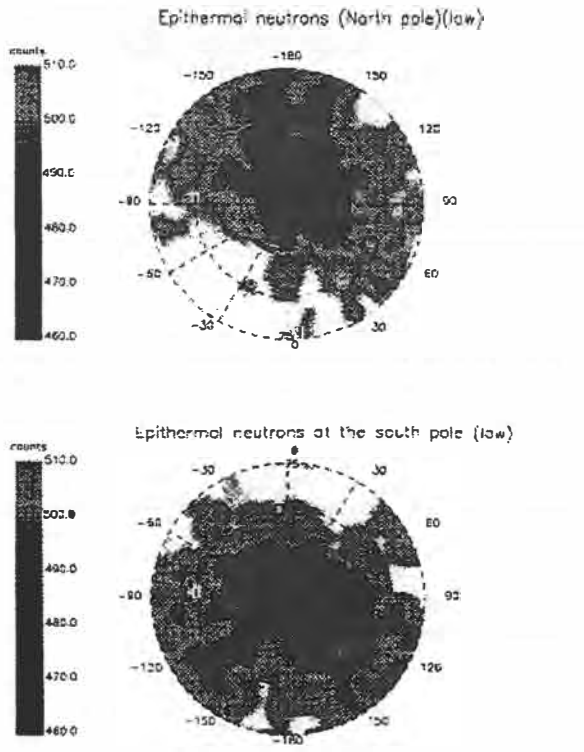

Fig. 1. Counting rates of (epithermal = 0.07 × thermal) neutrons poleward of ±75° latitude.

(2) the enhanced H within these craters must not be buried beneath the surface by more than ~10 g cm^{-2} (5 cm at a density of 2 g cm^{-3}), (3) the H abundance near both poles averages 100 ppm above that known from near-equatorial returned soil samples (50 ppm, [1]), and (4) the total mass content of H poleward of –75° is ~200 × 10^6 t, and that poleward of +75° is ~150 × 10^6 t. If the enhanced H within all regions of permanent shade near both poles is in the form of water ice, use of the area estimates given by Margot et al. [5] yields estimates of 135 (240) × 10^6 t in the 2250 (4000) km^2 of shaded areas poleward of –87.5°, and 62 × 10^6 t in the 1030 km^2 of shaded areas poleward of +87.5°.

We note, however, that neutron observations by themselves cannot uniquely identify the chemical form of H in lunar regolith. That is, LPNS data cannot discriminate solar-wind-implanted H from OH, H_2O, etc. In the absence of a temperature map of the lunar poles and a knowledge of the retentivity of H by lunar soil grains as a function of temperature, sufficient information is not yet available to uniquely identify water-ice deposits at the lunar poles. Nevertheless, the floors of permanently shaded polar craters are predicted to have temperatures sufficiently low that water ice should be stable for billions of years, yet uncratered surfaces near the polar cap are too high in temperature to retain water ice [6]. This suggests that at least some of the enhanced deposits of H identified by LPNS are in the form of water ice.

References: [1] Haskin and Warren (1991) in *Lunar Sourcebook, A User's Guide to the Moon* (G. H. Heiken et al., eds.), p. 357, Cambridge Univ. [2] Watson K. et al. (1961) *JGR, 66,* 1598. [3] Arnold J. (1979) *JGR, 84,* 5659. [4] Feldman et al. (1998) *Science, 281,* 1496. [5] Margot et al. (1999) *Science, 284,* 1658. [6] Vasavada A. R. et al. (1998) *Icarus,* submitted.

LASER ARGON-40–ARGON-39 AGE STUDIES OF DAR AL GANI 262 LUNAR METEORITE.

V. A. Fernandes, R. Burgess, and G. Turner, Department of Earth Sciences, University of Manchester, Oxford Road, Manchester M13 9PL, UK (vfernandes@fs1.ge.man.ac.uk)

Introduction: The lunar meteorite Dar al Gani 262 (DAG 262) was found in the Sahara Desert in Libya on March 23, 1997. This was the first lunar meteorite found in a desert and is the thirteenth lunar meteorite discovered. DAG 262 is a polymict anorthositic lunar highland breccia [1–2].

The ^{40}Ar-^{39}Ar dating technique has been applied to DAG 262 in an attempt to determine the crystallization age and shock events experienced by this meteorite. Previous studies have indicated that this meteorite may have suffered up to four shock events [3]. Due to the brecciated nature of the rock and the likelihood of multiple shock events, a laser-probe technique has been used to analyze individual components (minerals and clasts) of the meteorite.

Sample Description: The sample supplied to us (~1.5 g) shows two distinct clast types (1) feldspathic and (2) basaltic, the latter not having been previously described [1–4]. Plagioclases show fractures and undulatory extinction as the result of shock events [1–3]. The feldspathic clast has small, round low-Ca pyroxenes distributed within it. Electron-microprobe analyses of feldspar and pyroxene are given in Table 1. The bulk composition as determined by [4] suggests that the source of this clast is the ferroan-anorthositic suite.

The basaltic clast shows a very fine intergranular texture with some larger plagioclase grains. The two clasts are separated by a melt-glass matrix that contains plagioclase with the same chemical composition as those plagioclases within the feldspathic clast. A devitrified mafic-glass spherule of ~150 mm diameter was identified within the matrix as well as other small fragments of possible glass spheres. Some dendritic veins can be observed on the outer part of the section, which formed after breccia lithification[1–2].

Experimental Methods: Two laser ^{40}Ar-^{39}Ar experiments are being carried out: (1) infrared laser-stepped heating of feldspathic fragments that have been separated from the meteorite; and (2) ultraviolet laser spot fusion (50 μm) of a slice of meteorite (~1.0 × 0.5 cm) showing both clast types. Preliminary results from experiments (1) have been obtained so far. Three feldspathic fragments (DAG1-3, each weighing ~1 mg) have been heated using between 20–30 steps, of increasing laser output power, each of 1 min duration.

Argon-40–Argon-39 Age Constraints: Figure 1 is a plot of $^{36}Ar/^{40}Ar$ vs. $^{39}Ar/^{40}Ar$ for 20 extractions obtained from DAG3. Overall, the data show increasing $^{36}Ar/^{40}Ar$ and decreasing $^{39}Ar/^{40}Ar$ as heating proceeds. In detail the release is more complex; points 1–4 show a significant decrease in $^{39}Ar/^{40}Ar$ corresponding to an increase in apparent age from 1.3 to 5.1 Ga. This variation may be attributed to the combined effects of terrestrial alteration that result in loss of radiogenic ^{40}Ar and implantation of lunar ^{40}Ar in grain boundaries that lead to an increase in apparent age.

Points 5–20 define a linear correlation interpreted to represent mixing between radiogenic ^{40}Ar, released at intermediate temperature, and trapped Ar that dominates the high temperature release (Fig. 1). The intercept of the correlation on the $^{39}Ar/^{40}Ar$ axis corresponds to an age of 1.95 Ga. This age is low compared with other lunar meteorites and is most likely related to a shock event. The trapped component released at high-temperature has $^{36}Ar/^{40}Ar$ of ~2.8, which is close the value of ~2.5 reported previously for the bulk meteorite [2].

The increasing proportion of trapped Ar released at high temperature is contrary to the usual release pattern obtained for lunar soils [5]. Two possible explanations are given: (1) Ar loss from grain boundaries occurred at depth within the lunar regolith, while preserving trapped Ar with higher $^{36}Ar/^{40}Ar$ in the center of grains; or

TABLE 1. Electron-microprobe analyses of low-Ca Pyroxene and plagioclase and of a devitrified glass-spherule found within the matrix.

	Low-Ca Pyroxene	Plagioclase	Devitrified glass
SiO_2	38.35	44.23	35.19
TiO_2	0.1173	0.0145	0.0671
Al_2O_3	0.0840	35.3244	0.0000
Cr_2O_3	0.0845	0.0000	0.0338
FeO	21.42	0.19	36.47
MnO	0.3321	0.0000	0.4154
MgO	39.38	0.19	27.73
CaO	0.1625	19.6293	0.0623
K_2O	0.0000	0.0236	0.0025
Na_2O	0.0237	0.4024	0.0268
NiO	0.0490	0.0000	0.0000

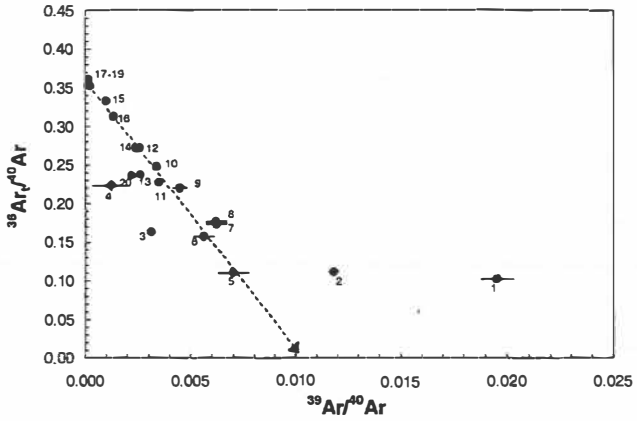

Fig. 1. Argon-36/Argon-40 vs. $^{39}Ar/^{40}Ar$ laser-stepped heating results for DAG3. The numbers adjacent to the data points indicate the laser extraction step.

(2) release of trapped Ar from a low-K-bearing mineral present in feldspathic fragments. Anomalously high apparent ages (>4.5 Ga) obtained at low temperature from steps 3 and 4 indicate that DAG3 contains implanted lunar atmosphere ^{40}Ar presumably acquired near the surface of the lunar regolith. This is inconsistent with the explanation (1) that loss occurred at depth. Fine-grained pyroxene is a common component in the matrix of DAG 262 [2], has low K content, and will retain Ar to a higher temperature than plagioclase making explanation (2) the most likely.

Release of Ar from fragment DAG1 was similar to that of DAG3 giving an indistinguishable intercept age of 2.0 Ga. However, DAG2 contained much lower levels of trapped Ar and 19% of the total ^{39}Ar released at high temperature gave an age of 3.05 Ga. This age is slightly below previously inferred total gas ages for lunar meteorites and may be related to the crystallization event.

Cosmic Exposure Ages: These are based on plots of $^{37}Ar/^{36}Ar$ vs $^{38}Ar/^{36}Ar$ and give ages of 185 Ma, 252 Ma and 122 Ma for DAG1, DAG2 and DAG3 respectively. The cosmic-ray exposure ages indicate the components of DAG 262 had different exposure histories, an expected result given that this meteorite is a breccia.

Chemistry: The K/Ca weight ratio calculated from $^{39}Ar/^{37}Ar$ of 3.6×10^{-3} is similar to the bulk ratio obtained by [2] of 3.8×10^{-3}. A much lower K/Ca of 0.6×10^{-3} obtained from feldspar by electron microprobe is evidence for the impurity of the feldspar separates analyzed for the age study. The low K/Ca ratio of the feldspar compared to the bulk indicates that there is an additional K-bearing phase in DAG 262 that remains to be identified.

Current investigations are aimed at using the UV laser to determine ^{40}Ar-^{39}Ar ages from individual minerals within DAG 262.

Acknowledgments: We wish to thank I. Franchi (Open University) for providing the sample of DAG 262. This work was supported by the European Commission via a TMR fellowship to VAF.

References: [1] Bischoff A. and Weber D. (1997) *MAPS, 32,* A13–A14. [2] Bischoff A. et al. (1998) *MAPS, 33,* 921–935. [3] Nishiizumi K. et al. (1998) *LPS XXIX,* Abstract #1957. [4] Joliff B. et al. (1999) *LPS XXIX,* Abstract #2000. [5] Burgess R. and Turner G. (1997) *MAPS, 33,* 921–935.

PROGRESS TOWARD CHARACTERIZATION OF JUVENILE MATERIALS IN LUNAR PYROCLASTIC DEPOSITS.

L. R. Gaddis, Astrogeology Team, U. S. Geological Survey, 2255 N. Gemini Drive, Flagstaff AZ 86001, USA (lgaddis@flagmail.wr.usgs.gov).

Introduction: In recent analyses, the 5-band Clementine UV-VIS data have been used to examine the compositions of lunar pyroclastic deposits [e.g., 1–3]. A primary goal of these analyses has been the characterization of the primary volcanic or juvenile components of these deposits. The compositions, physical and morphological characteristics, and spatial distributions of juvenile volcanic materials provide information on the distribution of primary mafic materials on the Moon, conditions required for their eruption at the surface, and the behavior of lunar volcanic processes over time. Using current analytical techniques with the new Clementine UV-VIS global mosaic [4–6], and data from the GLGM2 geophysical models [7], to supplement ongoing work with Earth-based spectral reflectance analyses and laboratory investigations, my colleagues and I have adopted a three-pronged approach to these issues involving: (1) compositional analyses of lunar pyroclastic deposits; (2) characterization of the relations between effusive and explosive lunar volcanism; and (3) examination of the global occurrence and distribution of lunar pyroclastic deposits. This report and related work [8] describe progress toward remote characterization of the compositions of juvenile materials in the pyroclastic deposits located at Taurus-Littrow and J. Herschel. These studies have implications for characterization of the relations between the products of effusive and explosive volcanism on the Moon.

Background: Analyses of lunar pyroclastic materials, primarily the juvenile picritic glasses, provide unique information on the composition of the mantle [9] and on the nature and origin of associated volatile elements in an otherwise volatile-depleted environment [10]. Possible fundamental differences between picritic glasses and mare basalts (e.g., lesser fractional crystallization and greater depth of origin for glasses [11]) support their identification as the best examples of primitive materials on the Moon, and attest to their importance in characterizing the lunar interior and as a starting place for understanding the origin and evolution of basaltic magmatism on the Moon. Remote-sensing analyses of these deposits have helped us to identify the characteristic components of some of these deposits [12–14], to begin to constrain the distribution of lunar volcanic deposits [15], and to understand the styles of eruption and emplacement of basalts on the Moon [1,16]. To fully appreciate the role of pyroclastic volcanism on the Moon, we must understand the ranges of composition, spatial and temporal distribution, relationship to effusive volcanic deposits, and modes of occurrence and formation of pyroclastic deposits. Until additional samples are available, remote analyses of lunar pyroclastic deposits are a primary means of fully characterizing these deposits.

More than 100 pyroclastic deposits are identified (see http://wwwflag.wr.usgs.gov/USGSFlag/Space/LunPyro) on the Moon. Their characteristics, summarized here briefly, are described in detail elsewhere [e.g., 1–3]. Lunar pyroclastic deposits are dark and smooth-surfaced, and they are observed in association with sinuous rilles, irregular depressions, or endogenic craters within highlands and/or on the floors of old impact craters situated along the margins of many mare-filled basins on the lunar nearside and farside. Lunar pyroclastic deposits are divided into two classes on the basis of size, morphol-

ogy, and occurrence [e.g., 14]. The ~12 large deposits are of regional extent (up to several tens of thousands km^2), while small deposits (~90 in number) are more localized, typically only several hundred km^2. Large deposits were probably emplaced via Strombolian-style or continuous fire-fountain eruptions, with wide dispersion of well-sorted pyroclasts [16]. A significant component of Fe^{+2}-bearing volcanic glass beads was identified in many of the regional pyroclastic deposits [e.g., 12–14]. At Taurus-Littrow (~50 km west of Apollo 17), black beads (the crystallized equivalent of Fe^{+2}-bearing orange glasses) are the characteristic ingredient of the regional pyroclastic deposit [12–13]. Both orange and black beads were recognized as pyroclastic, with variations in cooling time in a fire fountain producing quenched, crystallized, and/or composite droplets [10–12].

Small pyroclastic deposits were formed via Vulcanian-style or intermittent eruptions [17], with explosive decompression removing a plug of lava or caprock within a conduit and forming a vent depression. Small pyroclastic deposits were divided into three classes on the basis of their "1.0-mm" or mafic absorption bands [18]. Most Group 1 deposits are mixtures of highlands-rich country rock and glassy juvenile material with small amounts of basaltic caprock material. Group 2 deposits consist largely of fragmented basaltic material, with insignificant amounts of highland and glassy materials. Group 3 deposits are dominated by olivine and orthopyroxene; the olivine is almost certainly associated with juvenile material, and the orthopyroxene is likely to have been emplaced as a result of erosion and entrainment of the wall rock [14].

Recent Work: Although differing origins have been proposed for the large and small pyroclastic deposits, comparison of Clementine UV-VIS spectral reflectance data for these deposits shows a linear trend (Fig. 1), suggesting some compositional relationship between the two types of deposits. Weitz et al. [1], in studying several large pyroclastic deposits (Taurus-Littrow, Sulpicius Gallus, Mare Vaporum, Rima Bode, Sinus Aestuum, Aristarchus Plateau, and Orientale), proposed that this linear trend represents a "mixing line" between those large deposits with ~100% crystallized beads and those with ~100% glass beads. A Sinus Aestuum dark spot is the crystallized end member, and Aristarchus is the glass end member. However, the overlap between the small and large deposits and between the pyroclastic deposits and nearby mare and highlands units (Fig. 1) suggests that (1) the juvenile pyroclastic materials are not glasses in all cases and (2) substantial spectral contributions from highland and mare units may be observed for both large and small deposits [2].

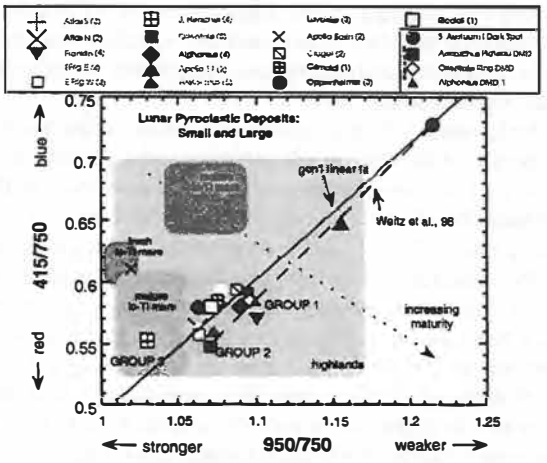

Fig. 1.

To characterize juvenile materials in lunar pyroclastic deposits, we are using the Clementine multispectral data at both UV-VIS and NIR wavelengths (~0.4–2.7 μm) to study the large deposit at Taurus-Littrow (TL) [8] and the small deposit at J. Herschel crater. Although black beads dominate the observed spectral reflectance at the TL site [12,13], sample data show that the pyroclastic eruption changed character, producing first orange glass and then black beads [10]. To assess the compositional variability of this deposit, especially our ability to distinguish and map the orange glasses, we apply techniques based on spectral mixture analysis to detect materials at subpixel scales. Preliminary detectability analyses using the Clementine UV-VIS data and the Orthogonal Subspace Projection technique with target and background spectra (from both the laboratory and the scene) indicate that orange soil at TL is detectable at the 90 and 80% abundance levels ([8] and references therein). To evaluate our ability to map the distribution of different types of juvenile pyroclastic materials at individual and multiple sites, and thus to provide constraints on their eruption mechanisms, we will apply these results to TL and to related deposits at Sulpicius Gallus, Rima Bode, Sinus Aestuum, and Mare Vaporum.

An additional approach to the characterization of the juvenile materials in lunar pyroclastic deposits focuses on spectral analysis of the small deposit at J. Herschel Crater. This deposit is somewhat unique in that it is the only current member of Group 3 and it appears to have a substantial olivine component [e.g., 19]. At visible to near-infrared wavelengths, olivine has a broad, relatively deep absorption band at 1.0 μm, but it has no absorption feature at 2.0 μm. Iron-bearing pyroclastic glass, which may be present in addition to or in lieu of olivine, has broad absorption bands at both 1.0 and 2.0 μm [e.g., 14]. To determine whether olivine is indeed the dominant juvenile component at J. Herschel, the Clementine NIR data were examined for this area. Although calibration of these data is currently under way and is thus incomplete at present, comparisons within the NIR dataset can be made. No absorption feature at 2.0 μm is observed at the volcanic vents at J. Herschel. This supports the identification of olivine as the primary juvenile component and the absence of volcanic glasses as major contributors to the spectral signatures in this area. Application of the Lucey-derived compositional (FeO and TiO_2) and maturity relations [20] shows affinities between the J. Herschel deposit and ancient maria in nearby Mare Frigoris.

References: [1] Weitz et al. (1998) *JGR,* 22725–22759. [2] Gaddis et al. (1999) *JGR,* in press. [3] Gaddis et al. (1999) *LPS XXX,* 1732. [4] Eliason et al., this volume. [5] McEwen et al. (1998) *LPS XXIX,* 1466–1467. [6] Pieters et al. (1997) online document. [7] Neumann et al. (1996) *JGR,* 16841–16863; Lemoine et al. (1997) *JGR,* 16339–16359. [7] Gaddis et al. (1998) *LPS XXIX,* 1807–1808. [8] Farrand and Gaddis, this volume. [9] Delano (1986) *Proc. LPSC 16th,* in *JGR, 91,* D201–D213. [10] Heiken et al. (1974) *GCA, 38,* 1703–1718. [11] Shearer and Papike (1993) *GCA, 57,* 4785–4812; Papike et al. (1998) *Rev. Mineral., 36,* ch. 5. [12] Adams et al. (1974) *LSC V,* 171–186. [13] Pieters et al. (1973) *JGR, 78,* 5867–5875. [14] Gaddis et al. (1985) *Icarus, 61,* 461–488. [15] Head (1974) *LSC V,* 207–222. [16] Wilson and Head (1981) *JGR, 78,* 2971–3001. [17] Head and Wilson (1979) *LPS X,* 2861–2897. [18] Hawke et al. (1989) *LPS XIX,* 255–268; Hawke et al. (1990) *LPS XX,* 249–258. [19] McCord et al. (1981). [20] Lucey et al. (1998a) *JGR, 103,* 3670–3699; Lucey et al. (1998b) *LPS XXIX,* Abstract #1356.

LATERAL AND VERTICAL HETEROGENEITY OF THORIUM IN THE PROCELLARUM KREEP TERRANE: AS REFLECTED IN THE EJECTA DEPOSITS OF POST-IMBRIUM CRATERS. J. J. Gillis and B. L. Jolliff, Department of Earth and Planetary Sciences, Washington University, St. Louis MO 63130, USA (Gillis@levee.wustl.edu).

Introduction: The Procellarum KREEPTerrane [1,2] displays the highest concentrations of Th on the Moon [3]. However, locations of elevated Th in this region appear to be random. As observed in the 5° per pixel equal-area Th data [3–4], and made more evident in the preliminary 2° data [5], Th is enhanced around the craters Aristillus, Aristarchus, Kepler, Mairan, the Apennine Bench formation, and the Fra Mauro region, while noticeably and unexpectedly lower in other locations (e.g., Archimedes, Copernicus, Eratosthenes, and Plato). We have examined the composition of the materials present in these regions with the goal of understanding the patchy nature to the distribution of Th and ultimately to decipher the geologic processes that have concentrated the Th.

At present time, the published resolution of the Lunar Prospector Th γ-ray data is low (5° per pixel [3–4]), but this will soon be superceded by significantly higher-resolution data (2° per pixel [5]). Even at this improved resolution, however, it is difficult to resolve the units that are the major source of Th. In an attempt to circumvent this problem, we employ the higher-resolution Clementine multispectral data for those regions mentioned above. We use the UV-VIS-derived compositional information and the spectral properties of craters, and their ejecta as drill holes through the mare-basalt surface to investigate the thickness and composition of underlying material. With this information we attempt to piece together the stratigraphy and geologic history of the Imbrium-Procellarum region.

Methods: We processed the five-band multispectral data from the Clementine Mission (415, 750, 900, 950, and 1000 nm [6]) using ISIS software and calibration parameters developed by the USGS, Flagstaff, Arizona [7,8]. Final image mosaics are in equal-area sinusoidal projection, and have a resolution of 250 m/pixel. Using the method of [9] we produced maps of FeO and TiO_2 composition. Here we examine the Th, FeO, and TiO_2 composition and spectral properties of the craters discussed above and their ejecta, with the goal of describing the materials they excavate (Table 1).

TABLE 1. The compositions of these areas were recorded utilizing Clementine derived FeO and TiO_2 [7] and Th from Prospector γ-ray data [2,3].

Area of Interest	Crater Diameter	Th ± 1 ppm	FeO ± 1 wt%	Basalt Thickness
Apennine Bench	—	7	10–14	0
Archimedes	83	6	12–16	0
Aristillus	55	7	10–14	4.4 km
Autolycus	35	6	14–16	>2.8
Copernicus	93	6	4–8	<7.4
Eratosthenes	58	6	10–14	0
Kepler	32	8	14–18	~3.2 km
Mairan	40	7	12–15	0
Plato	101	5	9–13	0

Model: One interpretation for the origin of the high-Th material is that subsurface KREEPy materials have been excavated by impact craters [1]. The material excavated may be either volcanic KREEP (e.g., Apennine Bench Formation), KREEPy impact-melt breccia formed by the Imbrium impact (e.g., Fra Mauro Formation) [1], or other KREEP-rich crustal material. Determining which type of material is responsible for the elevated Th and its extent is important to understanding the premare and possibly the prebasin stratigraphy of the Imbrium-Procellarum Region.

Merging the 5° Th data with the shaded relief map, we observe that the highest Th concentrations are not related to pre-Imbrium upper crustal materials. The Apennines, Alpes, and Caucasus Mountains represent the pre-Imbrian highlands material and do not express concentrations of Th, FeO, and TiO_2 as high as the most Th-rich materials exposed within the Procellarum KREEP Terrane. We observe that, in general, these massifs contain 10–14 wt % FeO [10] and 4–7 ppm Th [2–3].

Determining whether the Th signal is from KREEP basalts or KREEPy impact-melt breccias cannot be done with the Clementine data because the two rock types are compositionally and mineralogically too similar (e.g., the Th-rich, mafic impact-melt breccias in the Apollo sample collection are dominated by a KREEP-basalt like component [11]). Mapping the distribution and sizes of craters and whether they display elevated Th concentrations or not, should reveal the depth and thickness of the KREEP-rich materials, and whether they are ubiquitous (i.e., impact-melt breccia) or more randomly distributed; this might be taken as an indicator of localized KREEP-basalt flows.

Discussion and Conclusions: Within the southeastern region of the Imbrium basin, there are two Th hot spots. The first is associated with the crater Aristillus, and the latter with the Apennine Bench Formation [12]. Adjacent to these two hot spots are craters with a lower Th signature: Archimedes and Autolycus. We observe in the ejecta of Aristillus, a region of significantly lower FeO (10–14 wt%) relative to the surrounding mare basalt (Table 1; Fig. 1). The crater Autolycus, 50 km to the south, did not excavate similar low-FeO material. We suggest that the lower-FeO material in the ejecta of Aristillus corresponds to Th-rich material; the FeO content observed in Aristillus ejecta is comparable to that of KREEP basalt or mafic impact melt breccia (10–12 wt% FeO). We determine that this low-FeO, Th-rich material is volcanic KREEP, as opposed to Imbrium impact melt, on the basis that the low-Fe material is exposed more prominently in ejecta in the northern portion of Aristillus. Our assumption is that if the layer underlying Aristillus was continuous, a more widespread and uniform low-Fe signature would be observed in the ejecta deposit.

Archimedes, 110 km southwest of Aristillus, impacted the northern portion of the Apennine Bench prior to the eruption of KREEP basalt [12]. Archimedes rim material is not as enriched in Th as the Apennine Bench, and there are differences between the two in FeO concentration (Table 1) and in their continuum slope. Archimedes exhibits a much steeper or "redder" continuum slope than the Apennine Bench. This steep slope suggests the presence of glassy material [13]. The glassy material is concentrated around an unnamed crater on the southern rim of Archimedes (4.5°W, 28.2°N) and along the northern rim of Archimedes. We suggest two possibilities, or a combination of the two, to explain the low-Th signal from Archimedes: (1) The Apennine Bench prior to KREEP basalt eruption was lower in Th (4–7 ppm, e.g., similar to the Apennine massifs) and KREEP basalts are

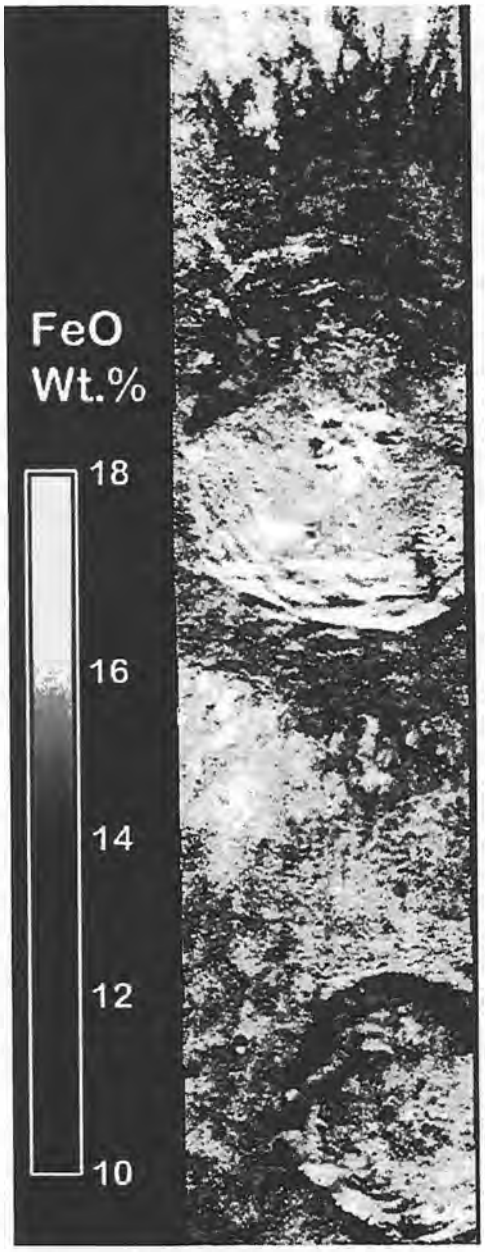

Fig. 1. Clementine-derived FeO from orbit 168 (center longitude 1°E). The central peak crater is Aristillus, and to the lower right is Autolycus. Aristillus has exposed a relatively low-FeO unit and it is likely that this material accounts for the increased Th detected in the Lunar Prospector γ-ray spectra. Extreme FeO values associated with steep-slope inside crater rims are an artifact of albedo variations on Sun-facing and shaded slopes.

absent in the rim of Archimedes; or (2) the glassy (possibly pyroclastic) material layering the rim of the Archimedes, dilutes any high-Th material present with low-Th material.

The craters Copernicus and Plato display some of the lowest Th values for craters within the Procellarum KREEP Terrane (Table 1). The impact that produced Copernicus was not only large enough to excavate through the mare basalt but also through a KREEPy layer, if present, beneath the basalt to expose low-FeO material in its ejecta. The volume of low-FeO material excavated by the impact was substantial enough to mask the high-FeO signature of mare basalt and the high-Th signal from a subsurface KREEPy material. On the other hand, the rim of Plato, like Archimedes, has a steep "reddish" continuum, indicating that it may be covered by a glassy, perhaps pyroclastic, material. Surrounding Plato are numerous rilles and volcanic vents, indicating that plains-type volcanism occurred in the area and supporting the possibility that these glassy materials are pyroclastic deposits. Therefore, the low-Th composition of the materials surrounding Plato may be explained by pyroclastic material covering the original basin rim material and concealing its inherent Th concentration, or it may simply have struck a region of lower-Th content.

The smallest crater in this study, Kepler, displays the highest concentration of Th (Table 1). Kepler and its ejecta have a noticeably higher-FeO concentration (14–18 wt% FeO) compared with other areas of elevated Th. We note that the unit on which Kepler is situated has a lobate morphology. This observation suggests that volcanic flows, containing a high concentration of Th, reached the surface in this area. These flows may represent KREEP basalt flows like those within the Apennine Bench Formation, or they may represent a higher-FeO variant.

We find that the compositional data from Aristillus, Autolycus, Archimedes, and Kepler favor the presence of KREEP basalt over "upper crustal," proximal ejecta. Moreover, the Fra Mauro Formation represents "deep crustal," more distal Imbrium ejecta [14]. Furthermore, this technique of analyzing the composition of crater ejecta not only allows us to estimate the composition of subsurface materials but also yields mare basalt thicknesses. A more comprehensive treatment of this is being prepared and will result in a high-resolution map of mare thickness.

Acknowledgments: This work was supported by NASA grants NAG5-6784 (BLJ) and NAG5-4172 (LAH).

References: [1] Jolliff B. L. et al. (1999) *JGR*, submitted. [2] Haskin et al. (1999) *JGR*, submitted. [3] Lawrence D. et al. (1998) *Science, 281*. [4] Gillis J. J. et al. (1999) *LPS XXX*, Abstract #1699. [5] Lawrence D. et al. (1999) *LPSC XXX*, Abstract #2024. [6] Nozette S. et al. (1994) *Science, 266*. [7] Eliason E. M. (1997) *LPS XXVIII*, Abstract #1198. [8] McEwen A. S. (1996) *LPS XXVII*. [9] Lucey P. G. et al. (1998) *JGR, 103*. [10] Bussey D. B. J. and Spudis P. D. (1998) in *Workshop on New Views of the Moon*, LPI. [11] Korotev R. L. (1999) *JGR*, submitted. [12] Hackman R. J. (1966) USGS Map I-463. [13] Wells E. and Hapke B. (1977) *Science*, 195. [14] Jolliff et al., this volume.

THE OPTICAL MATURITY OF EJECTA FROM LARGE RAYED CRATERS: PRELIMINARY RESULTS AND IMPLICATIONS. J. A. Grier[1], A. S. McEwen[1], P. G. Lucey[2], M. Milazzo[1], and R. G. Strom[1], [1]University of Arizona, Lunar and Planetary Laboratory, 1629 E. University Boulevard, Tucson AZ 85721, USA (jgrier@lpl.arizona.edu), [2]Hawai'i Institute of Geophysics and Planetology, University of Hawai'i at Manoa, 2525 Correa Road, Honolulu HI 96822, USA.

Introduction: Shoemaker [1–2] argued that several lines of evidence suggest a significant increase in the production of large craters on the Earth late in geological time (~200–300 Ma). We have conducted a preliminary test of this hypothesis via a study of large

recent craters on the Moon, and have concluded that the lunar record does not support this idea.

The relatively recent (<1 Ga) flux of asteroids and comets forming craters on the Earth and Moon may be accurately recorded by lunar craters whose ejecta are optically immature, and therefore distinguishable from the overall mature background soils. Lucey et al. [3–4] have developed a methodology for extracting an optical maturity (OMAT) parameter from multispectral images. We have generated a preliminary dataset of average radial profiles of OMAT values around large craters ($\geq$20 km diameter) that have been suggested or suspected of belonging to the Copernican time-stratigraphic system. Our survey covers the Moon from ±60° latitude.

Determining Relative Age: The average OMAT profile for each large crater is generated from nearside and farside OMAT mosaics. The profiles clearly fall into three bins based on their relative age. Young craters' profiles are characterized by high OMAT values near the rim and very steep dropoffs in OMAT value over a long distance away from the crater. Old craters whose profiles over their ejecta are essentially flat sloped and indistinguishable from background; their OMAT values at the rim are very low. Intermediate craters in this bin are between young and old; they have moderate OMAT values at the rim, and their profiles, while somewhat flat, are distinguishable from background some distance away from the crater rim. Profiles for a sample of large craters show a range of possible values and slopes; clearly the trend is a continuum [5].

These suggested bins are based on the absolute ages of a few lunar craters, such as Tycho and Copernicus (crater ages from [6] and [7]). Tycho and Copernicus are approximately the same size, but their OMAT profiles are quite different. Tycho is clearly young, with a high OMAT value at the crater rim and a steep dropoff in OMAT values as one follows the ejecta away from the crater. Copernican ejecta appears to be almost entirely mature, but there may be some suggestion of more immature ejecta within 2 crater diameters of the rim. Copernicus is therefore either old, or is on the old side of intermediate. Copernicus has been radiometrically dated at ~810 Ma, so the upper limit of this technique to identify and relatively date large craters must fall at less than ~800 Ma. Tycho is ~100 Ma. Craters with ejecta both much less and more mature than these craters have been identified [5].

Implications: The density of large craters classified as younger than Copernicus is at least 40% less than the density of farside craters with bright rays, which was suggested to represent a population of craters younger than Copernicus [8]. Furthermore, these craters have a "flatter" size-frequency distribution (relatively more large craters) than do the farside rayed craters or other lunar craters younger than 3.2 Ga. We suspect that there is an age-size bias to our classification, such that the OMAT profiles of smaller craters look like that of larger but older craters. Nevertheless, two large nearside craters previously mapped as Copernican, Eudoxus (67 km), and Aristillus (55 km), which are close in size to our "calibration" craters (Copernicus – 92 km and Tycho – 86 km), are now known to have optically mature ejecta. Thus it is likely that the density of large craters younger than Copernicus must be reduced from the estimates in [8], and the case for a modest increase in the cratering rate (in the past 800 m.y. versus the previous 2.4 b.y.) has been weakened. However, if Copernican ejecta are completely mature, then there may well be additional large craters younger than 800 Ma, and the cratering rate over the past 800 m.y. may have increased. Our preliminary investigation also shows no evidence for a change in the cratering rate since Tycho (~109 Ma) compared with the cratering rate since Copernicus (~810 Ma).

There are two additional results from this preliminary study that are relevant to lunar stratigraphy based on our analyses of Aristillus, Autolycu,s and Lichtenberg Craters. We find optically mature ejecta around the crater Lichtenberg (20-km diameter). Mare lavas are emplaced over the bright ejecta and rays of Lichtenberg; this has been cited as evidence for Copernican-age mare volcanism. Our data indicate that this superposition does not *require* an unusually young age for the mare lavas, based on the relative age of the crater [5]. Both Aristillus and Autolycus have been morphologically classified as rayed, due to the nature of their ejecta; Autolycus has been radiometrically dated at about 2 Ga and Aristillus at 1.3 Ga [7]. These ages seemed in possible contradiction with the supposition that rayed craters are all relatively recent. The OMAT profiles for both of these craters, though, are otherwise indistinguishable from OMAT background values and are very flat. The profiles indicate that the maturity of the ejecta from these craters is much greater than the ejecta of Copernicus, which is consistent with their radiometric ages. It is therefore clear that the presence of rays alone do not imply that a large crater is near or younger than the age of Copernicus [5]. Since these craters possess mature ejecta, and are classified as old, this does not support the suggestion by [7] that the cratering rate during the Copernican was ~2× lower than that during the Eratosthenian.

Conclusions: Definitive resolution of the flux history of asteroids and comets in the vicinity of Earth will probably eventually come from the Moon. The terrestrial crater record is much too altered, and reliable areas and dates for cratering rate estimates are available only for small numbers of craters. Although we are limited by few absolute age dates on Copernican units [9], much improved relative ages are possible with the Clementine multispectral dataset. The use of spectral parameterization of soil maturity via the OMAT profile method allows for the relative dating of craters whose ejecta has not matured to the point of being indistinguishable from its surroundings. Current accuracy allows for craters to be separated into three age groups based on the maturity of their ejecta. Examination of the crater interiors may provide another method for the identification and classification of Copernican craters [8,11]. In addition, counts of craters superposed onto the ejecta of large rayed craters will be considered along with radiometric ages to "calibrate" the classification scheme [10]. Further study and refinement of the process, as well as continued crater counts down to 1 km in diameter, could achieve a much better relative dating accuracy. The accuracy for small craters might be quite good, because the lunar age-color correlation is strongest for the youngest craters. As previously suggested [8], new isotopic ages on lunar craters will be needed to fully calibrate the Copernican cratering chronology, but the OMAT profile method of relative dating may enable greatly improved calibration with just a few carefully selected new dates rather than the ~100 dates previously advocated [12].

References: [1] Shoemaker E. M. (1984) in *Patterns of Change in Earth Evolution* (H. D. Holland and A. F. Trendall, eds.), Springer-Verlag, Berlin. [2] Shoemaker E. M. et al., eds. (1998) *Meteorites: Flux with Time and Impact Effects*, Geological Society, London. [3] Lucey P. G. et al. (1995) *Science, 268*, 1150–1153. [4] Lucey P. G. et al. (1998) *JGR, 103*, 3679–3699. [5] Grier et al. (1999) *LPS XXX*. [6] Wilhelms (1987) U.S. Geological Survey Prof. Paper #1348. [7] Ryder et al. (1991) *Geology*, 19. [8] McEwen A. S. et al. (1997) *JGR, 102*, 9231–9242. [9] Arvidson et al. (1975). [10] Grier

et al. (1999) *JGR*, in prep. [11] Lucey P. G. et al. (1999) *JGR*. [12] Hörz F. (1985) in *Lunar Bases and Space Activities of the 21st Century* (W. W. Mendell, ed.), LPI.

THE LUNAR IMAGER/SPECTROMETER FOR THE SELENE MISSION. J. Haruyama[1], H. Otake[1], T. Matsunaga[2], and the LISM Working Group, [1]Advanced Mission Research Center, National Space Development Agency of Japan, Sengen 2-1-1 Tsukuba Ibaraki 305-8505, Japan (Haruyama.Junichi@nasda.go.jp), [2]Department of Environmental Science and Technology, Tokyo Institute of Technology, 4259 Nagatuta Midori-ku, Yokohama Kanagawa 226-8502, Japan.

Introduction: The Moon is the nearest celestial body to the Earth. The investigation of the Moon gives clues as to the origin and evolution of not only the Moon itself, but also the Earth. ISAS (Institute of Space and Astronautical Science) and NASDA (National Space Development Agency of Japan) are cooperatively planning to launch a Moon explorer named SELENE (Selenological and Engineering Explorer) in 2003. Phase C study has been started since last April 1999. SELENE will load 14 mission instruments to obtain scientific data of the Moon. The scientific data will be also used for investigating the possibility of future utilization of the Moon. SELENE will carry out the orbiter mission for one year and subsequently separate the propulsion module that will be a lander and send the radio signal for the differential VLBI for two months. The orbiter will end its role when the propulsion module is separated. Imagery and spectral profiling are most useful techniques for understanding the structure and materials of a planetary surface. From the SELENE mission, we will obtain data with high spatial and spectral resolution by LISM (Lunar Imager/SpectroMeter). LISM consists of three sensors: a terrain camera (TC), a multiband imager (MI), and a spectral profiler (SP). We introduce LISM in this paper.

Lunar Imager/Spectrometer Overview: LISM will obtain digitized global imaging and spectral profiling data of the Moon with high-quality spatial resolution, wavelength resolution, and signal-to-noise ratio. Data of LISM will be also combined and analyzed with the data of other mission instruments of SELENE. The LISM group consists of about 20 researchers, who have responsibility on LISM development including science requirement decision, instrumentation, software development, and operation. The current status of LISM development is in phase C, or PM (preflight model) designing and making phase. From the next year, we will start designing FM (flight model).

Terrain Camera Overview: The main purpose of TC is global stereo mapping with high spatial resolutions. To investigate sub-kilometer size morphology for all over the Moon in detail, we used images with spatial resolution of 10 m and height resolution of 20–30 m. TC consists of two slant telescopes, each of which has a linear CCD detector, and takes images by pushbroom scanning. The swath of TC is 35 km when the altitude of SELENE orbiter is 100 km, so that images taken at serial paths are overlapped for across-track direction. DCT lossy compression method has been adopted to reduce the tremendous data. The data will be nominally compressed to 30% or less.

Multiband Imager Overview: The main purpose of MI is global multiband mapping of spatial resolution of 20 m for visible range, and 60 m for near-infrared range. MI consists of two telescopes, each of which has a two-dimensional detector with band-path filters. Data of several lines of the detectors, each of which correspond to band assignments, are read out. MI takes images by pushbroom scanning. The swath of MI is 20 km when the altitude of

TABLE 1. Terrain camera specification.

Mass (radiation unit)	<10 kg (with MI)
Power consumption	24 W
Focal length	72.5 mm
F number	4
Stereo angle	±15°
Detector type	1D CCD (4098 pixels)
Sensor pixel size	7 × 7 μm
Spatial resolution	10 m
Field of view	19.3°
Swath width on ground	35 km (nominal mode) 17.5 km (half mode) 40 km (full mode)
B/H	0.57
S/N	>100
Band width	450–700 nm
Quantization	10 bit
MTF	>0.2 @ Nyquist freq.
Data compression	DCT method
Pixel exposure time	1.625 ms 3.25 ms 6.5 ms
DCT table	32 patterns
Data amount per day	50 Gbit
Solar elevation angle in TC operation	<40°

TABLE 2. Multiband imager specification.

Mass (radiation unit)	<10 kg (with TC)
Power consumption	<17 W
Focal length	65 mm
F number	3.7
Band assignment	415,750,900,950,1000 nm (VIS) 1000,1050,1250,1550 nm (NIR)
Detector type	2D CCD (VIS) 2D InGaAs detector (NIR)
Sensor pixel size	13 × 13 μm (VIS) 40 × 40 μm (NIR)
Spatial resolution	20 m (VIS) 62 m (NIR)
Field of view	11°
Swath width on ground	19.3 km
Quantization	10 bit (VIS) 12 bit (NIR)
Band width	20 nm (for 415, 750, 900, 950 nm) 30 nm (for 1000, 1050, 1250 nm) 50 nm (1550 nm)
S/N	>100
MTF	>0.2 @ Nyquist freq.
Data compression	DPCM method
Compression rate	to < 80%
Pixel exposure time	2.0, 4.1, 8.2 ms (VIS) 6.6, 13.2, 26.4 ms (NIR)
Data amount per day	50 Gbit
Solar elevation angle in MI operation	30°–90°

TABLE 3. Spectral profiler specification.

Mass (radiation unit)	<8 kg
Power consumption	38 W (VIS, NIR1, 2)
Focal length	110 mm
F number	4
Detector type	Si pin photo diode (VIS)
	InGaAs (NIR1,2)
Sensor pixel size	50 × 500 μm (VIS) 50 × 200 μm
	(NIR1,2)
Spatial resolution	500 m
Field of view per pixel	500 m
Number of band	84 (VIS)
	100 (NIR1)
	112 (NIR2)
Cooler	peltier cooler (for NIR2)
Quantization	16 bit
Wavelength resolution	6–8 nm
Data compression	N/A
Pixel exposure time	selectable (TBD)
Data amount per day	0.7 Gbit
S/N	>2500 @ VIS
Solar elevation angle	0°–90°

SELENE orbiter is 100 km. We adopt a DPCM loss-less compression method to avoid irreparable loss of information about subtle difference of reflectance.

Spectral Profiler Overview: The main purpose of SP is to obtain detailed continuous spectral data of the Moon in the 500–2600-nm range to understand distribution and chemical composition of minerals on the surface. SP has one set of optics with three detectors for three ranges (VIS: 500–1000 nm, NIR1: 900–1700 nm, and NIR2: 1700–2600 nm). NIR2 is cooled to 220 K by a peltier cooler. The spatial resolution is 500 m for across-track and along-track directions. Since we require high accuracy to analyze SP data, we execute on-board calibration with using halogen lamps.

Lunar Imager/Spectrometer Operation Overview: The spectral profiler will be operated in all daytime. The total amount of data of TC and MI is so large that TC and MI are not operated at the same time. Still, operations of TC and MI should be carried out in limited daytime. To identify where SP is observing, however, highly compressed TC images or one-band images of MI are planned to be taken simultaneously with SP data.

THE COMPOSITION AND ORIGIN OF SELECTED LUNAR CRATER RAYS.

B. R. Hawke[1], D. T. Blewett[1], P. G. Lucey[1], C. A. Peterson[1], J. F. Bell III[2], B. A. Campbell[3], and M. S. Robinson[4], [1]Planetary Geosciences, Hawai'i Institute of Geophysics and Planetology, University of Hawai'i, Honolulu HI 96822, USA, [2]Center for Radiophysics and Space Research, Cornell University, Ithaca NY 14853, USA, [3]Center for Earth and Planetary Studies, National Air and Space Museum, Washington DC 20560, USA, [4]Department of Geological Sciences, Northwestern University, Evanston IL 60208, USA.

Introduction: The nature and origin of lunar crater rays has long been a source of major controversy. Some lunar scientists have proposed that rays are dominated by primary crater ejecta, while others have emphasized the role of secondary craters in producing rays [e.g., 1–3]. Pieters et al. [2] presented the results of a remote-sensing study of a portion of the ray system north of Copernicus. They provided evidence that the present brightness of the Copernicus rays in this sector is due largely to the presence of a component of highland ejecta intimately mixed with local mare basalt, and that an increasing component of local material is observed in the rays at progressively greater radial distances from the parent crater. These results have been questioned, and the origin of lunar rays is still uncertain [e.g., 4]. In an effort to better understand the processes responsible for the formation of lunar rays, we have utilized a variety of remote-sensing data to study selected rays associated with Olbers A, Lichtenberg, the Messier Crater Complex, and Tycho [6,9]. The data include near-IR reflectance spectra (0.6–2.5 μm) and 3.8-cm and 70-cm radar maps. In addition, Clementine UV-VIS images were used to produce high-resolution FeO, TiO_2, and maturity maps for the various rays using the methods presented by Lucey and et al. [10,11].

Results and Discussion: *Messier Crater Complex.* Messier (14 km in long dimension) and Messier A (diameter = 11 km) are located near 2°S, 47°E in Mare Fecunditatis. Major rays from these craters occur to the south and west of the parent craters. Spectra were obtained for portions of the rays west and south of the crater complex, as well as for Messier A and nearby mature mare regions.

The spectrum of Messier A exhibits an extremely deep (29%) ferrous iron absorption band centered at 0.98 μm, and a fresh mare composition is indicated. Both the near-IR spectrum and the FeO image clearly demonstrate that Messier A did not penetrate the Fecunditatis mare fill. In addition, Messier A crater exhibits strong returns on both the 3.8-cm and 70-cm depolarized radar images [6–8]. The spectrum collected for the ray west of Messier A has a 15% absorption feature centered at 0.99 μm. The ray has slightly enhanced values in the depolarized 3.8-cm radar image, but no enhancement is apparent in the 70-cm dataset. The mature mare unit adjacent to this ray has a spectrum with a shallower band depth (12%) and a similar band center. The FeO image indicates that the west ray exhibits FeO values similar to adjacent mare deposits. The brightness of the ray west of Messier A is due to the presence of large amounts of fresh mare basalt. Near-IR spectra as well as the FeO and maturity maps indicate that the ray south of the Messier complex is also dominated by fresh mare material.

Tycho Ray in Mare Nectaris. A major ray from Tycho Crater crosses much of Mare Nectaris. The 80-km long ray segment northeast of Rosse Crater (17.9°N, 35°E) has a somewhat conical shape, ranging in width from 8 km near Rosse to 16 km northwest of Bohnenberger Crater. Spectra were obtained for Rosse Crater (diameter = 12 km), mature mare units, and two small areas on the Tycho ray northeast of Rosse. Both of the spots on the ray are located near a Tycho secondary crater cluster ~1400 km from the center of the parent crater. The spectrum collected for a mature mare area east of Rosse exhibits an 8.5% absorption feature centered at 0.98 μm. Both ray spectra have 11.6% bands centered at ~0.99 μm. It appears that the ray in the areas for which spectra were collected are dominated by fresh mare debris. These results are in agreement with those presented by Campbell et al. [6]. These workers noted that the Tycho secondary craters in the cluster are easily seen in high-resolution 3.0-cm radar images, and a radar-bright area extends 10–15 km downrange of Tycho from the approximate center of the cluster. In addition, they noted that the radar-bright region exhibited a deeper "1-μm" feature in multispectral ratio images and suggested that fragmental

material was emplaced well downrange of the visible secondaries, perhaps by a secondary debris surge. The FeO and maturity images support this interpretation.

In summary, analyses of near-IR reflectance spectra, multispectral imagery, and a variety of radar data suggest that Tycho ray in Mare Nectaris is dominated by fresh local material excavated and emplaced by secondary craters. While some highlands material from Tycho is undoubtedly present in the ray, the major factor that produces the brightness of the ray is the immature mare basalt.

Olbers A Ray. This Copernican-aged impact crater (diameter = 43 km) located in the highlands on the Moon's western limb (8.1°N, 77.6°W) exhibits an extensive ray system. Eight near-IR reflectance spectra were obtained for a prominent ray that extends northeast of Olbers A across Oceanus Procellarum. Three of these spectra were for small (3–6 km in diameter) areas near the intersection of two major ray elements ~385 km northeast of Olbers A. Three spectra were collected for a portion of the ray immediately northeast of Seleucus Crater. This ray segment is ~550 km from the rim of the parent crater. Two spectra were obtained for diffuse ray elements in the same general area. Spectra were also obtained for Olbers A Crater as well as both mature mare and fresh craters near the ray.

All spectra were analyzed and spectral mixing model studies were conducted using the techniques described by Blewett et al. [5]. Three component mixing studies were performed using mature mare, fresh mare, and either fresh or mature highland material as end members. The spectra obtained for areas near the ray intersection are dominated by mare material. However, highland debris is quite abundant (contributing 30–50% of the flux to the spectra). Perhaps these high values are due to the fact that two rays cross in the area for which the spectra were collected. Surprisingly, even larger amounts (35–55%) of highland material were found to be present in portions of the ray northeast of Seleucus. Lesser amounts (26–38%) of highland debris were determined to be present in the more diffuse segments of the ray. Maturity and FeO maps produced from Clementine UV-VIS images suggest that the ray is less mature than the adjacent terrain and that it contains a significant amount of highlands debris.

Lichtenberg Crater Rays. Lichtenberg Crater (diameter = 20 km) is located in Oceanus Procellarum on the western portion of the lunar nearside (31.8°N, 67.7°W). This Copoernican-aged impact structure displays a relatively high-albedo ejecta blanket and ray system to the north and northwest. However, Lichtenbertg ejecta is embayed by mare basalt south and southeast of the crater. The FeO map produced for the Lichtenberg region indicates that the ejecta and rays north and northwest of the crater exhibit relatively low FeO abundances. These deposits appear to be dominated by low-FeO highlands debris. The maturity image demonstrates that these highlands-rich ejecta deposits and rays are fully mature. Hence, the Lichtenberg rays exhibit a relatively high albedo because of their composition. These mature highlands-rich rays appear bright in comparison to the adjacent mature mare surfaces. These "compositional" rays stand in stark contrast to the immaturity rays associated with the Messier Crater Complex.

References: [1] Shoemaker E. (1962) in *Physics and Astronomy of the Moon*, p. 283. [2] Pieters C. et al. (1985) *JGR, 90,* 12393. [3] Oberbeck V. (1971) *Moon, 2,* 263. [4] Schultz P. and Gault D. (1985) *JGR, 90,* 3701. [5] Blewett D. et al. (1995) *JGR, 100,* 16959. [6] Campbell B. et al. (1992) *Proc. LPS, Vol. 22,* 259. [7] Zisk S. et al. (1974) *Moon, 10,* 17. [8] Thompson T. (1987) *Earth, Moon, Planets, 37,* 59. [9] Hawke B. et al. (1996) *LPS XXVII,* 507. [10] Lucey P. et al. (1995) *Science, 268,* 1150. [11] Lucey P. et al. (1999) *JGR,* submitted.

LUNAR GRUITHUISEN AND MAIRAN DOMES: RHEOLOGY AND MODE OF EMPLACEMENT.

J. W. Head[1] and L. Wilson[2], [1]Department of Geological Sciences, Brown University, Providence RI 02912, USA, [2]Environmental Studies Division, Institute of Environmental and Natural Sciences, Lancaster University, Lancaster LA1 4YQ, UK.

Abstract: The lunar steep-sided Gruithuisen and Mairan domes are morphologically and spectrally distinctive structures that appear similar to terrestrial features characterized by viscous magma. We use the basic morphologic and morphometric characteristics of the domes to estimate their yield strength (~10^5 Pa), plastic viscosity (~10^9 Pa s), and effusion rates (~50 m^3/s). These values are similar to terrestrial rhyolites, dacites, and basaltic andesites and support the hypothesis that these domes are an unusual variation of typical highlands and mare compositions. Typical dike geometries are predicted to have widths ~50 m and lengths ~15 km. The magma rise speed implied by this geometry is very low, ~7×10^{-5} m/s, and the Reynolds number of the motion is ~2×10^{-8}, implying a completely laminar flow regime.

Introduction: The Gruithuisen and Mairan domes represent examples of topographically, morphologically, and spectrally distinctive structures on the Moon [1–2] that appear to be candidates for very viscous magma. In this analysis, we use the basic morphologic and morphometric characteristics of the domes as a basis for estimating of their yield strength, plastic viscosity, eruption rates, and dike feeder geometry (e.g., dike width and length). We begin by assuming that each dome is a single structure emplaced on a flat plain and use Blake's [3] treatment of domes modeled as Bingham plastics to establish the order of magnitude of the yield strength, (t), and plastic viscosity (h). Inferred values of t are ~3×10^5 Pa for the Gruithuisen domes and 1.0×10^5 Pa for Mairan features. Next we use an empirical formula given by Moore and Ackerman [4] to relate the plastic viscosity, to the yield strength. The most likely value of h for the Gruithuisen domes is ~ 1×10^{10} Pa s and for the Mairan domes is perhaps within a factor of two of 5×10^8 Pa s. As a specific example, we treat the Gruithuisen Gamma dome as an underlying symmetric dome of radius = 10 km and unknown thickness on which are superimposed three flow lobes; we assume that these merge toward the summit, where they have a common thickness. The values (t = 7.7×10^4 Pa; h = 3.2×10^8 Pa s) are, as expected, significantly less than the first approximations, which ignored the detailed morphology of the dome.

Summary of Rheological Parameters: Given the resolution of the images used and the consequent difficulties in mapping and measuring features, it might be argued that measurements for t and h represent a single Bingham plastic magma for which t = $(10 \pm 3) \times 10^4$ Pa and h = $(6 \pm 4) \times 10^8$ Pa s. Alternatively, we could separate the two groups of domes and characterize the Gruithuisen dome magma by t = $(12 \pm 3) \times 10^4$ Pa, h = $(10 \pm 5) \times 10^8$ Pa s and the Mairan dome magma by the slightly smaller values t = $(8 \pm 4) \times 10^4$ Pa, h = $(5 \pm 4) \times 10^8$ Pa s.

Eruption Rate Estimates: We now turn to the estimation of the eruption rates of the magmas forming the various dome units. To

do this we assume that the advance of the flow front of each flow unit or dome-forming episode was limited by cooling. Pinkerton and Wilson [5] show that a variety of types of lava flow cease to move when the Grätz number, a dimensionless measure of the depth of penetration into the flow of the cooled boundary layer, has decreased from its initially very high value to a critical value of ~300. Blake's model of Bingham plastic domes shows the way in which the radius of the dome grows as a function of time. The assumption that flow lobes are cooling-limited always leads to effusion-rate estimates of lower bounds. This is because any flow unit assumed to be cooling-limited may in fact have been volume-limited (i.e., ceased to flow simply because the magma supply was exhausted), implying that it had the potential to travel further than the observed distance and therefore had a higher effusion rate than that deduced. For each of the Gruithuisen domes we have either a second smaller dome or a flow lobe superimposed on a larger, earlier dome. It is very tempting to assume that the second unit in each case is a breakout at the vent caused by the magma supply continuing after the first unit has reached its cooling-limited length. This automatically implies that the effusion rates deduced from the large dome geometries (~ 48, 24, and 119 m^3/s for Gruithuisen Delta, Northwest, and Gamma, respectively) are the realistic estimates and that the rates found from the smaller units are underestimates. For the Mairan domes we are not able to resolve multiple lobe structures and must regard the effusion rates of ~ 50 m^3/s as lower limits on the true rates.

Geometries of Feeder Dikes: To explore the conditions under which the magmas erupted, we assume that in each case the melt reached the surface from a source region at the base of the anorthositic crust. In order to keep a dike filled with buoyant magma open from this depth, we require a driving pressure of ~33 MPa. Any driving pressure smaller than this value would allow the lower end of the dike to close and and so cause it to pinch shut from the magma source region. Thus the absolute pressure in the source region is at least ~490 MPa. The typical width of the dike held open by the above driving pressure is expected to be within a factor of 2 or 3 of ~80 m.

We now calculate the rise speed of magma driven by the source pressure through a dike of mean width and horizontal length. Using the mean rheological properties for all of the domes, $t = 10 \times 10^4$ Pa and $h = 6 \times 10^8$ Pas, together with an eruption rate of 50 m^3/s (typical of the majority of the values), we find W = 50 m and L = 15 km. The magma rise speed implied by this geometry is very low, ~7×10^{-5} m/s, and the Reynolds number of the motion is ~ 2×10^{-8}, implying a completely laminar flow regime. Considering the uncertainties in many of the parameters involved, a dike width of ~50 m is certainly consistent with the estimate, obtained from consideration of the static stability of the dike, that the width should be within a factor of 3 of ~80 m. In addition, a fissure length of ~15 km is consistent with the Delta dome being elongate with its main vents ~12 km apart, and the fact that the Gamma and Northwest domes together could be regarded as defining an underlying fissure about 18 km long. It is less clear whether the Mairan domes should be regarded as being fed by three separate dikes or in some combination by two dikes.

References: [1] Head J. W. and McCord T. B. (1978) *Science, 199,* 1433–1436. [2] Chevrel S. et al. (1999) *JGR,* in press. [3] Blake S. (1990) in *Lava Flows and Domes: Emplacement Mechanisms and Hazard Implications,* IAVCEI Proceedings in Volcanology, vol. 2. (J. Fink, ed.), pp. 88–128, Springer Verlag, Berlin. [4] Moore H. J. and Ackerman J. A. (1989) *NASA Tech. Memo TM-4130,* 387–389. [5] Pinkerton H. and Wilson L. (1994) *Bull. Volcan., 56,* 108.

A MULTISPECTRAL ANALYSIS OF THE FLAMSTEED REGION OF OCEANUS PROCELLARUM. D. J. Heather[1], S. K. Dunkin[1], P. D. Spudis[2], and D. B. J. Bussey[3], [1]Department of Physics and Astronomy, University College London, Gower Street, London WC1E 6BT, UK (djh@star.ucl.ac.uk), [2]Lunar and Planetary Institute, 3600 Bay Area Boulevard, Houston TX, 77058 USA, [3]European Space Research and Technology Centre, European Space Agency, Noordwijk, The Netherlands.

Introduction: According to Pieters et al. [1], the Flamsteed area of Oceanus Procellarum is representative of basalts that have yet to be sampled. They studied the area in detail using telescopic data to identify seven distinct mare flows. This diversity makes the Flamsteed region an ideal candidate for Clementine multispectral studies. The region studied here is far smaller than that covered by [1], but the higher spatial resolution of the Clementine data will allow us to make a fresh interpretation of the nature of our restricted area before expanding to encompass the surrounding regions. The primary aim of this work is to use Clementine UV-VIS data to analyze flows on a smaller scale and determine the stratigraphy of the mare, using impact craters as probes to measure the thickness of mare lavas wherever possible.

Data Reduction: We used the Clementine UV-VIS data to produce a multispectral image of the Flamsteed area from 0.60°N to 16.06°S and 308.34°E to 317.12°E. The data were processed at a resolution of 200m/pixel using the ISIS software program (available through the USGS), and the photometric coefficients tabulated in Blewett et al. [2]. In addition to the multispectral image, a "true color" image, FeO map using the algorithms of [2], and a TiO_2 map using the algorithms of [3] were generated. In conjunction with a 750-nm Clementine mosaic and Lunar Orbiter photographs, these images formed the dataset used for this analysis. For more details on the data-reduction procedure used, please contact the authors.

Mapping the Flows: The area studied here lies in the south-eastern portion of Oceanus Procellarum, and covers approximately 134,500 km^2, extending from the mare-highland boundary (to the south) up to and including the Flamsteed P ring. The number of spectrally distinct flows in the area is striking in the Clementine mosaics, ranging from high-Ti flows in and around Flamsteed P to low-Ti flows at the edges of the mare-highland boundaries. From a preliminary analysis, we have identified at least five flows in the multispectral image alone (Fig. 1). Sunshine and Pieters [4] found three distinct flows within the Flamsteed P ring using high resolution CCD images from a groundbased telescope. We find evidence for only two: a younger high-Ti flow (flow A in Fig. 1) overlying an older lower-Ti flow (flow C in Fig. 1). However, we have not yet reduced the data for the most eastern part of the ring, and it is possible that further flow(s) could be found in our missing section.

The low-Ti flows at some of the mare highland contacts to the south are exceptionally bright in the 750/415 nm channel of the multispectral image (flow E in Fig. 1). These areas correlate with intermediate FeO and TiO_2 content (the TiO_2 map is shown in Fig. 2), and seem to be the oldest flows visible on the surface, probably extending over a large area beneath the later flows.

The extent of each flow so far identified is shown in Fig. 1. Boundaries were defined according to multispectral and albedo properties. Detailed studies of the TiO_2 map (Fig. 2) and maturity data (taken through observations of crater densities from the Orbiter frames and an optical maturity image produced using the algorithm

Fig. 1. Outline map of the flows in the Flamsteed area. H = Highland material; A = young, high-Ti flow; B = high-Ti flow, perhaps linked to flow A; C = older low-Ti flow; D = intermediate-Ti flow; E = low-Ti flow, probably the oldest in the area, very bright in the red (750/415 nm) channel; Ha = Mons Hansteen. (To view this figure in color go to http://cass.jsc.nasa.gov/meetings/moon99/pdf/8032.pdf.)

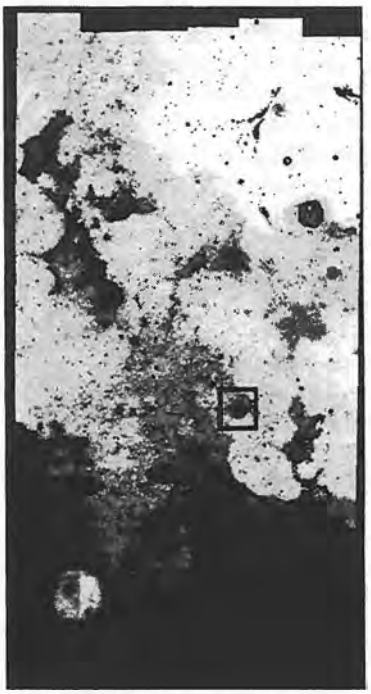

Fig. 2. A grayscale Clementine TiO_2 map of the Flamsteed region, clearly showing the distinct flow units of both high-and low-Ti content (lighter areas have a high TiO_2 content compared to the darker regions). 5-point spectra of the boxed crater, which may have excavated through the entire mare sequence, are shown in Fig. 3.

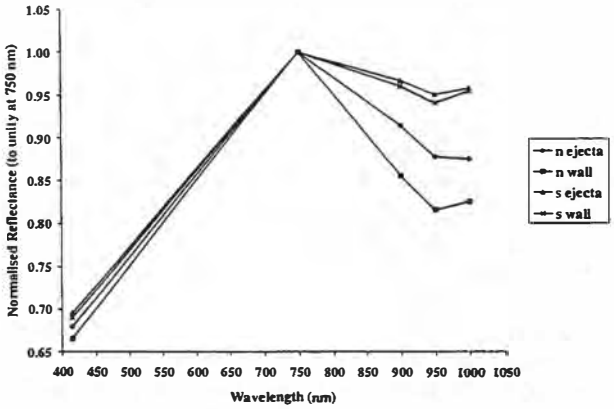

Fig. 3. A 5-point normalized reflectance plot of the crater boxed in Fig. 2. The wall and ejecta to the south show a far stronger mafic absorption band than the northern units, which are probably a mix of excavated highland and basaltic material. The 800-m depth of the crater therefore gives an upper limit for the mare thickness in the area.

of Lucey et al. [5]), will improve this map. Work is continuing in an attempt to delineate clearer flow boundaries.

Stratigraphy of the Region: The primary aim of this work is to determine the thickness of the mare flows as one moves out from the highland boundary into Oceanus Procellarum. First-order indications of thickness can be obtained by searching for highland outcrops within the maria. The Flamsteed area shows many such outcrops (see Fig. 1), and the lavas must be quite thin close to these.

A more absolute idea of basalt thickness can be obtained by calculating the depths of craters that have dug through the lavas to expose highland material below. These craters can be identified from multispectral images and 5-point spectra. Previous work has suggested that a cyan color in the multispectral frame represents highland material [6–7], and that yellows and greens are freshly excavated basalts [8]. However, we have recently found that a cyan color can also result from a freshly excavated high-Ti basalt. In order to differentiate between the high-Ti and highland signature, it is necessary to look at the FeO and TiO_2 frames and plot 5-point spectra to look for the absorption at 0.95 mm that is characteristic of pyroxenes in the basalts.

These observations have shown there to be candidate craters in the Flamsteed region which have excavated highland material, an example of which is shown in Fig. 3. The example crater displays a basaltic signature with a clear 0.95μm absorption in its south wall and ejecta, while the absorption in the north wall and ejecta is far weaker. The northern deposits are also relatively low in TiO_2 and FeO, and probably represent a mix of basaltic and highland material. The crater is 8 km in diameter, so will have excavated to a depth of ~800 m (using the depth:diameter ratio of 1:10 given by Croft [9]); this is therefore an upper limit to the thickness of the basalts at the crater's northern edge.

In addition, there are several areas where craters close together excavate spectrally distinct materials. These may indicate boundaries of subsurface mare flows, and will allow for a more detailed stratigraphic picture to be constructed.

Future Work: We intend to map the lava flow and crater distribution across the Flamsteed region, using craters to deduce depths to the highland-mare contact where possible. Flamsteed will

then be combined with adjoining areas of Oceanus Procellarum, gradually developing a complete picture of the stratigraphy and basalt thickness across the basin. This work will form part of a continuing project in which we aim to study maria across the whole Moon, providing a global perspective of lunar volcanic history.

Acknowledgments: We would like to acknowledge the continuing support of the USGS in the reduction of Clementine data. The ISIS software (distributed by the USGS) was run on Starlink facilities, funded by the Particle Physics and Astronomy Research Council (PPARC) in the UK. This work was carried out while SKD was a PPARC Research Fellow.

References: [1] Pieters C. M. (1980) *JGR, 85,* 3913–3938. [2] Blewett et al. (1997) *JGR, 102,* 16319–16325. [3] Lucey et al. (1998) *JGR, 103,* 3679–3699. [4] Sunshine J. M. and Pieters C. M. (1990) *LPI Tech. Rpt. No. 91-03,* 59–60. [5] Lucey et al. (1998) *LPS XXIX,* Abstract #1356. [6] Gillis and Spudis (1995) *LPS XXVI,* 459–460. [7] Bussey and Spudis (1996) *LPS XXVII,* 183–184 [8] Dunkin and Heather (1999) *LPS XXX,* Abstract #1180. [9] Croft S. K. (1980) *Proc. LPSC 11th,* 2347–2378.

PETROGENESIS OF MAGNESIAN-SUITE TROCTOLITES AND NORITES.

P. C. Hess and E. M. Parmentier, Department of Geological Sciences, Brown University, Providence RI 02912, USA.

Models for the petrogenesis of magnesian-suite troctolites and norites are severely constrained by a number of important geochemical features.

I. Most troctolites have olivines with Mg* values that range from 84 to 92 [1]. Rare spinel troctolites have extremely primitive olivines with Mg* 95–96 [2]. Hess [3] showed that a peridotite source with Mg*>91 was required to produce the most magnesian troctolite parent liquids known at that time. But these parent liquids were strongly undersaturated with respect to plagioclase at the low pressures expected of the lunar anorthosite crust. Such liquids must crystallize significant quantities of olivine in order to bring plagioclase onto the liquidus; the fractionation of olivine must reduce the Mg* value of the plagioclase-saturated liquids. It follows that troctolites with Mg* of 90–92 cannot be produced in this way. The problem is far worse for the spinel troctolite with Mg*96.

II. The crystallization sequence of magnesian suite magmas is non-tholeiitic; i.e., the crystallization of low-CaO pyroxene precedes high-CaO pyroxene [4]. Indeed, troctolites and norites are nearly free of discrete CaO-rich pyroxene [1], a feature implying a melt and a source with low normative diopside, certainly much lower than in typical terrestrial lherzolite.

III. The parent magmas for magnesian norites and troctolite have calculated REE contents typically between 1 and 2× high-K KREEP [5–6] or about 300–600× chondrite!

IV. The parent magmas to the most primitive troctolite are hot and have temperatures that exceed 1270°C at 1 bar [7].

V. Radiogenic isotope ages for magnesian norites imply that magma generation was long lived, contemporary with the formation of ferroan anorthosite and extending to (and possibly beyond) 4.2 AE [1,8].

Three models of petrogenesis are tested against the petrochemical features listed above. These models include (1) impact melting, (2) cumulate remelting, and (3) assimilation of cumulates by late-stage liquids of the magma ocean.

A. In this model, the parent magmas to the magnesian-suite troctolite are impact melts formed by melting the ferroan anorthosite crust and the early-most cumulates of the magma ocean. The mafic cumulates exist below the crust through the agency of cumulate overturn as the original cumulate pile establishes gravitational equilibrium [10]. A magma ocean with Mg* 84–88 is required to produce olivines with Mg* 92–95 [3]. Such high Mg* values require that the magma ocean experienced fractional rather than equilibrium crystallization even at the earliest periods of crystallization. The high and variable REE content is explained by melting of variable amounts of the KREEP layer that survived the overturn. The mafic cumulate cannot be solely of olivine, however, since the magnesian norites require an orthopyroxene-bearing source. An orthopyroxene-bearing dunite or even an olivine-rich harzburgite is required. This would imply that the magma ocean was less olivine normative than typical terrestrial mantle.

The impact model nicely reconciles constraints I to IV, whereas V simply requires multiple impacts. Indeed, since magnesian-suite rocks were collected from Apollo 11, 12, 14, 15, 16, and 17 [11], impact melting in this model was a common and widespread event. If this model is correct, why are the ferroan anorthosite and magnesian suite plutonic trends so distinct? Why isn't there a continuum of compositions? It is also noteworthy that upper mantle samples are rare to nonexistent in the lunar collection [1]. In fact, neither ferroan anorthosites or cumulate mantle samples are typically found within the ejecta deposits that include magnesian-suite samples [12].

B. In the cumulate remelting model, the high Mg* values of the magnesian troctolite are contributed also by a source dominated by early olivine cumulates of the magma ocean. The normative plagioclase and orthopyroxene components are supplied by sinking parcels of quenched crust of the convecting magma ocean [4] or perhaps by interaction with partial melts generated by melting the primitive interior of the Moon [13], if indeed such an interior exists. In either case, the mafic cumulates of olivine, perhaps with small amounts of orthopyroxene (see earlier discussion), must dominate the source. Pressure-release melting associated with the cumulate overturn creates the parent magmas for the magnesian suite. Sufficient melting is required to leave only orthopyroxene and olivine in the source to maintain low normative diopside contents.

This model satisfies constraints I, II, and IV but has difficulty with III, the high KREEP contents of the Mg-suite parent liquids. Possibly the high KREEP contents are the result of assimilation of high level KREEP deposits. However, if KREEP is akin to ferroan basalt then the assimilation of this mass would lower Mg* values. If KREEP is quartz normative and granitic, assimilation would compromise the olivine-normative character of the parent liquids; KREEP-rich troctolite parent liquids would evolve to norite parent liquids. This latter viewpoint is probably the more acceptable one.

If this model is correct, then convective overturn and pressure release melting must not only begin promptly to create old Magnesian-suite rocks but must also continue for 200–300 more m.y. to account for the youngest members of the Magnesian-suite [1]. The rapid formation of the cumulate pile is consistent with the ^{182}W-isotopic anomalies that require that heterogeneous and discrete source regions must be established in the first 50 m.y. of the origin of the Moon [14]. Perhaps thermal rather then chemcially driven convection is needed to explain the origin of young Magnesian norites.

C. Korotev [15] has proposed that Apollo 15 norite and the entire Magnesian-suite is the product of assimilation of olivine cumulate

mantle by the late stage KREEP liquid residual to the magma ocean. This would account for the KREEP paradox, i.e., the combination of high concentrations of incompatible elements and more refractory major elements as represented, for example by high Mg* values. This model has a number of problems, however: The KREEP liquid is produced by the cooling and fractional crystallization of the magma ocean. The residual liquid is a near-solidus phase and must exist at T <1100°C. In order to produce the parent liquids to the magnesian suite by assimilation, the KREEP liquid must somehow be reheated to temperatures of 1270°C or higher. How this is done is certainly problematic. Secondly, this residual liquid has an evolved major-element composition contrary to the refractory major-element character of troctolites and norites. Moreover, this liquid will be diopside-rich (normatively) contrary to constraint II. If this magma body exists beneath the "Great Lunar Hot Spot" at ~3.9 AE as required to produce Apollo 15 KREEP basalts, it is not clear how the gravity anomalies related to the Imbrium mascon (and others) can be maintained. A soft mantle would relax and eliminate the gravity anomaly. Finally, if the magma ocean was in existence at the time of the Imbrium impact, how did subsequent mare basalts readily pass through this zone and erupt without KREEP assimilation?

Conclusions: Models A and B are comparable and viable. Both suffer from the KREEP paradox, however: How are large masses of KREEP incorporated into the troctolite parent magma without compromising the high Mg* values? Several important conclusions nevertheless derive from this analysis: (1) cumulate overturn must bring olivine-rich cumulates to the upper mantle; (2) the magma ocean experienced fractional rather than equilibrium crystallization throughout most of its history; and (3) it is unlikely that large volumes of primitive Moon exist — tholeiite basalts do not exist on the Moon! Alternatively, the moon is depleted in normative diopside, and (4) olivines with Mg* > 90 require a bulk Moon with Mg* > 84.

References: [1] Papike J. J. et al. (1998) *Rev. Mineral., 36,* 5189. [2] Snyder G. A. et al. (1999) *LPS XXX.* [3] Hess P. C. (1994) *JGR, 99,* 19083–19093. [4] Hess P. C. (1998) *LPS XXIX.* [5] Papike J. J. et al. (1996) *GCA, 60,* 3967–3978. [6] Shervais J. W. and McGee J. J. (1998) *GCA, 56,* 3809–3823. [7] Morse S. A. (1980) *Basalts and Phase Diagrams,* Springer Verlag, p. 162. [8] Nyquist L. E. and Shih C-Y. (1992) *GCA, 56,* 2213–2234. [10] Hess P. C. and Parmentier E. M. (1995) *EPSL, 134,* 505–514. [11] Warren P. H. (1993) *Am. Mineral., 75,* 360–376. [12] Ryder G. et al. (1997) *GCA, 61,* 1083–1105. [13] Shervais J. W. and McGee J. J. (1999) *JGR, 104,* 5891–5920. [14] Lee D. C. et al. (1997) *Science, 278,* 1098–1103. [15] Korotev R. L. (1999) *LPS XXX.*

AGES OF OCEANUS PROCELLARUM BASALTS AND OTHER NEARSIDE MARE BASALTS.

H. Hiesinger and J. W. Head III, Department of Geological Sciences, Brown University, Providence RI 02912, USA (Harald.Hiesinger@Brown.edu)

Abstract: In a previous paper [1] we reported on crater size-frequency distribution data for 139 spectrally and morphologically defined basalt units in six nearside impact basins (Australe, Tranquillitatis, Humboldtianum, Humorum, Serenitatis, and Imbrium). We also presented results on the relationship between Ti concentration and age of a basalt unit, the influence of crustal thickness on the eruption of a basalt onto the lunar surface, and the flux of lunar mare volcanism. In this paper we expand our study to Oceanus Procellarum in order to include the largest mare basalt-covered area into our investigation.

Introduction: It is known that lunar mare basalts cover about 17% of the lunar surface, but represent only 1% of the volume of the lunar crust [2]. A significant portion of lunar mare basalts are exposed within Oceanus Procellarum, and for large areas absolute age data are still lacking. From geologic mapping we know that there are very young basalts around crater Lichtenberg, but how old are they really? How do Oceanus Procellarum basalts compare to basalts in the previously investigated basins? Whitford-Stark and Head [3] defined 21 basalt types in Oceanus Procellarum, and these basalts show ages from 3.8 Ga to 2.4 Ga [4]. Our approach is to use previously published maps [e.g. 3,5] as a basis to define homogeneous basalt units on Clementine color-ratio mosaics and to perform new crater counts for these basalts. This is similar to the approch we took for our previous study [6,7].

Results and Conclusions: On the basis of analysis of eastern and central nearside mare basins we addressed the following questions.

1. How long was lunar mare volcanism active? Our data show that lunar volcanism was active for at least 2.0 b.y. According to our data, volcanism started at about 4.0 Ga and ceased at ~2.0 Ga. However, numerous dark halo craters in the Australe region suggest the presence of a cryptomare. We conclude that volcanism must have been already active, at least in the Nectarian Period. Schultz and Spudis [8] suggested that lunar mare volcanism may have started as early as 4.3 Ga. The basalts that were dated in our previous study were erupted primarily in the Imbrian Period from 3.4 to 3.8 Ga. We found only a minor number of basalts that erupted during the Eratosthenian Period. In addition, there was no evidence for basalts of Copernican age in the six investigated impact basins, but such basalts are exposed in the Oceanus Procellarum [9]. In Oceanus Procellarum these basalts embay the Copernican crater Lichtenberg, and it is thought that these basalts are the very youngest basalts on the lunar surface with an age as low as probably <1 Ga [9]. In order to answer the question over what time span lunar volcanism was active, the absolute ages of the the Lichtenberg basalts have to be known. Therefore we will measure the crater size-frequency distribution of these basalts as well as other basalts north of Lichtenberg that were mapped as Copernican basalts by Wilhelms [9]. Geologic mapping [9] also revealed that significant portions of Oceanus Procellarum are covered with Erathosthenian basalts. From these maps it seems that Eratosthenian volcanism was more widespread in Oceanus Procellarum than in other lunar mare basalt regions besides Imbrium. We will determine absolute ages for Oceanus Procellarum basalts in order to investigate variations in the activity of mare volcanism with time.

2. What is the spatial distribution of ages? Soderblom et al. [10] reported differences in age, chemistry, and magnetism between basalts of eastern and western basins. According to this work, eastern basalts are generally older, more magnetized, and less radioactive than their western counterparts. Results from Lunar Prospector [11] show high concentrations of Th and K in and around the nearside western maria thus being consistent with Soderblom's observations concerning the amount of radioactive elements. So far we investigated basalts in six lunar impact basins that are distributed over the entire lunar nearside, therefore allowing us to study large-scale differences in age and geochemistry between eastern and western basalts. Based on this investigation, we found that volcanism was active longer in the western parts of the nearside than in the eastern

regions. However, this trend is not very pronounced in our data and westernmost parts, i.e., Oceanus Procellarum are still missing. Geologic maps [9] show that large areas within Oceanus Procellarum are covered with Eratosthenian basalts. These Eratosthenian basalts are exposed in the central parts of Oceanus Procellarum, and Imbrium basalts are located closer to the highland/mare boundaries. We will test for this distribution and provide new age data for the Oceanus Procellarum basalts.

3. How do es the Ti content vary with time? For basalts in the six investigated basins, we generally see that TiO_2-rich basalts tend to be older than TiO_2-poor basalts. Our results are consistent with the trend found in the sample collection that indicate that radiometric older basalts are generally richer in Ti than younger basalts. However, a very important result of our previous investigation is that the TiO_2 contents and ages of the basalts within each investigated basin are not correlated. Our data indicate that TiO_2-rich and TiO_2-poor basalts can erupt simultaneously in different locations within the basin. In each single basin, the TiO_2 concentrations can vary independently from the ages of the units. This probably suggests a highly heterogeneous mantle or source region. With the recent study we wish to test if this observation also holds for Oceanus Procellarum basalts. Spectral mapping of basalt types [5] indicates that for large parts of Oceanus Procellarum younger basalts are more Ti rich than older basalts, thus somewhat reversing the trend found in the returned samples. Because of the immense importance of this observation for the development of petrogenetic models, absolute age determinations are necessary for these basalts.

4. How much basalt was erupted with time? Once spectrally homogeneous units are mapped, their areal extent can easily be measured. In combination with reasonable assumptions [e.g., 12] of the thickness of a basalt, we are able to estimate the erupted basalt volume. In our previous study we assumed that a single basalt flow unit is ~10 m thick. For the basalts in the six investigated basins, we see that the main volcanic activity occured in the Imbrian Period and was at least larger by a factor of 3.5 between 3.4 and 3.7 b.y. compared to the period between 2.9 and 3.4 b.y. We conclude that mare volcanism was not equaly active over long periods of time but peaked in the Imbrian Period. As mentioned above, there are large areas in Oceanus Procellarum that were previously mapped as Eratosthenian in age [9]. We will investigate the influence of these basalts on the distribution of active mare volcanism over time. Is there a second peak of volcanic activity in the Eratosthenian Period, or are the Eratosthenian basalts of Oceanus Procellarum part of the decline of volcanic activity observed in the other areas?

5. How does crustal thickness influence basalt eruptions? Besides high-resolution color imaging data that are used for the definition of spectrally homogeneous units, Clementine provided us with estimates of the crustal thickness of most of the Moon [13]. In our previous study, we used this dataset and found that the maximum thickness of the crust where basalts occur is 50–60 km. Our results are consistent with the results of Yingst and Head [14] and imply that crustal thickness is a limiting factor for the eruption of lunar basalts onto the surface. We see that ascending magmas preferentially extrude to the surface where the crust is thin, i.e., the lunar nearside or the impact basins. On the farside, the crustal thickness is larger and therefore the magmas stall and cool in dikes before they reach the surface. Thickening of the crust with a related compressional stress field within the crust or sinking of the buoyancy trap over time makes it more and more difficult for dikes to extrude to the surface [15]. As a consequence, our data indicate that the youngest basalts are often exposed in or near areas with the relatively thinnest crust. On the basis of these observations, we conclude that in areas with a thinner crust, dikes still could reach the surface even later in lunar history, whereas in other regions the dikes stalled in the crust and could not propagate to the surface. In Oceanus Procellarum we will investigate the correlation between crustal thickness and corresponding age in order to test for if the youngest basalts are exposed over regions with systematically thinner crust and if our previous results also hold for the basalts in this area.

References: [1] Hiesinger H. et al. (1999) *LPS XXX,* Abstract #1199. [2] Head J. W. III (1976) *Rev. Geophys. Space Phys., 14,* 265–300. [3] Whitford-Stark J. L. and Head J. W. III (1980) *JGR, 85,* 6579–6609. [4] Boyce J. M. and Johnson D. A. (1978) *Proc. LPSC 9th,* 3275–3283. [5] Pieters C. M. (1978) *Proc. LPSC 9th,* 2825–2849. [6] Hiesinger H. et al. (1998) *LPS XXIX,* Abstract #1242. [7] Hiesinger H. et al. (1998) *LPS XXIX,* Abstract #1243. [8] Schulz P. H. and Spudis P. D. (1983) *Nature, 302,* 233–236. [9] Wilhelms D. E. (1987) *U.S. Geological Survey Spec. Paper 1348.* [10] Soderblom L. A. et al. (1977) *Proc. LSC 8th,* 1191–1199. [11] Lawrence D. J. et al. (1998) *Science, 281,* 1484–1489. [12] Gifford A. W. and El-Baz F. (1981) *Moon and Planets, 24,* 391–398. [13] Zuber M. T. et al. (1994) *Science, 266,* 1839–1843. [14] Yingst R. A. and Head J. W. III (1997) *JGR, 102,* 10909–10931. [15] Head J. W. III and Wilson L. (1992) *GCA, 56,* 2155–2175.

HIGH-RESOLUTION MAPPING OF LUNAR CRUSTAL MAGNETIC FIELDS: CORRELATIONS WITH ALBEDO MARKINGS OF THE REINER GAMMA CLASS. L. L. Hood[1], A. Yingst[1], D. L. Mitchell[2], R. P. Lin[2], M. Acuna[3], and A. Binder[4], [1]Lunar and Planetary Laboratory, University of Arizona, Tucson AZ 85721-0092, USA (lon@lpl.arizona.edu), [2]Space Sciences Laboratory, University of California–Berkeley, Berkeley CA 94720-7450, USA, [3]Goddard Space Flight Center, Greenbelt MD 20771, USA, [4]Lunar Research Institute, Gilroy CA 95020, USA.

During the last eight months of the Lunar Prospector mission (December 1999–July 1999), the spacecraft was placed in a relatively low-altitude (15–30-km perapsis), near-polar orbit that allowed high-resolution mapping of crustal magnetic fields. We report here initial studies of the correlation of locally strong magnetic anomalies with unusual, swirl-like albedo markings of the Reiner Gamma class. Based on this correlation, which is known from earlier studies of Apollo subsatellite magnetometer data [1], it has been proposed that the swirls represent regions whose higher albedos have been preserved via deflection of the solar-wind ion bombardment by strong crustal fields [2]. This model in turn depends on the hypothesis that solar-wind implanted H is at least one component of the process that optically matures exposed silicate surfaces in the inner solar system [3]. Specifically, it is hypothesized that implanted H acts as an effective reducing agent to enhance the rate of production of nanophase metallic Fe particles from preexisting silicates during micrometeoroid impacts. According to the model, the curvilinear shapes of these albedo markings are caused, at least in part, by the geometry of ion deflections in a magnetic field [4].

The improved resolution and coverage of the Prospector data allow more detailed mapping of the fields, especially on the lunar farside. This permits a more quantitative test of whether all albedo

markings of this class are associated with strong local magnetic fields. Only if the latter condition is met can the solar-wind deflection hypothesis be valid.

Field Mapping: The basic procedure for mapping crustal magnetic fields using Lunar Prospector magnetometer data follows that developed for analysis of Apollo subsatellite magnetometer data [5]. The specific mapping steps are (1) selection of mission time intervals suitable for mapping crustal fields; these are limited essentially either to times when the Moon is in a lobe of the geomagnetic tail or to times when the Moon is in the solar wind but the spacecraft is in the lunar wake; the data are transformed to a radial, east, and north coordinate system with measurements given as a function of spacecraft latitude, longitude, and altitude; (2) visual editing of individual orbit segments slected for minimal external field disturbances; (3) minimization of remaining low-frequency external fields for individual orbit data segments by quadratic detrending; and (4) two-dimensional filtering of individual orbit segments to produce a vector field map along the slightly curved surface defined by the spacecraft altitude; maps of the three field components (radial, east, and north), the field magnitude, and the spacecraft altitude are constructed. For data obtained at low to middle latitudes, the horizontal resolution of the field maps is limited by the orbit-track separation (~30 km at the equator).

Correlation Analysis: Maps of the field magnitude have been constructed within limited selenographic regions based mainly on data acquired in March, April, and May of 1999. This was a time period when the orbit plane was nearly aligned with the Sun-Moon line so that field mapping was possible at times when the Moon was in the solar wind as well as when the Moon was in the geomagnetic tail. Most of the coverage is across the lunar farside. However, Fig. 1 shows an example of a field map produced from solar-wind wake data for a region including Reiner Gamm on western Oceanus Procellarum (location: 58.5°W, 7.5°N). The contour interval is 3 nT and the mean spacecraft altitude is 18 km to within the accuracy allowed by the resolution of the map (30 km or ~1°); strong magnetic anomalies correlate closely with swirl locations. Individual orbit profiles (whose resolution along the orbit track is comparable to the spacecraft altitude of 18 km) also demonstrate a good correlation of field magnitude with surface albedo.

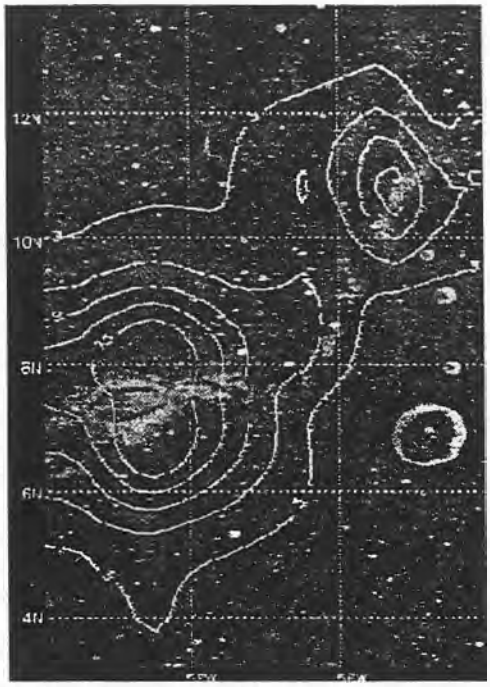

Fig. 1.

In order to investigate the correlation of magnetic fields with the location of swirl features, we have reexamined available lunar imagery (Lunar Orbiter, Apollo, and Clementine) to identify and map swirl locations within regions where swirls have previously been mapped [4–5]. In these images, swirls were distinguished from other high-albedo features such as crater rays by their curvilinear shapes and increased visibility in forward-scattered light. Digital maps of swirls identified by all available imagery were then superposed on maps of the field magnitude at the spacecraft altitude. Based upon analysis of these composite magnetic/geologic maps, we draw the preliminary conclusion that swirl features are associated with magnetic anomalies revealed by Lunar Prospector.

Detailed maps of these swirl features are currently being constructed for the magnetically strong regions antipodal to the Imbrium, Serenitatis, and Crisium Basins.

References: [1] Hood L. L. et al. (1979) *Science, 204,* 53–57. [2] Hood L. L. and Schubert G. (1980) *Science, 208,* 49–51. [3] Lucey P. G. et al. (1998) *LPS XXIX.* [4] Hood L. L. and Williams C. R. (1989) *Proc. LPSC 19th,* 99–113. [5] Hood L. L. et al. (1981) *JGR, 86,* 1055–1069. [6] Schultz P. H. and Srnka L. J. (1980) *Nature, 284,* 22–26.

SOLAR-WIND-IMPLANTED VOLATILES IN THE LUNAR REGOLITH. J. R. Johnson[1], T. D. Swindle[2], and P. G. Lucey[3], [1]U. S. Geological Survey, Branch of Astrogeology, Flagstaff AZ 86001, USA (jjohnson@flagmail.wr.usgs.gov), [2]Lunar and Planetary Laboratory, University of Arizona, Tucson AZ, USA, [3]Hawai'i Institute of Geophysics and Planetology, University of Hawai'i, Honolulu HI, USA.

Introduction: The epithermal neutron distribution from Lunar Prospector (LP) and the H abundance and maturity of returned lunar soils are being used synergistically to estimate global H distribution. The ability to determine lunar H abundance using a combination of remote sensing and laboratory analyses broadens our understanding of the retentivity of volatiles in the lunar regolith and the nature of the sources from which the volatiles arrived (i.e., solar wind, cometary impacts). This is relevant to the search for water ice at the lunar poles as well as other potential resources such as H-3. Knowledge of these possible resource-rich regions will be important for future mission planning, instrument selection, and landing-site analyses.

Methodology: The Level 1 calibrated epithermal neutron distribution maps (initially calibrated to remove major instrumental effects by the LP team) [1–2] have been used for first-order calibration to H abundance. The equation of Feldman et al. [3], i.e., [epithermal* = epithermal - (0.068 * thermal)] was used to minimize the effects of compositional variations between mare and highlands (likely due to major-element concentrations such as Ti, Fe) on the epithermal neutron counting rates. Figure 1 shows an example of a Clementine mosaic at the same scale as the epithermal* neutron flux maps.

Comparison of the average H abundances for the Apollo landing site soils with the epithermal* neutron counts for the landing sites from Fig. 1 results in the rather poor correlation shown in Fig. 2. Neglecting the Apollo 11 sample, the sense of the correlation is correct (fewer epithermal* neutrons implies greater H abundance), but the correlation is still mediocre ($r = -0.574$). This may result from using the average values for the landing sites as opposed to the individual soil sample values.

Results: It can be seen in the epithermal* map (Fig. 1) that the highest counting rates (likely the lowest H abundances) correspond well to regions of fresh, Copernican-age impacts (e.g., Tycho, Hayn, Jackson, possibly Stevinus). This implies a dearth of solar-wind-implanted gases, which could be explained by the immaturity of the regolith in these regions. But there are also mare regions near the limbs (Orientale, Crisium) with high values that require other explanations. Further, while the darker regions in the polar areas have been interpreted as water-ice-bearing regions [3], the low-valued highland terrain west of Sinus Iridium requires further study.

Overall, the solar-wind fluence model's predictions of highest volatile abundances on the central farside and lowest values on the central nearside are not immediately apparent in the epithermal* map. However, if the lower counting rates (higher H abundances) at longitudes 75°–180°E are real, it would be consistent with the solar-wind model (at least for that portion of the eastern limb and farside).

Future Work: Hydrogen contents of 54 Apollo bulk lunar soils [4–6] will be compared to the epithermal neutron counts for the landing sites to determine more precisely an average correlation. This will be applied to the LP data to estimate H content on the lunar surface. Because exposure age affects retained solar-wind-implanted volatile abundances, incorporation of soil maturity using the I_s/FeO parameter (reduced:total Fe ratio) [7–8] and/or spectrally-derived maturity data from lunar soils will also be used in conjunction with

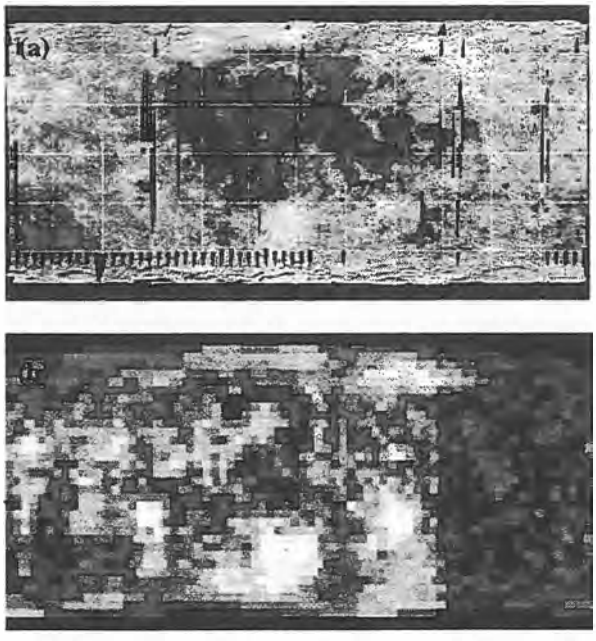

Fig. 1. **(a)** Clementine mosaic with craters Jackson (J), Tycho (T), Hayn (H), and Stevinus (S) marked and overlain with 30° latitude/longitude grid; **(b)** epithermal* neutron distribution map. Simple cylindrical projection, 0.25°/pixel, with 180° W at left edge.

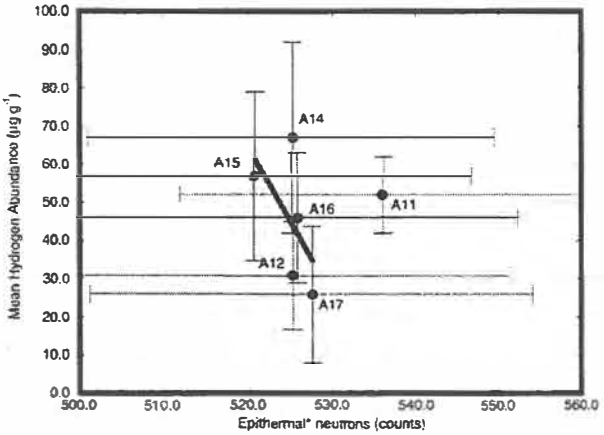

Fig. 2. Epithermal* neutron counts vs. average Apollo landing-site H abundances. Error bars represent standard deviations of epithermal* neutron counts and average H values among measured soils. Linear fit excludes the A11 sample ($r = -0.574$).

H abundances to refine the correlation. Once a H map is constructed, it will be used to test a solar-wind fluence model for the Moon developed previously [4,9] that represents relative solar-wind-implanted elemental abundances (assuming minimal variations in impact history and chemical composition of the soils, as well as minimal saturation of soils with volatiles). Deviations of the H distribution from the idealized solar fluence model will be investigated by incorporating the effects of local magnetic fields [10–14], composition (e.g., Ti, Fe) [15–18], and soil maturity [17].

Further, previous work by the authors has shown that abundances of H-3 (a potential lunar resource relevant as a fuel for future nuclear fusion power [19–23]) in the lunar regolith can be estimated using the fluence model in combination with surface maturity and Ti maps constructed using Clementine multispectral data [24–26]. The modeled solar-wind fluence distribution map will be updated based on observations of the epithermal neutron-derived H maps, and the Clementine and LP Ti-abundance maps will be incorporated with Clementine surface maturity maps to construct revised estimates of H-3 abundance.

Conclusions: The calibration of the LP neutron spectrometer data to provide maps of H abundance will be important in understanding the nature of the solar-wind-implanted volatiles in the lunar regolith, particularly the distribution, migration, and retentivity of H relevant to understanding the possible presence of water ice at the lunar poles. Hydrogen maps will be useful in separating the near-surface geologic history (e.g., solar-wind implantation and micrometeorite bombardment history related to surface maturity) from the underlying crustal evolution, the knowledge of which is a required component of our total understanding of the planetary history of the Moon. The preliminary observations made here regarding correlations of epithermal* neutron counts with geologic features are intriguing and will require further study. Potential improvements to models of solar-wind fluence will assist in mapping other volatiles in the regolith, particularly H-3, which along with H and water ice are some of the most promising potential lunar resources available on the Moon [e.g., 6,20].

References: [1] Binder A. B. (1998) *Science, 281,* 1475–1476. [2] Feldman W. C. et al. (1998) *Science, 281,* 1489–1493. [3] Feldman W. C. et al. (1998) *Science, 281,* 1496–1500. [4] Fegley

B. and Swindle T. D. (1993) in *Resources of Near-Earth Space,* pp. 367–426, Univ. Arizona. [5] Des Marais D. J. et al. (1974) *Proc. LSC 5th,* 1811–1822. [6] Carter J. L. (1985) in *Symposium on Lunar Bases and Space Activities of the 21st Century* (W.W. Mendell, ed.), pp. 571–581, LPI. [7] Morris R. V. (1976) *Proc. LSC 7th,* 315–335. [8] Morris R. V. (1978) *Proc. LPSC 9th,* 2287–2297. [9] Swindle T.D. et al. (1992) *LPS XXIII,* 1395–1396. [10] Hood L. L. and Huang Z. (1991) *JGR, 96,* 9837–9846. [11] Hood L. L. et al. (1979) *Science, 204,* 53–57. [12] Lin R. P. et al. (1998) *Science, 281,* 1480–1484. [13] Hood L. L. and Schubert G. (1980) *Science, 208,* 49–50. [14] Hood L. L. and Williams C. R. (1989) *Proc. LPSC 19th,* 99–133. [15] Lucey P. G. et al. (1996) *LPS XXVII,* 781–782. [16] Lucey P. G. et al. (1995) *Science, 268,* 1150–1153. [17] Lucey P. G. et al. (1998) *JGR, 103,* 3679–3699. [18] Elphic R. C. et al. (1998) *Science, 281,* 1493–1496. [19] Lewis J. S. (1991) *Space Power, 10,* 363–372. [20] Taylor L. A. (1994) in *Engineering, Construction, and Operations in Space IV, Proc. Space '94,* pp. 678–686, Albuquerque. [21] Wittenberg L. J. et al. (1986) *Fusion Technol., 10,* 167–178. [22] Jordan J. L. (1989) in *Space Mining and Manufacturing, Annual Invitational Symposium,* pp. 64–65, NASA SERC, Univ. Arizona, Tucson. [23] Jordan J. L. (1990) *LPI Tech. Rpt. 90-02,* 43–45. [24] Johnson J. R. et al. (1991) *JGR, 96,* 18861–18882. [25] Johnson J. R. et al. (1996) *Eos Trans. AGU, 77,* 446. [26] Johnson J. R. et al. (1999) *GRL, 26,* 385–388.

THORIUM ENRICHMENT WITHIN THE PROCELLARUM KREEP TERRANE: THE RECORD IN SURFACE DEPOSITS AND SIGNIFICANCE FOR THERMAL EVOLUTION.

B. L. Jolliff, J. J. Gillis, and L. A. Haskin, Department of Earth and Planetary Sciences and the McDonnell Center for the Space Sciences, Washington University, St. Louis MO 63130, USA (blj@levee.wustl.edu).

Introduction: The nearside-farside structural and compositional asymmetry of the Moon was recognized during the early days of Apollo and the suggestion was made [e.g., 1] that the migration of mantle melts to the nearside would have been favored by early Earth-Moon orbital dynamics and nonuniform planetesimal bombardment. Recent global geochemical mapping by Lunar Prospector has provided additional data, particularly in the Th distribution, that strongly supports the notion of global, preferential melt migration, which led in part to the development of the Procellarum KREEP Terrane (PKT) [2–5]. The surface distribution of Th was then reshaped by basin-forming impacts into the PKT, especially the Imbrium impact, which was the last and largest to strike in that region. The Imbrium event probably excavated material from a partially molten zone deep in the crust and delivered Th-rich ejecta Moon-wide [2]. A fundamentally important but poorly understood aspect of the global Th distribution is the concentration of Th in the subsurface rocks of the PKT crustal section. For example, depending on what assumptions are made, the PKT crustal section, which is ~12% of the crust and only ~1.2% of the whole Moon, may contain as much as 40% of the Moon's entire Th budget [4]. Such a distribution of Th and related heat-producing elements would have had a profound effect on melting, mixing, and the thermal evolution of the PKT and the underlying mantle [2]. In this abstract, we examine the compositions of terra formations within the PKT and relate them to some of the Th-bearing rock types known from the Apollo samples. It appears that the existence of the PKT may be a unifying concept for a number of petrologic and geochemical observations.

Remotely-sensed Thorium Distribution in the Procellarum KREEP Terrane: From the initial Lunar Prospector γ-ray spectrometer data (~5° resolution [6]) and from the preliminary low-orbit data [7], there appears to be a number of relatively hotter "spots" within the PKT in terms of Th concentration. Some of the hotter spots correspond to intermediate-sized craters that penetrated volcanic flows and excavated Th-rich, submare material, such as Aristarchus, Aristillus, and Kepler [8]. Other spots, however, correspond to surficial formations that constitute mainly rough topography associated with Imbrium ejecta or circum-Imbrium ring mountains and do not necessarily imply the presence of exposed KREEP basalts.

The Fra Mauro Formation south of Copernicus toward the Apollo 14 site and regions of the Alpes Formation southwest of Copernicus [9] in the vicinity of Reinhold lie within the most prominent hotspot; here the Th concentration is consistent with that found in the Apollo 14 soils (~12–13 ppm) when the proportions of Fra Mauro Formation and mare basalt are considered [5]. The area between Copernicus and Kepler and northwest of Copernicus in terra extending to the Carpathians is similarly enriched in Th. The Apennines from Eratosthenes toward the Apollo 15 site contain elevated Th concentrations, as does the northwestern quadrant of circum-Imbrium terra, especially between (but not including) La Condamine and Plato, and in the region northwest of the Jura mountains extending southward past Mairan to the Gruithuisen-Domes region. Within the main topographic rim of Imbrium, the Apennine Bench formation south of Archimedes appears to have relatively elevated Th concentration [8,10].

Comparing the map of Th distribution to a digital-elevation map derived from Clementine altimetry, it appears that most of the areas richest in Th occur where the surface is elevated relative to the majority of PKT volcanic plains. Not all rough topography within the PKT has such elevated Th, however. Based on an analysis of the 5° data, and using the calibration of [11], the mean Th concentrations for mainly volcanic-resurfaced terrain and rugged terrain are similar (~5.5 ppm) [4]. This occurs in part because craters that penetrated mare basalt excavated Th-rich material. Even so, there appear to be extensive areas of volcanic resurfacing that have no obvious extrinsic source of Th-rich material, suggesting that the basalts, themselves, may contain as much as 5–6 ppm Th [5]. High-FeO concentrations (18 to >20 wt%) indicate that these are not KREEP basalts but mare basalts. If so, this is surprising because most of the Apollo-sampled mare basalts have very low-Th concentrations (typically <2 ppm [12]).

Thorium-rich materials in the Apollo Samples: A variety of Th-rich materials occur in the sample collection, particularly in the samples from the Apollo 12, 14, and 15 sites. The most abundant Th-rich rock types are the mafic impact-melt breccias, which although found at all sites, are most abundant at Apollo 14, where they dominate the rock samples and make up some 40% of the rock particles in the soil. These have Th concentrations ranging up to ~30 ppm and averaging ~18 ppm [13]. The Apollo 14 soils contain ~13 ppm Th, reflecting the high abundance of this melt-breccia component (Fig. 1). At the nearby Apollo 12 site, the rocks consist mainly of mare basalts, and these have low-Th concentrations, mostly <1 ppm [12]. Among the nonmare rocks, however, a few such as complex breccia 12013 contain a variety of evolved lithologies and represent potential sources of Th-rich components ranging from 17

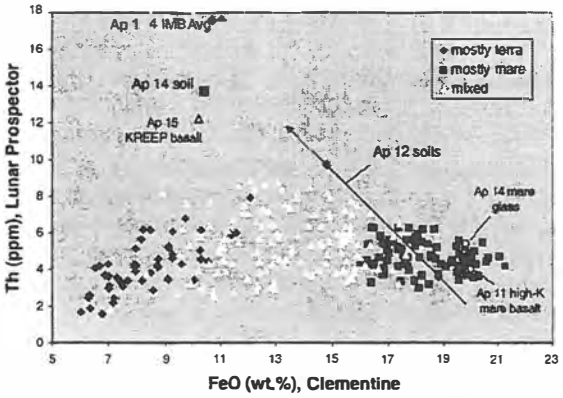

Fig. 1. Ferrous oxide vs. Th, Procellarum KREEP terrane, 5° data.

to 50 ppm [14]. A single fragment of KREEP basalt from the Apollo 12 soil contains ~50 ppm Th [15]. Despite the identification of highly Th-enriched lithologic components at the Apollo 12 site, the soils there vary linearly in composition so as to extrapolate to a moderate-Th KREEP-basalt component or a composition like that of the Fra Mauro formation as reflected by Apollo 14 soil (14 ppm Th at 10 wt% FeO, Fig. 1) [4]. The nearby Lansberg Crater (39-km diameter) is a likely candidate to have delivered submare material such as buried Fra Mauro or Alpes material [9] to the Apollo 12 site. The Apollo 15 site provided apparently endogenous KREEP basalt (~10 wt% FeO and 11–12 ppm Th) as well as a variety of impact-melt breccias and evolved rocks such as 15405 [16].

The existence of chemically evolved, Th-rich rock types such as granite, alkali anorthosite, quartz monzodiorite, and whitlockite monzogabbro, some of which have Th concentrations ranging from 20 to 66 ppm [12], reflect magmatic recycling and differentiation of KREEP-rich, primary, residual-melt products of the magma ocean. The isotopic systematics of the evolved rocks indicate magmatic ages ranging from 4.4 to 3.9 Ga [17] and derivation from an early differentiated (4.4 Ga) KREEP reservoir [18]. The average Th concentration of the PKT crust, however, is probably better represented by the main groups of mafic melt breccias, most of which probably derived from the Imbrium basin and thus sample the sub-Imbrium crust. The average Th concentrations of these groups range from ~4 to 18 ppm [12], and as products of a basin-forming impact, these presumably sampled large areas of the PKT crust. We note that the main-group (poikilitic) Apollo 17 impact-melt breccias have ~5 ppm Th; if they originated in the Serenitatis event, this suggests an enriched source at depth, although at the surface, the site lies outside of the PKT as defined in [4].

Although most of the sampled mare basalts have Th concentrations below 2 ppm, a few have higher concentrations and perhaps other unsampled mare basalts, particularly some of the presumed younger ones (e.g., 1–2 Ga [19]) have relatively high Th. Apollo 14 aluminous and very-high-K basalts have 2–3 ppm Th [12, 21], and some Apollo 11 high-K basalts have as much as 4 ppm [20]. A basaltic impact glass from Apollo 14 has 5.4 ppm Th and 19.7 wt% FeO [21]. The observation that large areas of mare volcanic plains in the PKT have Th as high as 4–7 ppm indicates that the basalts themselves are enriched in Th. Modest enrichment of Th in the Tranquillitatis basalts indicated by Lunar Prospector data [6] implies a heterogeneous distribution of Th in the sub-PKT and adjacent mantle.

Implications: Dynamic exchange of Th-rich (KREEP) residua between the lower PKT crust and the underlying mantle would have supplied the heat to continue to generate the youngest (and unsampled) nearside basalts, and would provide material for deep mixing and assimilation. Inversion of mantle cumulates in response to density instability, coupled with the exchange of heat-producing elements in the upper mantle, could provide a fertile source for the generation of magnesian-suite parental melts and would supply the magnesian olivine component needed to satisfy chemical mass-balance models [22] for materials derived within the PKT. Although the mechanism of concentrating KREEP residual melt into the PKT is not understood at this time, the consequences of that concentration appear to have been active crustal magmatism within the PKT, crustal relaxation following multiple basin impacts, and extended mantle melting and volcanic resurfacing of the terrane.

Acknowledgments: This research is supported by grants NAG5-6784 (BLJ) and NAG5-4172 (LAH).

References: [1] Wood (1973) *Moon, 8,* 73–103. [2] Haskin (1998) *JGR, 103,* 1679–1689. [3] Wieczorek and Phillips (1999) *JGR,* submitted. [4] Jolliff et al. (1999) *JGR,* submitted. [5] Haskin et al. (1999) *JGR,* submitted. [6] Lawrence et al. (1998) *Science, 281,* 1484–1489. [7] Lawrence et al. (1999) *LPS XXX,* Abstract #2024. [8] Gillis and Jolliff, this volume. [9] Wilhelms and McCauley (1971) *U.S. Geological Survey Map I-703.* [10] Etchegaray-Ramirez et al. (1983) *Proc. LPSC 13th,* in *JGR, 88,* A529–A543. [11] Gillis et al. (1999) *LPS XXX,* Abstract #1699. [12] Korotev (1998) *JGR, 103,* 1691–1701. [13] Jolliff (1998) *Intl. Geol. Rev., 10,* 916–935. [14] Quick et al. (1977) *Proc. LSC 8th,* 2153–2189. [15] Laul (1986) *Proc. LPSC 16th,* in *JGR, 91,* D251–D261. [16] Ryder (1976) *EPSL, 29,* 255–268. [17] Shih et al. (1993) *GCA, 57,* 4827–4841. [18] Lugmair and Carlson (1978) *Proc. LPSC 9th,* 689–704. [19] Schultz and Spudis (1983) *Nature, 302,* 233–236. [20] BVSP (1981) Pergamon, NY [21] Jolliff et al. (1991) *Proc. LPS Vol. 21,* 193–219. [22] Korotev (1999) *JGR,* submitted.

SPACE WEATHERING IN THE FINE SIZE FRACTIONS OF LUNAR SOILS: SOIL MATURITY EFFECTS.

L. P. Keller[1], S. J. Wentworth[2], D. S. McKay[3], L. A. Taylor[4], C. Pieters[5], and R. V. Morris[3], [1]MVA, Inc., 5500 Oakbrook Parkway, Norcross GA 30093, USA (lkeller@mvainc.com), [2]Mail Code C23, Lockheed Martin, NASA Johnson Space Center, Houston TX 77058, USA, [3]Mail Code SN, NASA Johnson Space Center, Houston TX 77058, USA, [4]Planetary Geosciences Institute, University of Tennessee, Knoxville TN 37996, USA, [5]Box 1846, Brown University, Providence RI 02912, USA.

Introduction: The effects of space weathering on the optical properties of lunar materials have been well documented [1–2]. These effects include a reddened continuum slope, lowered albedo, and attenuated absorption features in reflectance spectra of lunar soils as compared to finely comminuted rocks from the same Apollo sites. However, the regolith processes that cause these effects are not well known, nor is the petrographic setting of the products of these processes fully understood. A Lunar Soil Characterization Consortium has been formed with the purpose of systematically integrating chemical and mineralogical data with the optical properties of lunar soils [3]. Understanding space-weathering effects is critical in order to fully integrate the lunar sample collection with remotely-sensed

data from recent robotic missions (e.g., Lunar Prospector, Clementine, and Galileo).

We have shown that depositional processes (condensation of impact-derived vapors, sputter deposits, accreted impact material, e.g., splash glass, spherules, etc.) are a major factor in the modification of the optical surfaces of lunar regolith materials [4–6]. In mature soils, it is the size and distribution of the nanophase metal in the soil grains that has the major effect on optical properties [7]. In this report, we compare and contrast the space-weathering effects in an immature and a mature soil with similar elemental compositions.

Methods: For this study, we analyzed <10 μm sieve fractions of two Apollo 17 soils, 79221 (mature, Is/FeO = 81) and 71061 (immature, Is/FeO = 14). Details of the sieving procedures and allocation scheme are given in [8]. The results of other detailed chemical, mineralogical, and spectroscopic analyses of these soil samples are reported elsewhere [3]. A representative sample of each soil was embedded in low-viscosity epoxy, and thin sections (~70 nm thick) were obtained through ultramicrotomy. The thin sections used for these analyses typically contained cross sections of up to 500 individual grains. The thin sections were studied using a JEOL 2010 transmission electron microscope (TEM) equipped with a thin-window energy-dispersive X-ray (EDX) spectrometer. An individual thin section was selected from each soil, and for each grain in the section we determined (1) the elemental composition by EDX; (2) whether the grain was crystalline or glassy using electron diffraction and darkfield imaging; (3) the presence or absence of rims and accreted material; and (4) the distribution of nanophase Fe where present.

The results of these analyses are collected in Table 1. Most of the categories are self-evident; however, we divide the agglutinate-derived material into *agglutinitic glass* (glass with approximately the same composition as the bulk soil that contains nanophase Fe with or without vesicles) and *agglutinate fragments*, which are composed of crystalline grains and agglutinitic glass. *Lithic fragments* are defined as polymineralic grains with no glass. Pyroxene grains have been divided into high- and low-Ca groups.

Results and Discussion: As expected, there are a number of differences in the petrography of the <10-μm fractions of 79221 and 71061 given the great difference in their respective maturities, but we focus here on two major distinctions: agglutinate content and the number of grains with micropatina. Slightly over 50% of the particles in 79221 consist of agglutinitic glass and agglutinate fragments, while the remainder are predominantly crystalline mineral grains. The agglutinic glass particles contain abundant nanophase Fe and vesicles. Angular particles are rare, with most showing smooth, rounded exteriors. Of the mineral grains analyzed thus far, over 90% of the grains have amorphous rims that contain nanophase Fe (these rims are believed to have formed by vapor deposition and irradiation effects [7]). The nanophase Fe in these rims probably accounts for a significant fraction of the increase in Is/FeO measured in these size fractions [3]. In addition to the rims, the majority of particles also show abundant accreted material in the form of glass splashes and spherules that also contain nanophase Fe (Fig. 1). In stark contrast, the surfaces of the mineral grains in the 71061 sample are relatively prisitine (Fig. 2), as only ~14% of the mineral grains in the sample exhibited amorphous rims. Furthermore, the mineral particles are more angular and show greater surface roughness than in the mature sample. Accreted material on particle surfaces is rare. Agglutinitic material is a major component of the 71061 sample; however, nanophase Fe and vesicles are not as well developed as in the 79221 sample.

TABLE 1. Transmission electron microscopy modal mineralogy of <10-μm fractions of 79221 and 71061.

	79221,138		71061,170	
	#	%	#	%
Aggutinitic Material	55	51.4	33.0	30.6
Agglutinate Fragments	13	12.1	17	15.7
Agglutinate Glass	42	39.3	16	14.8
Anorthite	20	18.7	28	25.9
Ca-pyroxene	10	9.3	8	7.4
Low-Ca pyroxene	6	5.6	10	9.3
Ilmenite	5	4.7	11	10.2
Olivine	3	2.8	4	3.7
Cristobalite	3	2.8	5	4.6
Glass Spheres	5	4.7	3	2.8
Lithic Fragments	0	0.0	6	5.6
Total	107	100.0	108	100.0

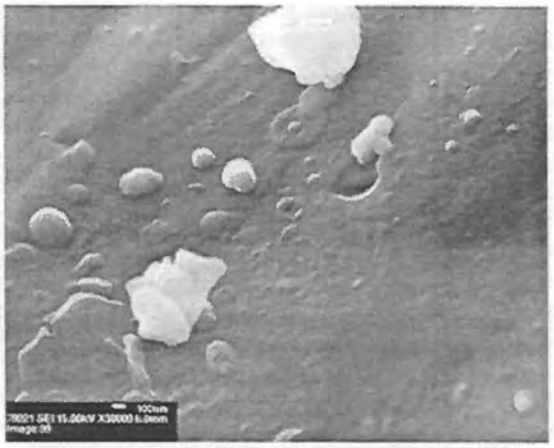

Fig. 1. A field-emission SEM image of a typical plagioclase grain from 79221 covered with micropatina showing a rounded, smooth surface with abundant splash glass (pancakes, etc.).

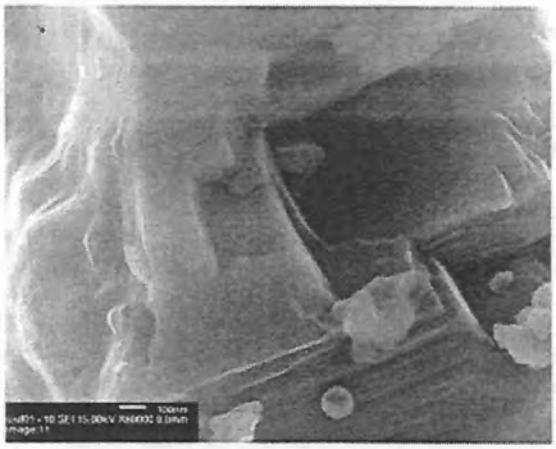

Fig. 2. A field-emission SEM image of a typical mineral grain (pigeonite) from the 71061 sample showing the surface roughness and lack of abundant accreted materials.

Summary: It is now recognized that nanophase Fe is probably the main agent in modifying the optical properties of lunar soil grains. The most important result of this study is the observation that in the fine size fractions of mature soils, nearly every grain has nanophase Fe within 100 nm of the particle surface.

References: [1] Pieters C. et al. (1993) *JGR, 98,* 20817. [2] Fischer E. (1995) Ph.D. thesis, Brown Univ. [3] Taylor L. A. et al., this volume. [4] Keller L. P. et al. (1999) *LPS XXX,* Abstract #1820. [5] Wentworth S. et al. (1999) *MAPS,* in press. [6] Keller L. P. and McKay D. S. (1997) *GCA, 61,* 2331. [7] Keller L. P. et al. (1998) *New Views of the Moon,* LPI, p. 41. [8] Taylor L. A. et al. (1999) *LPS XXX,* Abstract #1859.

THE DEEPEST LUNAR SPA BASIN AND ITS UNUSUAL INFILLING: CONSTRAINTS IMPOSED BY ANGULAR MOMENTUM CONSIDERATIONS. G. G. Kochemasov, Institute of Ore Deposits, Geology, Petrology, Mineralogy, and Geochemistry, Russian Academy of Sciences, 35 Staromonetny, Moscow 109017, Russia.

Successful applications of planetary wave tectonics [1] for predicting the shapes of small celestial bodies (asteroids, satellites), Phobos' rippling, the dumbbell shape of martian spheres, and fractionated martian crust, allow us to extend this method to lunar tectonics and related it to the chemistry of the enigmatic South Pole Aitken Basin.

The accepted origin by many (but not all) planetologists is an impact hypothesis of the SPA basin; we alternatively, consider it as a part of a global lunar sectoral structure centered in the Mare Orientale. Sectoral structures of celestial bodies are a result of interference of standing inertia-gravity waves proceeding in four directions (ortho- and diagonal). These warping planetary waves arise in them as a result of their movements in elliptical orbits with periodically changing curvatures and cosmic accelerations. Fundamental waves of long $2\pi R$ (R = body radius) produce tectonic dichotomy; waves of long πR (the first obertone) produce sectoring; and smaller waves length of which is proportional to orbital periods produce tectonic granulation. Segments, sectors, and granulas of differing radius-vectors (risen + and fallen – tectonic domains) tend to equalize their angular momenta by density of infilling matter. That is why oceanic and mare basins normally are filled with denser material (basalts) than lighter highlands.

On Earth one observes six antipodal centers of πR-structures (three pairs: (1) Equatorial Atlantic; (2) New Guinea; (3) The Pamirs-Hindukush; (4) Easter Island; (5) Bering Strait; and (6) Bouvet Island.) that regularly converge by common algorithm fallen normally oceanic and risen normally continental blocks. Around the Pamirs-Hindukush center, for example, are placed two differently risen sectors (African + +, Asian +) separated by 2 differently subsided ones (Eurasian –, Indoceanic – –). The six centers form vertices of an octahedron inscribed in the terrestrial sphere. The first antipodal pair lies in the equatorial zone, the second in tropics, and the third in the polar ring zones stressing profound connection between cosmic position of a body and its internal structure.

On the Moon we now know four antipodal centers of πR-structures: (1) Mare Orientale; (2) Joliot-Maxwell-Giordano Bruno area; (3) Daedalus-Heaviside; and (4) Ptolemaeus-Flammarion. Around the Mare Orientale, like on Earth, are two opposite differently subsided sectors (Procellarum Ocean –, SPA basin – –) separated by two differently uplifted ones (+ +, +), one of which (+ +) is the highest lunar highland region. Observing the angular momentum preservation law, the highest sector is composed of anorthosites, and even of the less dense Na-rich varieties of this rock. The deepest SPA basin sector with an abrupt northern boundary separating it from the highest sector (like the Indoceanic sector contacts with the highest African one) must be filled with denser rocks than the shallower Procellarum ocean sector filled with basalts and Ti basalts. The Clementine spectral data show a presence of orthopyroxene and an absence of plagioclase [2], favoring some dense ultrabasic rock. The obvious tendency to approach this type of rock would be to observe it in the Luna 24 samples from also very deep Mare Crisium. In fragments there prevail pyroxene and VLT-ferrobasalts (Mg-poor). Unusual melt matrix breccia with globules and crystals of Fe metal were also found [3]. In SPA basin fill some admixture of Fe metal and troilite could be also predicted. With this rock in mind we can construct a ladder of ascending UB-basic rock densities against descending topography: KREEP basalts, low-Ti basalts, high-Ti basalts, VLT-Mg-poor ferrobasalts, and pyroxene (with metal) rich rocks. On Earth, the density of basalt floods (their Fe/Mg ratio) also increases in the same direction. The lunar and terrestrial sectoral structures as well as tectonic dichotomies were formed in the very beginning of their geological histories.

References: [1] Kochemasov G. G. (1999) *Geophys. Res. Abstr., 1,* 700. [2] Pieters C. M. (1997) *Annales Geophysicae,* Suppl. III to v.15, 792. [3] Basu A. et al. (1977) *Conference on Luna 24,* Houston, LSI Contribution 304, 14–17.

NORTH-POLAR LUNAR LIGHT PLAINS: AGES AND COMPOSITIONAL OBSERVATIONS. U. Koehler[1,2], J. W. Head III[1], G. Neukum[2], and U. Wolf[2], [1]Box 1846, Department of Geological Sciences, Brown University, Providence RI 02912, USA (uli.koehler@dlr.de), [2]Deutsches Zentrum für Luft- und Raumfahrt, 12484 Berlin, Germany.

Abstract: Varying surface ages of lunar light plains in northern-nearside latitudes indicate an origin of these smooth terrae units not exclusively related to Imbrium and/or Orientale impact ejecta and subsequent processes. Multispectral data seem to support a more diversified history for many of these plains.

Introduction and Background: The nature, ages, stratigraphic position, composition, and mode of emplacement of lunar light plains have been discussed with controversy for more than three decades. Covering ~5% of the lunar terra surface, the relatively low-albedo plains are the most distinctive terra landforms after the more craterlike ejecta of the fresh basins [1]. Morphological properties, like their smoothness, lower crater densities, their superposition on the "Imbrian Sculpture," and frequent occurence as crater fill, are mare-like. Other features, such as relative (compared to mare basalts) high-albedo and geological/stratigraphical setting, are more highland-like. Not surprisingly, light plains were seen as both volcanic and impact related deposits (summarized in [2]). The Cayley Plains, a type locality in the central-nearside highlands, has been choosen as the landing site of the Apollo XVI mission partly to help resolve these interpretations. The astronauts collected samples — highly brecciated rocks — and concluded that the Cayley was indeed of impact origin ([3, and subsequent reports in *A16 PSR*]). These

findings have been extrapolated to stratigraphically similar plains units on the nearside, focusing on the Imbrium and Orientale impacts as responsible events for resurfacing terrae environment to form light plains [4]. In addition, theoretical modeling mechanisms have been provided that could explain how basin and crater ejecta were able to make up for the smoothness of light plains by stirring up local material through secondary-impact related processes [5, 6], or mega-impact induced seismic shaking [7].

However, subsequent age determinations showed that some light plains cannot be correlated to the Imbrium or Orientale event [8,9], the last two basin-forming impacts to occur on the Moon that had the ability to resurface areas thousands of kilometers away from their target site. An unknown form of highland volcanism was proposed as a contributing process in light-plains formation. The question remained unanswered whether processes other than impact-related processes were responsible for the formation of these enigmatic geological units, and how these processes might have worked. Focusing on light plains in the northern-nearside highlands, a chronological approach has been chosen to address these questions, and compositional information from multispectral data has been included to support our investigations.

Surface Ages: Mapping the northern-nearside light plains, earlier workers have recognized the stratigraphically and morphologically obvious bimodal distribution of smooth terrae units north and northeast of Mare Frigoris [10]. The older of these plains (Ip_1; based on stratigraphic relations and surface-crater densities) show gradual transition into (Imbrium-impact) Fra Mauro Formation units, whereas the younger unit (Ip_2) cannot be related to this relatively nearby-impact event. Instead, it was proposed that the impact of Orientale, despite the fact it is several thousand kilometers away, could have smoothed these terrae units with its ejecta stirring up local highland material [4], an interpretation that seems to be not very compelling, as these younger plains show quite homogeneous surfaces over extended areas. Determining precise surface ages of smooth surface units should help with getting a chronology of plains emplacement in these latitudes.

Based on the principle of crater-frequency distribution measurements and adjusting the cumulative crater-frequency distributions to a lunar standard distribution [11], and "fixing" the Orientale and Imbrium event with the absolute ages obtained by radiometric measurements of Apollo samples [12] to this distribution, one is able to determine reliable absolute-age data for surfaces after measuring the crater-frequency distribution on it. As the decline in impact frequency is rather steep during the first billion years in lunar history, the discrimination between surfaces of different age can be determined to a relatively high degree of reliability.

Forty-five smooth plains areas north and northeast of Mare Frigoris have been mapped for crater frequency. Some light plains have been disturbed by secondary cratering impact to a degree that made deduction of reliable age data impossible, so only 27 crater counts yielded useful absolute ages. A histogram of how these plains ages are distributed is shown in Fig. 1. For reference, the Imbrium and Orientale events are marked at their respective time of impact at 3.90 Ga, and 3.84 Ga respectively [13].

There are several observations that can be made in this distribution: (1) the ages do not cluster around one or two peaks; instead, the majority of light plains formed in a rather broad time span between 4.0 Ga and 3.65 Ga; (2) there are some light plains that seemed to have formed before the Imbrium impact event; (3) light plains formation peaked at the time of, or shortly after, the Orientale impact event; (4) light plains formation continued a significant time span after the Orientale basin impact; (5) there are light plains ages that are remarkably younger than the age of the Orientale basin, exposing surface ages that are only slightly older than the mare-basalt ages of their neighboring units at the eastern margin of Mare Frigoris; and (6) the time span of light-plains surface formation seems to extend from around 3.95–4.0 Ga to 3.60–3.65 Ga. In addition, there seem to be correlations between ages of light plains and their geographic position; oldest ages >3.90 Ga occur in the vicinity of the north pole, in and surrounding the craters Byrd, Main, Scoresby, and north of Anaxagoras. Plains with Imbrian-impact ages as young as the Orientale impact are clustered in and around craters Meton, Barrow, Barrow K, Baillaud, east of W. Bond, and Neison. Ages that are clearly younger than the Orientale impact can be found in the extended smooth plains area west, south, and southeast of crater Gärtner, northeast of Epigenes, east of De Sitter, Barrow K, and the areas bordering the eastern margin of Mare Frigoris. Except for the suspicious correlation between geographic occurence and absolute ages, the statistic pattern of light-plains ages is fairly well comparable to that of the central-highlands (Cayley Plains) units [14], where especially light plains of ages younger than the Orientale impact can be found — but in that case in no direct contact relations to mare units.

Multispectral Data: In order to get additional information on the light-plains areas that have been selected for crater statistics, multispectral data have been investigated from the second Earth/Moon encounter of the Galileo spacecraft (December 1992), which had excellent viewing geometry of the area of interest [15]. Based on previous work [16] it could be confirmed that the north-polar plains indeed show distinctive albedo behavior — being clearly brighter than maria but darker than highland units and showing less albedo variation than highland. Well-exposed mare-basalt units and well-exposed unambigous highland areas have been chosen to extract reference spectra in order to get clues to plains affinities. A number

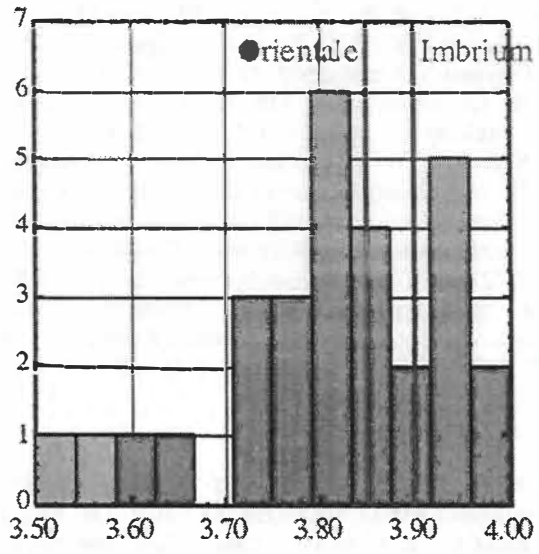

Fig. 1. Frequency (y-axis) of light plains ages (x-axis, billion years) in the northern-nearside hemisphere. Note that the two youngest ages (blue) are surfaces of mare-basalt units in eastern Mare Frigoris, adjacent to light plains units. Time of Imbrium and Orientale events are given as reference.

of fresh young craters in the light plains environment have been chosen to "sample" the material that is covered by the mature regolith. There are three interesting observations to report: (1) There are light plains showing clear highland affinities; (2) there are light plains that show definite mare affinities; and (3) the occurence of these two groupings is confined to areas in greater distance from Mare Frigoris for the first, and close to Mare Frigoris for the latter "spectral" group. In an ongoing process, application of spectral-mixing models to Galileo and Clementine multispectral data should help answering fundamental questions on compositional aspects here.

Conclusion: Based on the absolute ages of light-plains surfaces, the formation of these geologic units cannot be attributed to a uniform process. The fact that there are plains both clearly younger and older than the two largest last basin-forming impact events of Imbrium and Orientale, respectively, excludes an impact-ejecta origin related to these events, although Imbrium and Orientale ejecta deposition and their subsequent effects may certainly have played a major role in plains formation. Varying spectral characteristics confirm that probably more than a single process is responsible for the forming of these terra plains. As for the younger plains, it could be suggested that Late Imbrian craters contributed ejecta deposits to cover existing early mare basalts (making up for the smoothness of these surfaces) in the eastern Frigoris area, but the scarcity of dark-haloed craters does not support this idea — further investigations are necessary. The wide timespan of about 300 m.y. in plains ages further toward the north pole also requires a more detailed look at compositional aspects; due to some morphological evidence, unidentified forms of highland volcanism should be kept in mind, as it is known that nonmare volcanism occured elswhere in the Imbrium viciniy, on the Apennine Bench [17], forming a large unit of terra plains there.

References: [1] Wilhelms D. E. and McCauley J. F. (1971) *U.S. Geological Survey Misc. Geol. Inv. Map,* I-703. [2] Wilhelms D. E. (1987) *U.S. Geological Survey Prof. Paper, 1348,* pp. 20–22; 215–220. [3] Young J. W. et al. (1972) *NASA Apollo 16 Prelim. Sci. Rpt.,* 5-1–5-6. [4] Boyce J. et al. (1974) *Proc. LSC 5th,* 11–23. [5] Oberbeck V. R. (1975), *Rev. Geophys. Space Phys., 13,* 337–362. [6] Oberbeck V. R. et al. (1975) *Proc. LSC 5th,* 111–136. [7] Schultz P. H. and Gault D. E. (1975) *The Moon, 12,* 159–177. [8] Neukum G. et al. (1975) *The Moon, 12,* 201–229. [9] Neukum G. (1977) *The Moon, 17,* 383–393. [10] Lucchitta B. K. (1978) *U.S. Geological Survey Geol. Map 1:5,000,000,* I-1062. [11] Neukum G. et al. (1975) *Proc. LSC 4th,* 2597–2620. [12] Metzger A. E. et al. (1973) *Science, 179,* 800–803. [13] Neukum G. (1983) Habil. thesis, Munich University, 183 pp. [14] Koehler U. et al. (1993) *LPS XIV,* 813–814. [15] Belton M. J. S. et al. (1994) *Science, 264,* 1112–1115. [16] Mustard J. F. and Head J. W. (1995) *LPS XXVI,* 1023–1024. [17] Spudis P. D. (1978) *Proc. LPSC 9th,* 3379–3394.

LUNAR METEORITES AND IMPLICATIONS FOR COMPOSITIONAL REMOTE SENSING OF THE LUNAR SURFACE.

R. L. Korotev, Campus Box 1169, Department of Earth and Planetary Sciences, Washington University, St. Louis MO 63130, USA (rlk@levee.wustl.edu).

Lunar meteorites (LMs) are rocks found on Earth that were ejected from the Moon by impact of an asteroidal meteoroid. Three factors make the LMs important to remote-sensing studies: (1) Most are breccias composed of regolith or fragmental material; (2) all are rocks that resided (or breccias composed of material that resided) in the upper few meters of the Moon prior to launch [e.g., 15]; and (3) most apparently come from areas distant from the Apollo sites.

How Many Lunar Locations? At this writing (June 1999), there are 18 known lunar meteorite specimens (Table 1). When unambiguous cases of terrestrial pairing are considered, the number of actual LMs reduces to 13. (Terrestrial pairing is when a single piece of lunar rock entered Earth's atmosphere, but multiple fragments were produced because the meteoroid broke apart on entry, upon hitting the ground or ice, or while being transported through the ice.)

We have no reason to believe that LMs preferentially derive from any specific region(s) of the Moon; i.e., we believe that they are samples from random locations [15]. However, we do not know how many different locations are represented by the LMs; mathematically, it could be as few as 1 or as many as 13. The actual maximum is <13 because in some cases a single impact appears to have yielded more than one LM. Yamato 793169 and Asuka 881757 (Table 1, N = 12 and 13) are considered "source-crater paired" [15] or "launch paired" [1] because they are compositionally and petrographically similar to each other and distinct from the others, and both have similar cosmic-ray exposure (CRE) histories [12]. The same can be said of QUE 94281 and Y 793274 (Table 1, N = 9 and 10) [1]. Thus the 13 meteorites of Table 1 probably represent a maximum of 11 locations on the Moon.

The minimum number of likely source craters is debated and in flux as new data for different isotopic systems are obtained. Conservatively, considering CRE data only, a minimum of ~5 impacts is required. Compositional and petrographic data offer only probabilistic constraints. An extreme, but not unreasonable viewpoint, is that such data offer *no* constraint. For example, if one were to cut up the Apollo 17 landing site (which was selected for its diversity) into softball-sized pieces, some of those pieces (e.g., sample 70135) would be crystalline mare basalts like Y 793169 whereas others (e.g., sample 73131 would be feldspathic regolith breccias like MAC 88104/88105. However, nature is not so devious. Warren argues that LMs come from craters of only a few kilometers in diameter [15]. If so, even though CRE data allow, for example, that ALHA 81005 and Y 791197 (Table 1, N = 6 and 7) were launched simultaneously from the same crater, the probability is nevertheless low because the two meteorites are compositionally and mineralogically distinct. Thus, within the allowed range (5–11) for the number of locations represented by the LMs, values at the high end of the range are probably more likely.

Mare Meteorites: Three LMs consist almost entirely of mare basalt. Two, Y 793169 and Asuka 881757 (Table 1, N = 12 and 13), are unbrecciated, low-Ti, crystalline rocks that are compositionally and mineralogically similar (but not identical) to each other; they probably derive from a single lunar-mare location [16,12]. The third, EET 87521/96008, is a fragmental breccia consisting predominantly of VLT mare basalt. Thus, these LMs probably represent only two lunar mare locations. The basaltic LMs have mineral and bulk compositions distinct from Apollo mare basalts.

"Mixed" Meteorites: The petrography of Calcalong Creek has not been described in detail, but compositionally it is unique in that it corresponds to a mixture (breccia) of about one-half feldspathic material (i.e., the mean composition of the feldspathic lunar

meteorites, below), one-fourth KREEP norite, one-fourth VLT mare basalt (like EET 87521), and 1% CI chondrite. With 4 μg/g Th (Table 1) and correspondingly high concentrations of other incompatible elements, it is the only lunar meteorite that is likely to have come from within the Procellarum KREEP Terrane (PKT; see [3] for discussion of the terrane concept).

Yamato 793274 and QUE 94281 are together distinct in being fragmental breccias containing subequal parts of feldspathic highland material and VLT mare basalt. Jolliff et al. [4] estimate a mare to highland ratio of 54:46 for QUE 94281 and 62:38 for Y 793274; this difference is well within the range observed for soils collected only centimeters apart (in cores) at interface site like Apollo 15 and 17 [11]. Although the two meteorites were found on opposite sides of Antarctica, they are probably launch-paired. The strongest evidence is that the pyroclastic glass spherules that occur in both are of two compositional groups and the two groups are essentially the same in both meteorites [1].

Yamato 791197 (Table 1, N = 7) is nominally a feldspathic lunar meteorite (below), but among FLMs, it probably contains the highest abundance of clasts and glasses of mare derivation. As a consequence, its composition is at the high-Fe, low-Mg end of the range for FLMs and is not included in the FLM average of Table 1. Its composition is consistent with ~10% mare-derived material [8]. Similarly, the two small (Y 82) pieces of Y 82192/82193/86032 (Table 1, N = 5) are more mafic than the large (Y 86) piece, probably as a result of ~7% mare-derived material [8] (the mass-weighted mean composition is listed in Table 1).

Feldspathic Lunar Meteorites (FLMs): All Apollo missions went to areas in or near the PKT, and, consequently, all Apollo regolith samples are contaminated with Th-rich material from the PKT [7]. At the nominally "typical" highland site, Apollo 16, ~30% of the regolith (<1-mm fines) is Th-rich ejecta from the Imbrium impact [5,7] and ~6% is mare material probably derived from mare basins [5]. Thus Apollo 16 regolith is not typical of the highlands. Among Apollo *rocks*, the compositions of the FLMs correspond most closely to the feldspathic granulitic breccias of Apollo 16 and 17 [2,13].

The FLMs of Table 1, consequently and ironically, are especially important in that among lunar samples, they provide the best estimate we have of the composition of the Feldspathic Highlands Terrane [6]. All are regolith or fragmental breccias and, as such, are more likely to represent the composition of the upper crust in the area from which they were launched than any igneous rock that might have been excavated and launched from depth. FLMs contain little mare material (probably <<5%, on average). All have low concentrations of Th and other incompatible elements, indicating that they are also minimally contaminated (<3%) with material from the PKT. Thus, Th concentrations of the FLMs provide a reasonable lower limit to values that might be expected for large areas of the lunar farside as detected by Lunar Prospector [9].

The mean FeO concentration of the FLMs, 4.45 ± 0.6% (Table 1; ±95% confidence limit) is remarkably similar to the "global mode" of 4.5 ± 1.0% obtained from analysis of Clementine spectral reflectance data [10]. (Because the FLMs consist of near-surface regolith material, a significant fraction of the Fe in the FLMs is of meteoritic origin, largely from micrometeorites. For the purpose of estimating the composition of the upper few kilometers of feldspathic crust, this component must be removed, yielding 4.2% FeO for the upper crust [6]. However, for comparisons to Clementine results, the FLM mean of Table 1 is more appropriate.) Similarly, the mean TiO_2 concentration of the FLMs, 0.35 ± 0.15%, agrees well with the value obtained from Clementine, 0.45 ± 1.0% [10], giving credence at low-TiO_2 concentration to the technique used to derive the Clementine-based estimates.

The six FLMs are all similar in composition. Such similarity is expected if all were to derive from the same source crater. However, both Clementine and Lunar Prospector show that vast areas of the farside are consistent with the FLM composition; thus it is reasonable

TABLE 1. Lunar meteorites (lunaites): A list in order of increasing Fe concentration.

N	Name	Lunar rock type	Mass (g)	Where found	Al_2O_3 (%)	TiO_2 (%)	FeO (%)	MgO (%)	Mg′ (%)	Th μg/g
Feldspathic lunar meteorites (FLMs)										
1	Dar al Gani 400	regolith breccia	1425	Libya	*28.9*	*0.18*	*3.8*	*5.1*	*71*	*?*
2	MAC 88104/88105	regolith breccia	61 + 663	Antarctica	28.1	0.23	4.28	4.05	63	0.39
3	Dar al Gani 262	regolith breccia	513	Libya	28.4	0.24	4.35	*5.0*	*67*	0.37
4	QUE 93069/94269	regolith breccia	21 + 3	Antarctica	28.5	0.23	4.43	4.44	64	0.53
5	Yamato 82192/82193/86032	fragm. or reg. breccia	37 + 27 + 648	Antarctica	28.3	0.19	4.36	5.23	68	0.20
6	ALHA 81005	regolith breccia	31	Antarctica	25.7	0.27	5.47	8.2	73	0.28
	mean FLM				**28.0**	**0.22**	**4.45**	**5.3**	**67**	**0.35**
"Mixed" meteorites										
7	Yamato-791197	regolith breccia	52	Antarctica	26.4	0.31	6.1	6.1	64	0.35
8	Calcalong Creek	regolith breccia	19	Australia	21.3	0.83	9.7	*7.7*	*59*	4.0
9	QUE 94281	regolith breccia	23	Antarctica	17.2	0.59	13.1	9.6	57	1.0
10	Yamato 793274	regolith breccia	9	Antarctica	15.7	0.60	14.2	9.0	53	0.9
Mare lunar meteorites										
11	EET 87521/96008	fragmental breccia	31 + 53	Antarctica	13.2	0.97	18.8	6.8	39	1.0
12	Yamato 793169	mare basalt	6	Antarctica	11.4	2.15	21.0	5.7	32	0.75
13	Asuka 881757	mare basalt	442	Antarctica	10.0	2.42	22.6	6.2	33	0.45

Italics = preliminary or highly uncertain values. Mg′ = bulk mole % Mg/(Mg+Fe). Data compiled from a large number of literature sources.

that the FLMs may represent as many as six source craters. Among FLMs, ALHA 81005 is distinct in being richer in MgO and having a correspondingly higher Mg′ (Table 1). Although bulk compositions of the other FLMs are generally consistent with their derivation mainly from rocks of the ferroan-anorthosite suite [14], the mafic minerals, at least, in ALHA 81005 cannot derive from a source dominated by ferroan-anorthosite-suite rocks. Mafic rocks of the magnesian suite of lunar plutonic rocks are probably all special products of the PKT [7]. Thus ALHA 81005, as well as the high-Mg′ variety of Apollo feldspathic granulitic breccias [13,5], suggest that there are regions of the feldspathic crust dominated by nonferroan (i.e., high-Mg′) feldspathic lithologies. Locating such areas should be a high-priority goal of remote-sensing missions.

Acknowledgments: This work was funded by NASA (NAG5-4172).

References: [1] Arai T. and Warren P. H. (1999) *MAPS, 34,* 209–234. [2] Cushing J. A. et al. (1999) *MAPS, 34,* 185–195. [3] Jolliff B. L. (1999) *LPS XXX,* Abstract #1670. [4] Jolliff B. L. et al. (1998) *MAPS, 33,* 581–601. [5] Korotev R. L. (1997) *MAPS, 32,* 447–478. [6] Korotev R. L. (1999) *LPS XXX,* Abstract #1303. [7] Korotev R. L. (1999) *LPS XXX,* Abstract #1305. [8] Korotev R. L. et al. (1996) *MAPS, 31,* 909–924. [9] Lawrence D. J. et al. (1998) *Science, 281,* 1484–1489. [10] Lucey P. G. et al. (1998) *JGR, 103,* 3679–3699. [11] Morris R. V. et al. (1989) *Proc. LPSC 19th,* 269–284. [12] Thalmann C. et al. (1996) *MAPS, 31,* 857–868. [13] Lindstrom M. M. and Lindstrom D. J. (1986) *Proc. LSC 16th,* in *JGR,* D263–D276. [14] Warren P. H. (1990) *Am. Mineral., 75,* 46–58. [15] Warren P. H. (1994) *Icarus, 111,* 338–363. [16] Warren P. H. and Kallemeyn G. W. (1993) *Proc. NIPR Symp. Antarct. Meteorites, 6,* 35–57.

IRON ABUNDANCES ON THE MOON AS SEEN BY THE LUNAR PROSPECTOR GAMMA-RAY SPECTROMETER.

D. J. Lawrence[1], W. C. Feldman[1], B. L. Barraclough[1], R. C. Elphic[1], S. Maurice[2], A. B. Binder[3], and P. G. Lucey[4], [1]Mail Stop D-466, Los Alamos National Laboratory, Group NIS-1, Los Alamos NM 87545, USA (djlawrence@lanl.gov), [2]Observatoire Midi-Pyrénées, Toulouse, France, [3]Lunar Research Institute, Tucson AZ, USA, [4]University of Hawai'i, USA.

Introduction: Measurements of global-Fe abundances on the Moon are important because Fe is a key element that is used in models of lunar formation and evolution. Previous measurements of lunar-Fe abundances have been made by the Apollo γ-Ray (AGR) experiment [1] and Clementine spectral reflectance (CSR) experiment [2]. The AGR experiment made direct elemental measurements for about 20% of the Moon. However, these measurements had large uncertainties due mostly to low statistics [3] and an absence of thermal neutron data (see below). The CSR-derived Fe data has much better coverage (100% coverage equatorward of ±70° latitude) and spatial resolution (~100-m surface resolution vs. ~150-km surface resolution for the AGR data), but there have been questions regarding the accuracy of these data far from the Apollo landing sites [4].

Here we present preliminary estimates of the relative Fe abundances using the Lunar Prospector (LP) γ-ray spectrometer (GRS). While these data are important and useful by themselves, the ultimate goal of this study is to combine the LP Fe data with the CSR data to obtain a better calibrated and more accurate picture of the Fe abundances on the Moon.

Data Analysis: To derive Fe abundances, we are using two γ-ray lines near 7.6 MeV. These γ-rays are produced by thermal neutron capture. Here, Fe nuclei absorb thermal neutrons, become energetically excited, and then de-excite with the production of γ-rays. Because this process depends upon thermal neutrons, the measured flux of 7.6 MeV γ-rays is proportional not only to the Fe abundances, but also to the thermal neutron number density. Here, we use measurements from the LP neutron spectrometer (NS) [5] to correct for this thermal neutron effect. As seen in [5], this correction is quite large as the thermal neutron count rate varies over the Moon by a factor of 3. Many considerations need to be taken into account to make sure an appropriate correction is applied. These include (1) converting the measured thermal neutron flux into a true thermal neutron number density; (2) accounting for composition effects such as thermal neutron absorption due to Gd and Sm [6]; and (3) equating the instrument surface resolution for the GRS and NS. To take care of most of these considerations, detailed calculations need to be carried out. Yet with some assumptions, a preliminary estimate of the thermal neutron correction can be obtained.

To relate the measured thermal neutron flux to the thermal neutron number density, we assume that the thermal neutron energy distribution is Maxwellian and independent of soil composition. With this assumption, the measured neutron flux, F, is proportional to both the neutron number density, n, and the square root of the mean lunar surface temperature, T:

$$F \propto n\sqrt{T}$$

Here, the measured neutron flux also includes epithermal neutrons that contribute to the overall neutron number density. To obtain a global surface temperature, we have used a mean equatorial surface temperature of 250 K and scaled it as $\cos(\text{latitude})^{1/4}$. Because this scaling results in very low temperatures at the poles, a low temperature cutoff has been set at 130 K.

Results: For this study, we have used the high-altitude GRS data to obtain the relative Fe abundances. We correct for the thermal neutron effect using the low-altitude summed thermal and epithermal neutron data smoothed to the footprint of the high-altitude GRS data set. The resulting relative Fe abundance map is shown in Fig. 1. A comparison between this map and the published CSR Fe map shows a good correspondence. This correspondence is shown more quantitatively in Fig. 2, which is a scatter plot between the two datasets. Here, the CSR data has been smoothed to the footprint of the GRS data. As seen, for most of the Moon, there is a good correlation between the datasets with a correlation coefficient of 0.93. One region of some disagreement is in the South Pole Aitken (SPA) Basin (red points), where the CSR measurements correspond to a ~20% higher count rate than is observed with the GRS data.

In contrast to the corrected GRS data, the blue points show the GRS data before the thermal neutron correction is applied. The correlation coefficient between the uncorrected GRS data and the CSR data is poorer at 0.73. In addition, the spread of the GRS data at a given CSR abundance (~5 channels) is almost as large as the entire dynamic range of the uncorrected count rate (~6 channels), which implies that there are large uncertainties in the uncorrected data.

Because there are many assumptions leading to Fig. 1, the uncertainties of these data are not yet known. For example, it is not clear

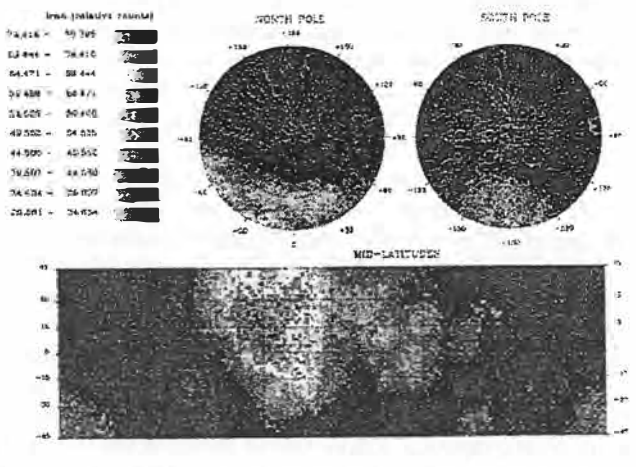

Fig. 1. Global map of relative Fe abundances from the LP GRS overlaid with a lunar surface features map. (To view Figs. 1 and 2 in color, go to http://cass.jsc.nasa.gov/meetings/moon99/pdf/8036.pdf.)

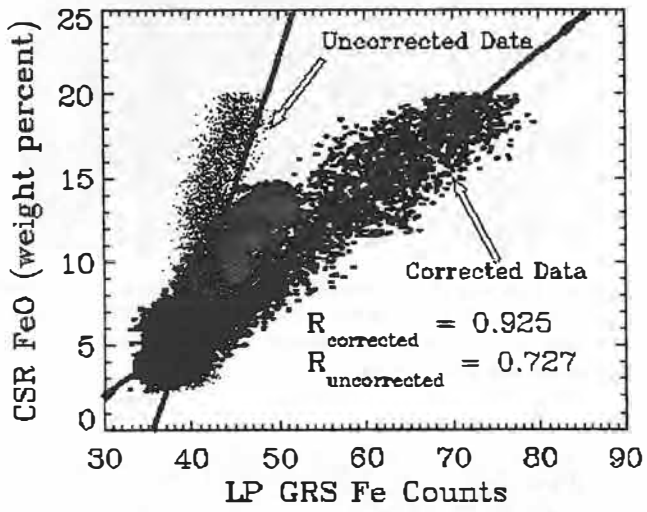

Fig. 2. Scatter plot of LP GRS Fe data vs. CSR FeO data. Uncorrected LP data shown in blue; corrected LP data shown in black.

if the discrepancy seen in SPA is real or is some effect of the simplified data-reduction technique. Even so, we are demonstrating the ability to compare LP and CSR Fe datasets and show that they may indeed agree quite well.

References: [1] Davis P. A. (1980) *JGR, 85,* 3209. [2] Lucey et al. (1998) *JGR, 103,* 3679. [3] Davis P. A. and Spudis P. D. (1987) *JGR, 92,* E387. [4] Clark P. E. and Basu A. (1998) *LPS XXIX.* [5] Feldman et al. (1998) *Science, 281,* 1489. [6] Elphic et al. (1998) *Science, 281,* 1493.

DISCRIMINATION BETWEEN MATURITY AND COMPOSITION FROM INTEGRATED CLEMENTINE ULTRAVIOLET-VISIBLE AND NEAR-INFRARED DATA.

S. Le Mouélic[1], Y. Langevin[1], S. Erard[1], P. Pinet[2], Y. Daydou[2], and S. Chevrel[2], [1]Institut d'Astrophysique Spatiale, Centre National de la Recherche Scientifique, Université Paris XI, Bât 121, 91405 Orsay cedex, France (lemoueli@ias.fr), [2]Unité Mixte de Recherche 5562, Group for Space Research and Geodesy, Centre National de la Recherche Scientifique, 14 av E. Belin, Toulouse, 31400, France.

Introduction: The Clementine UV-VIS dataset has greatly improved our understanding of the Moon. The UV-VIS camera was limited to five spectral channels from 415 to 1000 nm. The Clementine near-infrared (NIR) camera was designed to complement this spectral coverage. The NIR filter at 2000 nm allows the discrimination between olivine and pyroxene within identified mare basalts [1]. In addition, we will show that the integration of Clementine UV-VIS and NIR datasets allows a better evaluation of the ferrous 1-μm absorption band depth and gives access to the slope of the continuum. The discrimination between maturity and FeO composition can be achieved by a principal component analysis performed on spectral parameters.

Data Reduction: We selected 952 Clementine UV-VIS and NIR images to compute a multispectral cube covering the Aristarchus Plateau. Aristarchus Plateau is one of the most heterogeneous areas on the Moon. Highland-type materials, mare basalts, and dark mantle deposits have previously been mentioned [2]. The mosaic represents a set of ~500 × 600 nine-channel spectra. UV-VIS filters at 415, 750, 900, 950, and 1000 nm were calibrated using the ISIS software [3]. We applied the reduction method described in [4] to reduce the NIR filters at 1100, 1250, 1500 and 2000 nm. Absolute gain and offset values were refined for the NIR images by using eight telescopic spectra acquired by [5] as references. With this calibration test, we were able to reproduce the eight telescopic spectra with a maximum error of 1.8%.

Effects of Maturity on Extracted Spectra: The integration of UV-VIS and NIR spectral channels allows the visualization of complete low-resolution spectra. In order to investigate the spectral effects of the space-weathering processes, we focused our analysis on a small mare crater and its immediate surroundings (see arrow Fig 2a). According to the small size of the crater (~2-km) and its location on an homogeneous mare area [2], we can reasonably assume that the content in FeO is homogeneous. The impact event has induced a variation of the maturity of the soil by excavating fresh material. Figure 1a displays five absolute reflectance spectra extracted from this area. Figure 1b displays the same spectra divided by a continuum, which is considered to be a right line fitting the spectra at 0.75 and 1.5 μm. Spectrum 1 is extracted from the brightest part of the crater interior, and spectrum 5 is extracted from the surrounding mare material. Spectra 2, 3, and 4 are extracted from intermediate distances between the two areas.

The 1-and-2 μm absorption band depths and the overall reflectance increase from spectrum 5 (corresponding to a mature area) to spectrum 1 (the most immature area). Conversely, the continuum slope decreases from spectrum 5 to spectrum 1 (Fig. 1a). These three spectral effects of maturity have also been identified on laboratory spectra of lunar samples [6].

Depth of the 1-μm Feature and Continuum Slope: Most of the lunar soils exhibit a signature near 1 μm. This absorption band is

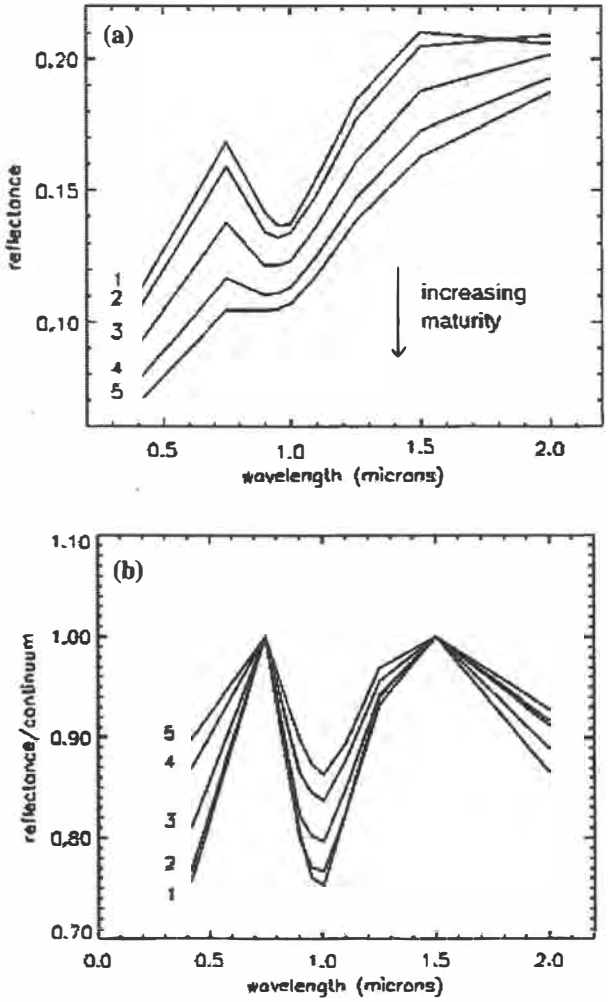

Fig. 1a and 1b. Spectra extracted from a fresh mare crater (see arrow in Fig. 2a). 1 = crater interior (immature): 5 = surrounding mare (mature). The overall reflectance and spectral contrast decrease with increasing maturity, while the continuum slope increases with maturity.

due to the presence of Fe^{2+} in mafic minerals such as orthopyroxene, clinopyroxene, and olivine. In the case of Clementine UV-VIS data alone, the depth of the 1-μm feature is evaluated by the 950/750-nm reflectance ratio. This ratio combined to the reflectance at 750 nm has been used to evaluate the global content in FeO of the lunar surface [7–8].

Near-infrared data makes a more precise evaluation of the 1-μm band depth possible by providing the right side of the band. The continuum in the vicinity of the band can be evaluated by an arithmetic mean or a geometric interpolation of both sides of the band, which are taken at 750 and 1500 nm. The geometric interpolation is less sensitive to residual calibration uncertainties. With this method, the 1-μm absorption band depth for the Aristarchus Plateau can be refined by as much as 10%. The difference is maximum on Fe-poor, highland-type materials.

Similarly, the NIR data provide the possibility to investigate the continuum slope of the spectra. The continuum slope is a key parameter in any spectral analysis. The continuum slope variations seem to be mainly dominated by maturity effects, as suggested by the high correlation with the independent evaluation of maturity (OMAT parameter) proposed by Lucey at al. [9]. We have also found a good correlation between the continuum slope and the OMAT parameter on laboratory spectra of lunar samples of the J. B. Adams collection (available at http://www.planetary.brown.edu).

The discrimination between maturity effects and composition effects can be achieved by using a principal component analysis (PCA) on three spectral parameters, which are the reflectance at 0.75 μm, the depth of the 1-μm feature, and the continuum slope. These parameters are mostly affected by maturity and FeO content. The effects of various glass content are assimilated to maturity. The aim of the PCA is to decorrelate the FeO content and maturity effects in the three input parameters. Figure 2a displays the first axis of the PCA, which accounts for 81.8% of the total variance. This image is at first order comparable with the OMAT parameter from Lucey [9]. Figure 2b corresponds to the second axis of variation (14.4%) re-

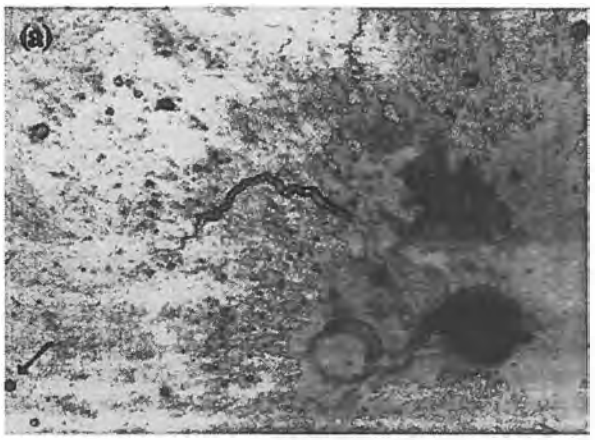

Fig. 2a. First axis of the principal component analysis. Impact craters and the walls of Valles Schröteri appear symmetrical. This image is at first order very similar to the continuum slope image and is controlled by maturity and glass content.

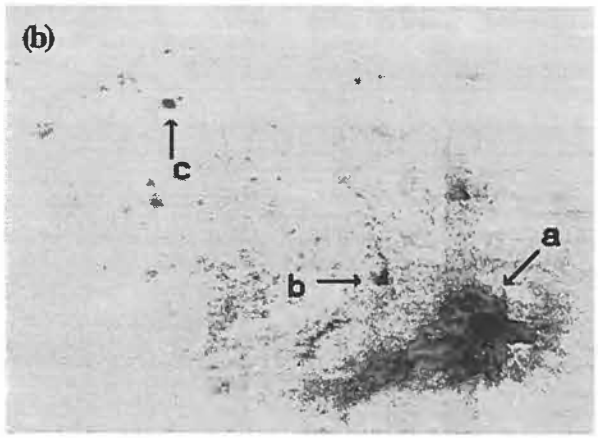

Fig. 2b. Second axis of the PCA. This image is very similar to the FeO image derived from Lucey et al. [8], with less sensitivity to the topography. Iron-poor highland type material is detected in the vicinity of the Aristarchus Crater (a), in the cobra head (b), and on Herodotus (c).

vealed by the PCA. This image is very consistent with the FeO image derived from Lucey et al. [8], with less improvement due to less sensitivity to the topography.

Conclusion: The integration of UV-VIS and NIR datasets allows for a better understanding of the spectral properties of the lunar surface by giving access to key parameters such as the 1- and 2-μm band depths and the continuum slope. The continuum slope can be combined with the depth of the mafic 1-μm absorption feature and the reflectance at 750 nm to discriminate between maturity and composition. NIR images of the sample return stations will be very interesting to refine absolute FeO content and maturity evaluations.

References: [1] Le Mouélic et al. (1999) *GRL, 26,* 1195. [2] McEwen A. S. et al. (1994) *Science, 266,* 1858–1862. [3] McEwen A. S. et al. (1998) *LPS XXIX,* Abstract #1466. [4] Le Mouélic S. et al. (1999) *JGR, 104,* 3833. [5] Lucey P. G. et al. (1986) *JGR, 82,* 344–354. [6] Fischer E. M. and Pieters C. (1994) *Icarus, 111,* 475–488. [7] Lucey P. G. et al. (1995) *Science, 268,* 1150–1153. [8] Lucey P. G. et al. (1998) *JGR, 103,* 3679–3699. [9] Lucey P. G. et al. (1998) *LPS XXIX,* Abstract #1356.

TOPOGRAPHIC-COMPOSITIONAL RELATIONSHIPS WITHIN THE SOUTH POLE AITKEN BASIN.

P. G. Lucey, J. Holtzmann, D. T. Blewett, G. J. Taylor, and B. R. Hawke, Department of Planetary Geosciences, Hawai'i Institute of Geophysics and Planetology, University of Hawai'i, 2525 Correa Road, Honolulu HI 96822, USA (lucey@pgd.hawaii.edu).

Introduction: The South Pole Aitken (SPA) Basin is an immense structure that dominates the geology of much of the farside of the Moon. Its floor is composed mostly of impact deposits, though it also has numerous relatively small regions of mare basalt. The basin floor exhibits a lower albedo and higher mafic mineral abundance than the surrounding highlands [1]. The origin of this mafic anomaly is a major question in lunar geology. Hypotheses for the presence of the mafic anomaly were briefly reviewed in [2] and include mare deposits mixed and obscured by basin or crater ejecta (cryptomaria), a large impact melt sheet that may have differentiated, exposed lower crustal material, and a significant component of excavated mantle. A study of mineralogy as revealed in Clementine UV-VIS imagery for limited portions of the basin found a predominantly low-Ca pyroxene (noritic) character [2], ruling out cryptomaria as an important contributor to the mafic enhancement. A few small cryptomaria, revealed by dark-halo impact craters and light plains units with high-FeO contents, have been found in SPA [3]; however, it appears that extensive cryptomaria are lacking in this basin. The uniformly noritic lithology within SPA led [2] to favor exposed lower crust or a homogenized melt sheet as the explanation for the mafic anomaly.

Models of basin formation predict that a basin the size of SPA should have excavated through the entire lunar crust (assuming non-oblique impact), potentially exposing or mixing a large component of material from the mantle. Comparison of SPA floor FeO and TiO_2 (derived from Clementine UV-VIS observations) [4] and also Th (from Lunar Prospector) [3] with model-mantle chemistries appears to be consistent with a mixture of approximately equal proportions of lower-crust and mantle material.

In the present study, we examine the relationship between the basin's topography and composition in order to provide further insight on the origin of the basin floor material.

Data: Clementine UV-VIS data at 1-km/pixel spatial resolution were placed in an orthographic projection centered on the basin (55°S, 180°E). Maps of Fe and Ti abundance were produced using the spectral algorithms of Lucey et al. [5]. A map of topography derived from Clementine laser altimeter measurements was retrieved from the Planetary Data System Web site [6] and reprojected to match the UV-VIS image and elemental maps.

Findings and Discussion: We find an inverse correlation between topography and FeO content for the basin interior (Fig. 1). The correlation coefficient between elevation and [1/(FeO)] is about 0.7. Figure 2 shows a typical east-west compositional profile across the basin compared to a model profile generated by a linear fit to the data in Fig. 1.

The occurrence of greater FeO contents at greater depths (Fig. 1) could be explained in several ways. The magma ocean model for the formation of the lunar crust predicts a crust that becomes more Fe rich with depth, so in SPA we may be seeing an exposed crustal column. An undifferentiated melt sheet composed of such a stratified crustal material is lower in FeO.

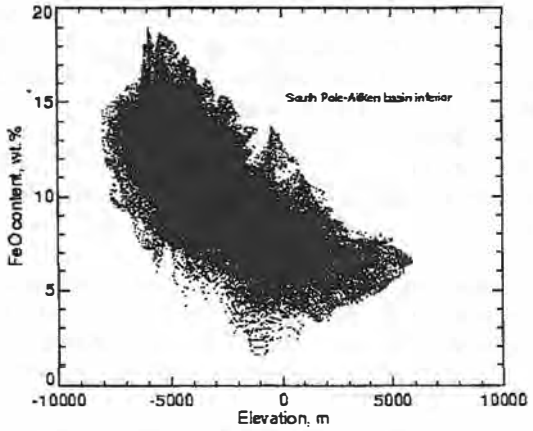

Fig. 1. Plot of FeO vs. elevation for the interior of South Pole Aitken Basin. An approximate fit of the data is FeO (wt%) = [(–0.0011) (elevation in meters)] + 7.2.

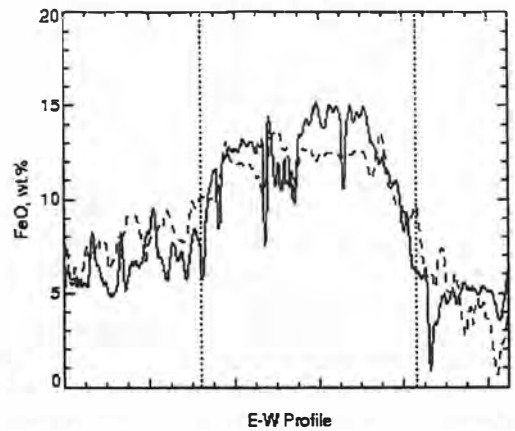

Fig. 2. Typical compositional profile across SPA. The solid line is an actual FeO profile. The dashed line is model FeO generated by applying a linear fit of the data in Fig. 1 to the topographic profile. Vertical dotted lines show the approximate location of the SPA Basin rim. SPA is ~2500 km in diameter.

Further speculation. The excavation of the SPA cavity would have been a massive unroofing event that could have triggered significant mafic igneous activity through pressure-release melting. The melts that were generated would tend to erupt and or collect in the low-elevation central portion of the basin. At higher elevations, progressively smaller quantities of magma and greater impact dilution with underlying more-felspathic rocks might lead to the observed correlation between elevation and Fe content. It is interesting to note that KREEP basalts, which may have originated in a similar manner in the Imbrium Basin [8], possess FeO of roughly 12 wt%, comparable to much of the floor of SPA.

References: [1] Belton M. et al. (1992) *Science, 255,* 570. [2] Pieters C. M. et al. (1997) *GRL, 24,* 1903. [3] Blewett D. T. et al. (1999) *LPS XXX,* Abstract #1438. [4] Lucey P. G. et al. (1998) *JGR, 103,* 3701. [5] Lucey P. G. et al. (1999) *JGR,* submitted. [6] Zuber M. T. et al., http://pds-geophys.wustl.edu/pds/clementine/. [7] Morrison D. (1998) *LPS XXIX,* Abstract #1657. [8] Ryder G. (1994) *Geol. Soc. Am. Spec. Paper 293,* 11.

HIGH-ENERGY NEUTRONS FROM THE MOON.

S. Maurice[1], W. C. Feldman[2], D. J. Lawrence[2], R. E. Elphic[2], O. Gasnault[3], C. d'Uston[3], and P. G. Lucey[4], [1]Observatoire Midi-Pyrénées, Toulouse, France (maurice@obs-mip.fr), [2]Los Alamos National Laboratory, Los Alamos NM, USA, [3]Centre d'Etude Spatiale des Rayonnements, Toulouse, France, [4]Hawai'i Institute of Geophysics and Planetology, University of Hawai'i, Honolulu HI, USA.

Introduction: Galactic cosmic rays that impact the lunar soil produce neutrons with energies from fractions of eV's to ~100 MeV. The high-energy band from 0.6 to 8.0 MeV is referred as the "fast neutron" band, which is measured by Lunar Prospector (LP) Gamma-Ray Spectrometer [1].

Fast neutrons play an important role in neutron spectroscopy [2] that may be summarized as follows: Fast neutrons define the total neutron input to the moderating process toward low-energy populations, so that epithermal and thermal neutron leakage currents must be normalized to the leakage of fast neutrons; they allow the determination of the burial depth of H, a measure necessary to understand characteristics of water deposits; they provide information on the surface content in heavy elements, such as Ti and Fe; and they provide a direct insight into the evaporation process. As discussed hereafter, fast neutrons may yield information on other oxides, such as SiO_2.

Datasets and Data Processing: This study uses fast neutron data from December 20, 1998 to May 22, 1999, when the spacecraft altitude was between 10 and 50 km. The data reduction includes normalization to the cosmic-ray rate, to the spacecraft height and latitude, and finally to the gain drift.

From all-Moon maps at a 2°× 2°-equal-area resolution, we learn the following: (1) All mare identified, from the largest ones, Imbrium, Frigoris, Fecunditatis, to the smallest ones, Undarum, and Spumans, are high-neutron emitters; (2) there are extended regions, such as South Aitken Basin, or the area around Schickard, which are medium-to-high-neutron emitters; (3) highlands are definitively low fast neutron emitters, which form the blue-background of the map; and (4) the largest craters are resolved in fast neutrons.

Figure 1 is a map of the central mare region. White data represent missing data. Mare have numerous features, that are resolved in fast neutrons. For instance, the region extending northwest of Aristarchus (23.7°N, 47.4°W) is clearly separated from Montes Harbinger (27.0°N, 41.0°W) by a high-emission channel, and Mare Vaporum (13.3°N, 3.6°E) is separated from Sinus Aestuun (10.9°N, 8.8°W) by a low-emission area.

Moon Composition: We present a new technique to extract information on soil composition from the fast-neutron measurements. The analysis is applied to the central mare region. There are two steps for the development of the technique.

1. For the first step, which has been fully completed [3], we assume that variations of fast-neutron counting rates are due solely to TiO_2 and FeO. Upon this assumption, we correlate Clementine Spectral Reflectance Fe and Ti oxide maps [4] with fast measurements. Above 16.5% of FeO, effects of TiO_2 variations show in LP data. Below 6.5% of FeO, Fe cannot be discriminated; this is the region of most highland terrains.

Under assumption of only two oxides to modulate the signal, we show that fast counts are 3.2× more sensitive to FeO than to TiO_2. The resolution in FeO is 1.2 wt% , in TiO_2 it is 3.8. These results are very satisfying, specially for the distribution of FeO. However, they do not permit reproduction of Clementine TiO_2 map from the residual of the fast counting rates and Clemetine FeO correlation. Particularly, the discrimination between hi-Ti and low-Ti mare is not striking.

2. The second step is still under development. We assume that variations of fast-neutron counting rates are primarily due to FeO, but also to TiO_2, SiO_2, CaO, Al_2O_3, MgO, and Na_2O. Gasnault et al. [5] have calculated the number of fast neutrons in our energy band of interest:

Na	1.28	Mg	1.68
Al	2.09	Si	2.26
Ca	1.75	Ti	3.02
Fe	2.81	O	0.165

per weight fraction of each element, for an average cosmic-ray flux. This simulation is for a FAN soil. It will have to be refined and iteratively adapted to the soil composition.

With information on TiO_2 and FeO distributions from Clementine and the coefficient above, we know the global soil content in the other oxides (weighted by Gasnault et al. coefficients). On the other hand, we have from return samples estimates of correlation between oxide concentrations. We demonstrate that such processing allows estimations of SiO_2 variations in the lunar regolith.

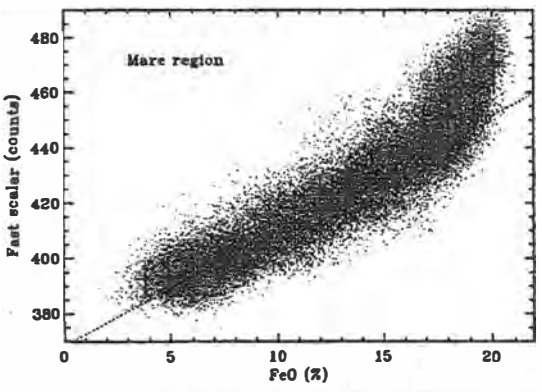

Fig. 1.

References: [1] Feldman et al. (1999) *NIM, 422,* 562–566. [2] Feldman et al., *Science, 281,* 1489. [3] Maurice et al. (1999) *JGR,* submitted. [4] Lucey et al. (1998) *JGR, 103,* 3679. [5] Gasnault et al. (1999) *JGR,* submitted.

THE INTERIOR OF THE MOON, CORE FORMATION, AND THE LUNAR HOTSPOT: WHAT SAMPLES TELL US.

C. R. Neal, Department of Civil Engineering and Geological Science, University of Notre Dame, Notre Dame IN 46556, USA (Neal.1@nd.edu).

Introduction: Remotely-gathered Lunar Prospector data have demonstrated the existence of a lunar "hotspot" on the near side of the Moon. This hotspot contains relatively high abundances of KREEPy incompatible trace elements (i.e., Th). It is generally accepted that primordial KREEP or *urKREEP* represents the residual liquid after the crystallization of a lunar magma ocean (LMO) [e.g., 1–2]. The crystalline products from the LMO formed the source regions for the mare basalts [e.g., 3]. Lunar volcanic glasses cannot be genetically related to the crystalline mare basalts [e.g., 4–5], and experimental petrology indicates they are derived from greater (>400 km) depths than the mare basalts [e.g., 6]. Questions to be addressed include: (1) What was the extent of LMO melting (whole vs. partial Moon melting)? (2) What is the composition of the core? (3) Are there distinct geochemical reservoirs in the Moon? (4) Is there evidence of garnet in the lunar interior? (5) What caused the formation of the lunar hotspot?

What was the extent of LMO melting and what is the composition of the lunar core? The scale of the LMO has been suggested to be whole Moon melting [cf. 7–9] or only the outer ~400 km [cf. 2]. If whole Moon melting is invoked, then differentiation of the Moon into a flotation plagioclase-rich crust, a mafic mineral cumulate mantle, and a Fe-rich core is more easily facilitated. However, as pointed out by [9], if the material that formed the Moon came primarily from the already-differentiated Earth mantle, there may not be enough Fe to form a metallic Fe core on the Moon. These authors suggested that the lunar core is made up of dense, ilmenite-rich, late-stage cumulates from the LMO. This can be tested by examining the Zr/Hf ratios of mare basalts and, where possible, the volcanic glasses. Partition coefficients for Zr and Hf in ilmenite are 0.29–0.32 and 0.4–0.43, respectively [cf. 10], with Zr being less compatible. Therefore, extraction of an "ilmenite" core would have a profound effect on the Zr/Hf ratio of urKREEP as ilmenite is a late-stage fractionating LMO phase. Assuming either a "primitive mantle" or chondritic starting material with a Zr/Hf ratio of 36–37, ilmenite extraction will increase this ratio in the residual liquid. Conversely, derivation of a melt from a source rich in ilmenite will produce a melt of lower Zr/Hf ratio. Hughes and Schmitt [11] defined a mean Zr/Hf for KREEP of 41.0 ± 0.4, ~39 for Apollo 15 basalts, and 30–32 for Apollo 11, 12, and 17 basalts, with the decreases in Zr/Hf broadly correlating with La/Yb. However, literature data for Apollo 15 KREEP basalts and the KREEP-rich Apollo 14 mare basalts exhibit little variation in Zr/Hf from 36 (Fig. 1), indicating the KREEP component did not result from a major fractionation of ilmenite and suggesting that the lunar core is probably metallic in overall composition [e.g., 12].

Are there distinct geochemical reservoirs in the Moon and is there evidence of garnet in the lunar interior? With volcanic glasses being unrelated to the mare basalts and derived from greater depths, compositional comparisons allow their source regions to be compared. Highly siderophile elements Au and Ir are more abundant in the glasses relative to the basalts (Fig. 2). As these elements are generally incompatible in silicate minerals, crystal fractionation experienced by the basalts will tend to increase the Au and Ir abundances. Therefore, the glasses may be derived from a source enriched in highly siderophile elements such as the platinum-group elements (PGEs) represented by Ir, relative to the source of the basalts. This observation can be accommodated with the basalts being derived from the LMO cumulates and the glasses derived from a source that represents "primitive Moon" that did not melt and, therefore, did not have its budget of PGEs and Au reduced through core formation.

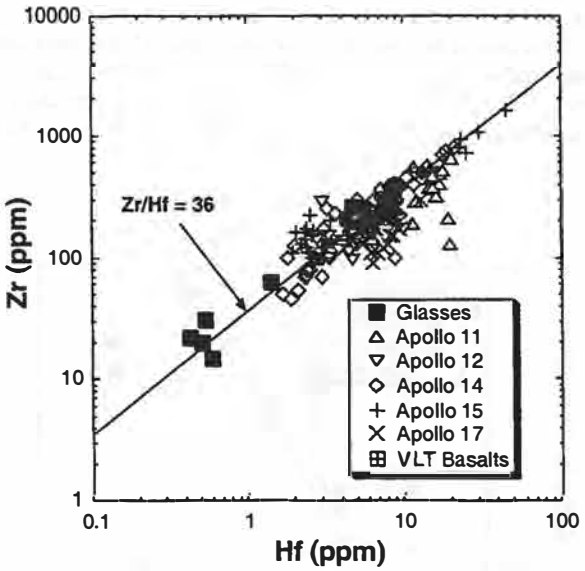

Fig. 1.

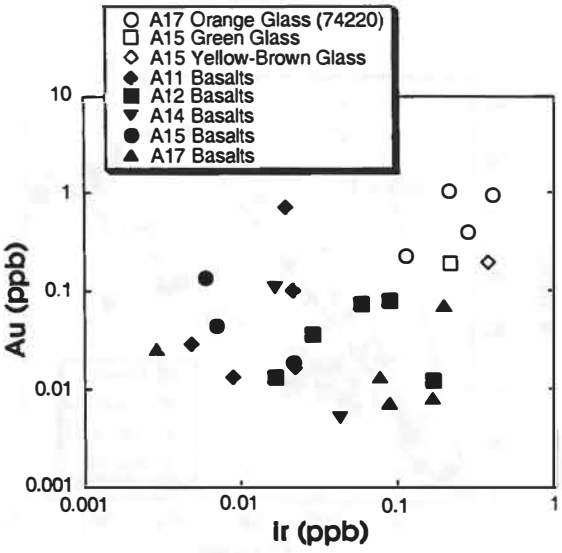

Fig. 2.

This can be tested by analyzing mare basalts and glasses for the PGEs. Although analytically challenging, the first PGE patterns in lunar samples were reported by [13] and demonstrated that the source regions for the different Apollo 12 basalts could not be differentiated on the basis of PGE budgets (Fig. 3), although the profiles are typical of silicate melts [e.g., 14]. Analysis of other trace-element data indicate that the high-field-strength elements can be used to differentiate between high- and low-Ti basalts. Also, the volcanic glasses were derived from a source with a higher Zr/Y ratio (Fig. 4) relative to the basalts, consistent with retention of garnet in the residue. If the glasses were derived from >400 km, garnet could be stable [see 15 and references therein]. It is concluded that the volcanic glasses were derived from a source that contained garnet, but escaped the melting that formed the LMO. The mare basalts were derived from the LMO cumulate pile.

What caused the formation of the lunar hotspot? Basaltic samples from Apollo 14 exhibit a range in ITE [e.g., 16–18]. They also exhibit a range of ages from 4.33 Ga to 3.96 Ga with the older basalts being KREEP-poor and the younger being KREEP-rich [e.g., 19–20].

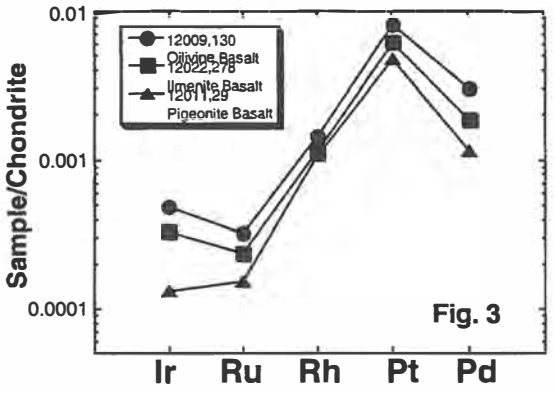

Fig. 3.

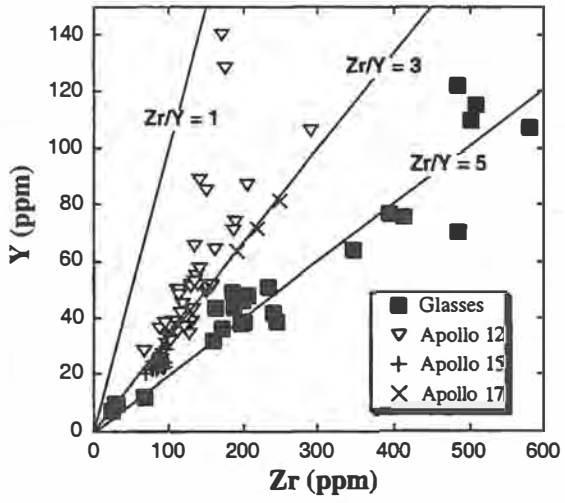

Fig. 4.

Prospector mapping has identified relatively high Th abundances in this area, suggesting a large KREEP component is present at or near the surface. LMO "layer cake models" have residual urKREEP sandwiched between the mafic cumulate mantle and the plagioclase flotation cumulate crust. However, late-stage cumulates and the residual liquid will be more dense that the early mafic cumulates resulting in gravitational instabilities and overturn of the cumulate pile [e.g., 21–23]. This could transport urKREEP to the base of the LMO cumulate pile, but above the glass source region. The effect of Earth on the symmetry of the Moon has displaced the low-density crust, producing a thicker crust on the farside [e.g., 24–25]. This has produced an offset of the center of mass for the Moon toward Earth. It is suggested that the gratitational forces of the Earth pooled the urKREEP beneath at the base of the LMO on the lunar nearside. Heating through radioactive decay produced thermal instabilities, resulting in a plume of hot, KREEPy material rising adiabatically beneath the Apollo 14 site. The oldest Apollo 14 basalts contain no evidence of a KREEPy component [cf. 26], suggesting diapiric rise of the KREEPy plume had not occurred at this time. However, by 4.1 Ga, isotopic and trace-element systematics of the Apollo 14 mare basalts reflect the inclusion of a KREEP component, which was more evident in those basalts erupted at 3.95 Ga [26].

References: [1] Smith et al. (1970) *Proc. Apollo 11 L SC,* 897. [2] Warren (1985) *Annu. Rev. Earth Planet. Sci., 13,* 201. [3] Taylor and Jakeš (1974) *Proc. LSC 5th,* 1287. [4] Delano (1986) *JGR, 91,* D201. [5] Longhi (1987) *JGR, 92,* E349. [6] Green et al. (1975) *Proc. LSC 6th,* 871. [7] Hess and Parmentier (1993) *LPS XXIV,* 651. [8] Hess and Parmentier (1994) *LPS XXV,* 541. [9] Hess and Parmentier (1995) *EPSL, 134,* 501. [10] McKay et al. (1986) *JGR, 91,* D229. [11] Hughes and Schmitt (1985) *JGR, 90,* D31. [12] Newsom (1984) *Eos Trans AGU, 65,* 369. [13] Neal et al. (1999) *LPS XXX,* Abstract #1003. [14] Barnes et al. (1985) *Chem. Geol., 53,* 303. [15] Taylor (1982) *Planetary Science: A Lunar Perspective,* 481 pp. [16] Dickinson et al. (1985) *JGR, 90,* C365. [17] Neal et al. (1988) *Proc. LPSC 18th,* 139. [18] Neal et al. (1989) *Proc. LPSC 19th,* 147. [19] Taylor et al. (1983) *EPSL, 66,* 33. [20] Dasch et al. (1987) *GCA, 51,* 3241. [21] Hughes et al. (1988) *GCA, 52,* 2379. [22] Snyder et al. (1992) *GCA, 56,* 3809. [23] Spera (1992) *GCA, 56,* 2253. [24] Kaula et al. (1972) *Proc. LSC 3rd,* 2189. [25] Kaula et al. (1974) *Proc. LSC 5th,* 3049. [26] Neal and Taylor (1990) *Proc. LPSC 20th,* 101.

ASYMMETRIC EVOLUTION OF THE MOON: A POSSIBLE CONSEQUENCE OF CHEMICAL DIFFERENTIATION.

E. M. Parmentier[1], S. Zhong[2], and P. C. Hess[1], [1]Department of Geological Sciences, Brown University, Providence RI 02912, USA, [2]Department of Earth, Atmospheric and Plantary Sciences, Massachusetts Institute of Technology, Cambridge MA 02139, USA.

Introduction: In its final stages of cystallization, a lunar magma ocean that creates the anorthositic crust will also precipitate ilmenite- and pyroxene-rich cumulates (IC). These cumulates will be significantly denser than earlier olivine-pyroxene cumulates (OPC), and buoyantly driven, thermally activated creep should allow them to sink into underlying cumulates. Since incompatible elements including heat-producing U and Th will also concentrate in the late-stage magma ocean liquids, the gravitational differentiation of the ilmenite cumulates has potentially significant chemical and thermal implica-

tions for the subsequent evolution of the Moon [1,2]. These include a deep, high-pressure origin for melts that may represent primitive mare basalt magmas [3] from source materials that should have crystallized at much shallower depths in the final stages of magma ocean solidification [cf. 2]. Transporting some fraction of heat-producing elements to depth and creating a stable chemical stratification that traps radiogenic heat in the deep interior may help to explain the existence of elastic lithosphere thick enough to support mascons [cf. 4–5] and the retention of heat needed to reduce the amount of global contraction due to cooling [6].

Hemispheric Asymmetries: The hemispheric asymmetry of surface distribution of mare basalts [cf. 7] is also fundamental to understanding the evolution of the Moon. The apparent correlation between mare and surface elevation had prompted the idea that mare basalt flooded topographically low areas. However, Clementine topographic data [8] indicate that while mare basalts clearly fill low areas, large areas of low elevation do not contain mare basalt. A possible explanation for the distribution is that it arises from the hydrodynamic instability of a chemically dense IC core or layer that becomes buoyant as is heated by radioactivity [13].

A radial distribution of Th around the Imbrium Basin is another important aspect of lunar asymmetry that may be explained by the excavation of a KREEP-rich layer from beneath a region of the Moon surrounding Imbrium [9,10]. Other large basins do not appear to excavate comparable amounts of Th-rich material. High Th also occurs in the basalts of Mare Procellarum, leading to the suggestion KREEP is preferentially concentrated beneath this region of the surface [9,11].

The existence of relatively shallow concentrations of KREEP and the later eruption of mare basalts in the same region of the Moon suggests a causal connection. Gravitational instability of the mixed layer as a single downwelling might explain this asymmetry [2]. If this downwelling formed prior to the complete solidification of the magma ocean, the residual liquid layer would deepen above the downwelling. This would draw residual liquid toward the downwelling and may explain a high concentration of KREEP-rich materials in the Procellarum region. After sufficient time for expansion due to heating, the buoyant rise of previously downwelled, IC-rich mantle could then account for the presence of mare basalts in this same region.

Fluid Dynamics of Differentiation: For an IC layer only 20–30 km thick, it is remarkable that such a large-scale downwelling would develop. As the final stages of magma-ocean solidification proceed, we envision that dense IC solids will collect at the bottom of the residual liquid layer and sink into the underlying OPC. This will create a mixed layer of IC and OPC that is denser than the underlying OPC. Gravitational instability of this mixed layer, if it is substantially thicker than a pure IC layer, may then account for the long wavelength downwelling needed to explain the observed asymmetries [2].

We have previously estimated the size of the sinking IC bodies, how deep they sink over the time that IC solidifies, and the scale of gravitational instability of the mixed OPC and IC layer thus created [2,10]. We find that the thickness of the mixed layer is independent of the rate of IC solidification. It is proportional to the thickness that an IC layer would have if no instability occurred and depends but only weakly on the ratio of the IC and OPC viscosities. We find a mixed layer that is about 5× the thickness of IC alone, and which therefore contains ~20% IC. It is thus denser than underlying OPC and gravitationally unstable.

The size of IC bodies in the mixed layer is, however, proportional to the square root of the IC solidification rate. This is important for understanding the physical character of the chemically heterogeneous source of mare basalts [1].

The wavelength of mixed-layer instability is examined on the basis of a simple model of Rayleigh-Taylor (RT) instability of a dense layer with viscosity m_{layer} surrounding a viscous sphere of lower density and different viscosity $m_{interior}$. The radius of the sphere and surrounding denser layer corresponds to the radius of the Moon. The RT growth time for a range of wavelength (spherical harmonic degree) are shown in Fig. 1 for a layer thickness of 100 km, a mixed-layer density corresponding to 20% IC [2], $m_{interior} = 10^{21}$ Pa-s, and a range of $m_{layer}/m_{interior}$ values. If $m_{layer}/m_{interior}$ is less than ~10^{-3}, spherical harmonic degree 1 grows more rapidly than the shorter-wavelength, higher-spherical harmonic degrees. Thus, in further assessing this model we need to undestand the conditions for which OPC just beneath the IC layer will have a viscosity sufficiently lower than that of OPC at greater depth.

The RT growth time, approximating the time for a downwelling to form, is proportional to $m_{interior}$. Even for $m_{interior}$ as high as 10^{22} Pa-s, a downwelling could form in times on the order of 10 m.y., which may be short compared to that required for the final stages of magma-ocean solidification. Note that this introduces a complication to the simple model above, which assumes that the mixed layer is already formed as the large-scale downwelling develops.

Further Implications for Lunar Evolution: This model also makes predictions for the geochemical heterogeneity of the Moon. Chemical fractionations that occur during the solidification of IC will influence not only the concentration of heat-producing elements that it contains [12], but also the subsequent isotopic evolution of the mare basalt source. It is important to understand if the predictions of this model are consistent with observed geochemical signatures.

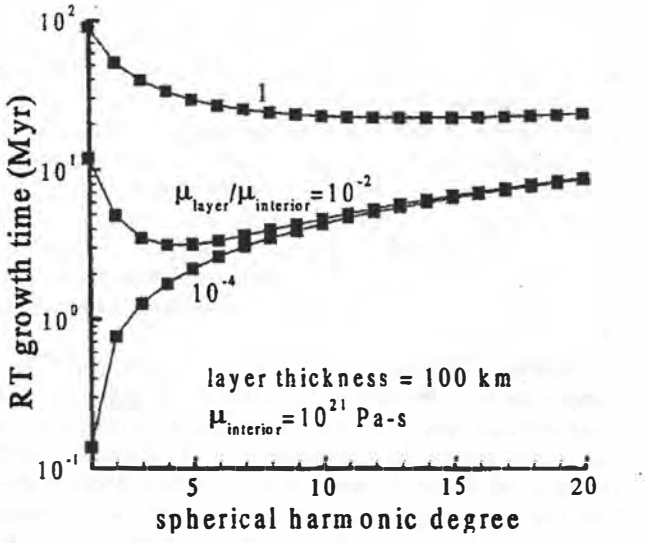

Fig. 1. Rayleigh-Taylor growth time as a function of spherical harmonic degree for a dense layer 100 km thick with viscosity m_{layer} at the outer surface of a 1600-km radius sphere with viscosity $m_{interior}$. For $m_{layer}/m_{interior}$ less than about 10^{-3}, spherical harmonic degree 1 is the fastest growing mode of buoyant instability.

References: [1] Ringwood A. E. and Kesson S. E. (1976) *Proc. LPSC 7th,* 1697. [2] Hess P. C. and Parmentier E. M. (1995) *EPSL, 134,* 501. [3] Delano J. W. (1986) *JGR, 91,* 201. [4] Parmentier E. M. and Hess P. C. (1998) *LPS XXIX,* Abstract #1182. [5] Alley K. M. and Parmentier E. M. (1998) *PEPI, 108,* 15. [6] Solomon S. C. and Chaiken J. (1976) *Proc. LPSC 7th,* 3229. [7] Lucey P. G. et al. (1998) *JGR, 103,* 3679. [8] Zuber M. T. et al. (1994) *Science, 266,* 1839. [9] Haskin L. A. et al. (1999) *LPS XXX,* Abstract #1858. [10] Haskin L. (1998) *JGR, 103,* 1679. [11] Lawrence D. et al. (1998) *Science, 281,* 1484. [12] Parmentier E. M. and Hess P. C. (1999) *LPS XXX,* Abstract #1289. [13] Zhong S. et al. (1999) *LPS XXX,* Abstract #1789.

THE DISTRIBUTION OF ANORTHOSITE ON THE LUNAR FARSIDE. C. A. Peterson[1], B. R. Hawke[1], P. G. Lucey[1], G. J. Taylor[1], D. T. Blewett[1], and P. D. Spudis[2], [1]Hawai'i Institute of Geophysics and Planetology, University of Hawai'i, Honolulu HI 96822, USA, [2]Lunar and Planetary Institute, Houston TX 77058, USA.

Introduction: There is much evidence to support the hypothesis that a giant impact on early Earth created the Moon and that a magma ocean was present on the young Moon [e.g., 1–2]. As the magma cooled and crystallized, plagioclase flotation could have produced the upper part of the Moon's original crust. But how much of this original crust has survived to the present? Has it been entirely disrupted, or do portions remain relatively unchanged? Remote sensing studies of the lunar highlands, combined with analysis of lunar materials returned from known locations on the surface of the Moon, have allowed the determination of the lithologies present in many locations on the Moon. Our study of the distribution of the various lunar-highland rock types has revealed large-scale patterns that suggest the broad outlines of the evolution of portions of the lunar crust.

Our previous efforts have used Earth-based spectra and Galileo SSI to study the lunar nearside. We have used Clementine UV-VIS data to extend our studies of the lunar highlands to the farside. Calibration of the Clementine UV-VIS data is essentially complete, and FeO and TiO_2 values derived from the Clementine data have been derived from this well-calibrated data. In addition, Lunar Prospector data are now available in preliminary form and can add to our understanding of the composition of highlands units on the farside. We can use this combined dataset to (1) study the composition of farside highlands units; (2) identify and determine the distribution of anorthosite on the lunar farside; and (3) investigate the stratigraphy of the farside crust.

Method: The great majority of the Moon's highlands surface is composed of only a few minerals, and these are easily distinguishable using reflection spectroscopy at wavelengths from the UV through visible light and into the near infrared [e.g., 3]. The mafic minerals pyroxene and olivine contain Fe that causes the minerals to absorb light with a wavelength near 1 μm. In contrast, plagioclase feldspar does not absorb light near 1 μm, although plagioclase can show absorption of light near 1.25 μm if it has not been highly shocked by impacts.

Through the use of Earth-based telescopic reflectance spectra, it is possible to determine the lithologies present in the area observed, typically from 2 to 6 km in diameter. The Galileo and Clementine spacecraft returned multispectral images of the Moon that, while of lower spectral resolution than Earth-based spot spectra, covered large areas of the Moon and used filters at wavelengths useful for determining the lithologies present. These spacecraft data have also been used to determine the abundance of FeO and TiO_2 present in lunar surface materials. Other products, such as band-ratio maps, have been produced, and spectra have been extracted from co-registered image cubes.

Lunar Prospector has collected a large quantity of γ-ray and neutron spectrometer data. While much of the data will require further processing before reliable quantitative interpretations can be made, some data from that mission have already been made available. In particular, the γ-ray spectrometer counting data for Th, K, and Fe [4] can be used to confirm and extend our knowledge of the composition of the lunar farside crust. A preliminary Th distribution map has been produced from the raw data by utilizing ground truth from the lunar landing sites [5].

Results: Noritic anorthosite and anorthositic norite are the predominant rocktypes at the surface of the nearside lunar highlands. Lesser amounts of anorthosite, norite, troctolite, and gabbroic rocks are also present [2]. Studies of Earth-based reflectance spectra initially revealed the presence of anorthosite in isolated outcrops extending in a narrow band from the Inner Rook mountains in the west to the crater Petavius in the east [e.g., 6]. More recently, additional outcrops of anorthosite have been identified in the central peaks of some craters, such as Aristarchus, and in the northern and northeastern nearside [7,8]. In most cases, these anorthosite deposits have been exposed by impacts that removed a more mafic overburden and raised them to the surface from deeper in the crust, for example in the peak rings of the Orientale, Humorum, and Grimaldi Basins [9–11]. Much of the nearside lunar highlands likely shares this stratigraphic sequence: a layer of pure anorthosite overlies a more mafic lower crust and is in tum overlain by a somewhat more mafic layer. Much anorthosite likely remains hidden by this surface layer on the nearside today.

On the lunar farside, the giant South Pole Aitken (SPA) Basin shows a mafic anomaly that is the dominant compositional feature on the farside. At 2500 km in diameter, SPA (centered at 55°S, 180°E) is the largest unambiguously identified impact basin in the solar system. It is also the oldest identified lunar basin except possibly for Procellarum. There is a 13-km difference in elevation from the interior of the basin to the surrounding highlands[12]. The interior exhibits a 7–10% FeO enrichment relative to the surrounding highlands, and portions of the interior exhibit enhanced TiO_2 values [13]. Portions of the interior also display elevated Th and K abundances.

The high-FeO values found inside SPA drop off with increasing distance to the north of the basin. The region between 100°E and 100°W and between 40°N and 70°N exhibits very low values of FeO and TiO_2. The new Lunar Prospector data show very low-Th and-K abundances there as well. FeO maps produced from high spatial resolution Clementine data reveal extremely low FeO values near the crater Fowler (43° N, 145° W) in the vicinity of the Coulomb-Sarton Basin. We interpret these data as indicating a region in which pure anorthosite is dominant. Many areas in this region appear to contain nothing but anorthosite.

Between SPA and the far north, the data generally indicate intermediate FeO values and low Th values. However, some lower-FeO values can be found in this intermediate region. In particular, very low FeO values are exhibited in the inner rings of the Hertzsprung and Korolev Basins. This case parallels the situation at nearside

basins, where anorthosite was exposed from beneath more mafic material.

Discussion: The striking difference between the distribution of lithologic types on the lunar nearside and that on the farside appears to be largely attributable to the enormous SPA impact event. Huge quantities of ejecta would have been deposited outside the basin, thickest near the basin rim and tapering off with increasing distance from the basin. This ejecta, especially that deposited nearest the basin rim, must have contained much material from the lower crust and possibly even some mantle material. If the original plagioclase flotation crust was largely intact at the time of the SPA impact event, the great thickness of more mafic ejecta deposited near the basin could have insulated that original upper crustal material (anorthosite) from all but the largest subsequent cratering events. Large impacts, such as those that produced the Orientale, Hertzsprung, and Korolev Basins, could have penetrated through the SPA ejecta deeply enough to expose anorthosite in their peak rings. Farther to the north, where the thickness of ejecta from SPA was much less, small basins such as Birkhoff and Coulomb-Sarton could have removed most of the overburden of SPA ejecta to reveal the underlying anorthosite crust.

If this scenario is accurate, it has great implications for the geologic history of the Moon. It is conceivable that large numbers of very large impacts preceded the SPA event and are not seen today simply because evidence of them has been erased by subsequent impacts. However, that possibility is argued against if most of the original plagioclase flotation crust was still present on the lunar farside at the time of the SPA impact event. This has important bearing on the question of the flux of large impactors during the early history of the inner solar system.

The Lunar Prospector data must be further calibrated and reduced, but the preliminary results have already added greatly to our understanding of the Moon. It is encouraging that groundbased data, Clementine data, and Lunar Prospector data are providing a consistent picture of the composition of the lunar surface. The complementary nature of the datasets enhances the value of each set. We eagerly await the additional insight that may be provided by the full set of Lunar Prospector data.

References: [1] Hartmann W. K. et al., eds. (1986) *Origin of the Moon,* LPI. [2] Heiken G. H. etal., eds. (1991) *Lunar Sourcebook,* Cambridge Univ. [3] Pieters C. M. and Englert P. A. J., eds. (1993) *Remote Geochemical Analysis,* Cambridge Univ. [4] Lawrence D. J. et al. (1998) *Science, 281,* 1484. [5] Gillis J. J. et al. (1999) *LPS XXX,* Abstract #1699. [6] Hawke B. R. et al. (1992) *LPS XXIII,* 505. [7] Tompkins S. and and Pieters C. M. (1999) *MAPS,* in press. [8] Spudis P. D. et al. (1997) *LPS XXVII,* 1361. [9] Hawke B. R. et al. (1991) *GRL, 18,* 2141. [10] Hawke B. R. et al. (1993) *GRL, 20,* 419. [11] Peterson C. A. et al. (1995) *GRL, 22,* 3055. [12] Spudis P. D. et al., *Science, 266,* 1848. [13] Blewett D. T. et al. (1999) *LPS XXX,* Abstract #1438.

THE MOON AS A SPECTRAL CALIBRATION STANDARD ENABLED BY LUNAR SAMPLES: THE CLEMENTINE EXAMPLE.

C. M. Pieters, Department of Geological Sciences, Brown University, Providence RI 02912, USA.

Spectral calibration of Clementine data relies on the Apollo 16 site and laboratory measurements of mature soil 62231. The process produces calibrated spectral reflectance factors.

What color is the Moon? A reflectance spectrum is essentially a measure of how much radiation incident on a surface (solar radiation) is reflected and how much is absorbed at each wavelength. To the eye the Moon is gray-white, but to photoelectric instruments it is various shades of red — that is, it exhibits an increase in brightness with wavelength. In the near-infrared there are absorptions diagnostic of minerals superimposed on the Moon's redness. For the Moon and other rocky bodies such as asteroids, most of the detectable absorptions arise from ferrous iron in various crystallographic sites. The wavelength, shape, and strength of these absorptions identify the minerals present, and allow their abundances to be estimated.

Accurately measuring these diagnostic mineral absorptions with remote detectors requires not only a quality instrument, but also excellent electronic calibration and either direct measurement of the light source (the Sun) or a proxy, or a well-known reference standard illuminated by the same light source. In the laboratory a white reference such as halon (or commercial Spectralon), is used which in turn has been extensively calibrated relative to a known radiance.

In space, or at the telescope, a separate reference must be found to mimic solar radiation and to eliminate instrumental and atmospheric effects. Radiation from stars to a first order follows a black body spectral curve with multiple emission and absorption lines superimposed. Because stellar lines vary with spectral type, and very few stars are really solarlike, it is actually quite difficult to use stars as spectral standards.

The Moon is a nearby atmosphereless body that reflects solar radiation. Because the Moon's surface itself does not change with time (at least within our lifetimes), it provides an excellent reference standard. The calibration challenge then reduces to identifying an area on the Moon whose measurable properties are exceptionally well known. The return of lunar samples allows their properties to be measured accurately in Earth-based laboratories. Since the samples were collected from known areas on the surface of the Moon, carefully selected samples can be used to represent the properties of that area.

For Clementine data, the Apollo 16 site was chosen as a calibration target because it is a relatively homogeneous area with no nearby units of a significantly different material. Since all remote data are acquired as bidirectional reflectance, we use i = 30°, e = 0° as the standard geometry. The calibration steps used and the assumptions made are discussed briefly below.

The absolute spectral calibration procedures for Clementine data include the following steps (see Table 1 for an estimation of errors):

(a) Select Apollo 16 site calibration standard target: a 12×33 pixel area to the west of the landing site free of crater rays.
(b) Select mature soil representative of the Apollo 16 site: 62231.
(c) Obtain bidirectional spectral reflectance measurement of 62231, $R_{62231}(\lambda,i,e)$, at standard geometry (i = 30, e = 0):
  (c1) measure brightness of 62231 relative to Halon: $B_{62231}(\lambda,30,0)$;
  (c2) obtain/derive correction for Halon reference standard: $R_h(\lambda)$;
  (c3) $R_{62231}(\lambda,30,0)=B_{62231}(\lambda,30,0)*R_h(\lambda)$; an average spectrum is shown in Fig. 1.
(d) Translate 62231 laboratory spectrum into Clementine 5-filter spectrum to obtain Apollo 16 "ground truth" data for Clementine filters, $R_{62231C}(\lambda, 30,0)$:
  (d1) obtain effective Clementine filter transmission curves, F(l);
  (dl 1) measure the transmission curve of each filter: $f(\lambda)$;
  (d12) estimate the solar spectrum: $S(\lambda)$;

(d13) estimate detector sensitivity: $D(\lambda)$;

(d14) $F(\lambda)=f(\lambda)*S(\lambda)*D(\lambda)*$normalization.

(d2) $R_{62231C}(\lambda, 30,0)=R_{62231}(\lambda, 30, 0) * F(\lambda)$. Clementine filters are shown in Fig. 2 and reflectance values are listed in Table 2.

(e) Correct Clementine DN values for all gain, offset, and flat field corrections (including row, column, and temperature-dependent variables) [1–2]: $DN_{Clem}(l,i,e)$.

(f) Photometrically calibrate Clementine DN values to i=30, e=0 [1] (the Moon is redder at larger phase angles): $DN_{PClem}(\lambda,30,0)= DN_{Clem}(\lambda,i,e)*Cphot\ (\lambda,i,\ e)$.

(g) Derive spectral calibration correction factor $Cr(\lambda)$ using the laboratory data for soil 62231 and the Clementine calibrated DN measurement of the Apollo 16 site: $Cr(\lambda)=R_{62231C}(\lambda,30,0)/ DN_{PClemAp16}(\lambda,30,0)$.

(h) Derive absolute Clementine *reflectance factor*# data R(l, 30, 0) for any lunar area: $R(\lambda, 30, 0)=DN_{PClem}(\lambda,30,0)*Cr(\lambda)$ *#reflectance factor* [3] = reflectance relative to a Lambertian surface under the same illumination. (Same as reflectance coefficient [3] and radiance coefficient [4], but *not* to be confused with radiance factor, which is reflectance relative to a Lambertian surface illuminated at i = 0 [3–4]).

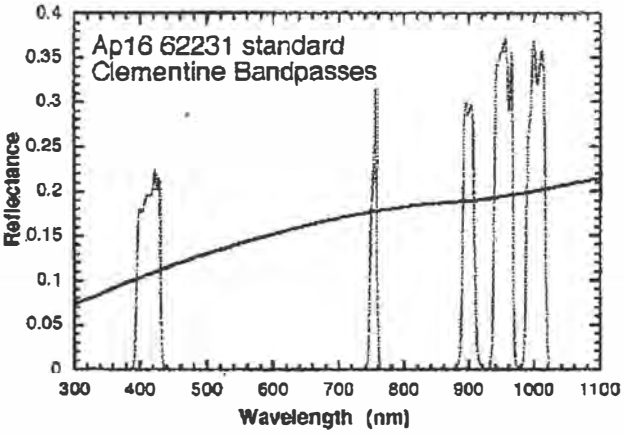

Fig. 2. Average bidirectional spectrum for 62231 used as a calibration standard. Ultraviolet-visible Clementine bandpasses are superimposed.

TABLE 1. Estimated value for sources of error.

$B_{62231}(\lambda,30,0)$	1%	Repeatability of laboratory measurements (absolute)
$R_h(\lambda)$	<0.5%	Accuracy of halon spectral correction (largely NBS)
$f(\lambda)$	N/A	Measurement accuracy of filter transmission
$S(\lambda)$	<<1%	Black body estimation for solar flux
$D(\lambda)$	N/A	Detector responsivity estimation
$DN_{Clem}(\lambda)$	1%	Calibrated Clementine DN values [1–2]
$DN_{ClemAp16}(\lambda)$	<1%	Variation within site representing Apollo 16
Cphot (λ,i, e)	1%	Photometric model [1]

TABLE 2. Spectrum for Apollo 16 soil 62231 resampled at Clementine UV-VIS wavelengths.

Effective Wavelength (nm)	$R_{62231C}(\lambda, 30,0)$
414.9	0.1077
753.3	0.1776
898.8	0.1893
951.5	0.1941
1000.4	0.2004

These values are used in the final U.S. Geological Survey Clementine mosaics.

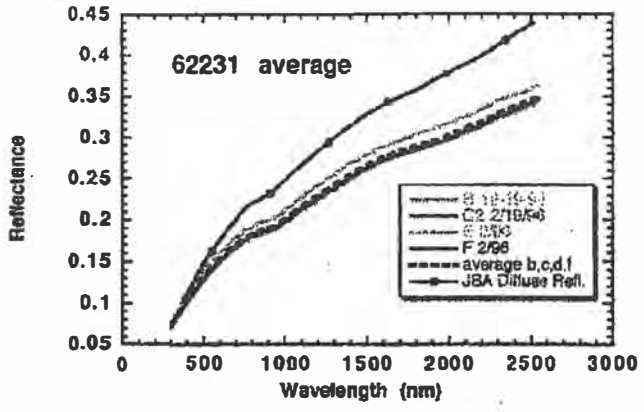

Fig. 1. Reflectance spectra for Apollo 16 soil 62231. Several bidirectional spectra taken at i = 30°, e = 0° are averaged. The previous "diffuse" (directional hemispheric) spectrum by J. Adams is shown for comparison.

These calibrations require several assumptions:

(1) *A mature soil represents the properties of the site seen remotely under the same viewing conditions.* This appears to be valid as long as regolith has been allowed to develop and there are no nearby fresh craters.

(2) *62231 is representative of mature Apollo 16 soils.* Spectra of several other Apollo 16 soils with comparable maturity all look similar to 62231; deviations are on the same magnitude as repeatability of individual measurements.

(3) *Non-Lambertian properties of Halon are insignificant at i = 30, e = 0.* Any deviation would be a small scalar correction.

(4) *The detector response properties used in calibration are invariant over the two-month period of measurements.* There is no guarantee that this is true, but no systematic month-to-month variations are detected that are not photometric errors.

(5) *Contribution from Clementine scattered light is compensated through in-flight measurements and calibration procedures.* There is also no guarantee that this is true, but no effects of scattered light have been able to be demonstrated in spectral analyses.

References: [1] McEwen (1996) *LPS XXVII,* 841; McEwen et al. (1998) *LPS XXIX,* Abstract #1466. [2] Pieters et al. (1996) www.planetary.brown.edu/ clementine/calibration.html. [3] Hapke B. (1993) Cambridge Univ. [4] Hapke B. (1981) *JGR, 86,* 3039.

REGIONAL DARK MANTLE DEPOSITS ON THE MOON: RIMA BODE AND SINUS AESTUUM ANALSYSIS.

S. Pinori and G. Bellucci, Consiglio Nazionale Ricerche/Instituto di Fisica dello Spazio Interplanetario, Area di Ricerca di Tor Vergata, Via del Fosso del Cavaliere 100, 00133 Roma, Italy (Sabrina.Pinori@ifsi.rm.cnr.it).

Introduction: Regional pyroclastic deposits on the Moon usually are located on mare basins borders, blanketing adjacent highlands [1–2].

We present the study of two Dark Mantle Deposits (DMD): Rima Bode and Sinus Aestuum. The statistical approach allows us to identify not only the dark mantle terrain, but also some areas spectrally different from the DMD that we have interpreted as a mixing of DMD and the neighboring soils.

Instrument and Data Analysis: The data (Table 1) have been obtained at the 1.5-m telescope of Sierra Nevada Observatory (Granada, Spain) using an imaging spectrometer working in the 0.4–1.0-μm spectral range, corresponding to 96 spectral bands.

The spectra have been normalized to Mare Serenitatis (MS2) average spectrum, a standard area centered at 21° 25' E, 18° 40' N [3].

Two different statistical procedures have been employed to analyze the two regions and to discriminate between the different geologic units, the Pixel Purity Index (PPI) and the Spectral Angle Mapper (SAM).

The PPI is a method of finding the most "spectrally pure," or extreme, spectra in multispectral images [4]. The PPI is computed by repeatedly projecting n-dimensional scatter plot onto a random unit vector. The extreme pixels in each projection are recorded and the total number of times each pixel is marked as extreme is noted. In this way it is possible to create a PPI image in which the DN of each pixel corresponds to the number of times that pixel has been recorded as extreme (see Fig. 1a and 1b).

The SAM is a method for comparing the image spectra to a set of spectra chosen as a *priori* end members [5–6]. The algorithm determines the similarity between two spectra by calculating the "spectral angle" between them, treating them as vectors in a space with dimensionality equal to the number of bands. For each reference spectrum chosen, the spectral angle is determined for each pixel and the final classification image shows a map where pixels of the same color represent regions of similar composition (see Fig. 2a and 2b). The DMD borders, obtained from the 0.7-μm albedo image, are overlapped on the maps.

Identification of Mixing Areas: Our analysis is devoted to the study of the relationship between the DMD and the adjacent terrain in order to better understand the spectral properties of the different terrain present in the area. The PPI procedures point up the spectral variability of the region and the DMD are clearly identified as "pure" or more extreme spectra. Both the DMDs present the highest values of the images (white and violet areas ranging from 200 to 400 DN) while the adjacent zones present intermediate values (red areas ranging from 100 to 200 DN). The maria and highlands present in the images have been classified as green areas (ranging from 0 to 100 DN). (To view Figs. 1 and 2 in color, go to http://cass.jsc.nasa.gov/meetings/moon99/pdf/8019.pdf.)

Rima Bode deposit presents a narrow and long shape and an extensive red area, while the Sinus Aestuum dark mantle deposit is heart shaped and shows a not vast red area. Rima Bode deposit (Fig. 1a) is more homogeneous than Sinus Aestuum, where some patches (white areas) corresponding to the more extreme spectra are present.

Using the analysis the PPI image, we have chosen five different end members for each region to apply the SAM procedure. The results are shown in Fig. 2, and in Fig. 3 the mean spectra of the DMD and the mixing areas classes are presented .

TABLE 1. Characteristics of the datasets.

Lunar region	Date	Time (U.T.)	Coordinates
Rima Bode	March 19, 1997	20:58	3°W 13'N
Sinus Aestuum	December 7, 1998	01:26	7°W 5'N

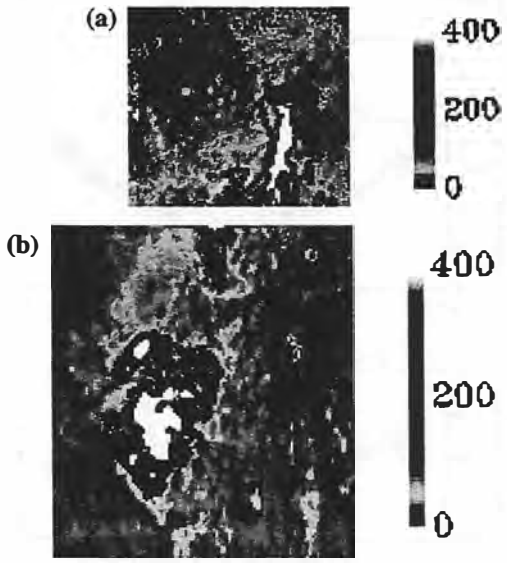

Fig 1. Pixel Purity Index results for (a) Rima Bodeand and (b) Sinuus Aestum regions.

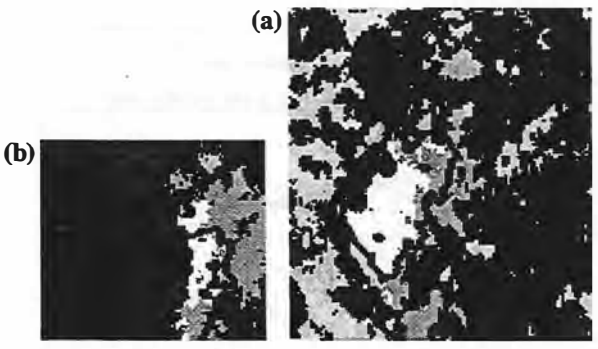

Fig. 2. Classification map obtained from the Spectral Angle Mapper technique: (a) Rima Bode deposit, (b) Sinus Aestuum deposit.

On the basis of the spectra and of the position we identify the red class as highland, the blue class as mare, the yellow class as pure DMD, and the cyan class as crater ejecta. The last two classes, the green and the sea-green, have been interpreted as mixing soils of pyroclastic products and highland, the green one, and DMD and mare the sea-green.

Sinus Aestuum mean DMD spectrum shows a deep absorption band with the minimum at 0.7 μm in the visible range and symmetrical wings at the extremes. Rima Bode DMD spectrum presents less absorption in the visible and a lower NIR-VIS value. The difference suggests an effective distinct mineralogical composition: The Sinus Aestuum deposit could be dominated by crystallized beads, while Rima Bode could be a mixing of volcanic glasses and black beads.

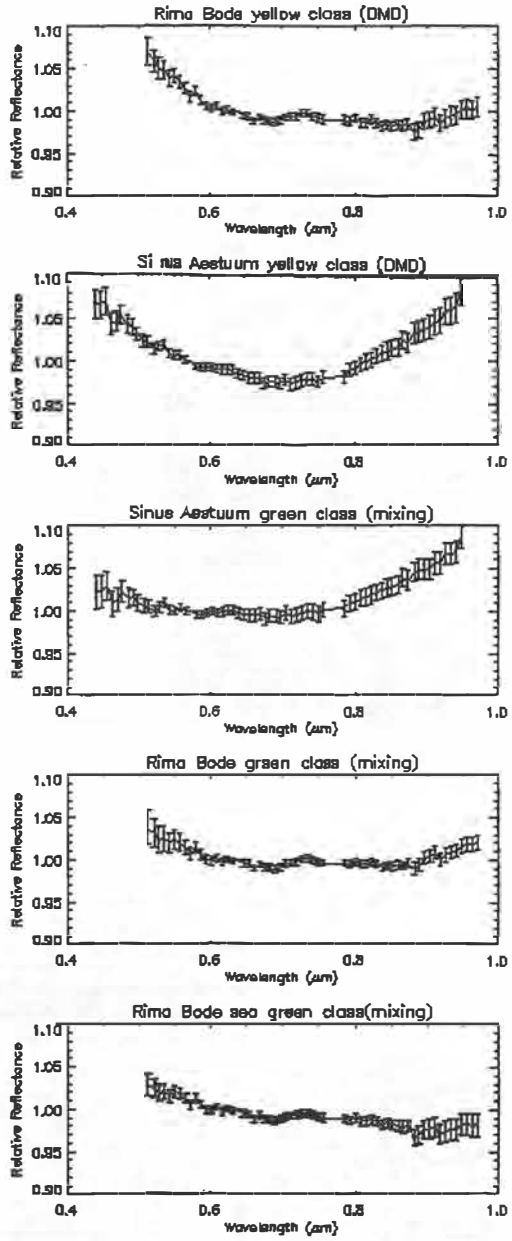

Fig. 3. Mean spectra (normalized to 1 at 0.56 μm) of the classes obtained by using the SAM classification.

We expect that DMDs mixed with the highland soils show a decrease in the UV-VIS slope [2]. This effect is visible in both the spectra corresponding to the green areas.

The analysis points up the presence of another mixing area (the sea-green color in Fig. 2a) in the Rima Bode region between DMD and the mare. The mean spectrum of this class shows a negative slope.

Conclusions: The new statistical techniques allow us to identify some mixing areas with mare or highland soils. These regions are spectrally distinct from the DMDs and can help us to better understand the possible evolution of the eruptions that led to the deposits emplacement.

References: [1] Gaddis L. R. et al. (1985) *Icarus, 61,* 461–489. [2] Weitz et al. (1998) *JGR, 103,* 22725–22759. [3] McCord T. B. et al. (1972) *JGR, 77,* 1349–1359. [4] Boardmann J. W. et al. (1995) *Fifth JPL Airborne Earth Science Workshop, JPL Publ. 95-1, 1,* 23–26. [5] Yuhas F. A. and Goetz A. F. H. (1993) *Proc. 9th Thematic Conf. on Geologic Remote Sensing,* 503–511. [6] Kruse et al. (1993) *Remote Sensing of Environment, 44,* 145–163.

LUNAR ELEMENTAL ABUNDANCES FROM GAMMA-RAY AND NEUTRON MEASUREMENTS.

R. C. Reedy[1] and D. T. Vaniman[2], [1]Mail Stop D436, Los Alamos National Laboratory, Los Alamos NM 87545, USA (rreedy@lanl.gov), [2]Mail Stop D462, Los Alamos National Laboratory, Los Alamos NM 87545, USA (vaniman@lanl.gov).

Introduction: The determination of elemental abundances is one of the highest science objectives of most lunar missions. Such multi-element abundances, ratios, or maps should include results for elements that are diagnostic or important in lunar processes, including heat-producing elements (such as K and Th), important incompatible elements (Th and rare earth elements), H (for polar deposits and regolith maturity), and key variable elements in major lunar provinces (such as Fe and Ti in the maria). Both neutron and γ-ray spectroscopy can be used to infer elemental abundances; the two complement each other.

These elemental abundances need to be determined with high accuracy and precision from measurements such as those made by the γ-ray spectrometer (GRS) [1] and neutron spectrometers (NS) [2] on Lunar Prospector. As presented here, a series of steps, computer codes, and nuclear databases are needed to properly convert the raw γ-ray and neutron measurements into good elemental abundances, ratios, and/or maps.

Lunar Neutron Spectroscopy: Lunar Prospector (LP) is the first planetary mission that has measured neutrons escaping from a planet other than the Earth [2]. The neutron spectrometers on Lunar Prospector measured a wide range of neutron energies. The ability to measure neutrons with thermal ($E < 0.1$ eV), epithermal ($E \sim 0.1$–1000 eV), and fast (E~0.1–10 MeV) energies maximizes the scientific return, being especially sensitive to both H (using epithermal neutrons) and thermal-neutron-absorbing elements [3].

Neutrons are made in the lunar surface by the interaction of galactic-cosmic-ray (GCR) particles with the atomic nuclei in the surface. Most neutrons are produced with energies above ~0.1 MeV. The flux of fast neutrons in and escaping from the Moon depends on the intensity of the cosmic rays (which vary with solar activity) and the elemental composition of the surface. Variations in the elemental

composition of the lunar surface can affect the flux of fast neutrons by ~25% [2,4], with Ti and Fe emitting more fast neutrons than light elements like O and Si.

Most elements moderate neutrons to thermal energies at similar rates. The main exception is when neutrons scatter from H, in which case neutrons can be rapidly thermalized [3].

The cross sections for the absorption of thermal neutrons can vary widely among elements, with major elements like Ti and Fe having high-capture cross sections. Some trace elements, such as Sm and Gd, have such large neutron-absorption cross sections that, despite their low abundances, can absorb significant amounts of thermal neutrons in the Moon [5].

Because the processes affecting neutrons are complicated, good modeling is needed to properly extract elemental information from measured neutron fluxes. The LAHET Code System (LCS) can be use to calculate neutron fluxes from GCR interactions in the Moon [4].

Lunar Gamma-Ray Spectroscopy: The main sources of planetary γ-rays are the decay of the naturally occurring radioactive isotopes of K, Th, and U and the interactions of GCRs with atomic nuclei in the planet's surface. Most "cosmogenic" γ-rays are produced by fast and thermal neutrons made in the planet's surface by GCRs, and their production rates can vary with time. Over 300 γ-ray lines have been identified that can be emitted from planetary surfaces by a variety of production mechanisms [5]. There exist nuclear databases that can be used to identify and quantify other γ-ray lines. Use will be made of γ-rays from major elements, particularly those from Si and O, that have not been routinely used in the past.

The fluxes of γ-rays from a given element can vary depending on many factors besides the concentration of that element. For example, the fluxes of neutron-capture γ-rays in the planetary region of interest depend on (1) the total cross section for elements to absorb thermalized neutrons [5] and (2) the H content of the top meter of the surface [e.g., 3]. The fluxes of the fast neutrons that induce inelastic-scattering and other nonelastic-scattering reactions can vary with the composition of the surface [4].

Data Analysis: There are several key steps in preparing γ-ray data into a form from which accurate elemental abundances can be determined. One needs to identify, quantify, and remove or correct for all backgrounds in the γ-ray spectra. Among the more important of these backgrounds are features made by the decay of radioactivities made in the GRS by cosmic-ray particles and the prompt and decay γ-rays emitted from the material surrounding the active elements of the LP GRS and from the LP spacecraft. Gamma-ray spectra obtained during the cruise to the Moon or those measured while LP was at various distances from the Moon can be used to distinguish features in the γ-ray spectra that are from the Moon and those that are made on the LP spacecraft.

Each background-corrected spectrum will be analyzed with existing γ-ray spectral-unfolding codes to identify the energies and intensities of all peaks. These peaks will be examined when there are potential interferences in the analysis of a given γ-ray line [5]. Such interferences could be a problem for determining Mg and Al using some of their inelastic-scattering γ-rays, such as the 1.369-MeV γ-ray from Mg that is also readily made from Al and Si.

The key data needed to get elemental abundances from the fluxes of γ-rays in the processed spectra are good values for the fluxes of γ-rays that should be emitted from a given region for known or nominal elemental abundances. Such flux determinations were done for analysis of the Apollo γ-ray data [5]. The codes to do such calculations and the nuclear data used in such calculations have been improved much since then.

Since about 1990, improved computer codes, such as LCS [4], that numerically simulate the interactions of GCR particles with matter have been developed at Los Alamos. These codes have been well tested using measurements from lunar samples and meteorites and at accelerators. The output from LCS includes the fluxes of protons and neutrons as a function of depth in the Moon and the fluxes escaping from the Moon. These particles produce the nonelastic-scattering γ-rays. LCS can also calculate the rates for the capture of thermal neutrons by various elements.

These LCS-calculated particle fluxes or capture rates need to be converted into production rates for the γ-rays of interest as a function of depth in the Moon's surface using several sets of nuclear data, such as cross sections for nonelastic-scattering reactions or γ-ray yields for neutron-capture reactions. The fractions of these γ-rays that escape into space without undergoing an interaction will then be calculated to give the expected fluxes of γ-rays at the LP GRS.

Preparing and Interpreting Elemental Maps: The elemental abundances and ratios obtained from γ-ray and neutron spectra for various regions and features of the Moon will be compiled. The precision and accuracy of these results need to be examined closely. Large regions of the Moon with known or well-inferred compositions need to be identified that could be used for "ground truth" in testing these elemental results. Ground-truth regions and counting rates for various energy bands in the LP GRS data for those lunar regions can be used to create additional elemental maps in a manner similar to that done for Th, Fe, and Ti from the Apollo GRS.

Scientific Studies: A few of the studies of the Moon that we want to do are noted below.

Mapping of highland lithologies. Some of the key parameters in lunar highland analysis, such as Ca/Al and Al/Si ratios, are unlikely to be determined accurately enough from the LP data to be useful. However, other questions in highland studies are almost certain to be addressable with elements that will be well determined from the LP GRS and NS data.

The question of lunar granite occurrences is still open. Granitic impact products suggest granitic areas large enough to contain significant impacts without large-scale admixture of nongranitic regoliths or lithologies; we can test whether these zones of impact are large enough to be seen by the LP instruments. Regions with high contents of Si or high K/Th ratios might represent granite or other rare lunar components.

Although KREEP may be principally derived from a localized region beneath the lunar nearside [e.g., 1], there is no certainty that other lunar incompatible-element enrichments have not been isolated at other times and places in the highlands. Maps of K, Th, and REE across the entire Moon can extend KREEP studies into a more complete understanding of late-stage lunar crustal evolution.

It may be possible to map volatile-element depletions from Lunar Prospector data. Silica volatilization is known from a variety of Si-depleted compositions. The Si/O ratio could be used to test for the presence of Si-depleted impact melts extensive enough to approach the scale of the footprints for the LP GRS.

Mapping of mare basalt lithologies. In mapping mare basalts, the elements most readily measured with the Lunar Prospector γ-ray instrument (Ti, Fe, Th, K) are particularly suited to recognize and

map the principal known varieties of lunar basalts, including "high-Ti" and "high-K" basalt types. Distinguishing low-Ti from very-low-Ti (<1.5% TiO_2) classes may be difficult. Some high-K basalts (>0.4% K_2O) may be readily identifiable, but it will again be important to determine to how low a level the γ-ray K data are reliable for mapping.

Mapping of soil maturity and hydrogen indexes. The Lunar Prospector neutron data can provide a new view of regolith maturity using H content, which should vary directly with regolith maturity. Effects such as enhanced H retention in ilmenite-rich regolith can be addressed by the examination of Ti abundances and Ti/Fe ratios along with the epithermal (and thermal and fast) neutron data. The value of a global map of lunar soil maturity is immense. Our present understanding of regolith maturity is largely biased toward mare regions and away from heavily cratered terranes. This implies an incomplete understanding of the most evolved lunar regoliths. Mature regolith has value in resource applications and in targeting future exploration for understanding impact and solar-emission history in the vicinity of Earth.

Acknowledgments: This abstract describes work that we plan to do with G. Heiken and D. Drake as part of NASA's Lunar Data Analysis Program.

References: [1] Lawrence D. J. et al. (1998) *Science, 281,* 1484–1489. [2] Feldman W. C. et al. (1998) *Science, 281,* 1489–1493. [3] Feldman W. C. et al. (1991) *GRL, 18,* 2157–2160. [4] Reedy R. C. et al. (1998) *MAPS, 33,* A127–A128. [5] Reedy R. C. (1978) *Proc. LPS 9th,* pp. 2961–2984.

LUNAR SOUTH POLE TOPOGRAPHY DERIVED FROM CLEMENTINE IMAGERY.

M. R. Rosiek, R. Kirk, and A. Howington-Kraus, U. S. Geological Survey, Astrogeology Team, Flagstaff AZ 86001, USA (mrosiek@usgs.gov).

Introduction: During the Clementine Mission both oblique and vertical multispectral images were collected. The oblique and vertical images from a single spectral band collected during the same orbit form a stereo pair that can be used to derive the topography. These stereo pairs are being used to derive the topography of an area (90°S to 65°S latitude) surrounding the lunar south pole. Work on the lunar north pole topography will start after completion of the south pole topography. This report provides an update on the initial results for the lunar south pole topography.

Clementine Data: In 1994, the Clementine spacecraft acquired digital images of the Moon at visible and near-infrared wavelengths [1]. Onboard there were four camera systems and a laser altimeter. During the first pass, periapsis was at 30°S and the highest resolution images were obtained in the southern hemisphere [2]. Over the northern polar area, a series of oblique and vertical images were obtained with the ultraviolet-visible (UV-VIS) camera on each orbit. During the second pass, periapsis was at 30°N and the image acquisition strategy was reversed.

Imagery. The UV-VIS camera image size was 384 × 288 pixels with five spectral bands and one broad band. The 750-nm-band stereo pairs are the primary image source for this study. The ground-sample distances (GSD) for oblique images range from 300 to 400 m. The GSD for the vertical images, acquired at the end of an orbit, are slightly larger and range from 325 to 450 m. Using the formula for stereo-height accuracy [2], an estimate of height accuracy is 180 m. This formula is $IFOV_{max}/(K \cdot B/H)$ with $IFOV_{max}$ defined as Maximum Instantaneous Field of View; B/H is the base-to-height ratio and K is an estimate of pixel measurement accuracy on the imagery.

Altimeter. The Clementine laser altimeter (LIDAR) data were used previously to produce a global topographic model of the Moon [3]. The model has a vertical accuracy of ~100 m and a spatial resolution of 2.5°. Altimetry data were collected between 79°S and 81°N. These data were filtered and then interpolated to fill in the polar regions where the altimeter did not collect data. A global topography model was then derived based on spherical harmonic expansion [3].

Image mosaic. A global image mosaic of the Moon was produced from the 750-nm Clementine data [4,5]. The mosaic includes high-resolution, oblique, and vertical images. Match points were picked to tie the imagery together, and the camera pointing angles were adjusted to align the imagery. This adjustment used a spherical surface, and the elevation of all points was held to a constant value, 1737.4 km. This produced a seamless image mosaic with latitude and longitude information but no information on the elevation [4–5].

Analytical Aerotriagulation: The imagery and support information were downloaded to our digital photogrammetric workstation from the Integrated Software for Imagers and Spectrometers (ISIS) system. The support data included the camera location and pointing angles. Match points used to produce the image mosaic were also downloaded. The camera angles were adjusted to account for the elevation of the match points. This was accomplished with the Multi Sensor Triangulation (MST) software from LH Systems SOCET Set software package [6]. The revised camera angles allowed for the derivation of a digital elevation model (DEM) from the stereo pairs.

Initial estimate. The match-point latitude and longitude from the global image mosaic are accurate and used for an initial estimate of the horizontal position. The elevations of the match points were estimated from the altimetry data. The camera angles used in the altimetry processing and in the creation of the image mosaic were adjusted independently. Hence, the horizontal position of the altimetry data and the image mosaic are not aligned correctly. Clementine was designed so the altimeter shared the optical system of the HIRES camera system. The HIRES and UV-VIS camera systems were aligned so the HIRES image was centered in the UV-VIS image [1]. We therefore made an adjustment so that the altimetry points would fall near the centerline of the UV-VIS imagery.

A DEM was created from the altimetry data using the adjusted position and the match-point elevations were estimated from the adjusted DEM. These points were used in the HATS software, which allows for the use of weights on the estimated position based on the accuracy of the point. The horizontal positions were given a weight of 1 km, and the vertical estimates were given a weight of 5 km.

Stereo adjustment. In forming the Clementine Mosaic, over 3600 images and 29,000 match points were used in the southern polar region, an area defined as 64°S or less. Different techniques were tried in adjusting the images and match points. Limitations of computer memory required breaking the data into blocks that would be solved separately and then brought back together. Initial results had large elevation errors in the DEMs derived from different stereo pairs. This was most likely caused by the fact that although the stereo models overlapped, they did not share similar match points. One solution for this problem would require transferring all 29,000 match points to all the images they fall on within the set of 3600 images. This would be a tremendous amount of work. The solution used was to

thin the images to just the stereo pairs (983 images) and to thin the match points to cover the area (973 points.) The MST software was then used to add match points with the criteria that each image should have nine match points distributed throughout the image. This process added 1181 points. During editing and checking the match points, 45 more match points were added. The number of match points within an image ranges from 3 to 30 points, with 96% of the images having nine or more points and the average image having 16 points.

For the adjustment procedure an iterative least-squares solution is used; this allows the camera angles and match-point ground locations to change during the adjustment. The final root mean square (RMS) error of the match points was 0.68 pixels. Generally, a value of below 1 pixel is acceptable.

Elevation Extraction: The SOCET SET software provides an automated routine to extract elevation data. For every stereo model, a correlation point was determined every 1 km in ground distance. These patches of the DEM were first merged along an orbit path, and then the DEM from adjacent orbits were merged together. The stereo pairs do not completely cover the entire south pole, and these small gaps could be filled with other images or other techniques such as photoclinometry.

Initial Results: Data were collected starting with the models closest to the south pole. DEMs were collected from 108 stereo models, and the imagery was from 23 different orbits. Errors were summarized by number of points, RMS, standard deviation, bias, and percentage of points that were blunders (Table 1). The elevation errors in overlapping models within an orbit were looked at first.

TABLE 1. Average of errors (Models: n=108, Orbits: n=23).

	Points	RMS	St. Dev.	Bias	% Blunders
Models	2125	692 m	212 m	636 m	2.7%
Orbits	8248	447 m	336 m	222 m	1.5%

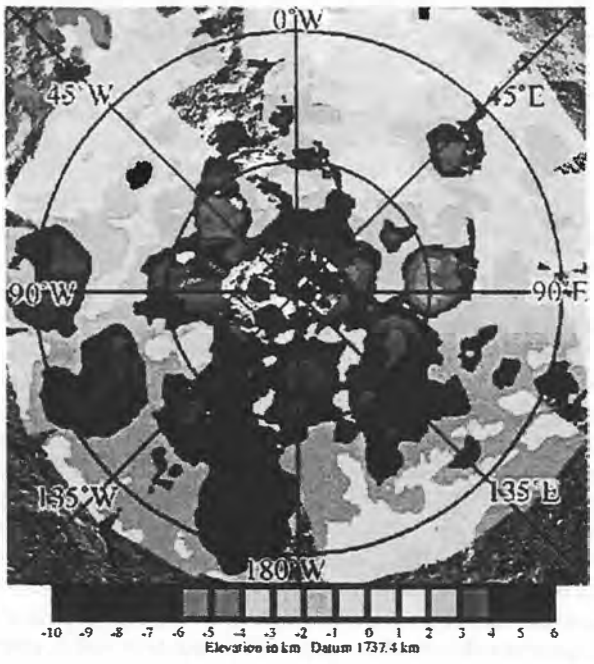

Fig. 1. Lunar south pole topography.

Within models, the RMS and bias errors were similar. This is probably caused by a tilt between the models. The standard deviation of 212 m is close to the expected precision of 180 m. The DEMs, from each model within an orbit, were merged together with an averaging and smoothing procedure. The elevation errors in overlapping orbits were looked at next. The bias error drops to 222 m; since the orbit DEMs are based on averaged data the tilt in the models was probably averaged out. The standard deviations of the elevation errors increase to 336 m.

The orbit DEMs were merged together and exported to ArcView Geographic Information System (GIS) for analysis and viewing. Figure 1 provides a false-color image of the lunar south pole topography. (To view fig. 1 in color, go to http://cass.jsc.nasa.gov/meeings/moon99/pdf/8046.pdf.) The area shown covers to 80°S. This will be expanded to 65°S. Work will begin on the lunar north pole topography in September 1999.

References: [1] Nozette S. et al. (1994) *Science, 266,* 1835–1839. [2] Cook A. C. et al. (1996) *Planet. Space Sci., 44,* 1135–1148. [3] Smith D. E. et al. (1997) *JGR, 102,* 1591–1611. [4] Eliason E. M. (1997) *LPS XXVIII,* 331–332. [5] Isbell C. E. et al. (1999) *LPS XXVIII,* 1812–1813. [6] Miller S. B. and Walker A. S. (1993) *ACSM/ASPRS Annual Convention and Exposition, Technical Papers, Vol. 3,* 256–263.

INTENTION AND INTENSION IN THE INTEGRATION OF LUNAR DATA SETS: THE GREAT INSTAURATION.

G. Ryder, Lunar and Planetary Institute, Center for Advanced Space Studies, 3600 Bay Area Boulevard, Houston TX 77058-1113, USA (zryder@lpi.jsc.nasa.gov).

Thus have I made as it were a small globe of the intellectual world, as truly and faithfully as I could discover.

— Francis Bacon, 1561–1626

Language was invented so that people could conceal their thoughts from each other.

— Charles-Maurice de Talleyrand, 1754–1838

Introduction: In formulating a lunar initiative in the integration of diverse datasets, we have tended to concentrate on the advantages of the end product, while glossing over the difficulties inherent in the process. As a rough guide, we can say that our objective is to obtain as full an understanding of the Moon as we can get by using all sources of data about it in combination in addressing key problems.

Integration, collaboration, and datasets have become increasingly important concepts over the digital age of the last two decades. Integration to the point of unity of knowledge was an Enlightenment concept, and has its modern counterpart in the metaphysical view of the integration of science, social science, and humanities [1]. The Geological Society of America, The Ecological Society of America, and the U.S. Geological Survey have recognized the importance of understanding integration, beginning to discuss the factors that bring about successful operation of a functional collective across agencies and institutions [2]. But our goal is of a lesser degree than that: integration within a few disciplines of science around the explanation of a common physical object. The technological advances that have made databases common and accessible allow (and produce) a mas-

sive sea of data whose archiving and exchange offer unprecedented opportunities. At the same time, there are problems of documentation (metadata) that influence identification, suitability, processing, and analysis [3].

Unfortunately, the words *integration* and *dataset* have also become buzzwords that are frequently empty. The meaning of words is important, and although a rose by any other name would smell just as sweet [4], attempting to invoke the smell of a rose in someone else by calling it a rat would fail; calling something a rose when it smells like a rat would also fail. Defining what a dataset is (and whether it should be one word or two) is neither a trivial nor a meaningless task.

Integration and Intention: Integration even within our initiative has different levels of meaning. The prosthetic extensions of our senses have produced varied kinds and amounts of data about the Moon. The integration of these data into concepts about the Moon is not merely a multidisciplinary approach, but needs to be intellectually immersive and synergistic to be successful. Purely multidisciplinary approaches can probably provide incremental advances on specific problems, but the goal of any significant project (other than engineering or technological projects with clearly defined tasks) is discovery.

Most significant questions are *epigenetic*: We now ask questions about the role of plagioclase elutriation from a magma ocean in influencing subsequent lunar evolution, but no such question existed prior to the Apollo program of investigation that eventually produced such a question. Thus a major intent of the integration initiative should be to derive new questions (or problems) and not just address existing ones. Nonetheless, these existing questions are themselves epigenetic, and remain questions of some importance. We need to see how using data from one discipline can be used in perhaps unexpected ways to address questions typically thought to belong to some other discipline, and not just think traditionally about "common" problems. One beauty of science is the recognition of the unity of complex phenomena that to direct observation appear to be quite separate things. An example might be magnetic variations in ocean basins, topography of mid-ocean ridges, and chemistry of lavas in orogenic chains, all united by plate tectonics. Geologists in fact do this sort of integration continually, both in the field and out of it, and at varied scales. Continued unification of our lunar understanding is one of our intentions.

Integration and Intensions: One problem of integration across disciplines and datasets is communication. Words or terms have both *extensions* and *intensions* (in formal logic; note distinction of *intension* and *intention*). Using the definition of Dennett [5], the *extension* is the thing (or set of things) to which the word or term refers; the *intension* is the particular way the extension is picked out or determined. (As a simple example, Dennett uses the terms *equilateral triangles* and *equiangular triangles,* which pick out the same set of things, and thus have the same *extension*, but clearly do not mean the same thing. They have different *intensions*.) Roughly, the intension of a word consists of the properties a thing must have in order to be in the extension of that word. There is no doubt that both the intensions and extensions of particular terms are used differently by members of different disciplines, leading to confusion (identified by Bacon four centuries ago as the direst of errors). This is compounded by the fact that many of our important terms are for abstract and variedly arbitrary concepts. Thus "anorthositic gabbro" for me denotes a rock containing easily visible grains, mainly plagioclase and clinopyroxene with the former dominant, and of igneous origin (intensional definition). To many remote sensers of the Moon, it merely means something (usually an average soil over a few square kilometers area) with low Fe, whose chemical composition by inference approximates that of an anorthositic gabbro. Anorthositic gabbro in *my* mind conjures up images of a magma differentiating in a large subterranean chamber over a period of thousands of years, slowly growing crystals and eliminating or trapping liquid in between crystals, and atoms of europium preferentially being incorporated in the growing plagiocase, and so on. (It is also a chunk of rock in a drawer that has a particular look about it.) I do not know what image is conjured up in the mind of a remote senser whose main interest is not petrology. This makes it difficult to produce a simple, adequate, all-useful glossary of the terminology used in lunar science. How do I relate the anorthositic gabbro used by remote sensers to the anorthositic gabbro used by a geophysicist (which in the lunar case is probably an anorthositic norite anyway) and to the anorthositic gabbro used by me?

This problem of intension is important in integration in a cognitive way. For instance, we can (and do, currently) define a set of basaltic rocks as high-Ti mare basalts. These are defined (stipulative definition) as volcanic, have high Fe (all have more than 15% FeO), and under the Neal and Taylor [6] definition have between 9 and 14% TiO_2 (see accompanying abstract for more critical discussion). This intensive stipulative definition leads to a certain set of basalts (the extension) that have these properties. (It is actually the existence of the extensions that has invoked the intension.) But what are the ramifications of this? What else might these basalts have in common? Are there other chemical features that this extensional set also has (as the intensional definition of equilateral triangles also leads to the same extensional set as the intensional definition of equiangular triangles), such as Sc? Or do these basalts all come from a clinopyroxene-bearing source? Some of these possible characters might be assumed (even if not demonstrated) by some petrologists, yet not even alluded to by a remote senser.

Datasets: Huge amounts of information have been generated about the Moon, with varied means. Various manifestations of groups of such information are commonly referred to as datasets. Some of these are sets, others are not. It is important to understand the true coherency of anything referred to as a dataset. Even coherent, digital datasets go through various transformations, e.g., from an original collection of some sort of instrument response with some sort of time tag (transformed into location?) through transductions and manipulations into something more directly informative to a user. For example, γ-ray data needs to be (for me to use) in some form of element intensity/location set, preferably deconvolved with geological input. This requires sequential datasets, of different uses to different workers, with varied metadata dependent on the genetic database and intended uses. Some of these datasets might be commensurable, and thus at one technical level relatively easy to integrate. Some datasets are much less easy to define. For example, some people have requested production of, and access to, the lunar sample chemical dataset. However, lunar sample analyses do not form a coherent set; different workers use different techniques, with different element sets, different uncertainties (and different outright errors), and varied sample sizes that quite differently represent – or fail to represent – whole rocks. Many analyses were collected without any intention of the analysis being representative; others have inadequate metadata (such as sample size). Thus to be useful, extensive metadata are needed for such "sets." Some specific subgroups of data

might form fairly coherent sets, e.g., neutron activation analyses of lunar soils from one laboratory. These are significant issues to address in attempting cognitive integration of varied information in understanding the Moon.

There is one aspect of data to be considered that results from human cognition and evolution: The natural world contains an embarrassment of riches, and much incoming information has to be filtered out. The choice of filtering depends on what is being addressed by the inspection of that information. It is a greater cognitive challenge than most people consider.

Conclusion: A look behind the apparent simplicity of integration as an exercise demonstrates that there are cross-discipline issues that need to be carefully thought about. These range from the new and old themes to be addressed, the terminology used, the nature of datasets, and the cognitive aspects of integration. Combined with the varied scales that data are collected on, these promise to make integration a challenging and rewarding exercise in returning the Moon to a prominent position in planetary science: The Great Instauration.

References: [1] Wilson E. O. (1998) *Consilience,* Alfred Knopf, New York. [2] May C. et al. (1999) *GSA Today,* April 1999, 4. [3] Vogel R. L. (1998) *Eos Trans. AGU, XX,* 373–380. [4] Shakespeare W. (1595?) *Romeo and Juliet.* [5] Dennett D. C. (1996) *Kinds of Minds: Towards an Understanding of Consciousness,* Harper Collins. [6] Neal C. and Taylor L. A. (1992) *GCA, 56,* 2177.

NAMING LUNAR MARE BASALTS: QUO VADIMUS REDUX.

G. Ryder, Lunar and Planetary Institute, Center for Advanced Space Studies, 3600 Bay Area Boulevard, Houston TX 77058-1113, USA (zryder@lpi.jsc.nasa.gov).

Introduction: Nearly a decade ago, I noted that the nomenclature of lunar mare basalts was inconsistent, complicated, and arcane [1]. I suggested that this reflected both the limitations of our understanding of the basalts, and the piecemeal progression made in lunar science by the nature of the Apollo missions.

Although the word "classification" is commonly attached to various schemes of mare basalt nomenclature, there is still no classification of mare basalts that has any fundamental grounding. We remain basically at a *classification of the first kind* in the terms of Shand [2]; that is, things have names. Quoting John Stuart Mill, Shand discussed *classification of the second kind*: "The ends of scientific classfication are best answered when the objects are formed into groups respecting which a greater number of propositions can be made, and those propositions more important than could be made respecting any other groups into which the same things could be distributed."

Here I repeat some of the main contents of my discussion from a decade ago, and add a further discussion based on events of the last decade.

Labels and Classification: A necessary first step of sample studies that aims to understand lunar mare basalt processes is to associate samples with one another as members of the same igneous event, such as a single eruption, lava flow, or differentiation event. This has been fairly successful, and discrete suites have been identified at all mare sites, members that are eruptively related to each other but not to members of other suites. These eruptive members have been given site-specific labels, e.g., Luna 24 VLT, Apollo 11 hi-K, A12 olivine basalts, and Apollo 15 Green Glass C. This is classification of the first kind, but is not a useful classification of any other kind. At a minimum, a classification is inclusive (all objects have a place) and exclusive (all objects have only one place). The answer to "How should rocks be classified?" is far from trivial, for it demands a fundamental choice about nature and ordering. Classification functions as a primary tool of perception, opening up ways of seeing things and sealing off others. Lacking a classification, mare-basalt petrology appears immature with little consensual perception of the qualities and significances of the basalts. The appearance may or may not be the reality, but it demonstrates a need for a functioning, communicatory classification, in particular for the dissemination of ideas and the furtherance of studies.

Inconsistency of Nomenclature: Names are inconsistent both among lunar rocks and between lunar and terrestrial rocks. Samples are labeled by elements, chemistry with tags, chemistry cast into mineralogy, or a mineralogical attribute (respective examples A14 VHK, A17 high-Ti Group B1, A15 quartz-normative, A-12 pigeonite). Such inconsistency is bound to lead to confusion. Chemical descriptions mean different things in mildly different contexts: A low-K Fra Mauro basalt (not a basalt!) contains slightly more K than an Apollo 11 high-K basalt. High-alumina means more than about 11% Al_2O_3 for mare basalts, but 21% for highlands "basalts." Volcanic KREEP basalts, ~18% Al_2O_3, are not (usually) qualified with "high-alumina." Yet for terrestrial basalts, high-alumina means more than ~17% Al_2O_3. Further, even very-low-Ti mare basalts have Ti abundances (~0.5–1.5% TiO_2) as great as typical terrestrial basalts. Thus, parallels between lunar and terrestrial nomenclatures are nonexistent (reinforced by the fact that a mare-basalt composition found on Earth would be too ultramafic to name basalt at all). A separate type of name exists for mare-basalt glasses, which are identified by site, color, and a letter for any subsequent distinctions, e.g., A15 Green Glass C.

Arcane Character of Nomenclature: While the inconsistencies cited above by themselves make nomenclature arcane, a greater source of difficulty is the common use of acronyms such as VHK and VLT. Most of these are partly chemical acronyms, but degrading the symbol Ti to T (for instance) makes them unintelligible and devoid of information even to the intelligent, educated non-expert.

Toward a Classification of Lunar Mare Basalts: Classifications have functions. A major one must be communication; i.e., a name for a mare basalt provides a common understanding of what the basalt is. For the small number of suites currently available, the present labels (though inefficient and insufficient) may work; with continued recognition of more basalts, Antarctic meteorite samples, orbiter data, sample returns, and lunar base studies, labels will become increasingly inefficient. Clementine and Prospector data have made mapping of mare basalts a much more visible activity than it was, and increasingly common ground among sample petrologists and remote sensers has emerged.

To establish a usable classification, there must be some criteria for relationships. Petrologists need to decide what the most significant characters are, and how these can be translated into a classification. The common distinction on the basis of Ti (the major element with the greatest variation) may or may not be appropriate. It remains to be established whether the use of Ti is of fundamental value both in relating basalts to each other and in communication, or merely an historical accident or response to its variance.

A great deal of discussion among interested parties will be required to arrive at a clear, functional, and consistent classification of mare basalts. A classification would need to be such as could be used by a range of workers including remote-sensing specialists, and thus would need to be hierarchical, according to what data are available. Acronyms should be eliminated, but some form of coded classification of use in computer databases could be a useful supplement to a classification. There are several key questions to address: (1) Do we know enough about mare basalts to yet formulate a classification, or is the field indeed too immature? (2) Should basalts should be classified at the suite scale (presupposing quite a lot of information about several samples) or at the hand-sample scale, and how would such classifications satisfy remotely sensed information? (3) How should chemistry and texture be balanced in any classification; should texture merely be a qualifier? (4) Are there natural divisions among mare basalts? Can arbitrary divisions still facilitate communication?

Any classification must avoid a detailed genetic base. Obviously the genesis might be debatable or the consensus change, but more importantly, there is not "an" origin for a given mare basalt. It has an origin going back to lunar formation, and combining source production, crystallization, source mixing, partial melting, assimilation, and so on. It would be difficult to incorporate 5% assimilation into a genetic classification.

The Current State of Mare Basalt Classification, 1999 Edition: All reviews of mare basalts state categorically that the classification of mare basalts is based on Ti content [3–5]. There is rarely any discussion at all on why that is so, or why particular divisions are preferred. Neal and Taylor [3], for instance, unilaterally eliminated a field of intermediate-Ti mare basalts. There *is* one considerable practical advantage to classifying mare basalts on the basis of Ti contents: Titanium can be detected and measured by a wide variety of techniques on samples and from orbit, and with the global-Ti acquisitions from Clementine and Prospector a whole field of mapping opened up. Furthermore, there is no doubt that Ti both varies widely among basalt suites and is abundant enough in lunar mare basalts (uniquely) to be a major element. However, is it the most fundamentally useful in a petrogenetic sense?

Titanium would be fundamentally useful if there were definite other characters of petrogenetic significance that varied in parallel with it. It is widely perceived among knowledgeable petrologists at least that there are such parallels; for instance, many high-Ti mare basalts are also high in other incompatible elements and in Sc. Furthermore, there is a common perception that high-Ti mare basalts are derived from sources containing ilmenite and clinopyroxene in contrast with lower-Ti basalts containing a low-Ca pyroxene (both in addition to olivine). However, the consistencies here are not great, especially when volcanic glasses are taken into account. There is no very consistent picture from isotopic data. There was a common concept early in lunar sample studies that high-Ti basalts were derived from shallower sources than low-Ti basalts, but further work has tended to deny that generalization too.

Neal and Taylor [3] proposed a new "classification" of mare basalts, first based on Ti differences, then on alumina differences, and then on K differences. The boundaries of this classification are arbitrary and have no fundamental petrological significance (that I am aware of). The division of high-Ti basalts from low-Ti basalts is set at 9% TiO_2, for instance, and in fact all the boundaries are orthogonal in this three-dimensional chemical space. It is unlikely that natural divisions in nature would be so orthogonal; most terrestrial classification boundaries on the basis of chemistry are best looked upon as equations that are not of the form y (or x) = constant. Some individual extrusive events can produce basalts that cross such boundaries. Thus, while the boundaries can be useful for communication, there is no indication that they are useful for petrogenetic purposes.

The classification of mare basalts on the basis of Ti has an unfortunate consequence: This division is used as inevitable, and subsequent investigations are aligned with that difference in mind. Thus basalts are commonly plotted on diagrams separated on the basis of Ti, and comparisions are made *within* Ti divisions rather than *across* the whole spectrum; it may well be that fundamental regularities are being missed by this first cutting.

Another unfortunate consequence is that the Ti classification gives too much emphasis to high-Ti basalts. On the basis of volume extruded, as far as we can tell, high-Ti basalts are only a small fraction of the total. An even greater disproportion is probably given to the pyroclastic glasses in most minds by their distinction as a group. Important though they are in a petrological sense, their absolute abundance is trivial compared with the total mass of extant mare lava.

References: [1] Ryder G. (1991) *LPS XXII,* 1157. [2] Shand S. J. (1927) *Eruptive Rocks,* Hafner Publishing. [3] Neal C. and Taylor L. (1992) *GCA, 56,* 2177. [4] Taylor G. J. et al. (1991) *The Lunar SourceBook,* Cambridge Univ. [5] Papike J. J et al. (1998) *Rev. Mineral., 36.*

ORIGIN AND EVOLUTION OF THE MOON: APOLLO 2000 MODEL. H. H. Schmitt, Department of Nuclear Engineering and Engineering Physics, University of Wisconsin–Madison, P.O. Box 90730, Albuquerque NM 87199, USA.

Introduction: A descriptive formulation of the stages of lunar evolution [1] as an augmentation of the traditional time-stratigraphic approach [2] enables broadened multidisciplinary discussions of issues related to the Moon and planets. An update of this descriptive formulation [3], integrating Apollo and subsequently acquired data, provides additional perspectives on many of the outstanding issues in lunar science.

Stage 1: Beginning (Pre-Nectarian) — 4.57 Ga
Stage 2: Magma Ocean (Pre-Nectarian) — 4.57–4.2(?) Ga
Stage 3: Cratered Highlands (Pre-Nectarian) — 4.4(?)–4.2(?) Ga
Stage 4: Large Basins — (Pre-Nectarian – Upper Imbrium) — 4.3(?)–3.8 Ga
Stage 4A: Old Large Basins and Crustal Strengthening (Pre-Nectarian) — 4.3(?)–3.92 Ga
Stage 4B: Young Large Basins (Nectarian – Lower Imbrium) — 3.92–3.80 Ga
Stage 5: Basaltic Maria (Upper Imbrium) — 4.3(?)–1.0(?) Ga
Stage 6: Mature Surface (Copernican and Eratosthenian) — 3.80 Ga to Present.

Lunar Origin: Increasingly strong indications of a largely undifferentiated lower lunar mantle and increasingly constrained initial conditions for models of an Earth-impact origin for the Moon [4–7] suggest that lunar origin by capture [8] of an independently evolved planet should be investigated more vigorously. Capture appears to better explain the geochemical and geophysical details

related to the lower mantle of the Moon and to the distribution of elements and their isotopes. For example, the source of the volatile components of the Apollo 17 orange glass apparently would have lain below the degassed and differentiated magma ocean (3) in a relatively undifferentiated primordial lower mantle. Also, a density reversal from 3.7 gm/cm^3 to approximately 3.3 gm/cm^3 is required at the base of the upper mantle to be consistent with the overall density of the Moon. Finally, Hf/W systematics allow only a very narrow window, if any at all for a giant impact to form the Moon [3,9,10].

Origin of the Oldest Magnesium-suite Rocks: Continued accretionary impact activity during the crystallization of the magma ocean would result in the "splash intrusion" of residual liquids into the lower crust of the Moon as soon as the crust was coherent enough to resist re-incorporation into the magma ocean. For Mg-suite rocks with crystallization ages greater than about 4.4 Ga, impact-dominated dynamics of crustal formation resulted in the injection of liquids from the magma ocean into the crust. Such a process probably helps to account for the apparent increasingly mafic character of the crust with depth [11–12].

Thermal Requirement for Rhenium-melting the Magma Ocean Cumulates: Creation of a mega-regolith during the cratered highland stage constituted a necessary prerequisite for the later remelting of magma ocean cumulates to produce mare basalt magmas. The increasingly insulating character of the pulverized upper crust would slow the cooling of the residual magma ocean. It also would have allowed the gradual accumulation of radiogenic heat necessary to eventually partially remelt the source regions in the upper mantle that produced the mare basalts and related pyroclastic volcanic eruptions. The reverse wave of heating would proceed downward into the upper mantle from the still molten and significantly radio-isotopic urKREEP residual liquid zone at the base of the crust.

Heterogeneous vs. Homogeneous Early Moon: The potential effects of a giant, Procellarum basin-forming event ca. ~4.3 Ga [2] and of a geographically coincident Imbrium event ca. ~3.87 Ga [2] can explain the surface concentration of KREEP-related materials in the Procellarum region of the Moon [13]. Lunar Prospector γ-ray spectrometer data indicate that the Procellarum event excavated only relatively small amounts of material related to KREEP. This strongly suggests that urKREEP magmas had yet to move into the Moon's lower crust. The extensive movement of such liquids across and possibly along the crust-mantle boundary region to beneath Procellarum, however, may well have occurred in response to the regional reduction in lithostactic pressure. The coincidental formation of another large basin, the 1160-km diameter Imbrium basin, near the center of Procellarum resulted in the redistribution of KREEP-related materials roughly radial to the younger basin. This scenario may make unnecessary recent proposals of a chemically asymmetric Moon [14–18] to account for the surface concentration of KREEP-related material around Imbrium.

Geochemical Dichotomy Between the Lunar Nearside and Farside: The timing of the giant, South Pole Aitken Basin-forming event at the end of the cratered highland stage (~4.2 Ga.) [3] can account for the lack of both extensive KREEP-related material [13] and basaltic maria [19] associated with South Pole Aitken. The absence of an Imbrium-size event in South Pole Aitken would have kept hidden any KREEP-rich crustal province. As would be expected with the removal of most of the insulating upper crust, relatively little mare basalt has erupted in South Pole Aitken [19], except possibly in its northern portions [20].

Source of Large Basin-forming Objects: After the cratered highlands stage and before the basaltic maria stage, objects from a discrete source region formed about 50 large basins on the Moon over ~400 m.y. Four possibilities for sources of the impactors of the large basin stage appear plausible at this time [8,21–23]. Of these possibilities, the initial breakup of the original Main Belt planetesimal would appear to be the best present choice as a discrete impactor source.

UrKREEP Mobilization: The striking differences between young, mascon basins (~3.92–3.80 Ga) and old, nonmascon basins (~4.2–3.92 Ga) indicate that the older, isostaticly compensated basins triggered the regional intrusion, extrusion, and solidification of mobile urKREEP-related magmas prior to the formation of the younger, uncompensated basins [24]. This suggests that the fracturing of the lunar crust by the older basin-forming events permitted urKREEP liquids to migrate into the crust, removing the potential for rapid, post-basin isostatic adjustment by urKREEP magma movement at the crust-mantle boundary.

Cryptomaria: The clear stratigraphic correlation of cryptomaria [25–29] with the old large basin substage suggests that these units are related to KREEP basalts or to partially melted, low-Ti late cumulates of the magma ocean. They underlie ejecta from the young large basins and may be represented in the Apollo samples by basalts of ages clearly greater than 3.92 Ga [30–31] or by KREEP-related basalts with model ages of 4.2–4.4 Ga [32].

Core Formation: The association of lunar magnetic anomalies with the antipodes of post-Nectaris basins [33–34] and the initially low accretion temperature of the lower mantle suggest that the $Fe_xNi_yS_z$ liquid separated from the early magma ocean did not coalesce into a circulating core until about 3.92 Ga. As anomalies do not appear to be antipodal to the Nectaris basin, and are apparently of lower intensity antipodal to Orientale, then a dipole field may have been active only between about 3.92 and 3.80 Ga, the respective apparent ages of these basins.

Vesicles in Crystalline Melt Breccias: Remobilized solar-wind H imbedded in the megaregolith of the cratered highlands probably was the dominant component of the fluid phase that formed vesicles in crystalline melt breccias produced by large basin-forming events [35].

Vesicles in Mare Basalt Lavas and Volatiles Associated with Pyroclastic Eruptions: Remobilized H, derived from the decomposition of primordial water, presumably was the dominant component of the fluid phase associated with mare basalt vesicles [36] and pyroclastic eruptions. The total absence of any indication of water associated with this fluid phase demonstrates that all primordial water in the source materials for the magma ocean has been lost to space or decomposed by $Fe_xNi_yS_z$ liquid separation [37] and migration.

Hydrogen Concentrations at the Lunar Poles: The probability is high that the epithermal neutron anomaly detected over the lunar poles [38] is largely if not entirely the consequence of concentrations of solar-wind H rather than cometary water ice [38–39]. Hydrogen and other solar-wind volatiles can be expected to be concentrated in permanently shadowed areas [41]. A continuous blanket of cometary water ice, unless fortuitously covered by protective ejecta from larger but very infrequent impacts, probably would erode [3] and be lost in a geologically short interval.

References: [1] Schmitt H. H. (1991) *Am. Mineral. 76*, 773–784. [2] Wilhelms D. E. (1987) *U.S. Geological Survey Prof. Paper*

1348. [3] Schmitt H. H. (1999) in *Encyclopedia of the Space* (H. Marks, ed.), Wiley. [4] Halliday, A. N. and Drake M. J. (1999) *Science, 283,*1861–1863. [5] Cameron A. G. W. (1999) *LPS XXX,* Abstract #1150. [6] Agnor C. B. et al. (1999) *LPS XXX,* Abstract #1878. [7] Jacobsen S. B. (1999) *LPS XXX,* Abstract #1978. [8] Alfven H. and Arrhenius G. (1972) *The Moon, 5,* 210–225. [9] Lee D. et al. (1997) *Science, 278,* 1098–1103. [10] Palme H. (1999) *LPS XXX,* Abstract #1763. [11] Kahn A. and Mosegaard K. (1999) *LPS XXX,* Abstract #1259. [12] Pieters C. M. and Tompkins S. (1999) *LPS XXX,* Abstract #1286. [13] Lawrence D. J. et al. (1998) *Science, 281,* 1484–1485. [14] Haskin L. A. et al. (1999) *LPS XXX,* Abstract #1858. [15] Feldman W. C. et al. (1999) *LPS XXX,* Abstract #2056. [16] Wieczorek M. A. et al. (1999) *LPS XXX,* Abstract #1548. [17] Korotev R. L. (1999) *LPS XXX,* Abstract #1305. [18] Jolliff B. L. et al. (1999) *LPS XXX,* Abstract #1670. [19] Feldman W. C. et al. (1998) *Science, 281,* 1489–1493. [20] Blewett D. T. et al. (1999) *LPS XXX,* Abstract #1438. [21] Morbidelli A. (1998) *Science, 280,* 2071–2073. [22] Murray N. and Holman M. (1999) *Science, 283,* 1877–1881. [23] Fernandez J. A. (1999) in *Encyclopedia of the Solar System* (P. R. Weissman et al., eds.), pp. 554–556, Academic Press. [24] Schmitt H. H. (1989) in *Workshop on Moon in Transition, LPI Tech. Rpt. 89-03,* (G. J. Taylor and P. H. Warren, eds.), pp. 111–112. [25] Hawke B. R. et al. (1999) *LPS XXX,* Abstract #1956. [26] Bell J. and Hawke B. R., *JGR, 98,* 6899–6910. [27] Clark P. E. and Hawke B. R. (1991) *Earth, Moon, Planets, 53,* 93–107. [28] Head J. W. et al. (1993) *JGR, 98,* 17165–17169. [29] Williams D. A. et al. (1995) *JGR, 100,* 23291–23299. [30] Taylor L. A. et al. (1983) *EPSL, 66,* 33–47. [31] Heiken G. H. et al. (1991) *Lunar Sourcebook,* 209 pp. [32] Heiken G. H. et al. (1991) in *Lunar Sourcebook,* pp. 218–219. [33] Lin R. P. et al. (1998) *Science, 281,* 1481. [34]] Lin R. P. et al. (1999) *LPS XXX,* Abstract #1930. [35] Schmitt H. H. (1973) *Science, 182,* 682. [36] Schmitt H. H. et al. (1970) *Apollo 11 LSC,* 11–13. [37] Agee C. B. (1991) in *Workshop Phys. Chem. Magma Oceans* (C. B. Agee and J. Longhi, eds.), pp. 11–12, LPI. [38] Feldman W. C. et al. (1998) *Science, 281,* 1496–1500. [39] Nozette S. et al. (1999) *LPS XXX,* Abstract #1665. [41] Watson K. et al. (1961) *JGR, 66,* 3033.

MAGMATISM OF THE LUNAR HIGHLANDS AND THE EARLY PALEOPROTEROZOIC MAGMATISM OF THE EARTH: SIMILARITIES AND DISTINCTIONS.

E. V. Sharkov and O. A. Bogatikov, Institute of Ore Deposits Geology, Petrology, Mineralogy and Geochemistry, Russian Academy of Sciences, Moscow 109017, Russia (sharkov@igem.ru).

Important feature of tectonic-magmatic activity on the Moon is it closeness to the Earth's early Palaeoproterozoic stage of evolution. The most ancient magmatism of the Moon was begun at highlands from low-Ti melts of the magnesian suite, which were rather close in composition of rocks, their mineralogy and geochemistry to the early Palaeoproterozoic terrestrial magmatism of the siliceous high-Mg (boninite-like) series (SHMS). Around 3.8 Ga, it was changed by basaltic magmatism of maria, where high-Ti varieties were common. This type of magmatism is resembled the oceanic-type magmatism of the Earth (including Fe-Ti basalts of oceanic islands), which firstly appeared in the late Palaeoproterozoic ca. 2 Ga. On the Moon are lacking both analogs of the Archean type of activity of the Earth, when formation of granite-greenstone terranes occurred, and the Phanerozoic subduction-related magmatism.

On Earth, the SHMS rocks of 2.5–2.1 Ga formed large igneous provinces within the Archean granite-greenstone cratons. For example, on the Baltic Shield such province evolved on territory measuring ~1 million km^2 and represented by different volcanics (low-Ti picrites, Mg basalts, high-Al basalts, andesites, dacites, and rhyolites, where basalts predominated) in riftlike structures, gabbronorite dyke swarms, and large layered intrusions [1]. The latter consist of dunites, harzburgites, pyroxenites, norites and gabbronorites, including pigeonite varieties, gabbro-anorthosites, Mgt gabbronorites, and diorites. The SHMS rocks on their major, rare, and rare earth elements contents were rather close to the Phanerozoic calc-alkaline series related to subduction zones, but on its geological position they had within-plate tectonic settings and look like the continental flood basalt province. The $\varepsilon_{Nd}(T)$ value of –1 to –2 is characteristic for the studied SHMS-rocks, indicating that the origin of such melts was linked with large-scale assimilation of crustal rocks by high-temperature, mantle-derived magmas during their ascending to the surface.

Potassic granites and monzodiorites and K-enriched volcanics, varied from low-Ti picrites and trachybasalts to alkaline andesites and dacites, are not uncommonly associated with the SHMS rocks. According to isotopic data, these rocks also had mixed mantle-crustal origin.

Around 2.2–2.0 Ga, practically on the whole Earth simultaneously , the Fe-Ti picrites and basalts of different alkalinity, similar to the Phanerozoic within-plate rocks were appeared, and substituted the SHMS rocks as a main type of within-plate magmatic activity [2].

The lunar magmatism of the highlands was rather close to the early Paleoproterozoic magmatism of the Earth. The earliest (4.45–4.25 Ga) magnesian-suite magmatism, which intruded the primary anorthositic crust, was represented by volcanics and intrusive rocks [3–4]. Pristine intrusive rocks of this suite are represented by dunites, harzburgites, troctolites, norites, gabbronorites, and anorthosites (ANT-series). Important role in these rocks play orthopyroxene and pigeonite; Cr spinel, orthoclase, quartz, apatite, and Ti phases occur in many varieties. On their composition these intrusive rocks rather close to the rocks of the early Paleoproterozoic layered intrusions.

As a whole, all these rocks on their major, rare and rare earth elements pattern are rather close to the terrestrial early Palaeoproterozoic SHMS. What is more, the $\varepsilon_{Nd}(T)$ value in the rocks of the lunar magnesian suite is about –1, which correlates with data for the terrestrial SHMS rocks (from–1 to–2). The main difference between these lunar rocks from terrestrial rocks is a lower alkali content and very subordinate role of acid and intermediate melts. According to Snyder et al. [3–4], the origin of these rocks was linked with contamination of high-temperature mantle-derived magmas by lunar crustal material during their ascension to the surface.

Rocks of the 4.3–4.0 Ga KREEP series are the second type of magmatism of the highlands, where they are associated with the rocks of the magnesian suite [3–4]. They are characterized by elevated K content, REE and P alkalinity, and are represented by volcanics (mainly basalts) and their intrusive analogs "alkaline series" — "alkaline" anorthosites, gabbro and gabbronorites, monzodiorites and potassium granites could be finite members of the series. The rocks of these composition and tectonic settings closely resemble the enriched K in the early Paleoproterozoic terrestrial rocks of cratons.

Thus, the lunar magmatism is close to only one (the Palaeo-

proterozoic), stage of terrestrial magmatism evolution. The cause of this could be both in some different primordial composition of the silicate mantles of these planetary bodies, and the different degree of their differentiation during solidification of their planetary magma oceans: it suggests that the depth of the latter in the case of the Moon was ~200–300 km, whereas in the Earth it was ~700 km.

References: [1] Sharkov E.V. et al. (1997) *Petrology, 5,* 448–465. [2] Sharkov E. V. and Smolkin V. F. (1997) *Precambr. Res., 82,* 133–151. [3] Snyder G. A. et al. (1995) *JGR, 100,* 9365–9388. [4] Snyder G. A. et al. (1995) *GCA, 59,* 1185–1203.

MARE MAGMATISM OF THE MOON AND OCEANIC MAGMATISM OF THE EARTH: SIMILARITIES AND DISTINCTIONS. E. V. Sharkov and O. A. Bogatikov, Institute of Ore Deposits, Geology, Petrology, Mineralogy and Geochemistry, Russian Academy of Sciences, 35 Staromonetny, Moscow 109017, Russia (sharkov@igem.ru).

1. *Maria* with mafic basaltic floors are the second major type of morphostructures of the Moon, which were formed in the late stages of its evolution from 3.8 to 3.2 Ga [1]. They form large rounded depressions (10-km depths, [2]) in the lunar relief. On their structure (presence of mid-maria moundlike rises and local rises), and on basaltic rocks composition they resemble oceanic segments of the Earth with its mid-oceanic ridges and within-plate oceanic islands. These types of the Earth's structures also began to form later than continental segments of the lithosphere, from ca. 2 Ga [3].

2. Like on the Earth, two types of basalts are typical for the lunar *maria:* low-Ti and high-Ti, which could be correlated with the mid-oceanic ridge basalts (MORB) and oceanic island Fe-Ti basalts (OIB) consequently. This type of tectonic-magmatic activity survived until now on the Earth; its petrogenesis associated with ascending of the mantle plumes that originated on the core-mantle boundary (CMB), in the layer D". For the terrestrial plumes it is characteristically a presence of specific fluid components, enriched in Fe, Ti, alkalies, •, ••, Zr, •••, etc. Concentration of the fluid components is low in MORB and the highest in the within-plate Fe-Ti basalts.

3. Ocean-island basalt magmatism has a limited range in the Earth's oceans and is often localized on the mid-oceanic ridge slopes or far from them. With distance from the ridges axes composition of melts became more alkaline and titaniferous. The same picture is common for the continental traps provinces, whose origin is linked with superplume ascension; close to the MORB tholeiitic basalts are predominate, and alkaline Fe-Ti basalts present in a limited range. Traps appearance often preceded oceans opening and in this sense they could be defined as the first stage of the ocean development.

4. By analogy of the Earth, it is suggested that petrogenesis of the *mare* basalts could be also linked with plume activity, which were ascended from the lunar CMB of that time. Instead of the Earth, the lunar outer (liquid) core did not survive until present, but had to be active during the *maria* formation. The main difference of a fluid components of these plumes from the Earth's analog was the practical absence of H_2O in them; this indicates a mineral composition of the *mare* basalts, where important role-play mineral phases formed under reduce conditions.

5. Another important difference is linked with the lunar high-Ti basalts, which are characterized by a strong negative Eu anomaly; however, such an anomaly has not been found in the very low-Ti (VLT) varieties. Traditionally, the presence of such an anomaly is associated with fractionation of plagioclase in magmatic processes. However, we suggest that in this particular case this phenomenon is more likely linked with reduced character of the Moon interior, because in magmatic systems a value of Eu^{2+}/Eu^{3+} ratio depends on f_{O_2}, and in reducing systems all Eu is represented by Eu^{2+}, which accumulated in the basic plagioclase. In contrast to the terrestrial basalts, where both Eu isotopes occur and removing one of them smoothed off through accumulation of the second, here only Eu^{2+} occurred and so its fractionation led to strong depletion of the residual melt in Eu. Consequently, appearance of the Eu anomaly could be linked with fractionation of plagioclase in transitional magmatic chambers (intrusions) in the form of different gabbroids. Because Eu content in basalts quickly rises under growth of Ti [4], this process is most effective in the case of the high-Ti melts.

6. Beneath the lunar *maria* excess of masses (mascones) occurs and the lunar crust becomes thinner above them. In general, such a situation resembles a character of distribution of Earth's crust above continental rifts. Probably, the mascones are solidified mantle-plume head, which are known on the Earth as large lens like bodies of anomalous mantle beneath mid-oceanic ridges and continental rift zones [5].

7. So, there are essential similarities in structure and origin of the lunar *maria* and terrestrial oceans. However, instead of the Earth, the ancient lunar crust did not disrupt with formation of the lithosphere of oceanic type and further development according to a plate-tectonics model. The process ended on the first stage, analogous to the terrestrial continental traps formation.

References: [1] Snyder G. A. et al. (1994) *GCA, 58,* 4795–4808. [2] Spudis P. D. (1996) *The Once and Future Moon,* Smithsonian Inst., 308 pp. [3] Bogatikov O. (1999) *Magmatism and Geodynamics: Terrestrial Magmatism in the Earth's History,* Gordon and Breech, London, in press. [4] Wilson M. (1989) *Igneous Petrogenesis, A Global Tectonic Approach,* Univ. Hyman, London, 466 p. [5] Anderson D. L. (1992) *Science, 256,* 1645–1650.

MARE BASALTIC MAGMATISM: A VIEW FROM THE SAMPLE SUITE WITH AND WITHOUT A REMOTE-SENSING PROSPECTIVE. C. K. Shearer[1], J. J. Papike[1], and L. R. Gaddis[2], [1]Institute of Meteoritics, Department of Earth and Planetary Sciences, University of New Mexico, Albuquerque NM 87131, USA, [2]U. S. Geological Survey, Astrogeology Program, Flagstaff AZ 86001, USA.

Introduction: It has long been recognized that the lunar-sample suite returned by the Apollo and Luna missions is biased with regard to its representation of lunar mare basalts [1–3]. This sampling bias is reflected in both an incorrect portrayal of the volume of mare basalt types and the absence of many basalt groups known to exist from spectral data [1–2]. This bias obviously affects models for the petrogenesis of mare basalts and the interior of the Moon. Here, we explore the implications of this bias and compare models for lunar magmatism that are derived solely from samples with potential models derived from combined sample and remote-sensing data. We focus on the implications of these contrasts in several areas: volume, distribution, and age of mare basalts, KREEP enrichment on the nearside of the

Moon, heat sources for melting, and depth of mare basalt source regions.

Volume, Distribution, and Age of Mare Basalts: *Volume of mare basalt groups.* The mare basalt sample suite indicates that the TiO_2 distribution of crystalline mare basalt samples is bimodal, with a majority of the mare basalts occurring in the range of 1.5–5.5 and 10–13 wt% TiO_2. A compositional gap appears to exist between 6 and 9 wt% TiO_2. Although the population of picritic mare glasses also exhibits a bimodal distribution with regard to TiO_2, it is dominated by very low-Ti glasses (<1 wt% TiO_2) and high-Ti glasses (8–16 wt% TiO_2) and exhibits a very broad compositional gap between 1 and 8 wt% TiO_2. The simplest interpretation of the bimodal Ti distribution is that two distinct sources were melted to produce the mare basalts: late, rather shallow, Ti-rich lunar magma ocean (LMO) cumulates and early, rather deep, Ti-poor LMO cumulates. More recently, on the basis of Galileo SSI and Clementine UV-VIS data, global TiO_2 distribution has been interpreted to be continuous in the maria with no hint of biomodality and an abundance peak between 1 and3.5 wt% TiO_2 [3]. These new observations indicate a mare source model in which a small volume of late, ilmenite-bearing LMO cumulates mixed with a large volume of early LMO cumulates in which ilmenite was absent. These differences in models have implications for heat sources for generating mare basalts, the relative depth of various mare basalt sources, and the early dynamics of the lunar mantle.

Distribution of mare basalts. Although remote optical and spectral observations of the lunar surface document the concentration of mare basalts on the nearside of the Moon [e.g.,1], our limited sampling of basalts does not define the overall distribution of mare basalt compositions. The relative distribution of high-Ti basalts should shed light on the asymmetry of LMO cumulates and refine or refute mare basalt models that require recycling of late, high-Ti cumulates into the deep lunar mantle.

Lunar pyroclastic glasses have been identified at all of the Apollo sites. Based on samples, the compositional variation of these glasses is bimodal and their overall abundance is unknown. Understanding both their compositional diversity and distribution is critical to deciphering how these near-primary magmas were transported to the lunar surface from great depths and how they are related to crystalline mare basalts. Based on Clementine data and previous work, more than 100 lunar pyroclastic deposits have been proposed [4] and potentially a large number consist of high-Ti glass beads [5]. The existence of so many deposits that could consist of near-primary basaltic magmas implies that mechanisms for their transport to the surface are not extraordinary and that density contrasts between melts and surrounding mantle do not significantly impede their source segregation and movement, at high pressure, to the lunar surface.

Age of mare basalt groups. While radiometric age dating of lunar mare basalts provides a precise means of dating individual samples, when it is combined with relative age relationships determined by remote sensing (e.g., crater counts) it becomes a method for reconstructing magmatism on a planetary scale [e.g., 6]. Two examples where this approach has provided useful information and will continue to bear fruit are the duration and early history of lunar volcanism and the relationship between mare basalt composition and eruptive history.

Although the petrologic record has been obscured by the early catastrophic impact history of the Moon, there is abundant evidence of pre-3.9 Ga nonmare basaltic volcanism [e.g., 7–8]. Most of this record is retained in small clasts from highland soils and breccias or has been identified through remote sensing. The relationship between the samples and units identified through remote sensing is speculative. Further identification and delineation of older episodes of volcanism and their relationship to episodes of crustal plutonism (Mg and alkali suites) is critical to our interpretation of mantle evolution following magma ocean crystallization and prior to the onset of mare volcanism. Combined sample and remote sensing data sets will allow us to better distinguish among the wide range of models that have been proposed for these early periods of lunar magmatism (Mg suite, alkali suite, KREEP basalts). These models include (1) impact origin; (2) magma ocean crystallization; (3) melting and remobilization of late magma ocean cumulates and/or KREEP infiltrated lower crust; (4) melting of the lower portions of the cumulate pile followed by assimilation of KREEP or anorthositic crust; and (5) melting of deep, hybrid mixed cumulate sources.

The relationship between mare basalt TiO_2 content and age is subject to controversy. Based on the sample suite, researchers have concluded that there is no correlation [9–10], a weak correlation [11], or a significant correlation [7]. On the basis of remotely-sensed data, researchers have concluded that TiO_2-rich basalts tend to be older than TiO_2-poor basalts, but within individual basins TiO_2 content and age are not correlated [6]. A simple time-composition correlation implies a systematic relationship between sequence of melting and source region. Such a relationship suggests a model in which melting could be initiated in shallow high-Ti cumulates and progress into the deep lunar mantle. Both the lack of composition-time correlation within individual basins [6] and a potential deep-mantle origin for all primary mare basalts [8,12] require a much more complex process that involves the extent of magma ocean cumulate mixing, distribution and composition of mantle reservoirs for heat-producing elements, and the mechanism(s) for magma transport to the lunar surface.

KREEP Enrichment on the Nearside of the Moon: Perhaps the bias of our lunar samples is best illustrated by recent global data for Th (≈KREEP) abundance [13], which implies that the Apollo collection sites were all within a large, high-KREEP bulge on the nearside of the Moon. If KREEP distribution on the lunar surface reflects a real and preferred distribution of heat-producing elements in the lunar mantle, this has significant implications for our models for lunar magmatism. First, it suggests either an asymmetry in the crystallizing LMO or an episode of KREEP remobilization. Second, the irregularity of KREEP distribution early in lunar history will modify our models for the generation of both premare, highland, and mare magmatism. For example, if assimilation is an important process in producing premare magmas, highland magmas outside the KREEP bulge may not have a KREEP signature at all. On the other hand, if KREEP was recycled into the lunar mantle and was instrumental in initiating the mantle melting that produced the highland magmas, the highland units such as the Mg suite may largely be a nearside phenomena.

Parental Magmas for the Mare Basalts and the Depth of Mare Source Regions: Much of the debate concerning the origin of mare magmas has focused upon the nature of parental mare magmas and their depth of origin in the lunar mantle. Two possible models are (1) that parental magmas to the mare basalts are similar in composition to the picritic glasses and were derived from initial melting in the deep lunar mantle (>400 km) or (2) that mare basalts represent the

crystallization of more Fe-rich, olivine-poor primary magmas that were produced at shallower depths. Combined analysis of sample and remote-sensing data may allow us to address these problems. First, if crystalline mare basalts and picritic mare glasses define the same ranges in TiO_2 and overlap in age, this could be interpreted as indicating that they were produced by melting of similar mantle assemblages under comparable conditions. Second, crystalline mare basalts have all the chemical attributes (lower Ni, Mg′, higher Al) associated with substantial olivine fractionation. Although picritic mare glasses and crystalline mare basalts in most cases were not related by shallow fractional crystallization, calculated liquid lines of descent are parallel [14–15]. Therefore, the preservation of primitive magmas (i.e., picritic mare glasses) may be a function of magma transport and eruptive mechanism rather than dramatically different source regions. Third, is the generation of mare basalts from a shallow, subcrustal source between 3.9 and 3.0 Ga reconcilable with the thermal nature of the upper lunar mantle? The liquidus temperatures of mare basalts exceed 1200°C at depths corresponding to ~0.5 Gpa [16]. There is no mechanism to reheat the shallow lunar mantle 600 m.y. after the formation of the Moon and to maintain this temperature for over 700 m.y. Furthermore, the existence and preservation of mascons in multiringed basins that formed at ~3.9 Ga could indicate a relatively cool and rigid upper mantle incapable of producing basalts.

References: [1] Pieters (1978) *Proc. LPSC 9th,* 2825–2849. [2] Pieters (1990) *LPI-LAPST Workshop on Mare Volcanism and Basalt Petrogenesis: Astounding Fundamental Concepts (AFC) Developed Over the Last Fifteen Years,* 35–36. [3] Giguere et al (1999) *LPS XXX.* [4] Gaddis et al. (1999) *LPS XXX.* [5] Weitz et al. (1990) *JGR,* 22725–22759. [6] Hiesinger et al. (1999) *LPS XXX.* [7] Snyder et al. (1999) in *Origin of the Earth and Moon* (R. Canup and K. Righter, eds.), in press. [8] Shearer and Floss (1999) in *Origin of the Earth and Moon* (R. Canup and K. Righter, eds.), in press. [9] Papike et al. (1976) *Rev. Geophys. Space Sci., 14,* 475–540. [10] BVSP (1981) *Basaltic Volcanism on the Terrestrial Planets.* Pergamon, New York. [11] Nyquist and Shih (1992) *GCA, 56,* 2213–2234. [12] Delano J. W. (1986) *Proc LPSC 16th,* in *JGR, 91,* D201–D213. [13] Lawrence et al. (1999) *LPS XXX.* [14] Longhi (1987) *Proc. LPSC 17th,* in *JGR, 92,* E349–E360. [15] Shearer and Papike (1993) *GCA, 57,* 4785–4812. [16] Longhi (1992) *GCA, 56,* 2235–2251.

STRUCTURE AND COMPOSITION OF THE LUNAR CRUST.

P. D. Spudis[1], D. B. J. Bussey[2], and B. R. Hawke[3], [1]Lunar and Planetary Institute, Houston TX 77058, USA (spudis@lpi.jsc.nasa.gov), [2]European Space Research and Technology Centre, European Space Agency, Noordwijk, The Netherlands, [3]Planetary Geophysics Division, University of Hawai'i, Honolulu HI 96822, USA.

Since the first return of lunar samples indicated that global differentiation of the Moon had occurred, numerous models of crustal structure have been proposed [summarized in 1]. With the completion of the first global reconnaissance mapping by Clementine [2] and Lunar Prospector [3], we are now in position to re-evaluate crustal structure and composition at a global scale. Although this is a difficult and complex task, and one requiring significant study, some first-order results are apparent now and are quite telling. We here summarize our current view of crustal structure and identify some required knowledge to better understand the origin and evolution of the lunar crust.

Models of Crustal Structure: Wood et al. [4] attempted to estimate the amount of plagioclase in the crust, based on the average elevation difference between mare and highlands and some simple assumptions about anorthosite and basalt as responsible for the principal lunar rock types. Later, more complex models emerged, involving layered crusts of feldspathic material over more basaltic material [5–6] or a laterally variable crust, with Mg-suite plutons intruding a grossly anorthositic crust [7]. Later models attempted to reconcile these contrasting styles by incorporating both features [e.g., 8]. In part, crustal structure was inferred by the envisioned mode of crustal formation. A decade-long debate on the reality of the lunar "magma ocean," stimulated by the provocative notion of Walker [9] that the Moon never had a magma ocean, and the recognition that the anorthosites and Mg suite probably recorded different and unrelated magmatic events [10]. Such a scenario leaves much about crustal structure an open question, but allows for both lateral and vertical heterogeneity, thus accommodating both principal crustal models.

New Data from Clementine and Lunar Prospector: Global maps of Fe [11], Ti [11–12], and Th [13] both confirm old ideas and create new problems. It is clear that vast areas of the lunar highlands are extremely low in Fe [11], consistent with a significant amount of anorthosite. Such a distribution supports the magma ocean. However, the average lunar highlands composition is, as long suspected, that of "anorthositic norite" [11,14], a mixed rock type, somewhat similar to many of the lunar meteorites (e.g., ALHA 81005 [15] and more mafic than pure ferroan anorthosite. Anorthosite proper does occur on the Moon; it is found almost exclusively within the inner rings of multiring basins [16]. These basins span a range of ages and distributions [17]. Mafic provinces occur in the central Procellarum region of the front side and on the floor of the South Pole Aitken Basin. In these areas, the lunar surface is "highland basaltic" composition (FeO ~9–10 wt%). Additional highland basaltic areas occur in the vicinity of nearside basins, such as Serenitatis. The major lunar "hot spot" of high Th concentration (~10 ppm) occurs within a broad, oval depression approximately coincident with Oceanus Procellarum. Slightly less elevated amounts (~4 ppm) are associated with the basaltic floor of SPA Basin on the farside. Aside from this, Th highs are isolated and minor.

A "New" Crustal Model: On the basis of the new global data, as well as from our continuing study of the composition of basin ejecta to probe the deep crust [17], we have modified slightly our existing crustal model [8] to accommodate the new findings (Fig. 1). We propose a three-layer model of crustal configuration. The uppermost zone, down to depths of ~15–20 km, consists of megabreccia of mostly anorthositic norite composition (FeO ~ 4–6 wt%; Al_2O_3 ~26 wt%). This zone is neither laterally or vertically uniform [14], displaying anomalous compositional zones at scales of tens to hundreds of kilometers, but is remarkably homogeneous at planetwide scales. In bulk composition, it resembles the "ferroan anorthositic norite" suite of mixed rocks described by Lindstorm et al. [18] and many of the highlands regolith breccias found as lunar meteorites [15]. It is also similar to the average crustal composition inferred by Taylor [19], on the basis of Apollo granulitic breccias and limited orbital chemical data. Although some areas on the northern farside appear very anorthositic [11], most areas of the upper highlands

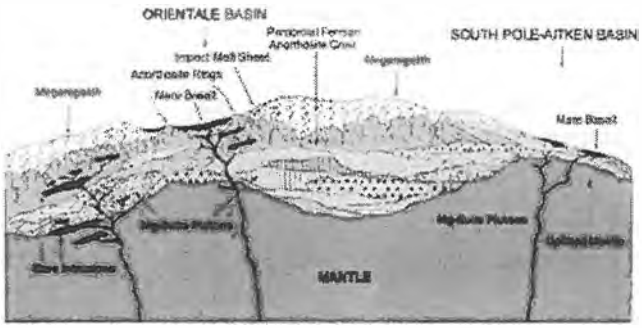

Fig. 1. Proposed model of the lunar crust.

different from this composition are more mafic, not more feldspathic, showing affinities to highland basalt, with or without KREEP.

The next zone of the crust is found at depths between 15 and ~35 km. It appears to consist largely of nearly pure, ferroan anorthosite (FeO < 2 wt%; Al_2O_3 > 33 wt%). Outcrops of pure anorthosite principally occur on the Moon in the inner rings of multiring basins (Fig. 1), which are structurally uplifted blocks from midcrustal levels [20], or rarely, as central peaks in some selected craters (Alphonsus, Aristarchus [16]. The anorthosite is apparently confined to middle levels in the crust; moreover, it appears to be at least partly of global extent, as basin rings of anorthosite are found in basins spanning the globe, from Orientale [16–17] to Humboldtianum [21]. Because anorthosite is most likely to represent the primordial crust [10], we interpret this global "layer" of anorthosite as the remnant of the original crust of the Moon.

The petrological nature of the roughly half of the crust below the anorthosite zone (depths of 35– 65 km) remains obscure, but several observations may be made about the likely nature of rocks to be found there. First, where most of the upper crust has been removed by large, basin-forming impact (such as the floors of the SPA [22] and Imbrium Basins [23]), the crustal composition appears to be that of highland basalt (FeO ~ 9–12 wt%; Al_2O_3 ~ 18–20 wt%). Second, a plot of the total Fe content of basin ejecta (determined from orbital measurements; [11]) against basin size shows that larger basins excavate more mafic (Fe-rich) material [24]. This relation suggests that the lower levels of the crust are more "basaltic" than middle or upper levels. Finally, basin impact melts, typified by the Apollo 15 and 17 impact melt breccias [1,8], are of highland basaltic composition, and were probably formed by massive melting of middle-to-lower crustal levels [5,6, 8]. These observations in total suggest that the lower crust is broadly "highland basalt" in composition. The petrological nature of the lower crust remains obscure, but the high Mg# and KREEP trace-element signature of basaltic impact melts from the Moon indicate that the Mg suite must represent a major contributor to the bulk composition (Fig. 1).

Origin of the Highlands "Megaregolith": The upper zone of the Moon's crust has been heavily processed by repeated impact cratering. In our model, it is analogous to the regolith found at any Apollo site in a shallow maria, such as Apollo 11 [1]. In that case, a thin lava flow overlies a feldspathic, highlands substrate. Regolith formation by postmare craters mixes minor amounts of highlands debris into a ground-up layer of mostly basaltic composition. The resulting regolith is thus slightly contaminated with feldspathic material, although dominantly basaltic.

In the highlands crust, the inverse case holds. The original feldspathic, anorthosite crust of the Moon overlies a more mafic, "basaltic" lower crust. The massive impact bombardment of this target produces a megaregolith of dominantly feldspathic, anorthositic composition. However, small amounts of the underlying, mafic lower crust is admixed into the megaregolith, making it slightly more mafic than the anorthosite layer it rests on. As in the case at the Apollo 11 site, the dominant character of the "regolith" is that of the zone it immediately rests on, but is "contaminated" by the contrasting composition of the deep layer below it.

References: [1] Heiken G. et al. (1991) *Lunar Sourcebook*, Cambridge. [2] Clementine issue (1994) *Science, 266,* 1777–1916. [3] Lunar Prospector issue (1998) *Science, 281,* 1475–1500. [4] Wood J. et al. (1970) *Proc. Apollo 11 LSC,* 965. [5] Ryder G. and Wood J. (1977) *Proc. LSC 8th,* 655. [6] Charette M. et al. (1977) *Proc. LSC 8th,* 1049. [7] James O. (1980) *Proc. LPSC 11th,* 365. [8] Spudis P. D. and Davis P. A. (1986) *Proc. LPSC 17th,* in *JGR, 91,* E84. [9] Walker D. (1983) *Proc. LPSC 14th,* in *JGR, 88,* B17. [10] Warren P. (1985) *Annu. Rev. Earth Planet Sci., 13,* 201. [11] Lucey P. et al. (1995) *Science, 268,* 1150; (1998) *JGR, 103,* 3679. [12] Blewett D. et al. (1997) *JGR, 102,* 16319. [13] Lawrence D. et al. (1999) *GRL,* in press; Tompkins S. and Pieters C. (1999) *MAPS, 34,* 25. [14] Warren P. et al. (1989) *EPSL, 91,* 245. [15] Hawke B. R. et al. (1995) *LPS XXVI,* 563. [16] Bussey D. B. J. and Spudis P. D. (1999) *JGR,* in press. [17] Lindstrom M. et al. (1986) *Proc. LPSC 16th,* in *JGR, 91,* D263. [18] Taylor S. R. (1982) *Planetary Science,* LPI , 300 pp. [19] Spudis P. D. (1993) *Geology Multi-ring basins,* Cambridge Univ., 263 pp. [19a] Bussey D. B. J. and Spudis P. D. (1996) *Eos Trans AGU, 77,* F448. [20] Lucey P. et al. (1998) *JGR, 103,* 3701. [22] Bussey B. et al. (1998) *LPS XXIX,* Abstract #1352. [23] Spudis P. D. et al. (1996) *LPS XXVII,* 1255.

THE MINERALOGY OF THE YOUNGEST LUNAR BASALTS.

M. I. Staid and C. M. Pieters, Box 1846, Department of Geological Sciences, Brown University, Providence RI 02912, USA.

Summary: The last stage of lunar volcanism produced spectrally distinct basalts on the western nearside of the Moon, which remain unsampled by landing missions. The spectral properties of these late-stage basalts are examined using high-spatial-resolution Clementine images to constrain their mineralogic composition. The young high-Ti basalts in the western Procellarum and Imbrium Basins display a significantly stronger ferrous absorption than earlier mare basalts, suggesting that they may be the most Fe-rich deposits on the Moon. The distinct long-wavelength shape of this ferrous absorption is found to be similar for surface soils and materials excavated from depth. The pervasive character of this absorption feature supports the interpretation of abundant olivine within these late-stage lunar deposits.

Late-Stage High-Titanium Basalts: Important distinctions exist between the early-stage eastern maria and the late-stage western basalts, even though both appear to be Ti-rich. For example, the western maria are more radiogenic than eastern deposits [1–3]. Telescopic spectra of the high-Ti western maria also exhibit a unique

combination of a strong 1-μm feature and a relatively weak or attenuated 2-μm absorption [4]. Pieters et al. [4] concluded that the unusual strength and shape of the 1-μm absorption in western basalts results from an additional absorption from abundant olivine and/or Fe-bearing glass. Either mineralogy could produce the strong long-wavelength 1-μm band, but a glassy Fe-rich surface could only form by rapid cooling along the exterior surfaces of flows.

Clementine Imagery: Clementine UV-VIS data of late-stage basalts are examined for regions in Oceanus Procellarum (HDSA) and Mare Imbrium (hDSA). The spectral properties of western regions are compared to the sampled Apollo 11 basalts in Mare Tranquillitatis, which contain similar albedos and UV-VIS spectral properties. For reference, the western basalts are also compared to the low-Ti and Fe-rich basalts in Mare Serenitatis (mISP). Serenitatis basalts have the strongest mafic absorption of any eastern nearside maria in Clementine imagery [5].

Unlike previous Earth-based and Galileo imagery, Clementine data resolve the spectral properties of immature crater deposits small enough to sample individual volcanic flows [5–6]. A strategy has been developed to reevaluate lunar basalt types using Clementine imagery of such fresh mare craters and their associated soils [5,7]. To allow direct comparisons between regions, scatter plots of useful spectral parameters were constructed by sampling a fixed number of evenly spaced pixels from each mare region. Scatter plots comparing the mare study areas are shown in Figs. 1 and 2. Since mature soils dominate the surfaces exposed, the density distribution of each data cloud has been presented after a root stretch to enhance the visibility of the less-abundant immature materials. Five-color spectra were also collected for all fresh craters within each mare region and grouped according to size.

Results: *Titanium content.* The UV-VIS ratio has been used extensively to estimate Ti in mature soils [8–9] and plots of this parameter against 0.75-μm reflectance are included for each mare region in Fig. 1. The UV-VIS ratio coupled with the 0.75-μm parameter has been applied more recently to estimate Ti content across many lunar materials [10–11]. High-Ti basalts plot in the upper left portion of Fig. 1 because of their low-albedo and high-UV-VIS ratio values.

Clementine UV-VIS ratio values for the Procellarum HDSA unit are similar to, but slightly lower than, HDWA Apollo 11 basalts (purple and dark blue respectively in Fig. 1). These values are consistent with previous evaluations of the western high Ti basalts using telescopic [9,12] and Apollo γ-ray data [13], which suggest only a minor difference in TiO_2 contents between these mare deposits. The Imbrium hDSA and Serenitatis mISP basalts (light blue and orange in Fig. 1) are seen to be progressively less dark and blue, consistent with the previously noted decreasing amount of weight percent TiO_2 [10,12,14].

Mafic mineralogy. The scatter plot in Fig. 2 captures the 1 μm absorption strength and albedo of large areas for each study region over a range of optical maturities. This scatter plot allows trends related to maturity to be evaluated [5,15–17]. Materials whose soil surfaces have not achieved optical maturity are slightly brighter and display a stronger ferrous band. For each basalt type, the result is a roughly parallel range of values for these spectral parameters forming a distinct "weathering cloud" of data [5].

The western HDSA and hDSA basalts show a much stronger mafic ratio than the Tranquillitatis basalts for both mature soils and immature crater materials (Fig. 2). Despite a higher abundance of

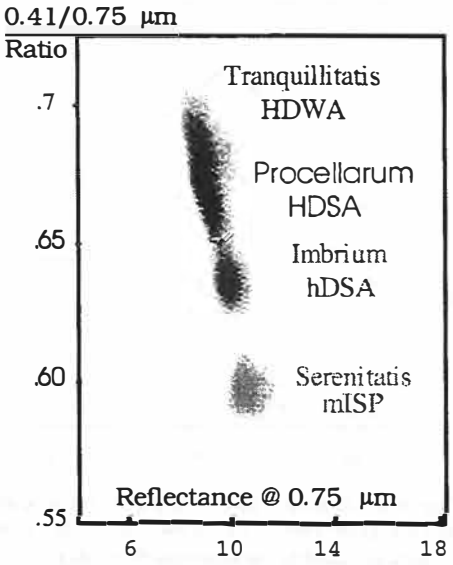

Fig. 1: Scatter plot of the Clementine UV-VIS ratio vs. 0.75-μm reflectance for each mare study area.

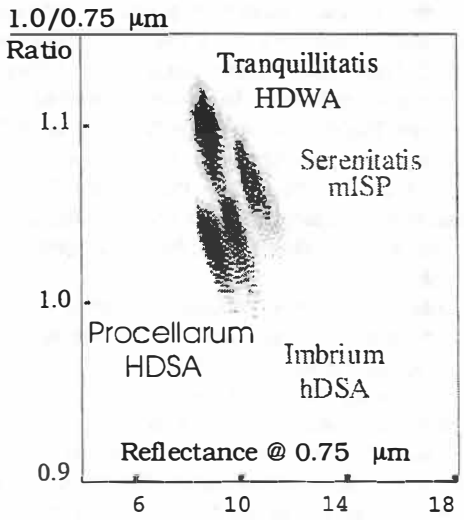

Fig. 2. Scatter plot of the Clementine mafic ratio vs. 0.75-μm reflectance for each mare study area.

opaques (which should subdue absorption features) the western HDSA and hDSA mare units also exhibit a stronger mafic ratio than the Fe-rich Serenitatis basalts. These combined properties indicate an exceptionally high abundance of mafic minerals and suggest that the Eratosthenian deposits within Procellarum may be the most Fe-rich basalts extruded on the surface of the Moon. It is difficult to estimate the FeO content of these young basalts since returned samples demonstrate that all lunar soils contain a fraction of foreign materials and mare soils have a lower weight percent FeO than their associated basalts [18–19]. We are in the process of considering such

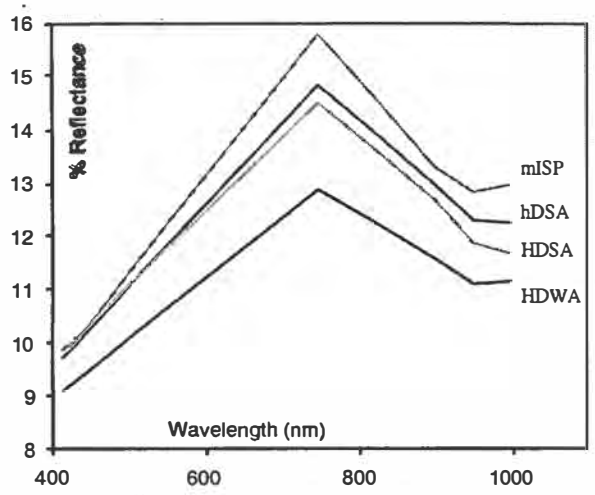

Fig. 3: Five-color Clementine spectra of the least weathered materials identified in each study region. (To view this figure in color, go to http://cass.jsc.nasa.gov/meetings/moon99/pdf/8026.pdf.)

sample information and mixing issues in order to estimate the actual FeO abundances of the mafic-rich western basalts.

Regions that represent the most immature materials within each mare area were selected by identifying pixels that correspond to the lower-right limit of each mare unit's 1-μm vs. 0.75-μm scatter plot cloud in Fig. 2. These spectra, shown in Fig. 3, allow comparisons of the strong ferrous absorption for the most crystalline materials within each basalt type. The shape of the 1-μm feature is much flatter and centered at a longer wavelength in the spectra of the western Procellarum basalts compared to the eastern Serenitatis and Tranquillitatis basalts. Spectra of immature materials from the HDSA unit exhibit the strongest downturn in the ferrous band at 1 μm of all the mare units in Fig. 3.

A strong and long-wavelength mafic absorption was found to be pervasive throughout the fresh materials excavated by craters of different size groups. Mature soils within the western high-Ti deposits also have a strong and long-wavelength ferrous band [4]. The presence of this absorption throughout the soils and crater deposits of western high-Ti basalts indicates that this optical property is inherent to the mineralogy of the basalts. This observation excludes a glassy flow surface as a source for the 1-μm feature and instead supports the alternate interpretation of abundant olivine [4] within these Fe-rich basalts.

References: [1] Soderblom L. A. et al. (1977) *Proc. LSC 8th*, 1, 1191–1199. [2] Adams J. B. et al. (1981) *BVTP*, 438–490. [3] Lawrence D. J. et al. (1998) *Science, 281*, 1484–1489. [4] Pieters C. M. et al. (1980) *JGR, 85*, 3913–3938. [5] Staid M. I. and Pieters C. M. (1999) *Icarus*, submitted. [6] Staid M. I. and Pieters C. M. (1996) *LPS XXVII*, 1259–1260. [7] Staid M. I. and Pieters C. M. (1998) *LPS XXIX*, Abstract #1853. [8] Charette M. P. et al. (1974) *JGR, 79*, 1605–1613. [9] Pieters C. M. (1978) *Proc. LPSC 9th*, 2825–2849. [10] Lucey P. G. et al. (1998) *JGR, 103*, 3679–3699. [11] Blewett D. T. et al. (1997) *JGR, 102*, 16319–16325. [12] Johnson J. R. et al. (1991) *JGR, 96*, 18861–18882. [13] Davis P. A. (1980) *JGR, 85*, 3209. [14] Melendrez et al. (1994) *JGR, 99*, 5601–5620. [15] Fischer E. M. and Pieters C. M. (1996) *JGR, 101*, 2225–2234. [16] Lucey P. G. et al. (1995) *Science, 268*, 1150–1153. [17] Lucey P. G. et al. (1998) *JGR, 103*, 3679–3699. [18] Haskin L. A. and Warren P. (1991) in *The Lunar Sourcebook*, pp. 357–474. [19] Laul J. C. and Papike J. J. (1980) *Proc. LPSC 11th*, 1307–1340.

THE LUNAR ATMOSPHERE AND ITS INTIMATE CONNECTION TO THE LUNAR SURFACE: A REVIEW.

S. A. Stern, Southwest Research Institute, Boulder CO 80302, USA (astern@swri.edu).

Due to the lack of optical phenomena associated with the lunar atmosphere, it is usually stated that the Moon has no atmosphere. This is not correct. In fact, the Moon is surrounded by a tenuous envelope with a surface number density and presure not unlike that of a cometary coma. However, the analogy ends there: The lunar atmosphere is essentially everywhere collisionless, unlike a cometary coma, its composition is quite different from that of any comet, and the extant lunar species do not create optically bright emissions. Since the lunar atmosphere is in fact an exosphere, one can think of its various compositional components as "independent atmospheres" occupying the same space.

Upper limits derived by Apollo-based instruments indicate that the entire native envelope weighs only ~100 t. However, the complexity and scientific value of this atmosphere are not commensurate with its low mass.

The lunar atmosphere contains vital information about the location of near-surface volatiles, including water; it also acts as a reservoir of gases released from the interior and may even mirror the composition of certain surface-lying mineralogical units. Furthermore, the lunar atmosphere is the most accessible of the solar system's SBEs, and offers a rich variety of physical processes to study as analogs to other SBEs across the solar system. An important advantage of the Moon for such studies is that we enjoy abundant surface samples and orbital geochemical data that provide key "boundary conditions" to the physics and chemistry at work, unlike any other similarly exposed planetary surface.

In this review I will summarize the present state of knowledge about the lunar atmosphere, describe the important physical processes taking place within it, and provide a comparison of the lunar atmosphere to other tenuous atmospheres in the solar system. Particular emphasis will be placed on the intimate connection between the lunar atmosphere and its source, the lunar regolith.

APOLLO 17 SOIL CHARACTERIZATION FOR REFLECTANCE SPECTROSCOPY.

L. A. Taylor[1], C. Pieters[2], A. Patchen[1], R. V. Morris[3], L. P. Keller[4], S. Wentworth[3], and D. S. McKay[3], [1]Planetary Geosciences Institute, University of Tennessee, Knoxville TN 37996, USA (lataylor@utk.edu), [2]Department of Geological Sciences, Brown University, Providence RI 02912, USA, [3]Mail Code SN, Johnson Space Center, Houston TX 77058, USA, [4]MVA, Inc., Oakbrook Parkway, Norcross GA 30093, USA.

It is the fine fractions that dominate the observed spectral signatures of bulk lunar soil [1–5], and the next to the smallest size fractions are the most similar to the overall properties of the bulk soil [4]. Thus, our Lunar Soil Characterization Consortium [6–8] has concentrated on understanding the inter-relations of compositional, mineralogical, and optical properties of the <45-μm size fraction and its component sizes (20–44-μm, 10–20-μm, and <10-μm size frac-

tions). To be able to generalize our results beyond the particular sample set studied, it is necessary to quantitatively identify the observed effects of space weathering and evaluate the processes involved. For this, it is necessary to know the chemistry of each size fraction, modal abundances of each phase, average compositions of the minerals and glasses, I_s/FeO values, reflectance spectra, and the physical makeup of the individual particles and their patinas. This characterization includes the important dissection of the pyroxene minerals into four separate populations, with data on both modes and average chemical compositions. Armed with such data, it should be possible to effectively isolate spectral effects of space weathering from spectral properties related to mineral and glass chemistry.

Four mare soils from the Apollo 17 site were selected for characterization based upon similarities in bulk composition and their contrasting maturities, ranging from immature to submature to mature. The methodology of our characterization has been discussed previously, [e.g., 9]. Results of the Apollo 17 mare soils, outlined herein, are being prepared for publication in *MAPS*.

Modal Analyses: As shown in Fig. 1, *with decreasing grain size, the agglutinitic (impact) glass content profoundly increases.* This is the most impressive change for the mare soils. In several soils we have examined, there is an over two-fold increase in the agglutinitic glass contents between the 90–150-μm and the 10–20-μm size fractions [7–9]. Accompanying this increase in agglutinitic glass is a *definite decrease in pyroxenes and to lesser extents, the oxides (ilmenite), volcanic glass, and olivine.* Unexpectedly, however, the *absolute plagioclase abundances stay relatively constant* throughout the different grain sizes, although the abundance of plagioclase relative to the mafic minerals increases with decreasing particle size.

Soil Chemistry: These soils were chosen for study based upon their similarities in FeO and TiO_2 content, allowing for direct comparisons between evolutions of chemistry between size fractions and among different maturities of soils. The bulk chemistry of these fractions was determined by EMP analyses of fused glass beads.

In contrast to the systematic variations in bulk chemistry discussed below, the relatively uniform composition of agglutinitic glass with grain size and soil maturity is illustrated in Fig. 2. The composition of the bulk fraction of each size fraction becomes more feldspathic with increasing maturity, with the effect being most pronounced for the finest fractions. The composition of the agglutinitic glass, however, is relatively invariant and more feldspathic (i.e., rich in Al_2O_3) than even the <10-μm fraction. This relation not only strengthens the "fusion of the finest fraction" (F^3) hypothesis [11–12], but also highlights the important role of plagioclase in the formation of agglutinitic glass.

As described by Taylor et al. [8], with decreasing grain size, FeO, MgO, and TiO_2 contents decrease, whereas CaO, Na_2O, and Al_2O_3 (plag components) increase for all soils. This relationship is illustrated in Fig. 3. These chemical variations would appear to be coupled with the significant increase in agglutinitic glass and decrease in oxide (ilmenite), pyroxene, and volcanic glass. *These changes in chemistry do not appear to be due to distinct changes in the compositions of individual phases but to their abundances.*

I_s/FeO Values: As shown in Fig. 3, *values of I_s/FeO increase with decreasing grain size,* even though the bulk FeO contents decrease. That is, the percentage of the total Fe that is present as nanophase Fe° has increased substantially in the smaller size fraction. Note that the increase in nanophase Fe° in smaller size fractions is significantly greater than the increase in agglutinitic glass content,

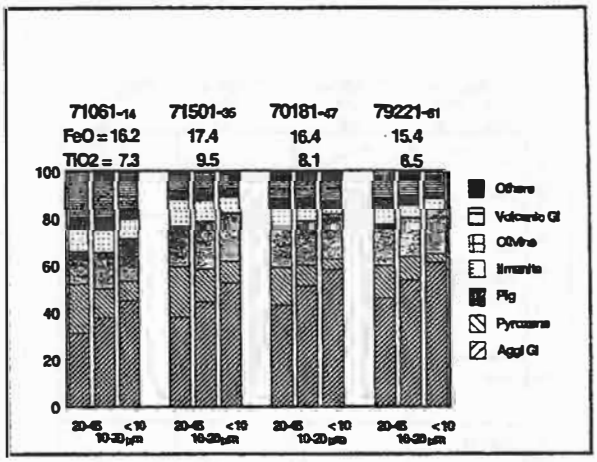

Fig. 1. Cumulative modal percentage of Apollo 17 mare soil components.

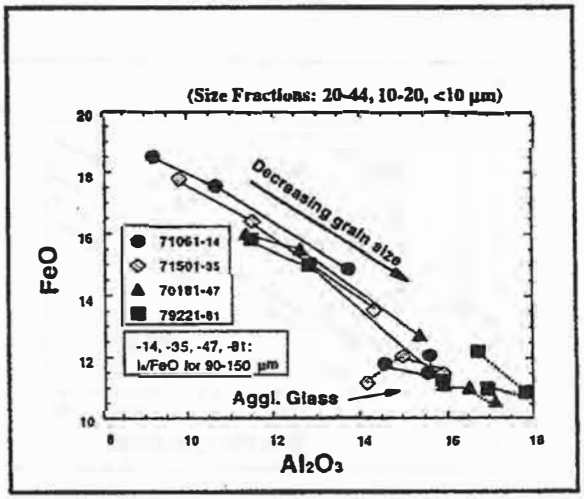

Fig. 2. Apollo 17 mare soil chemistry.

with its single-domain Fe° component. This would seem to indicate that at least some of the Fe° is surface correlated. To illustrate this effect, if it is assumed that the nanophase Fe° is entirely surface correlated, then equal masses of 15-μm and 6-μm spheres should have ~3× as much Fe° in the finer fraction. The recent findings of Keller et al. [13–18] of the major role of vapor-deposited, nanophase Fe°–containing patinas on most soil particles is a major breakthrough in our understanding of the distribution of Fe° within agglutinitic glass and upon grain surfaces.

Reflectance Spectra: Bidirectional reflectance spectra for a representative Apollo 17 soil (70181) are shown in Fig. 4. The size separates all have similar albedo in the blue and follow a regular sequence in which the continuum slope increases, ferrous bands weaken, and albedo increases with decreasing particle size. The bulk <45-μm soil is typically close to the 10–20 μm spectrum. It is important to note that although *the finest fraction* (<10 μm) is close in composition to the abundant agglutinitic glass in each size fraction

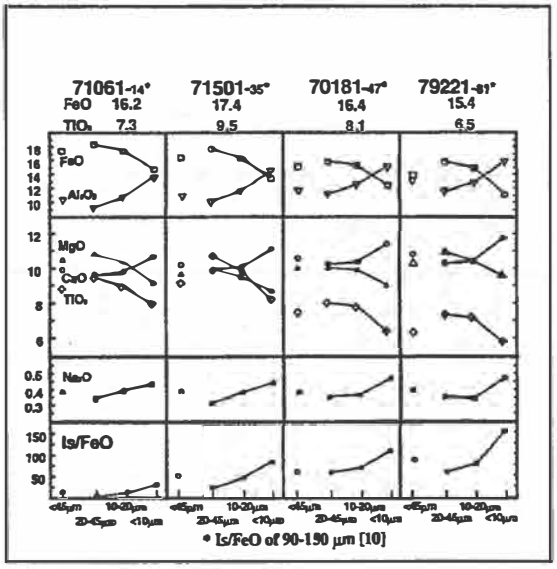

Fig. 3. Soil chemistry.

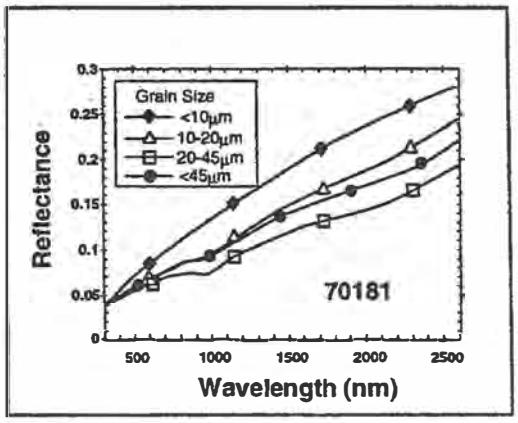

Fig. 4. Bidirectional reflectance spectrum.

(see above), this size fraction is relatively featureless and *does not dominate the spectrum* of the bulk <45-μm soil.

Volcanic Glass: It has long been suspected that agglutinitic glass, to a large extent, is the product of melting of the finest fraction of the soils [11–12], with a dominance of plagioclase. Given the low abundance of pyroxene in the finest fractions of each soil (Fig. 1), the source of the FeO in these Apollo 17 agglutinitic glasses is not fully identified. We suspect the abundant volcanic glass in these samples may be a significant contributor and this hypothesis will be tested with the suite under study from other Apollo sites. If the abundance of Fe-rich volcanic glass plays a significant role in the composition of agglutinitic glass in these soils, it may account for the significantly lower albedo observed remotely for areas with abundant volcanic glass.

References: [1] Pieters (1993) *Remote Geochem. Anal.*, Cambridge Univ., 309 pp. [2] Fischer and Pieters (1994) *Geol. Remote Sens.*, 1287. [3] Fischer and Pieters (1994) *Icarus, 111,* 475. [4] Fischer (1995) Ph.D. dissertation, Brown Univ. [5] Pieters and Taylor (1998) *New Views, LPI Contribution No. 958,* 6. [6] Taylor et al. (1998) *LPS XXIX.* [7] Taylor et al. (1998) *New Views, LPI Contribution No.958,* 71. [8] Taylor et al. (1999) *LPS XXX.* [9] Taylor et al. (1996) *Icarus, 124,* 5596. [10] Morris (1977) *Proc. LSC 8th,* 3719. [11] Papike et al. (1981) *Proc. LPC 12B,* 409. [12] Walker and Papike (1981) *Proc. LPSC 12B,* 421. [13] Keller and McKay (1997) *GCA, 61,* 2331. [14] Keller et al. (1998) *LSC XXIX.* [15] Keller et al. (1998) *New Views, LPI Contribution No. 958,* 44. [16] Keller et al. (1999) *LPSC XXX.* [17] Wentworth et al. (1999) *MAPS,* in press. [18] Keller et al., this volume.

GLOBAL GEOCHEMICAL VARIATION ON THE LUNAR SURFACE: A THREE-ELEMENT APPROACH.

D. R. Thomsen[1], D. J. Lawrence[1], D. Vaniman[1], W. C. Feldman[1], R. C. Elphic[1], B. L. Barraclough[1], S. Maurice[2], P. G. Lucey[3], and A. B. Binder[4], [1]Mail Stop D-466, Los Alamos National Laboratory, Los Alamos NM 87545, USA (thomsend@lanl.gov), [2]Observatoire Midi-Pyrenees, 14 ave Ed Belin, 31400 Toulouse, France, [3]Hawai'i Institute of Geophysics and Planetology, University of Hawai'i, Manoa HI, USA, [4] Lunar Research Institute, 1180 Sunrise Drive, Gilroy CA 95020, USA.

Introduction: We present a method for displaying the relative abundances of three important elements (Th, Fe, and Ti) on the same map projection of the lunar surface. Using Th-, Fe-, and Ti-elemental abundances from orbital geochemical data and assigning each element a primary color, a false-color map of the lunar surface was created (Fig. 1). This approach is similar to the ternary diagram approach presented by Davis and Spudis [1] with some important differences, discussed later. For the present maps, Th abundances were measured by the Lunar Prospector (LP) Gamma-Ray Spectrometer (GRS) [2]. The new LP GRS low-altitude dataset was used in this analysis [13]. Iron and Ti weight percentages were based on Clementine spectral reflectance data [3] smoothed to the LP low-altitude footprint. This method of presentation was designed to aid in the location and recognition of three principal lunar compositions: ferroan anorthosite (FAN), mare basalts (MB), and the Mg suite/KREEP-rich rocks on the lunar surface, with special emphasis on the highlands and specific impact basins [1,4–12]. In addition to the recognition of these endmember rock compositions, this method is an attempt to examine the relationship between elemental compositions that do not conform readily to previously accepted or observed endmember rocks in various specific regions of interest, including eastern highlands regions centered on 150° longitude, and a northern highlands Th-rich region observed by Lawrence et al. [13].

Method: The LP low-altitude data has full width at half-maximum spatial resolution of ~40 km [13]. The Clementine spectral reflectance datasets were adapted using an equal-area, gaussian smoothing routine to this footprint. In addition, these datasets, reported in weight percent of FeO and of TiO_2, were adjusted to Fe and Ti weight percentages. Each dataset was then assigned one of the three primary colors: blue for Th, red for Fe, and green for Ti. For each element, the data range was normalized to represent the ratio of each point to the maximum in the dataset. This color table provides a scheme as follows: pure red, green, or blue indicates the presence of the pure form of the respective element; white indicates the maximum values of all three elements (Th ≈10.3 μg/g, Fe ≈15.6%,

and Ti ≈ 7.5%); black indicates the lack of or exceedingly low values of each of the three elements. Any other color indicates a different mixture of the three. (To view the color table, go to http://cass.jsc.nasa.gov/meetings/moon99/pdf/8033.pdf.) The full range of lunar longitudes is represented, but due to the lack of coverage of the Clementine data for latitudes > 70° and <–70°, the data for these regions is excluded. The differences between this approach and the ternary diagram approach of Davis and Spudis [1] eliminate some of the uncertainty and ambiguity of the ternary diagram approach. Rather than using a ratio of Th to Ti normalized to CI chondritic ratios, and a ternary diagram with ternary apexes located at specific endmember compositional values, elemental compositions were used independently, eliminating the errors resulting from dividing numbers that can have high uncertainties, especially at low concentration [13].

The three elements used in this method of presentation were chosen for several reasons. One reason for the inclusion of Th in this study is that it is an accurate indicator of KREEP. Iron and Ti concentrations are both low in highland regolith, causing any small fluctuations in Th to stand out very well. In addition, Fe and Ti are good compositional indicators of different mare basalts. Mixed with red for Fe, the green for Ti produces a yellow signal in high-Ti basalts. While universally high in Fe relative to the surrounding highlands, mare basalts have a diverse range of Ti values, making Ti concentration a valuable asset to the classification and identification of different basalt types. Finally, an important constraint in element selection is the availability of the global data, both from LP and Clementine results. Data for Th, Fe, and Ti are among the highest quality of existing lunar remote-sensing data. In addition, LP data for Fe and Ti will become available, enabling these data to be incorporated into the analysis.

Results: Using upper-limit values for endmember rock compositions calculated from Korotev et al. [14], attempts were made to locate the different endmember compositions of terranes on this diagram. Most strikingly, ferroan anorthosite (Th ≤ 0.37μg/g; Fe (wt%) ≤ 2.29; Ti (wt%) ≤ 0.22) [13], which should appear as an almost black, reddish color, does not appear on the diagram at any noticeable frequency. Based on this analysis, the suggestion of extensive FAN regions on the lunar surface is not strong, especially at the presently accepted values for Fe and Th. However, to make sure this

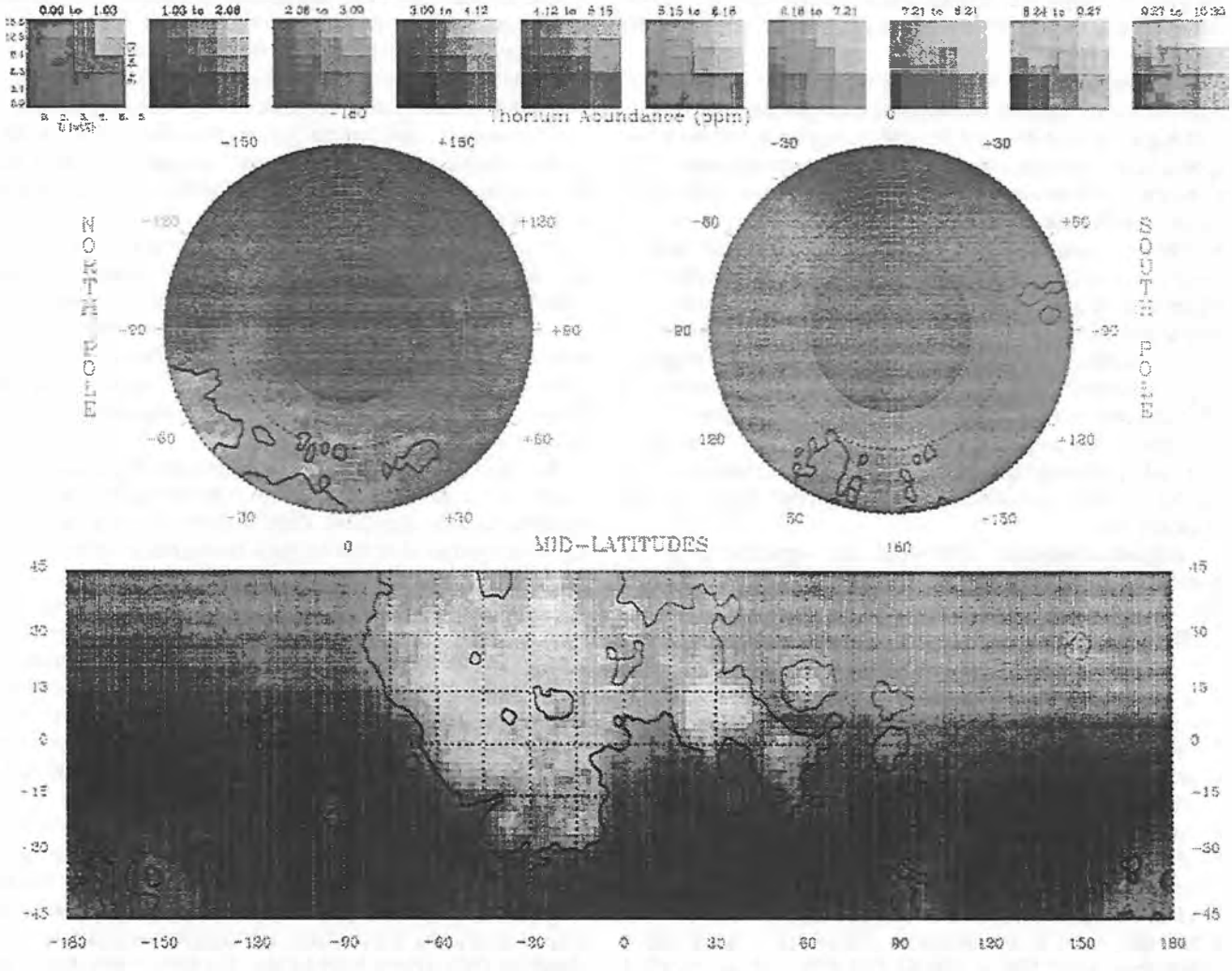

Fig. 1.

effect is not due to systematic errors, a thorough investigation of the precision, accuracy, and uncertainties of the Fe, Ti, and Th abundances needs to be carried out, especially at low concentrations.

A particular region of interest is an area of high Th concentrations relative to Fe and Ti content north and east of Humboldtianum Crater. First observed by Lawrence et al. [13], this region does not coincide with any visible impact structure and comprises one of the closest approximations to pure blue (high Th, very low Ti and Fe) on the lunar surface. Such an elemental composition does not lend itself readily to classification, and presents something of an anomaly. More detailed analysis of this region is needed to understand its structure and origin.

There seems to be a longitudinal asymmetry in the Th concentrations of the highlands regolith. High-Th, low-Ti, and Fe regions are located between 135° and 180° longitude and between –30° and +30° latitude. While the Th levels are not high enough to attract attention in a single elemental display, the variation in the abundance of Th relative to Fe and Ti abundances can be clearly seen. The composition that these data suggest is not well represented in the sample-return suite. In addition, these regions were largely missed by the Apollo orbital ground tracks, which only covered the outer edge of the areas of interest [15]. The LP orbital Th data represent the first information about the Th concentrations in these regions of the highlands.

Regions containing MB and Mg suite/KREEP-rich compositions are readily apparent. MB deposits (average composition: Th ≈ 0.913μg/g, Fe ≈ 14.4%, and Ti ≈ 2.5%) appear as yellowish and appear in the Serenitatis-Tranquilitatis region, among others. This particular rock type is the most varied in color because of widespread variation in Ti content, and the contamination of these provinces by KREEP-rich material. Mafic, KREEP-rich impact melt breccias (average composition of Th ranging from 5 mg/g to concentrations higher than 10 μg/g , Fe ≈ 7.18%, and Ti ≈ 0.83%) are shown on the map as pink regions such as the ones near Copernicus and in the Jura mountains. This three-element mapping technique is advantageous in the visualization of different KREEP-rich terranes because, in contrast to the single-element Th map, this technique allows Fe and Ti compositional variations within KREEP-rich regions to be readily seen, aiding in the identification of underlying rock types and allowing for a better understanding of the processes behind KREEP emplacement.

Acknowledgments: This work was supported in part by Lockheed Martin under contract to NASA and conducted under the auspices of the U.S. Department of Energy.

References: [1] Davis P. and Spudis P. (1987) *Proc. LPSC 17th*, in *JGR, 92*, in E387–E395. [2] Lawrence D. J. et al. (1998) *Science, 281*, 1484–1489. [3] Lucey P. G. et al. (1999) *GRL*, submitted. [4] Duncan A. R. et al. (1976) *Proc. LSC 7th*, 1659–1671. [5] McKay G. A. et al. (1978) *Proc. LPSC 9th*, 661–678. [6] Longhi J. and Boudreau A. E. (1979) *Proc. LPSC 10th*, 2085–2105. [7] Norman M. D. and Ryder G. (1978) *Catalogs of Pristine Nonmare Rocks*, NASA JSC-14565 and -14603. [8] Ryder G. (1979) *Proc. LPSC 10th*, 561–581. [9] Norman M. D. and Ryder G. (1980) *Proc. LPSC 10th*, 317–331. [10] Walker D. (1983) *Proc. LPSC 14th*, in *JGR, 88*, B17–B25. [11] Davis P. and Spudis P. (1985) *Proc. LPSC 16th*, in *JGR, 90*, D61–D74. [12] Davis P. and Spudis P. (1986) *Proc. LPSC 17th*, in *JGR, 91*, E84–E90. [13] Lawrence D. J. et al. (1999) *GRL*, submitted. [14] Korotev R. et al. (1998) *JGR, 103*, 1691–1701. [15] Arnold J. et al. (1977) *Proc. LSC 8th*, 945.

SIDEROPHILE ELEMENT SYSTEMATICS AND THE MOON'S CORE-MANTLE DIFFERENTIATION HISTORY.

P. H. Warren, Institute of Geophysics and Planetary Physics, University of California, Los Angeles, Los Angeles CA 90095-1567, USA (pwarren@ucla.edu)

The most highly siderophile elements (HSEs), i.e., the most sensitive indicators of planetary metal-silicate differentiation, are the heavier platinum-group elements: Os, Ir, and Pt, and their periodic-table neighbors Re and Au. The HSE that has been determined most often and most successfully in lunar rocks is Ir. Even so, previous estimates of the concentration of Ir in the lunar mantle indicate great uncertainty, as they range from 0.01 [1] to 4 [2] ng/g, or 0.00002 to 0.009 × CI chondrites. This uncertainty stems from several factors, including the "nugget effect" and other analytical difficulties. The lunar HSE database is scattered amidst many papers, and in most cases analyses for Ir (and other HSE) did not simultaneously determine compatible-lithophile elements. Previous interpretations of these data in terms of mantle concentrations have involved little more than comparison between mean concentrations in lunar vs. terrestrial basalts [3]. Such interpretations are inadequate, because basalts are diverse. Even the most extremely siderophile elements exhibit compatible behavior under metal-absent conditions [4]. I have compiled a database that is a comprehensive blend of siderophile data with compatible-lithophile data for identical basaltic samples. Over 50% of the HSE data are from the compilation of Wolf et al. [5]; many of the other data are from past publications from my UCLA lab. This database manifests correlations between siderophile elements and several compatible elements that imply relatively tight constraints on the lunar mantle siderophile composition.

The notion that FeNi metal may have been a residual mantle phase that determined the HSE compositions of lunar basalts [3] is precluded by a correlation between W (which would be markedly siderophile in the presence of metal) and U [6]. Conceivably residual sulfides controlled the HSE. But textural-mineralogical observations preclude S saturation in the low-Ti basalts [7], and experimental data [8] indicate that even the most S-rich high-Ti types erupted ~50% undersaturated in S.

Nickel, although not quite a HSE like Ir, is a strongly siderophile element with a very extensive database. A plot of MgO vs. Ni (Fig. 1) manifests clearly significant, albeit nonlinear, correlation trends. The lunar trend parallels that for Earth basalts and komatiites (and a similar trend for martian rocks [9]), but is displaced to lower Ni. The MgO contents of the two mantles differ slightly, but mostly this offset reflects an ~5× lower (Ni) in the lunar mantle vs. its terrestrial counterpart. The terrestrial trend passes through the MgO content of Earth's mantle at Ni ≈ 2200 μg/g. The implied Ni content of the lunar mantle is ~ 400 μg/g. The hypothesis [2] that (Ni) is the same in the lunar and terrestrial mantles is clearly untenable. Ni shows similarly strong correlations vs. Cr and V (except among terrestrial rocks, where V is generally incompatible with olivine).

A plot of MgO vs. Ir (Fig. 2) shows greater scatter, but the same basic relationships. Again, the lunar data form a trend that parallels the Earth trend, but at a displacement indicating ~6× lower (Ir) in the lunar mantle vs. its terrestrial counterpart. This same inference extends at least to Os, which shows an excellent correlation vs. Ir, at chondritic Os/Ir, among lunar basalts. The lunar mantle Re/Ir (and Re/Os) is also at least nearly chondritic; Au/Ir, however, gives some indication of being as much as 3× greater than chondritic. The

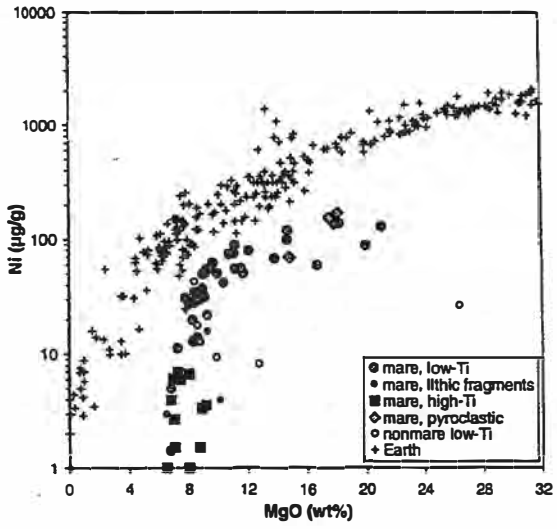

Fig.1.

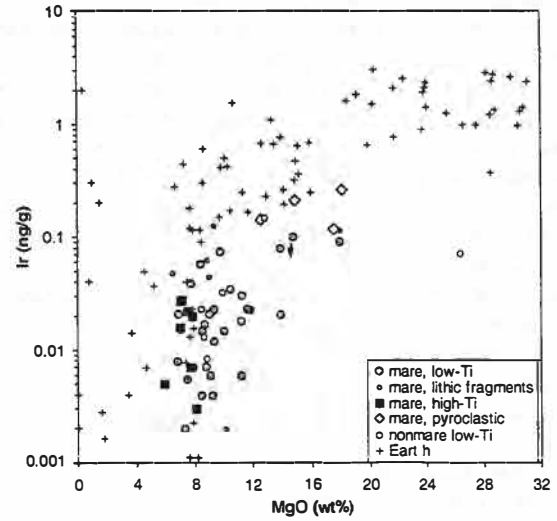

Fig. 2.

inferred composition implies that Ni/Ir is enhanced in the lunar mantle by nearly the same factor, ~30 × CI chondrites, as in Earth's mantle.

In a sense, it is remarkable that the lunar mantle siderophile depletions are not much greater. In the case of the Earth and Mars, the hypothesis that siderophiles were added as a veneer after differentiation of the core [e.g., 9] remains controversial. In the case of Earth, high-pressure dampening of metal/silicate partitioning behavior [e.g., 10] may have played a more important role. Recent Lunar Prospector results indicate that the Moon possesses a core amounting to 1–2 wt% of its bulk mass [11]. The depletion factor Δ implied by an equilibrium between the silicate portion of the planet and its core can be calculated from the simple mass balance

$$\Delta = 1/(Dc+[1-c])$$

where c is the weight fraction of the core and D is the core/silicate (metal/silicate?) distribution coefficient. With a low-pressure metal/silicate D of the order 5×10^5 [12] and perhaps much higher [13], Ir should have been depleted in the lunar mantle to about 0.0002× the bulk-Moon concentration (which in any event is presumably not chondritic for siderophile elements, given the Moon's gross depletion in Fe metal). For Ni, the metal/silicate D is roughly 25× lower [12], so core-mantle equilibration for Ni should have resulted in Δ ≈ 0.005 and Ni/Ir ≈ 25× the bulk-Moon ratio (and the implication regarding Ni/Ir is approximately the same for all finite values of c).

By many models [e.g., 2], the Moon formed largely from, and thus inherited its bulk composition largely from, Earth's mantle. If a core subsequently formed within the Moon, the Moon-mantle Ir/Ni should have been depleted by an additional factor of 25 vs. the Earth-mantle value. Thus, it is remarkable that Ir/Ni is so nearly identical in the two mantles. A gross disequilibrium between the mantle and core, i.e., accretion of a "late veneer," is most unambiguously implied for the Moon, even though the proportion of the veneer (0.1 wt% of CI-like material, based on Ir) is much less for the Moon's mantle than often suggested (~ 0.7 wt% [e.g., 9]) for the Earth's mantle.

References: [1] Newsom H. E. (1986) in *Origin of the Moon,* pp. 203–229. [2] Ringwood A. E. (1992) *EPSL, 111,* 537–555. [3] Wolf R. and Anders E. (1980) *GCA, 44,* 2111. [4] Naldrett A. J. and Barnes S.-J. (1986) *Fortschr. Mineral., 64,* 113–133. [5] Wolf R. et al. (1979) *Proc. LPSC 10th,* 2107–2130. [6] Palme H. and Rammense W. (1981) *Proc. LPS 12th,* 949–964. [7] Brett R. (1976) *GCA, 40,* 997–1004. [8] Danckwerth P. A. et al. (1979) *Proc. LPSC 10th,* 517–530. [9] Warren P. H. et al. (1999) *GCA,* in press. [10] Tschauner O. et al. (1998) in *Origin of the Earth and Moon,* pp. 48–49. [11] Konopliv A. S. et al. (1998) *Science, 281,* 1476–1480. [12] Jones J. H. (1995) in *Rock Physics and Phase Relations: A Handbook of Physical Constants* (T. J. Ahrens, ed.), pp. 73–104. [13] Borisov A. and Palme H. (1995) *GCA, 59,* 481–485.

THE TRANSPORT OF MAGMA FROM THE MARE SOURCE TO THE SURFACE.

M. A. Wieczorek and R. J. Phillips, Campus Box 1169, Department of Earth and Planetary Sciences, Washington University, One Brookings Drive, St. Louis MO 63130, USA (markw@wurtzite.wustl.edu).

Introduction: Alhough it has been known from the beginnings of the space age that the lunar mare basalts are primarily located on the nearside of the Moon, the definitive cause of this phenomenon has remained a mystery. One popular explanation is that the hydrostatic pressure of the mare source controls the eruption of mare basalts. In this scenario, the depth of the mare source controls the maximum height that magma can rise in the crust. If the maximum depth of the mare source was globally uniform, then mare basalts would only be able to erupt at the surface below a critical elevation. Following the discovery of the Moon's 2-km center-of-mass/center-of-figure offset [1], many have suggested that the higher elevations of the lunar farside could have prevented farside magmas from reaching the surface due to their lack of the necessary pressure in their source [e.g., 2–3].

Recent data obtained from the Clementine and Lunar Prospector missions suggest that this scenario may be a bit simplistic. Using Clementine altimetry data, the full topographic extent of the South Pole Aitken Basin has been determined [4]. Even though the lowest elevations of the Moon were found to occur within this basin's floor, mare flows in this basins are volumetrically insignificant when compared to the nearside basins and Oceanus Procellarum. If elevation

was the only factor controlling the eruption of basalts, then this basin should surely have been completely flooded [5] . Gamma-ray data from the Lunar Prospector mission [6] also suggest that elevation is not the only factor that controls the eruption of mare basalts to the surface. Based on the surface distribution of KREEP, as well as results from previous studies [e.g., 7–9], it has recently been argued [10–13] that the Procellarum and Imbrium region of the Moon is a unique geochemical crustal province enriched in incompatible and heat-producing elements (named the "Procellarum KREEP terrane," or PKT). Wieczorek and Phillips [11] have noted that more than 60% of the Moon's mare basalts reside within this province, and have argued for a genetic relationship between the two. Specifically, by placing a layer of KREEP basalt in this province, their thermal models predict that the lunar mantle should have partially melted only beneath this province. The eruption of mare basalts thus may be primarily controlled by the distribution of heat sources in the Moon.

In this study, we reexamine some of the factors that control the eruption of mare basalts on the Moon. We first show that the distribution of mare basalts is indeed limited by elevation, consistent with the hydrostatic-eruption hypothesis. Though this observation suggests a shallow depth of the mare basalt source (<135 km), the petrologically constrained depth of origin (based on the premise that the picritic magmas were multiply saturated with olivine and pyroxene in their source) suggests a deeper origin (360–500 km). We postulate and discuss three possible resolutions to this apparent paradox: (1) The eruption of mare basalts is not primarily controlled by hydrostatic forces, but rather by their buoyancy; (2) the petrologically constrained depth of origin is either not valid, or has been misinterpreted; and (3) the petrologically constrained depth of origin is correct, but mantle partial melts accumulated in shallow subcrustal magma chambers before erupting onto the surface.

The Evidence in Favor of a Hydrostatic Mechanism of Mare Emplacement: Figure 1 shows the elevation of the lunar mare referenced to the geoid. We reference the mare elevations to the geoid for two reasons. First, magma on the surface of the Moon would flow down the geopotential gradient (i.e., downhill). Secondly, for a given hydrostatic pressure in the mare source, the maximum height a column of magma can extend is a function of elevation referenced to the geoid. In Fig. 2 we plot histograms of elevation referenced to the geoid for the entire Moon, the mare within the confines of the Procellarum KREEP terrane, and the remainder of the mare outside this terrane. From this plot it is found that the eruption of mare basalts does indeed appear to be limited by elevation. In particular, no mare

Fig. 1. Elevation of the mare referenced to the lunar geoid. The spatial distribution of mare is taken from the mapping of [19], and the location of the mare/highland contacts is estimated to be accurate to within 60 km.

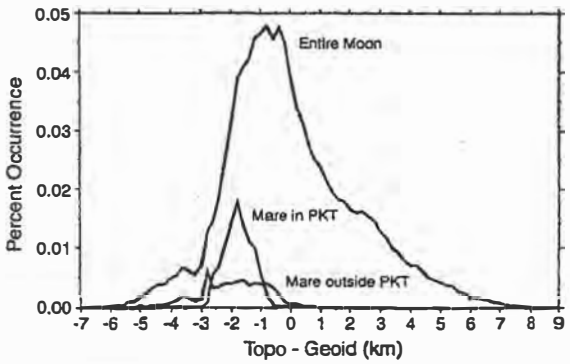

Fig. 2. Histograms of lunar elevation referenced to the geoid for the entire Moon, the mare inside of the PKT, and the mare outside of the PKT.

flows occur above an elevation of 2.6 km, and the vast majority of flows occur below ~0.5 km. This is true for both mare basalts that erupted inside and outside the confines of the PKT. This result is consistent with the hypothesis that hydrostatic forces in the mare source control the eruption of basaltic magmas, if the maximum depth of the mare source is globally uniform.

The maximum elevation of mare basalts can be used to determine the maximum depth of the mare source by performing a simple force balance. For mechanical equilibrium, the pressure at the base of a column of magma must be balanced by the Moon's reference hydrostatic pressure at this depth. We have attempted to maximize the depth of the mare source in this calculation by taking extreme values of the density and bulk modulus of the mare basaltic magmas. These values were computed at the material's liquidus temperature using the technique of Delano [14] and the data of [15] and [16] for the mare basaltic reference suite of [17]. The variation in density of this magma with depth was determined using the second-order Birch-Murnaghan equation of state, and gravity was computed as a function of depth.

If mare basalts only erupt below an elevation of 2.6 km, then from the above considerations, a column of magma in hydrostatic equilibrium at this elevation would extend to a depth of 135 km below the surface. If this column of magma were to extend deeper into the lunar mantle, then it would have been possible for mare basalts to erupt at elevations higher than are observed. It is natural to interpret this depth as the maximum depth of the mare source, and as a working hypothesis we assume this to be the case. We note, however, that this interpretation appears to be inconsistent with the petrologically constrained depth of the mare source. Assuming that the picritic glasses were multiply saturated in olivine and pyroxene in their source, the mare basalts (which are likely derived from these magmas) should have all been derived from depths between 360 and 500 km [e.g., 18]. In addition, if the magmas parental to the picritic glasses fractionated olivine before erupting, then these depths should be interpreted as a lower limit.

In the following sections, we briefly discuss three possible scenarios that may rectify the disparity between the depth of the mare source based on hydrostatic and petrologic arguments.

The Eruption of Basalts Is Controlled by Buoyancy: If the density of mare basaltic magmas was less than that of the surrounding crust, then these melts would have been able to rise to the surface based on buoyancy forces alone. Though the upper anorthositic crust

of the Moon is certainly less dense than most mare basaltic magmas, many have argued [e.g., 20–22] that the lunar crust becomes progressively mafic with increasing depth below the surface. A typical cited value for the density of the lower crust of the Moon is about 3.1 g/cm^3, and we find that all of the mare basaltic magmas are less dense than this value.

Geophysical crustal thickness modeling [23] and investigations of the composition of basin ejecta [e.g., 24] suggest that the upper anorthositic crust may have been completely excavated during the impact events that formed the multiring basins. If this is true, then, based on buoyancy forces alone, mare basalts could have been able to rise to the surface within the confines of these basins. The crustal thickness models of [23] show that mare basalts are indeed present wherever the upper crust is predicted to be absent (most notably, the nearside basins and SPA), consistent with this hypothesis.

Though this explanation does not account for the presence of mare basalts in the Australe Basin and Oceanus Procellarum, we note that our understanding of crustal composition and structure is incomplete, and that the crust in these regions may in fact be more mafic than the geophysical crustal thickness models predict.

The Petrologically Constrained Depth of Origin Is Not Valid or Has Been Misinterpreted: It has commonly been assumed that the pressure at which the picritic glasses are multiply saturated with olivine and pyroxene represents the hydrostatic pressure of the mare source. Using a relationship between pressure and depth in the Moon, this assumption necessarily constrains the depth of origin of the mare basalts.

This assumption may be flawed in two ways. First, if large degrees of melting occurred in the mare source (on the order of 40%), then olivine would have been the only phase present in the crystalline residuum. The depth of the mare source based on the multiple-phase saturation assumption would, in this case, be an *overestimate*.

Secondly, it is well known that when rocks melt at constant pressure, the volume of the melt is ~10% greater than the corresponding solid phases [e.g., 15]. If melting were to occur under constant volume conditions (as may be appropriate in the lunar mantle), the process of melting would give rise to an excess pressure in the mare source. Using the data of [15] and [16], 17% melting of the mantle at a depth of 135 km would give rise to an excess pressure of about 12 kbar. The pressure of the mare source in this case would correspond to the reference hydrostatic pressure of the Moon at a depth of ~400 km.

Dikes Do Not Extend All the Way from the Mare Source to the Surface: Even though melting may have occurred at depths greater than 500 km in the Moon, there is no guarantee that open fractures will exist from this depth all the way to the surface. For instance, magma transport in the mantle may have occurred primarily by porous flow. Only when this rising magma reached a rheological barrier (such as the base of the crust or lithosphere, or a layer of depleted mantle) would it begin to accumulate and intrude the lower portion of the crust as dikes. As magma continued to accumulate at these barriers, dikes would intrude to higher levels in the crust, and would eventually erupt onto the surface.

Conclusions: Each of the above scenarios appears to reconcile the disparity between the hydrostatic and petrologic depth of the mare source. Though all three may play a role, we are continuing to investigate the relative importance of each.

References: [1] Kaula W. M. et al. (1972) *Proc. LSC 3rd,* 2189. [2] Solomon S. C. (1975) *Proc. LSC 6th,* 1021. [3] Head J. W. and Wilson L. (1992) *GCA, 56,* 2155. [4] Zuber M. T. et al. (1994) *Science, 266,* 1839. [5] Smith D. E. et al. (1997) *JGR, 102,* 1591. [6] Lawrence D. J. et al. (1998) *Science, 281,* 1484. [7] Metzger A. E. et al. (1973) *Science, 179,* 800. [8] Warren P. H. and Wasson J. T. (1979) *Rev. Geophys., 17,* 73. [9] Wasson J. T. and Warren P. H. (1980) *Icarus, 44,* 752. [10] Haskin L. A. (1998) *JGR, 103,* 1679. [11] Wieczorek M. A. and Phillips R. J. (1999) *JGR,* submitted. [12] Jolliff B. L. (1999) *JGR,* submitted. [13] Korotev R. L. (1999) *JGR,* submitted. [14] Delano J. W. (1990) *Proc. LPSC 20th,* 3. [15] Lange R. A. and Carmichael I. S. E. (1987) *GCA, 51,* 2931. [16] Kress V. C. and Carmichael I. S. E. (1991) *Contrib. Mineral. Petrol., 108,* 82. [17] BVSP (1981) *Basaltic Volcanism on the Terrestrial Planets*. [18] Longhi J. (1992) *GCA, 56,* 2235. [19] Wilhelms D. E. (1987) *U.S. Geological Survey Spec. Paper 1348.* [20] Ryder G. and Wood J. A. (1977) *Proc. LSC 8th,* 655. [21] Spudis P. D. and Davis P. A. (1986) *Proc. LPSC 17th,* in *JGR, 91,* E84. [22] Wieczorek M. A. and Phillips R. J. (1997) *JGR, 102,* 10933. [23] Wieczorek M. A. and Phillips R. J. (1998) *JGR, 103,* 1715. [24] Spudis P. D. et al. (1984) *Proc. LPSC 15th,* in *JGR, 89,* C197.

A VIEW OF THE LUNAR INTERIOR THROUGH LUNAR LASER RANGE ANALYSIS.

J. G. Williams, D. H. Boggs, J. T. Ratcliff, C. F. Yoder, and J. O. Dickey, Jet Propulsion Laboratory, California Institute of Technology, Pasadena CA 91109, USA (James.Williams@jpl.nasa.gov).

Introduction: Laser ranges between observatories on the Earth and retroreflectors on the Moon started in 1969 and continue to the present. Recent range accuracies are 2 cm while earliest ranges are an order of magnitude less certain. Four retroreflectors are ranged: three located at the Apollo 11, 14, and 15 sites and one on the Lunakhod 2 rover. Accurate analysis of the range data determines a number of lunar science parameters. The lunar interior variables include a fluid-core parameter.

Data Analysis: The Lunar Laser Ranging effort is reviewed in [1]. Many parameters are detected through their influence on rotation. Also detected are solid-body tides and accurate selenocentric reflector locations. Determined through the rotation are moment-of-inertia differences, gravitational harmonics, potential Love number, and dissipation effects due to tides and molten core. The rotation of the Moon is not at its minimum energy state; some recently active process has caused free librations [2]. The moment differences contributed to the recent improvement of the Moon's moment of inertia from the Lunar Prospector gravity field [3]. The Love numbers provide bulk elastic properties. Future possibilities for measurement include oblateness of the core-mantle boundary and core moment.

Dissipation: A study of dissipation signatures in the rotation determines tidal Q vs. frequency and concludes that the Moon has a molten core [4]. At 1 month the tidal Q is 37 and at 1 yr it is 60. The core radius is ≤352 km for Fe and ≤374 km for the Fe-FeS eutectic. The core detection exceeds 3× its uncertainty. The spin of the core is not aligned with the spin of the mantle and torque arises from the velocity difference at the boundary. Yoder's turbulent boundary layer theory [5–6] is used to compute the radii.

Tidal Heating: The present heat generation from tides and core interaction is minor compared to radiogenic heating. The heating for

ancient times is more interesting. Peale and Cassen [7] investigated lunar tidal heating while the lunar orbit expanded due to tides on Earth. Their calculations predate the measurement of Q and should be multiplied by 3.45 to match the lunar-laser-determined Love number and monthly Q. Tidal-heating computations depend on how fast the lunar orbit evolved and whether the tidal dissipation is localized. Neither is known, but plausible assumptions lead to early central region temperature increases of several hundred degrees. Most of the energy is deposited early in the Moon's history.

Core Heating: The turbulent boundary layer theory allows a prediction of energy dissipated at the core-mantle boundary during orbit evolution. Under the assumption that the properties of the early core are the same as at present, the energy dissipated by core-mantle interaction is about the same as for tidal dissipation, but it is deposited in a smaller volume. This source of energy is capable of promoting convection in an early fluid core and driving a dynamo. This is a transient phase with a duration depending on the rate of orbit evolution. Plausible assumptions lead to a duration of a few hundred million years. Thus, the remnant magnetization of many lunar rocks is compatible with a brief global magnetic field powered by dynamical energy dissipation.

Future Data: Analysis of the lunar laser ranges is providing information on lunar geophysics. Future data will improve accuracies of present solution parameters, and several more interior effects should be detectable.

References: [1] Dickey et al. (1994) *Science, 265,* 482–490. [2] Newhall and Williams J. G. (1997) *Celestial Mechanics and Dynamical Astronomy, 66,* 21–30. [3] Konopliv A. S. et al. (1998) *Science, 281,* 1476–1480. [4] Williams et al. (1999) *LPS XXX,* Abstract #1984. [5] Yoder C. F. (1981) *Phil. Trans. R. Soc. London A, 303,* 327–338. [6] Yoder C. F. (1995) *Icarus, 117,* 250–286. [7] Peale S. J. and Cassen P. (1978) *Icarus, 36,* 245–269.

A STUDY OF AN UNMANNED LUNAR MISSION FOR THE ASSAY OF VOLATILE GASES FROM THE SOIL.

L. J. Wittenberg[1], I. N. Sviatoslavsky[2], G. L. Kulcinski, and E. A. Mogahed, [1,2]Fusion Technology Institute, University of Wisconsin-Madison, 1500 Engineering Drive, Madison WI 53706, USA (kulcinski@engr.wisc.edu).

Introduction: The success of a manned lunar outpost may require that indigenous resources be utilized in order to reduce the requirements for the periodic resupply from Earth for the human inhabitants. Some indigenous lunar resources do exist. For instance, studies of the lunar regoliths, acquired by the Apollo and Luna missions from several maria, indicate that upon heating in a vacuum, these soils evolve the volatile gases: helium (He), hydrogen (H_2), carbon dioxide (CO_2), carbon monoxide (CO), nitrogen (N_2), and sulfur dioxide (SO_2). The He, H, C, and N were originally implanted by.solar wind [1]

These gases would be valuable to supply life-support systems. For instance, the H_2 could be used as a rocket fuel, or alternatively, reacted with the mineral ilmenite ($FeTiO_3$), indigenous to the lunar soil, to yield water (H_2O). In an enclosed structure irradiated by solar energy, the H_2O, N_2, and CO_2 could be utilized to grow edible plants for lunar inhabitants. Alternatively, the H_2O could be electrolyzed, using photovoltaic cells, yielding breathable O. The inert gas, He, would be useful for filling inflatable structures. In addition, the lunar He contains a high abundance of the rare isotopic ^{3}He, which has been identified as a potentially valuable fuel for nuclear-fusion space power systems.

In order to determine the economic potential of these lunar volatiles, we need information to assess the *in situ* quantities of these gases and identify the most abundant sites. In order to acquire such information, a large number of soil samples must be acquired and analyzed because it is not known if these volatile gases in the soil vary widely over the distance of a few meters or several kilometers. In addition, all of the lunar soil samples were analyzed on Earth, after being contaminated by terrestrial air and water. For these reasons, therefore, a mobile, robotic vehicle has been proposed that would be landed on a lunar maria and assay the volatiles evolved by heating the indigenous lunar regolith.

A lunar rover platform with the sample equipment attached has been designed. This science platform was conceptionally designed to fit on a small Marsokhod Rover (75 kg) with a 100-km range.

Sample Collection and Analysis: The proposed sampling protocol would be to collect two samples, nearly adjacent. If the results agreed within the experimental deviation, the rover would proceed 0.5 km along the planned route and select two new samples. The progress of the rover and the results of the analyses would be continuously monitored from Earth so that the sampling protocol could be revised as needed.

The scientific equipment would accomplish the assay of the regolith samples in the following sequence: (1) retrieve a sample of regolith from the lunar surface by use of a scoop mounted on the platform; (2) reduce the sample to ~1 g of particles <200 μm; (3) weigh the sample; (4) characterize the mineral content (TiO_2); (5) heat the sample to 1200°C in a vacuum furnace; (6) collect the volatiles; (7) characterize the volatile products; and (8) transmit the data.

Analytical Equipment: The components of the scientific package were conceptually designed and are briefly described:

1. *The heater unit.* A 1-g sample of the surface regolith would be placed in a ferritic steel crucible 0.8 cm OD × 1.57 cm high. This container would be placed in a coiled electrical heater inside an evacuated 1-L container. Heat transfer calculations indicate that the sample would attain 1200°C in 14 min with a 25-W heater. For a high-Ti maria regolith sufficient gases are released to create a pressure of 70 Pa at 30°C, which is a sufficient sample for the mass spectrometer.

2. *Determination of metallic elements.* Before the sample is heated, a laser beam delivers 0.45–2.0 Joules per pulse at a wavelength of 1 μm to the surface of the sample. The absorption of the laser energy vaporizes some of the minerals in the soils. The vaporized ions are quantitatively determined by the mass spectrometer.

3. *Mass spectrometer.* This instrument must be utilized to characterize the mineral content of the soil and the volatile gases, essentially from 1 to 72 AMU range. A Fourier Transform Mass Spectrometer (FTMS) may be particularly useful for this analysis, but requires testing.

4. *Power supply.* The initial power subsystem assumed the availability of a general purpose heat source, or a Radioisotope Thermoelectric Generator. If the launch of an RTG is forbidden for safety reasons, alternative power supplies would be considered such as solar-electric or beamed microwave sources.

References: [1] Heiken G. H. et al. (1991) *Lunar Sourcebook: A User's Guide to the Moon,* Cambridge Univ.